NUMERICAL SIMULATION OF DYNAMIC CENTRIFUGE TESTS ON CONCRETE FACED ROCKFILL DAM

BY

MUHSIN ACAR

THESIS

Submitted in partial fulfillment of the requirements
for the degree of Master of Science in Civil Engineering
in the Graduate College of the
University of Illinois at Urbana-Champaign, 2018

Urbana, Illinois

Adviser:

Professor Youssef M. A. Hashash

ABSTRACT

The design details of concrete faced rockfill dams (CFRDs) have depended extensively on empirical relations and experience. Empirical relations may become insufficient, however, as the height of the dam increases, or when geometric complexities are involved and coupled with complex loading conditions such as seismic loads. To make up for these limitations, numerical tools can give valuable insight into how CFRDs respond to both static and seismic loading conditions. This thesis utilizes numerical simulations using finite element method to study nonlinear dynamic responses of CFRDs.

The first part of the study reviews the current state of design details of CFRDs. The design details include properties of commonly used embankment zones, concrete faces, and plinths, including compaction methods of zones, particle sizes, thickness of layers during placement, slab and plinth dimensions, etc. In addition, the performance of some well-documented CFRDs are summarized.

The second part of the study evaluates the computed seismic response via numerical simulations representing prototype centrifuge experiments performed on a CFRD model. The effects of two factors on the computed response are investigated: (1) impact of un/reloading rules (hysteretic behavior), and (2) interface type between concrete face and rockfill (welded and friction contact) on the computed seismic response of the CFRDs. The numerical results are evaluated by comparing with measurements in terms of accelerations, bending moment increments of the concrete face, spectral accelerations and lateral deformations. The comparisons show that the proper representation of the hysteretic damping of the rockfill and the interface type have a key role in capturing the measured response of the dam. The analyses demonstrate the effectiveness of employed numerical tools in representing the seismic response of CFRD.

ACKNOWLEDGEMENTS

I would first like to express my very deep appreciation to my advisor, Professor Youssef M. A. Hashash for his advice, encouragement, and patient guidance throughout this project. His assistance and directions allowed me to exceed my own expectations and I greatly value the opportunity to work with him as his student.

I would like to express my sincere appreciation and gratitude to graduate researcher Ozgun A. Numanoglu, who have made great contribution to my education, for his consistent collaboration and patience in both academic and non-academic matters throughout my research.

I would also like to express my special thanks to graduate researchers Yuamar Imarrazan Basarah and Okan Ilhan, who were also the members of the research team I involved in. Their assistance and support made all the difference. I would also like to thank Professor Dong-Soo Kim of the Korea Advanced Institute of Science and Technology, Republic of Korea for sharing the data recorded during the centrifuge tests, which proved essential to the completion of my research.

This study would not have been possible without the financial support from the General Directorate of State Hydraulic Works of Turkey. Their support is sincerely appreciated.

To my family

TABLE OF CONTENTS

LIST OF TABLES

LIST OF FIGURES

CHAPTER 1

INTRODUCTION

1.1 Development of Concrete Faced Rockfill Dams

The advantages of Concrete Faced Rockfill Dams (CFRDs) over other types of dams have caused an increase in the popularity of CFRDs in the last decades. CFRDs are preferable to other types of dams (e.g., gravity or arch dams) because the field requirements for foundations are fewer and easier to meet, the dams are more stable, and they allow for a more flexible construction schedule (C. Marulanda & Marulanda, 2015). Furthermore, the concrete face on the upstream side of the dam prevents leakage of water, which keeps the dam body dry. As a result, the pore water pressure is not generated in the dam body during earthquakes (Sherard & Cooke, 1987).

Figure 1.1 shows the development of the height of constructed CFRDs since 1900, where the dots represent dumped CFRDs and the circles indicate compacted CFRDs. As can be seen, the height of the CFRDs started increasing after the compaction method began to be used in rockfill in the middle of the twentieth century. The increased height of rockfill dams is due to developments in technology and equipment that enabled the compaction of rockfill, allowing for less compressible material. The benefits of the use of compaction methods, which enabled designers to increase the height of rockfill dams, is also evidenced by Figure 1.2, which shows heights of various rockfill dams, including earth-core rockfill dams (ECRD), concrete faced rockfill dams (CFRD), and asphalt-core rockfill dams (ACRD), with an overall trend of increased height over time after the 1960s.

1.2 Scope of This Study

The current design of CFRDs emerged from experience and former design details of past CFRDs (Cooke, 1984). As can be seen from Figure 1.1 and Figure 1.2, the height of CFRDs has increased dramatically. However, as the height of the dams increased, construction approaches based on empirical relations and experience were not able to satisfy stability requirements (C. Marulanda & Marulanda, 2015). In several cases, severe damage occurred to the concrete face of high dams after reservoir filling, such as at the Barra Grande (Brazil), Campos Novos (Brazil), and Mohale (South Africa) dams (Marulanda-Escobar & Marulanda-Posada, 2008). Such damage not only results in expensive repair, but also threatens the safety of the dams. Earthquakes can cause even more catastrophic consequences. Therefore, predicting the behavior of CFRDs in the design process is crucial to prevent unstable conditions that may threaten the static and dynamic performance of the dam.

The focus of this study was to investigate seismic response of concrete faced rockfill dams by focusing on the hysteretic damping of the rockfill and the connection type between rockfill and concrete face using finite element method. A dynamic centrifuge test performed on a CFRD model was selected as a case study to investigate the seismic response. The measured results from dynamic centrifuge experiments were compared to the computed results from nonlinear dynamic simulations of the prototype model.

1.3 Layout of Study

Chapter 2 introduces a general overview on the construction details of CFRDs using literature reviews. The rockfill material, concrete face slab, and plinth parts of CFRDs are detailed along with the current state of the practice. Chapter 3 investigates the observed static performance

of some CFRDs considering deformations of the rockfill, deflections of concrete face and leakage rate through the dam body. Some empirical relations developed to estimate behavior the CFRDs are also presented. Chapter 4 presents nonlinear dynamic of a prototype CFRD which represents a centrifuge CFRD model used for conducting dynamic centrifuge experiments using the finite element method. In Chapter 5, the conclusions of this study are presented.

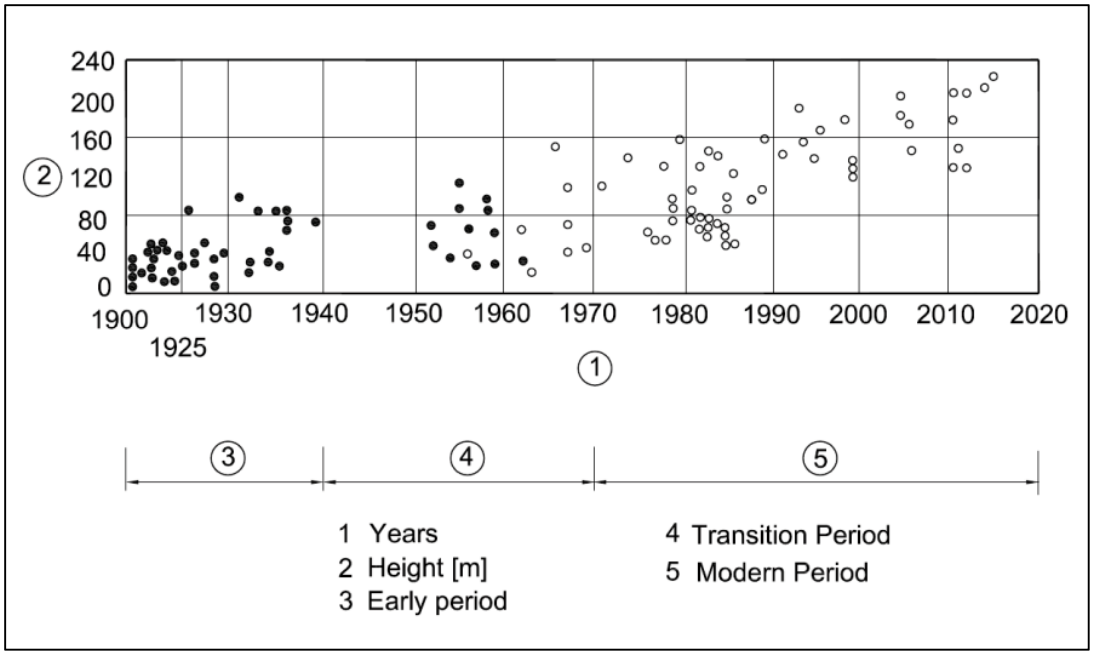

Figure 1.1: Trends in the height of concrete faced rockfill dams (CFRDs) over time (C. Marulanda & Marulanda, 2015).

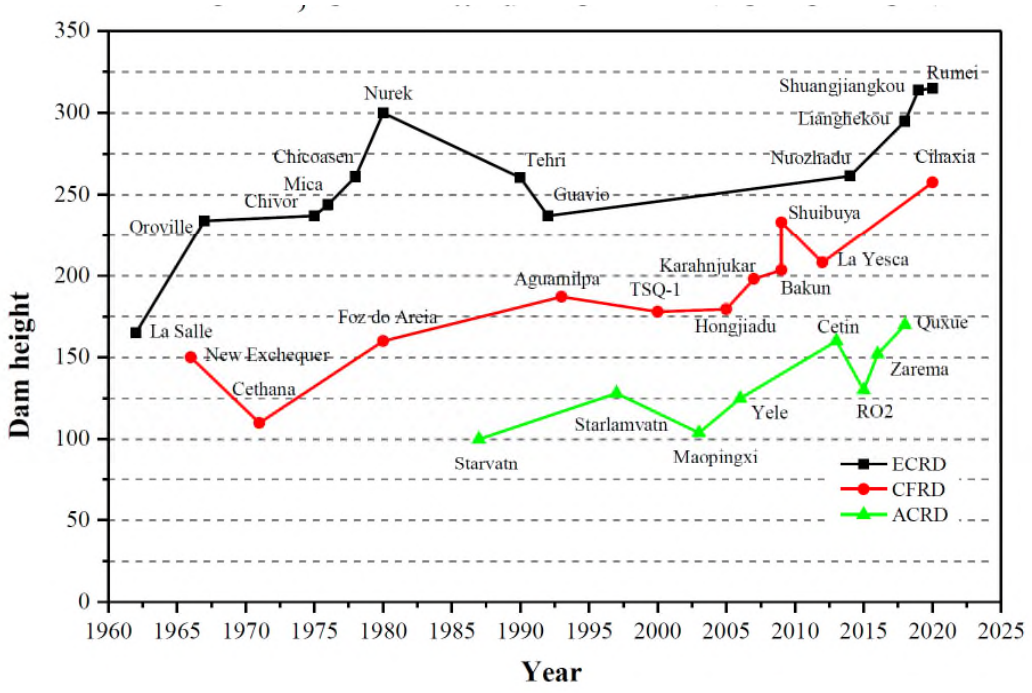

Figure 1.2: Evolution of the height of rockfill dams (m) (Xu, 2015).

CHAPTER 2

DESIGN PROCEDURE OF CFRDS

2.1 Zoning in CFRD

The main requirement to keep CFRDs operational is the prevention of cracks in the concrete slab and openings in the joints (e.g. joints between vertical panels or joints between plinth concrete face slabs). Such distresses can be prevented if the deformation of the rockfill due to reservoir load, long-term creep deformation, and seismic loads are kept small (Fitzpatrick et al., 1985). The performance of a CFRD relies on the selection of materials, the placing process of the face slab, measures taken to prevent leakage between joints, and the selection of zones. The proper selection of zones plays a key role in the performance of the dam. The dam body might consist of different rockfill material regarding characteristic of the rockfill, placement methods, particle sizes, compaction frequencies, etc., which leads to having different zonings in the dam. The typical cross section of CFRDs shown in Figure 2.1 has been extensively used as the standard zones for CFRDs. This zoning designation was proposed by Cooke and Sherard (1987). The main function of Zone 1A is to provide protection to the plinth (toe slab) and the concrete face. The material in this zone consists of impermeable cohesionless soil, such as clay or silt. Any openings in perimeter joints and cracks in the concrete face at low heights are supposed be filled with this fine-grained soil to block the water flow path through cracks (Cooke & Sherard, 1987). There is no restriction on material type in Zone 1B since its main purpose is to protect Zone 1A. These two zones can also provide buttressing to the concrete face before reservoir filling and are recommended to be put in place and compacted in layers with a thickness between 20-30 cm (ICOLD, 2010).

Zone 2 was previously used only as a bedding layer consisting of small size rockfill material under the concrete face to provide uniform support to the face slab before it started to be used as a filter material (Cooke & Sherard, 1987). This small size of the rockfill material also eased the placing process of the concrete slab and the trimming of the upstream slope. Then the function of Zone 2 evolved to be a semi-permeable layer through the addition of sand-sized particles. The use of finer particles at upstream zone decreases permeability and prevents segregation (Sherard, 1985). Such particle grading in Zone 2 reduces leakage rate due to concrete-face cracking or openings in water stops (Cooke & Sherard, 1987). It is important to obtain well-graded material for Zone 2 to minimize segregation during the construction process and to obtain uniform permeability. Nonuniform or segregated Zone 2 material is the sign of different permeability characteristics across the zone, which may cause different leakage rates across the parts of this zone in case of cracks in the concrete face. The uniform distribution of Zone 2 material also helps the concrete face to uniformly settle on the rockfill material. A grain size distribution proposed by ICOLD (1989) to set a basis for gradation of Zone 2 material is shown in Table 2.1. This grain size curve assures 40% fines (lower than No. 4 sieve), as recommended by Cooke and Sherard (1987). However, the amount of fine material in Table 2.1 was determined to be so high that it leads to cohesion and low permeability. This cohesion and low permeability indicates that cracking in this zone might occur as the rockfill experiences settlement. There are several cases where cracking in Zone 2 has been observed due to differential settlements between the rockfill zones, such as the Xingo Dam (Brazil) and the Tianshengqiao Dam (China) (ICOLD, 2010). Therefore, it was necessary to decrease the amount of fine materials to minimize the cohesion and increase the permeability. The gradation requirements for Zone 2 presented in Table 2.1 needed to be modified in order to let this zone accommodate rockfill deformations without causing cracks and

segregation, as shown in Table 2.2. The change mainly focused on decreasing the allowed percentage of fine particles (No. 200 sieve). Cohesive soil was also eliminated to make the zone flexible enough to adjust to settlement without cracking. As a result of these modifications, a well-graded Zone 2 material is expected to have a permeability of around 10^{-2} cm/s. The compaction is applied with a vibratory roller machine in 0.4-0.5 m layers (Cooke & Sherard, 1987).

Zone 3 forms the main body of the dam and consists of three subzones (3A, 3B, and 3C). The main function of Zone 3A is to filter the material of Zone 2. This filtration is needed because, without the transition material, the larger particles of the main body of the dam would allow material to infiltrate into Zone 3 and weaken the support of the concrete face. The transition material is placed simultaneously within Zone 2 in the same layer thickness as in Zone 2 (Cooke & Sherard, 1987). Zone 3B is the major carrier zone of the water load. The deformation control of this zone is important for dam safety against excessive deformations and consequent leakage. The compaction method and layer thickness are important to obtaining a low compressibility of the rockfill. This zone is recommended to have maximum rockfill size of 1 m (Cooke & Sherard, 1987). Fewer limitations are applied to Zone 3C compared to Zone 3A and Zone 3B due to less impact of water load. A maximum size of 2 m rockfill in 2 m layer thickness is recommended for use during placement for a satisfactory performance.

2.2 Placement of Rockfill

Cooke (1984) states that a stratified rockfill placement method would result in desirable properties of compacted rockfill in terms of density, strength, and permeability. This method is illustrated in Figure 2.2 for the placement of a 1 m thick layer. According to this placement process, large-sized rocks are pushed ahead of smaller rocks to fill the bottom of the lift. Then small-sized

rocks are spread in the upper part of the lift, which causes stratification. There are several advantages to this approach: (1) the contribution of compaction is considerably high on the small-sized rocks in the upper part of the lift and on horizontal interparticle contact of large-sized rocks in the bottom of the lift, (2) a smooth surface on the top of the lift is created, which is cost-effective considering that the equipment might be damaged on an otherwise irregular surface, and (3) this approach results in high horizontal permeability in the bottom layer, which allows the flow to easily be transferred downstream.

2.3 Sluicing Rockfill During Construction

The major benefit of adding water to rockfill during placement is to reduce the amount of settlement observed after construction, as it makes the fines content soft and reduces the strength of large-sized particles (Cooke & Sherard, 1987). However, this benefit depends on the strength of the rock, the height of the dam, and the amount of fines content. Cooke and Sherard (1987) described the efficiency of sluicing regarding these parameters. Softening small-sized particles results in high contact interaction between small-sized and large-sized particles. However, sluicing may not provide sufficient contribution to the behavior of low- to medium-height CFRDs with high-strength rocks.

2.4 Plinth Foundation

The connection between the foundation, including the abutment terrain and the concrete face, is secured via the plinth. Special care is required during the construction process of the plinth foundation, as the plinth ensures the contact between the concrete face and abutments and serves as the cap of the grout curtain which is built to reduce seepage forces in the foundation (Marulanda & Pinto, 2000). Other functions of the plinth are to protect the foundation against erosion and

seepage underneath (Romana, 2015). The plinth is generally built on groutable rock that is hard, sound, durable and able to withstand piping. However, it is not always the case that high-quality and non-erodible plinth foundations and abutments can be found in the field (Cooke & Sherard, 1987). Therefore, foundation treatment is necessary to mitigate the unfavorable conditions of lower quality rocks. Covering the foundation surface with shotcrete to decrease hydraulic gradient improves resistance against erosion. Another consideration of favorable foundation conditions is that a smooth and regular plinth pattern decreases the possibility of breaking the face. Sharp changes in plinth alignment should be avoided to prevent shear failures on the edges of the concrete face slab (Romana, 2015).

2.4.1 Dimensions of Plinth

The width of the plinth plays a key role in enhancing the stability of contact between the rock and the plinth foundation. Three factors are taken into consideration: (1) hydraulic gradients, (2) geologic characteristics of the foundation, and (3) foundation geometry (Cruz, et al., 2009). In modern dams a correlation between rock mass rating (RMR) using Bieniawski classification and allowed hydraulic gradient (H/L), where H is hydraulic head and L is width of the plinth, is used to design the width of the plinth foundation (Cruz et al., 2009). The correlation is illustrated in Table 2.3.

A cross section of the plinth foundation used in the Barra Grande and Campos Novos dams is shown in Figure 2.3, with dimensions. The thickness of the plinth in CFRD is nowadays recommended to be 0.9 ~ 1 m in the river bed and 0.4 ~ 0.6 m on the abutments. A thickness of 0.3 m is widely used for internal plinth.

Another assessment of plinth width design is introduced in Table 2.4. The width of plinth is adjusted considering hydraulic gradient and type of foundation under different geologic conditions (Sierra et al., 1985). This approach has been applied to the plinth design of the Salvajina Dam, where variable foundation types were found along the perimeter of the plinth.

2.5 Concrete Face Slab

After completing the major work of construction of rockfill, the concrete face is placed. It is substantial to start the construction of the concrete face after the rockfill experiences primary settlement due to its self-weight. Otherwise, the concrete face would have severe deformation issues if it were placed simultaneously with rockfill placement. The concrete face slab is the main water barrier of CFRDs. Therefore, it should be well designed in all aspects to ensure that the concrete slab conforms with rockfill deformation without losing its efficiency of impermeability. Sealing, durability, and strength of the concrete face are the most important requirements for a slab design (Cruz et al., 2009). The performance of the dam is fully dependent on deformation of the underlying rockfill, which implies that the strength of concrete becomes insufficient if large deformations in rockfill are experienced. Therefore, out of these three features, the strength design of the concrete slab (28-day concrete strength of 20 MPa to 24 MPa) is less important than the other two factors (Cooke & Sherard, 1987). The design details of the concrete face of the Cethana Dam (Australia, 1971), as described by Fitzpatrick et al. (1985), was founded on the following considerations: (1) bending should not be given attention since a face slab exposed to water load is supported uniformly by underlying rockfill, (2) the face slab should be thick enough to assure durability and waterstop equipment and reinforcement should be installed with a satisfactory thickness, (3) compression and tension in the face slab are independent of the slab thickness, (4)

large movements should be compensated at the perimetric joint without damaging the waterstops, and (5) regions experiencing tension need additional reinforcement.

The concrete face slab is poured on-site on the upstream side of the rockfill using vertical panels, which usually have a width range of 12 m to 18 m in longitudinal section. The construction of these disjointed panels leads to having joints between the edges of panels. These joints separate not only the adjacent slab panels but also the plinth from the slab. The following joint types can be defined based on their applications in several dams: (1) Perimetric Joints which connect the concrete face slab and the plinth, (2) Vertical Expansion Joints at the locations where tension is observed, (3) Vertical Compression Joints between the vertical panels usually at the middle of the concrete slab where compression is observed, and (4) Horizontal Construction Joints in long vertical panels where concrete pour is delayed by unexpected unfavorable conditions such as weather or equipment malfunction (ICOLD, 2010). Waterstops must be used in these joints to prevent leakage from upstream to downstream. A common method used in these joints consists of multiple layers of water barriers using several combined materials, such as mastic, PVC, copper, neoprene cylinder, and fine materials (Cruz et al., 2009). Typical details of perimeter and vertical joints are illustrated in Figure 2.4 and Figure 2.5, respectively. As shown in Figure 2.4, the function of fly ash placed on the upstream side of the joint is to fill any gaps in case of an opening resulting from the deformations of the dam. The fly ash is protected by a metal material. PVC material is used in the middle of joint and a copper waterstop is used on the bottom of joint. A compressive material can be used in vertical compressible joints to protect the concrete face slab from compression stresses.

2.5.1 Thickness Selection of Face Slab

The thickness of the face slab decreases linearly from bottom to top as a function of the hydrostatic head variable (H), where H is in meters. When dumped rockfills were constructed in the 1950s, the slab thickness was 0.3 + 0.0067H (m) and a slab thickness of 0.003H to 0.002H was used in the compacted rockfill dams (Cooke & Sherard, 1987). Nowadays, the widely used equation of face thickness is 0.3 + (0.002~0.003)H (Xu, 2015).

Currently, the reinforcement ratio cannot be calculated with satisfactory accuracy based on the stresses in the face slab (Marulanda-Escobar & Marulanda-Posada, 2008). The ratio of reinforcement used in the concrete face is similar to those used in the prior projects. After the compacting method became popular, the reinforcing ratio was decreased from 5% to 4~3% in each direction (Cooke & Sherard, 1987). Table 2.5 illustrates design details of the face slabs in some CFRDs concerning thickness and reinforcement ratios.

2.6 Shear Strength of Rockfill Material

The increasing rate of rockfill dam constructions has led to study of the mechanical properties of rockfill. However, the limitation of large-size testing devices has resulted in less investigation of large-size particles than of fine-grained soil. Parallel gradation technique (Lowe, 1964) is the most commonly used method to reduce sample sizes to laboratory scale without changing the uniformity coefficient (C_u). Triaxial tests have been conducted by researchers to determine the shear response of rockfill materials (Fu et al., 2017; Leps, 1970; Marsal, 1973; Varadarajan et al., 2003; Xiao et al., 2014).

Leps (1970) examined the shear behavior of rockfill and gravel materials as reported in large-scale triaxial tests. Leps showed a relation between friction angle and normal pressure based

on the collected data that can be seen in Figure 2.6. The main finding from this study is that friction angle is highly dependent on normal pressure. Friction angle is higher at low normal pressure than at high normal pressure. Leps also reached the following conclusions: (1) even though there is no adequate published data for normal pressure below 10 psi (70 kPa), the trend shows that average friction angle of 50˚and 55˚ is expected for good quality dumped and compacted rockfills, respectively, (2) shear strength of high density rockfills is higher than that of low density rockfills, (3) as the angularity of material increases, shear strength increases, (3) higher shear strength is obtained in well-graded materials, and (4) shear strength of saturated materials is lower than that of dry materials. The last item can be correlated with the benefits of sluicing during compaction of rockfill, as watering the rockfill causes breakage of particles during compaction, thus more settlement is observed during construction. This settlement during compaction results in less post-construction settlement in rockfill.

Varadarajan et al. (2003) conducted large-scale drained triaxial tests using rockfill materials collected from two different dam sites: Ranjit Sagar dam and Purulia dam (India). The study investigated the influences of particle size, particle shape, and material characteristics on the strength and deformation of rockfill material by applying different confining pressures. The particle shape of the Ranjit Sagar dam was classified as rounded/subrounded, whereas the material of the Purulia dam was found to have angular/subangular particle shape. The materials from both sites were sieved based on parallel gradation technique (Lowe, 1964) to obtain specimens with maximum particle sizes of 80, 50, and 25 mm. Impact, crushing, and Los Angeles abrasion tests were also performed on the materials. Based on the results of those strength tests, the rounded/subrounded rockfill material of the Ranjit Sagar site was found to be more durable than the angular/subangular material of Purulia. This was proved by the observation of a higher

breakage rate of particles from the Purulia site with increasing confining pressure, as shown in Figure 2.7. It is essential to note that the relation between maximum particle size and friction angle did not follow the same trend in both samples. While friction angle increased with particle size in the Ranjit Sagar dam material, an opposite relation was observed in the Purulia dam material (see Figure 2.8). This observation is consistent with findings by Lambe and Whitman (1969), which state that larger particles generate both greater interlocking, which yields higher friction angle, as well as greater particle breakage, which decreases friction angle. The breakage factor rate of the Purulia dam material at a confining pressure of 1.2 MPa increased by 7.3% when going from small to large particle size, while the factor rate increase was only 3.25 % in the Ranjat Sagar dam material at 1.4 MPa confining pressure. Thus, the increase in breakage factor of the Purulia material was high, and therefore the contributions of interlocking to shearing resistance could not help as much as expected (Varadarajan et al., 2003).

As can be seen in Figure 2.9, contractive behavior was observed in the Ranjit Sagar dam material because of crushing and rearrangement of rounded particles during shearing. The rockfill material of Purulia dam, however, showed dilative behavior because of interlocking resulted from the angularity of particles after initial contraction. The initial contraction indicated that the particle breakage occurred due to compression (Varadarajan et al., 2003). Another difference in the shear response between these two rockfill dam materials is that in the Purulia dam material the deviatoric stress of small-size particles was higher than that of large-size particles at high confining pressure, whereas in the Ranjit Sagar dam material the higher deviatoric stress was obtained from the large-size particles.

Another set of large-triaxial compression tests was performed on rockfill material by Xiao et al. (2014) to study the effects of density and confining pressure on the strength and deformation

of the rockfill. The volumetric strain and deviatoric strain measurements shown in Figure 2.10 represent the data obtained at the end of tests. An increase in volumetric strain behavior was observed as the initial confining pressure and initial void ratio increased. In contrast, deviatoric strain descended as initial confining pressure and initial void ratio increased.

2.6.1 Dynamic Properties of Rockfill

Design and construction procedures of CFRDs have made significant progress in the decades after the modern CFRDs era started in around the 1990s. With improved understanding of the soil strength of rockfill via laboratory and field tests, numerical analysis started being used to determine the design details of CFRDs. The importance of numerical analyses can be further appreciated to improve our knowledge about the behavior of dam considering the seismic effects on the performance of the dams.

The seismic performance of CFRDs is influenced by the strength of the rockfill, topography, the geometry of dam, the strength of underlying foundation, dynamic properties of rockfill, etc. The small-strain shear modulus (G_{max}) is a parameter by which rockfill's behavior under seismic loading can be described along with some other parameters, such as Poisson's ratio, increase in shear strain, hysteretic damping ratio, and reduction in secant shear modulus. Using the experimental data of rockfill from the literature, G_{max} was presented as dependent on effective mean confining pressure (σ_m) (Seed et al., 1985). Thus, small-strain shear modulus may be obtained from the following equation,

$$G_{max} = 1000(K_2)_{max}(\sigma_m)^{1/2} \tag{2.1}$$

where, K_2 is a small-strain stiffness dependent coefficient. Uddin and Gazetas, (1995) reported the coefficient of K_2 to be in a range of 40-70 (the units of stresses are in kPa) for compacted gravels

and rockfill. The determination of K_2 is important in calculating the maximum shear modulus, as it is unique for each material.

The small strain shear modulus (G_{max}) of soil can also be calculated from the shear wave velocity (V_s) of soil with the Eq. (2.2),

$$G_{max} = \rho\,(V_s)^2 \tag{2.2}$$

where, ρ is density of material.

2.7 Seismic Design of CFRDs

The performance of CFRDs under strong earthquakes is not well understood yet as most of them have been constructed in low-seismic areas. Cooke and Sherard (1987) have emphasized the inherent stability of CFRDs considering their resistance to potential threats from earthquakes and leakage. Cooke (2000) states the inherent safety advantages of CFRDs as following:

- Water flow-through does not threaten the safety of the dam, which allows for the reduction of the thickness of concrete face, decreasing the cost of construction.
- There is no need to be concerned about uplift and pore pressure.
- Rockfill materials have high shear strength.
- The resistance against seismic loading is high.

However, earthquakes can lead to severe damage to CFRDs since the concrete face integrity is sensitive to external loads and deformations. Also, there is only few case histories of high and modern CFRDs that were shaken by strong earthquakes, which clearly urges the need to investigate the dynamic behavior of CFRDs.

Next chapter further demonstrates both static and seismic performance of several CFRDs reported in the literature.

Table 2.1: Gradation limits for Zone 2 in Bulletin 70 (ICOLD, 1989).

US Standard Sieve	Size in mm	Percent Passing, by Weight (%)
3”	76.20	100
$1^1/_2$”	38.10	70-100
$^3/_4$”	19.10	55-80
No. 4	4.76	35-55
No. 30	0.59	8-30
No. 200	0.074	5-15

Table 2.2: Modified gradation limits for Zone 2 in Bulletin 141 (ICOLD, 2010).

US Standard Sieve	Size in mm	Percent passing, by weight
3”	76.2	100
$1^1/_2$”	38.1	70-100
$^3/_4$”	19.1	55-80
No. 4	4.76	35-60
No. 16	1.19	18-40
No. 50	0.297	6-18
No. 200	0.074	0-7 (non-cohesive)

Table 2.3: Correlation between RMR and hydraulic gradient (Cruz et al., 2009).

RMR	Gradient
80-100	18-20
60-80	14-18
40-60	10-14
20-40	4-10
<20	Use deeper foundation or a cut-off wall

Table 2.4: Width of toe slab of Salvajina dam (Sierra et al., 1985).

Type of Foundation	Description	Max. Hydraulic Gradient		Width of Toe Slab (m)
		Acceptable	Actual	
Original Design	Hard groutable rock	18	-	4-8
I	Competent rock	18	17.5	6-8
II	Intensely fractured rock	9	6.2	15-23
III	Intensely weathered rock sedimentary	6	3.1	15-18
IV	Intensely weathered rock (Residual soil from weathering of diorite)	6	1.3	13-14

Table 2.5: Face slab design of CFRD dams (adapted from Cruz et al., 2009).

Name	Country	Year	Height (m)	Face Slab Thickness (m)	Reinforcement (%)
Cethana	Australia	1971	110	0.3+0.002H	0.6
Foz do Areia	Brazil	1980	160	0.3+0.0034H	0.5
Aguamilpa	Mexico	1993	187	0.3+0.003H	0.3(H):0.35(V)
Xingó	Brazil	1993	145	0.3+0.003H	0.4
Campos Novos	Brazil	2006	202	0.3+0.002H (H≤100 m) 0.005H (H>100 m)	0.5 [0.3(H):0.4(V) in central]
Barra Grande	Brazil	2006	185	0.3+0.002H (H≤100 m) 0.005H (H>100 m)	0.5 [0.3(H):0.4(V) in central]
El Cajón	Mexico	2006	188	0.3+0.003H	0.4

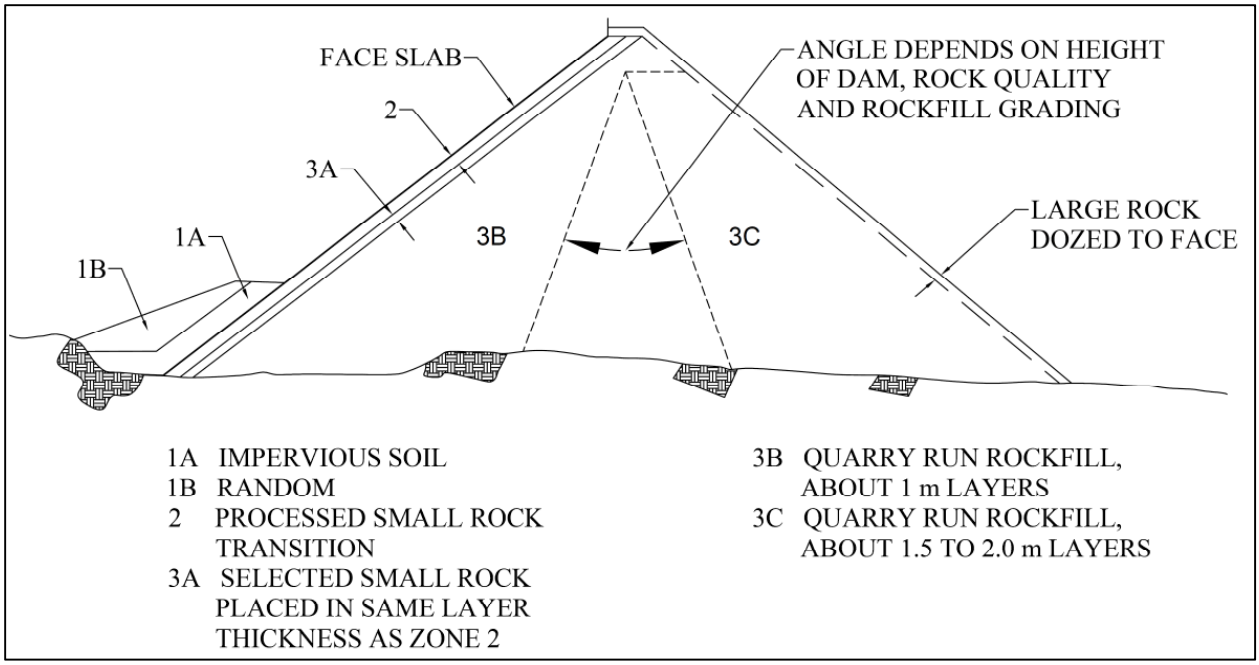

Figure 2.1: Zone designations for CFRD of sound rockfill (adapted from Cooke and Sherard, 1987).

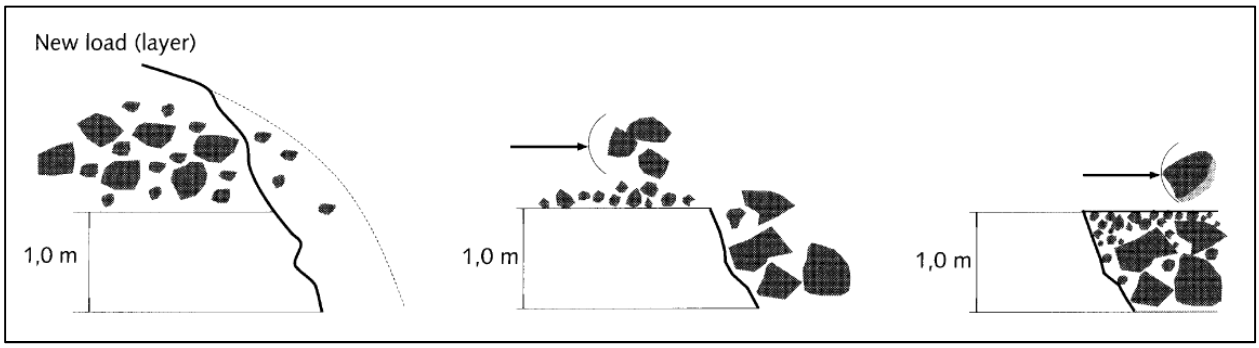

Figure 2.2: Spreading of rockfill during placement (Cooke, 1984 adapted from Cruz et al., 2009).

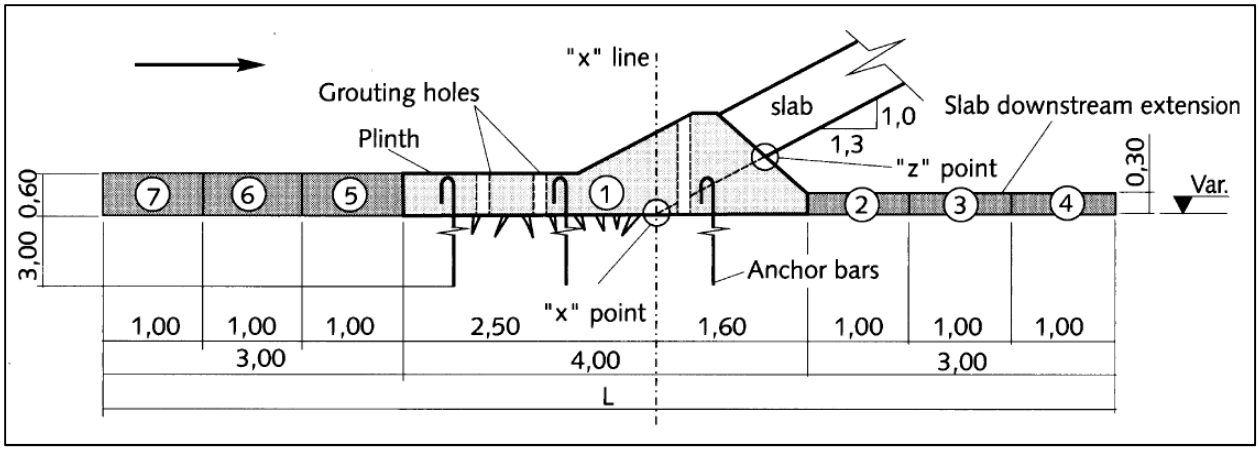

Figure 2.3: Dimensions of plinth in Barra Grande and Campos Novos dams (Cruz et al., 2009).

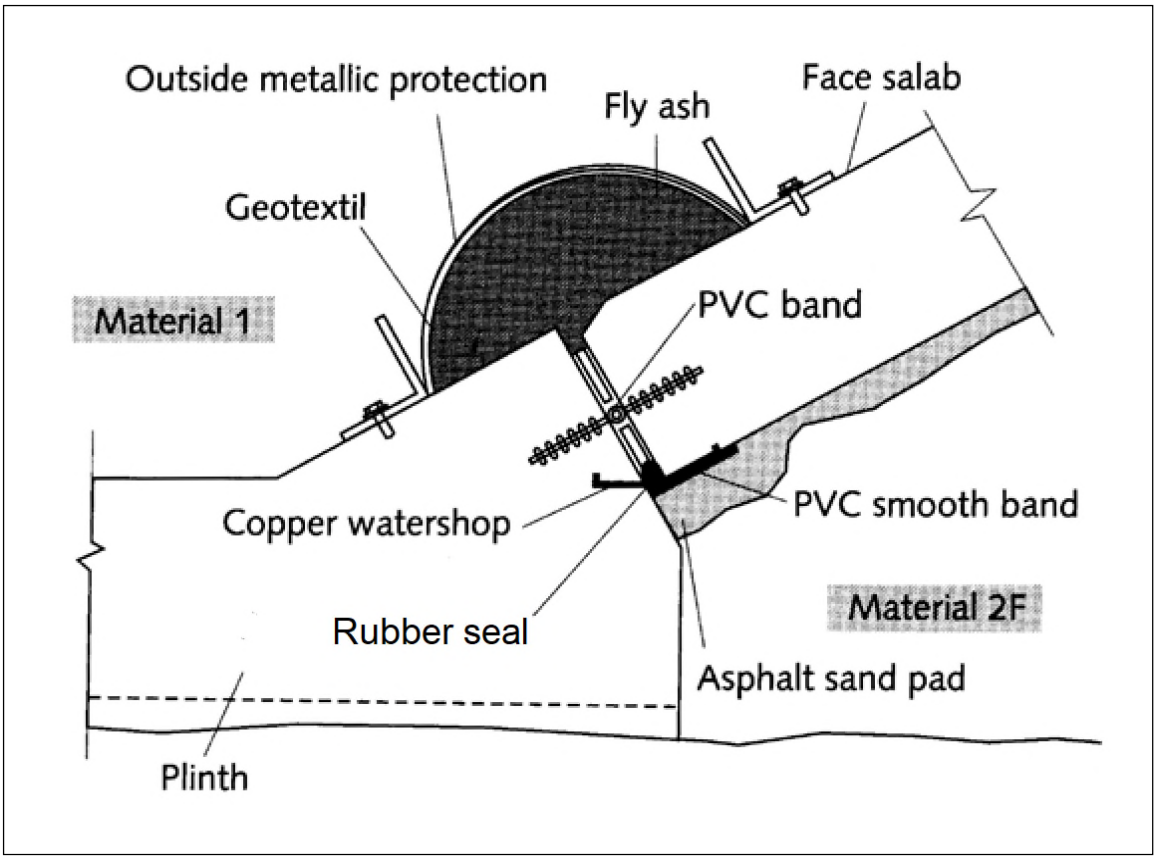

Figure 2.4: Detail of perimeter joints used in Aguamilpa dam (Cruz et al., 2009).

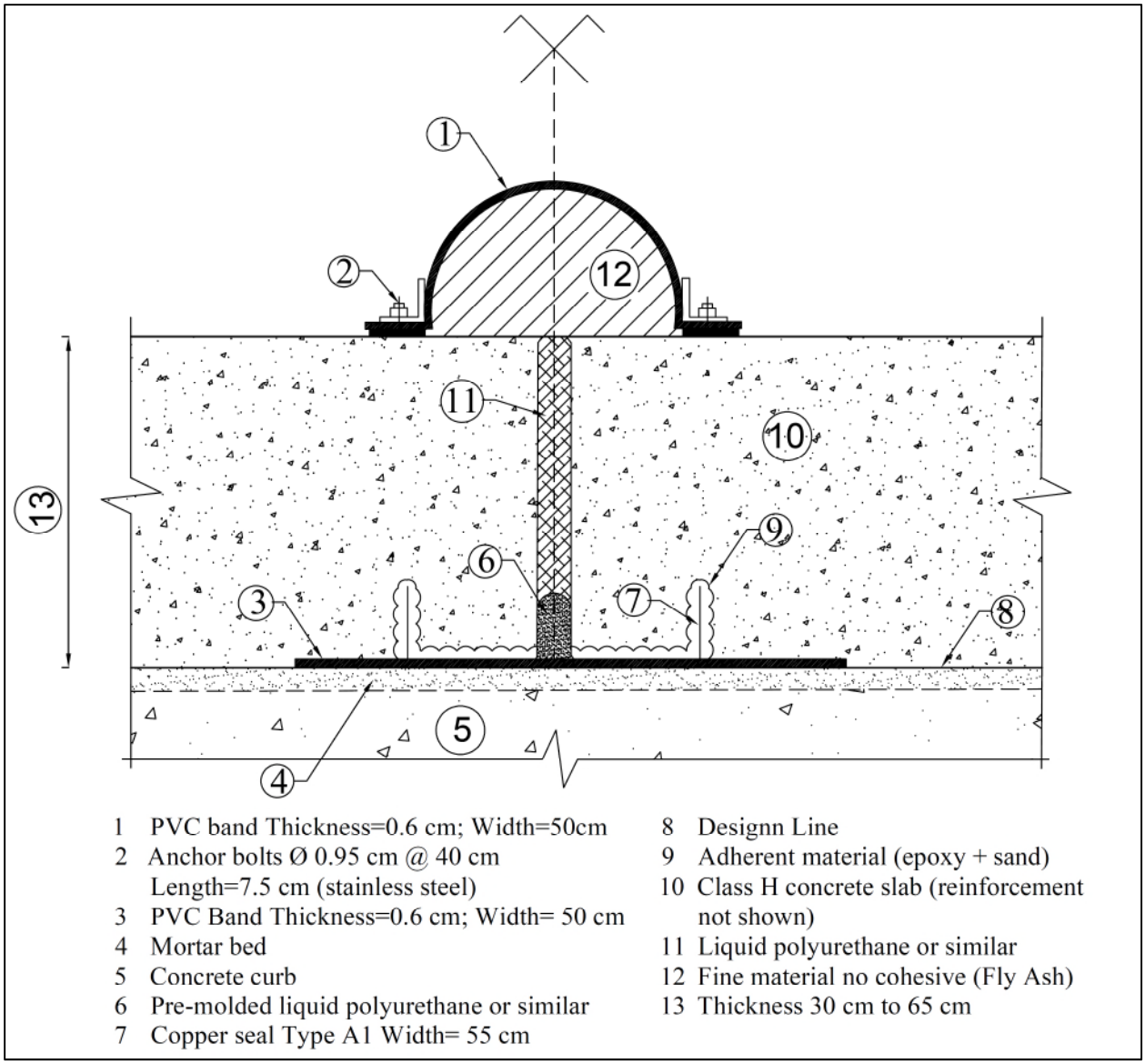

Figure 2.5: A typical vertical compressible joint (reprinted from C. Marulanda & Marulanda, 2015).

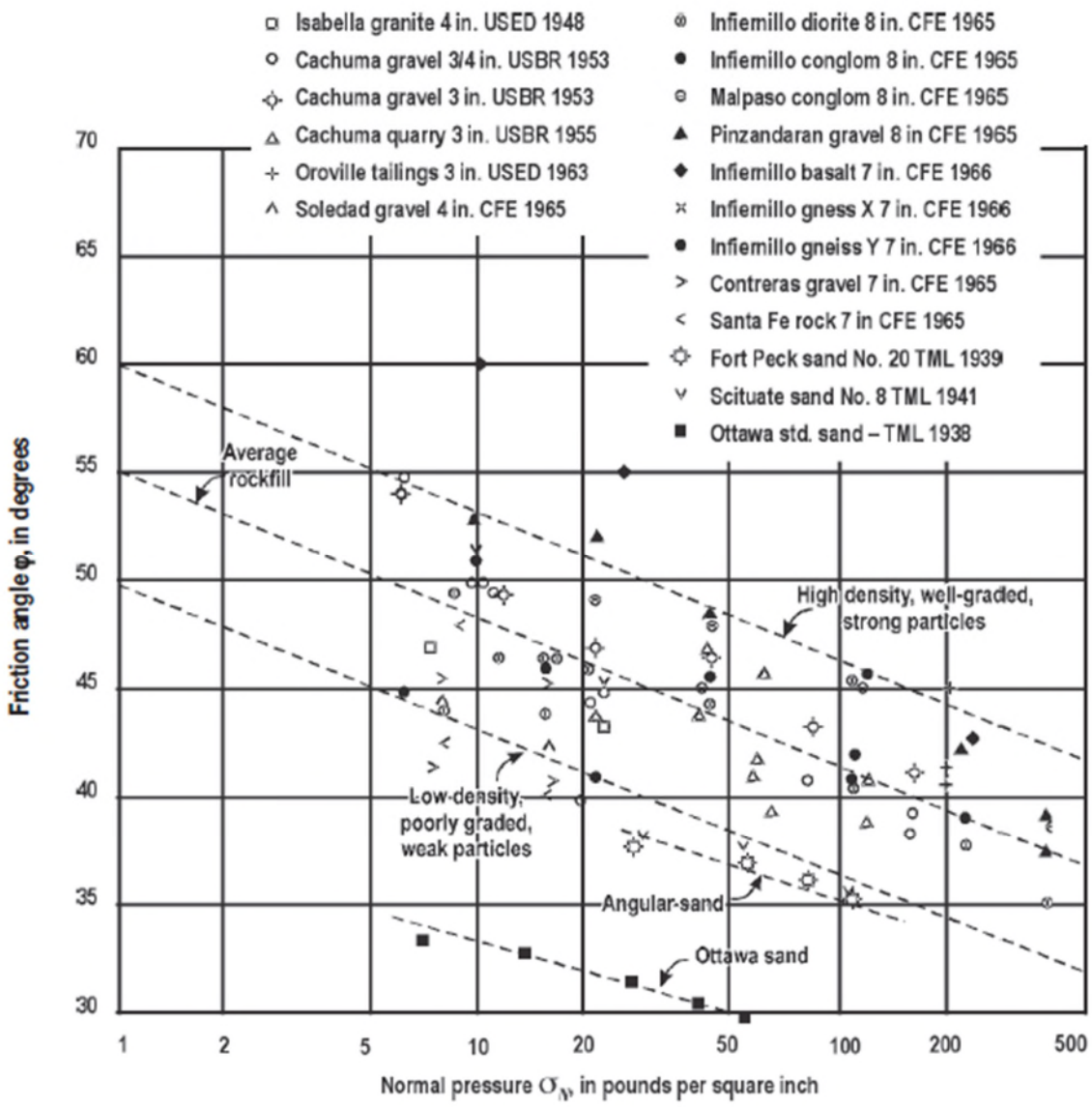

Figure 2.6: Friction angle of rockfills from large-scale triaxial tests (Leps, 1970).

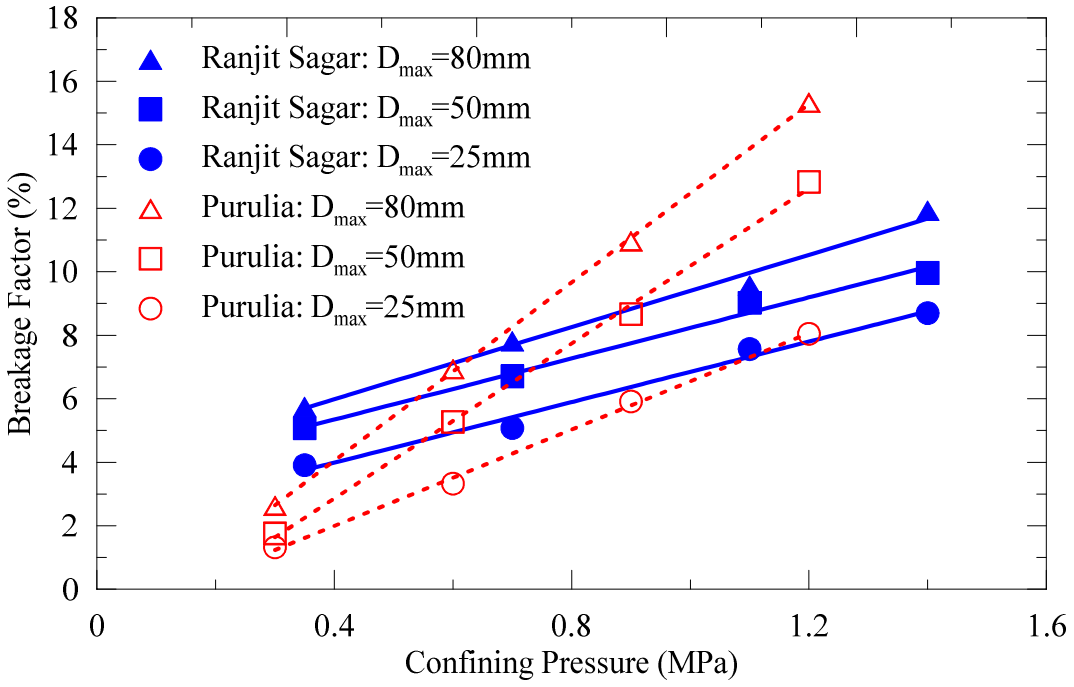

Figure 2.7: Relation between breakage factor and confining pressure (Varadarajan et al., 2003).

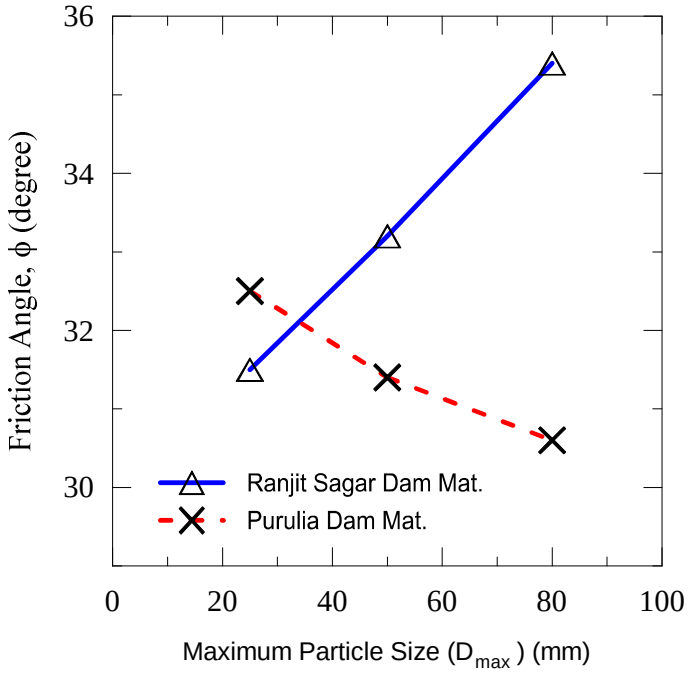

Figure 2.8: Variation in friction angle with maximum particle sizes of Ranjit Sagar and Purulia dam materials (Varadarajan et al., 2003).

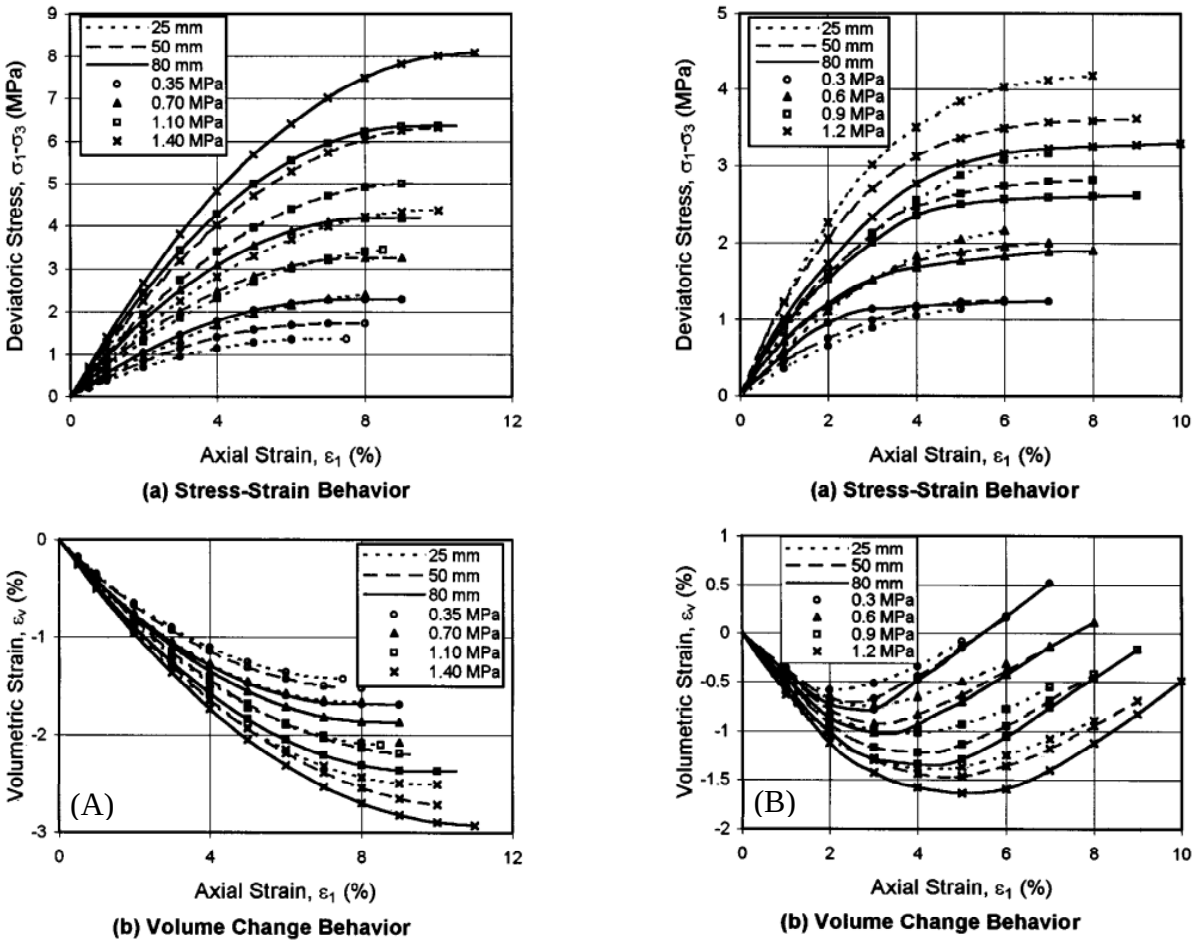

Figure 2.9: Triaxial test results of two rockfill materials: A) Ranjit Sagar dam, B) Purulia dam (Varadarajan et al., 2003).

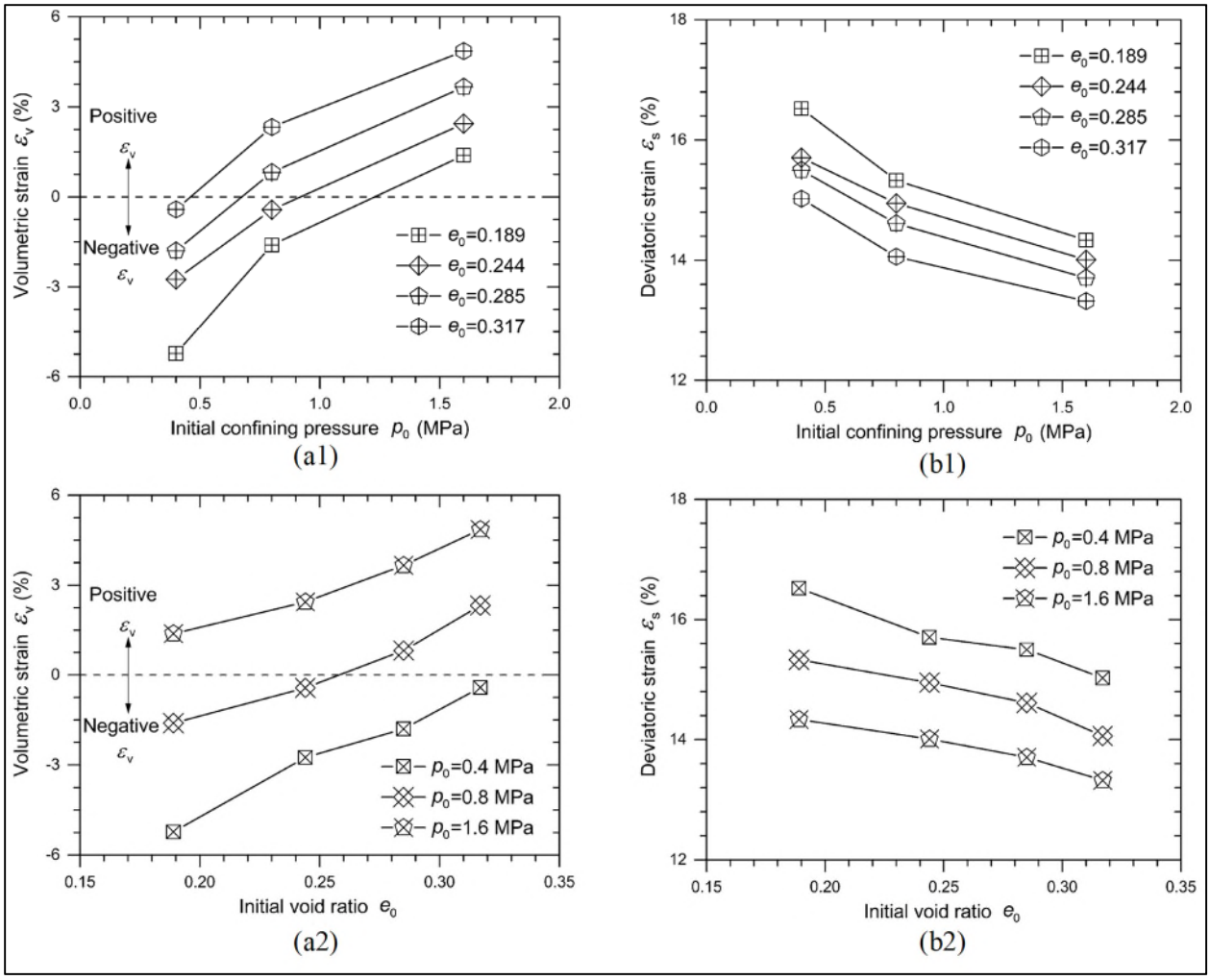

Figure 2.10: Variations in volumetric strain of rockfill material: (a1) initial confining pressure, (a2) initial void ratio; Variations in deviatoric strain of rockfill material: (b1) initial confining pressure, (b2) initial void ratio (Xiao et al., 2014).

CHAPTER 3

POST-CONSTRUCTION PERFORMANCE OF CFRDS

3.1 Introduction

The key factor related to the performance of CFRDs is the cracks occurring on the concrete face due to the large compression and tension stresses that may arise from deformation of rockfill and/or the concrete face itself. This chapter discusses both static and seismic performance of some CFRDs regarding post-construction deformations, deflections of concrete face slab, and leakage with case histories. Some empirical relations developed in the literature to estimate the behavior of CFRDs is also reviewed.

It is expected from a well-built CFRD that the magnitude of deformations will be low so that the concrete face will not suffer from excessive deflections, and thus threats will be minimized. Deflections and stresses of the face slab are heavily affected by deformation of rockfill. The density of rockfill can be controlled by compaction, which is applied to get low compressibility. Good-quality rockfill material is preferred to reduce the deformation, however, and the gradation of rockfill is also an important factor in obtaining favorable deformations. Marsal (1973) states that well-graded rockfill that has relatively more soft particles than hard particles experiences lower deformation than poorly graded rockfill having mostly hard particles. Differential settlement in different zones causes non-uniform deformations, which can lead to severe damage to the face slab. Thus, the settlement of all zones should be coordinated together.

The amount of deformation in rockfill dams is related to density, topography of the valley, rock properties, size distribution of the rockfill, height of the dam, etc. If the dam is built in a narrow valley, arching effects are likely to be seen in the dam behavior. Arching effects cause the

crest settlement to take a longer time than that of dams built in broad valleys (Sherard & Cooke, 1987). Settlements and lateral deformations of dams start during construction and continue after first reservoir impounding. Initial settlement phases are much higher than long-term settlement, which is also known as creep deformation. The creep deformation rate is generally considered to get slower with time as a dam accommodates and stabilizes. In Figure 3.1, observed long-term deformations of some dumped and well-graded compacted rockfill dams are illustrated. The settlement of the crest continues even after decades. The effect of compaction method on the behavior of rockfill can be clearly seen, as the magnitude and rate of settlement of compacted rockfill is clearly much smaller than that of dumped rockfills dams. Sherard and Cooke (1987) also emphasizes a considerable discrepancy between observed dumped and compacted rockfill dams with heights of 75-160 m for both short and long-term crest settlements. They reported that the magnitude of crest settlement of dumped rockfill is almost 5 and 8 times higher than compacted rockfill dams for the period of a 3-year operation and a 30-year operation, respectively. The predicted crest settlement of 100 m-high CFRD is 15-25 cm 5 years after construction of the dam and 15-25 cm after100 years (Sherard & Cooke, 1987).

Hunter and Fell (2003) studied the performance of 35 CFRDs to evaluate the crest settlements. Most of the dams had a height range between 75 m and 150 m. The authors concluded that compacted rockfills with heights between 50 m and 100 m with medium to high strength rockfill may experience crest settlements that range between 0.05H% and 0.15H%, while the crest settlements of dams with heights between 100 m and 150 m may range from 0.1H% to 0.15H% during first reservoir impounding. Compacted rockfills with very high strength rockfill may have a crest settlement lower than 0.05H%. As for the face deflections, Fitzpatrick et al. (1985) stated

that 60% of settlements observed at crest were usually equal to the deflection amount of concrete face slab.

3.2 Observed Static Performance of Some CFRDs

3.2.1 Miaojiaba Dam (China, 2011)

Installed instrumentations in the Miaojiaba dam provide good information about the behavior of a CFRD dam. The construction of the Miaojiaba dam was completed in 2011 in China. The height (H) and crest length (L) of the dam are 111 m and 348.2 m, respectively. The plan view and cross section of the dam with locations of instruments installed in the dam are shown in Figure 3.2 and Figure 3.3, respectively. The material of rockfill and transition zones were comprised of metamorphic tuff from the quarry with a compressive strength of 102-131 MPa, while the cushion zones were mainly made of sand and gravel. The material compaction frequency is shown in Table 3.1. The dam was built on 44-50m-thick river gravel. Therefore, a cut-off wall was built to prevent seepage through foundation under the dam. The gravel foundation was compacted to densify for minimizing the amount of settlement of the dam resulting from foundation (Wen et al., 2017).

Wen et al. (2017) states that the magnitude of maximum settlement is found to be larger than the settlements commonly seen for those types of dams. The middle of the dam height usually experiences the maximum settlement in CFRDs (Fitzpatrick et al., 1985). However, the location of maximum settlement that occurred in the Miaojiaba dam is near the foundation, which is not commonly observed in the behavior of rockfill dams. Wen et al. (2017) has attributed this behavior to settlement that occurred in the gravel foundation of the dam.

The settlement of the crest along dam axis is illustrated in Figure 3.4 for the stages before reservoir impounding, immediately after reservoir impounding, and nine months after reservoir

impounding. The water load has led to remarkable crest settlement. The middle of the crest (CS4) has experienced the maximum settlement of 279 mm within the 9-month period after reservoir impounding. The recorded settlement readings in long term across the dam cross section at elevation of 715.00 m is shown in Figure 3.5. Most of the settlement at this elevation occurred during construction. The settlement rate induced by reservoir was not as fast as the settlement induced by self-weight of the dam during construction. TC1-4 settlement gauge recorded the maximum settlements of 910 mm (0.83H%) within 1 year after reservoir impounding completion.

The lateral deformation of the dam was seen to occur towards both upstream and downstream directions before the reservoir filling stage, as illustrated in Figure 3.6. The magnitude of horizontal displacements in the upstream and downstream sides from dam axis was found to be symmetrical before the reservoir filling stage with maximum values close to slopes. The reservoir impounding has led the dam to move towards downstream with a maximum incremental movement of 25 cm (Wen et al., 2017).

The observed deformations of concrete face slab and cut-off wall were heavily affected by the reservoir load, as shown in Figure 3.7. Before reservoir impounding, the maximum deformation of cut-off was seen at the top and the direction was towards upstream, similar to dam body movement. With the reservoir impounding, the direction of movement shifted to downstream. The maximum deflection of concrete face slab was recorded at a location near dam base with value of 30 cm (0.27H%) 1 year after reservoir impounding completion.

Overall, larger deformations in rockfill and higher face deflection in concrete slab are observed in the Miaojiaba dam compared to CFRDs constructed on bedrock because the gravel foundation has experienced deformation. However, it was reported that the dam has performed

well. The measured leakage rate was 30 l/s. The overall performance of the Miaojiaba dam has indicated that CFRDs can adapt to different foundation conditions (Wen et al., 2017).

3.2.2 Aguamilpa Dam (Mexico, 1993)

The Aguamilpa dam was constructed on the Santiago River in Mexico in 1993. It was ranked as the highest CFRD in the world from 1993 to 2006 in the world, with height of 187 m and a crest length of 642 m. The maximum cross section of Aguamilpa is illustrated in Figure 3.8. The concrete face slab was constructed with 44 vertical slabs and the thickness was determined with the empirical equation of t = 0.3+0.003H (m) (Macedo-Gomez et al., 2000).

A series of extensive laboratory tests were conducted on the strength of PVC and copper waterstops for the design of perimetric joints. Based on the test results, it was decided to use 1 mm-thick PVC waterstop in the center of the joint and 12 mm-thick copper waterstop in the lower portion of the slab in the perimetric joint in order to compensate the deformations resulting from rockfill settlement with no damage (Montanez-Cartaxo, 1992) . The top of the joint was covered with fly ash, since fly ash provides satisfactory capability of decreasing the leakage rate from joint openings in case of rupture occurring in the both PVC and copper waterstops. The details can be seen in Figure 2.4.

The compaction procedure of each material used in the zones given in Figure 3.8 is represented in Table 3.2. The thickness layer of rockfill zone (3C) is 60 cm, whereas the alluvial gravel zone (3B) was compacted in 60 cm-thick layers. It was observed that there was significant difference in deformation modulus between upstream zone (3B) and downstream zone (3C), as illustrated in Table 3.3. This difference in deformation modulus has led to the 3C zone to settle more than the 3B zone.

The maximum settlement of rockfill and concrete face before reservoir filling was recorded in June 1993 with magnitudes of 170 cm (0.9H%) and 5 cm, respectively. The deformation of the concrete face was considerably small. The reservoir filling started on June 23. The equal settlement contours during three stages of reservoir filling are shown in Figure 3.9. When the reservoir water reached the elevation of 116.21 in August 1993, only 2 cm of maximum settlement measured on the upstream face, whereas the crest experienced 7 cm settlement on the downstream side. In March 1994, the amount of recorded crest settlement increased to 19 cm. The difference in settlements of upstream and downstream materials gradually increased as the reservoir level increased. In January 1995, the crest settlement was 25 cm when the water level reached the elevation of 218.10 m, while it was 9 cm on the upstream slope.

The leakage rate of the dam during 7-year operation along with precipitation rate and reservoir level is presented in Figure 3.10. The leakage performance of the Aguamilpa dam was satisfactory by March 1994, when only 6 l/s of leakage rate was measured. However, the leakage rate increased to 218 l/s within about 7 months. After the concrete face was examined in 1997, a horizontal crack with a width of about 150 m and a maximum opening of 1.5 cm was detected at elevation of 180 m. The authors have attributed this crack formation to the deformations that occurred in downstream zone 3C because of its low modulus. The rainy seasons increase the reservoir level, thus the leakage through the crack increases. Some repair work of sealing the crack with silty sediments after 1997 has gradually lowered the leakage, as can be seen in Figure 3.10. The maximum deflection observed at maximum cross section was 23 cm in 1999 as illustrated in Figure 3.11. A linear deflection behavior was seen in the face slab on the river bed section until June 1995 for an elevation up to 200 m, whereas the trend of line bent in 1996 at the elevation of

180 m. This bend can be attributed to nonuniform settlements that occurred between the rockfill zones of 3B and 3C due to great difference between rockfill modulus of these zones.

3.2.3 Foz do Areia Dam (Brazil, 1980)

Foz do Areia was the first CFRD constructed in Brazil. The zoning of the dam with material types and the compaction process of these zones are shown in Figure 3.12. The slopes of both upstream and downstream are 1.4H:1.0V. The height of the dam is 160 m, and the crest length is 828 m. The main rockfill was built in two stages. The upstream zone was raised to EL. 685 m in the first stage and acted as the upstream cofferdam to protect the construction site from floods during construction. The dumped rockfill material was spread from upstream to downstream and compacted with 10 t vibratory roller. The concrete face slab was built in two stages with a thickness of t=0.3+0.00357H m (Pinto, Materon, & Marques Filho, 1982) .

The settlement during construction is given in Figure 3.13. The middle of the dam has experienced the maximum settlement with a magnitude of 358 cm (2.2H%) because of low compressibility modulus obtained in the main rockfill zones (average compressibility modulus of 45 MPa for 1B and 1D zones; 30 MPa for 1C zone). This amount of settlement is almost 5-8 times higher than the settlements observed in other similar kind of dams such as the Cethana and Alto Anchicaya dams. (Pinto et al., 1985).

The maximum settlements measured in the rockfill after reservoir filling is illustrated in Figure 3.14 and Figure 3.15 for different time periods. The equal settlement contours given in Figure 3.14 show that the impact of water load on the settlement decreases from upstream to downstream. The maximum recorded settlement until the end of 1980 was 57.5 cm on the upstream face at elevation 670 m.

The measured maximum face deflection in the Foz do Areia dam was 69 cm due to the load of first reservoir impounding in 1980 as illustrated in Figure 3.16. The face deflection of the Foz do Areai dam was also relatively higher than that of other dams. In 1985, the recorded maximum deflection reached 77.5 cm in the Foz do Areia (Pinto et al.,1985), while it was 47 cm for the Xingo (Brazil, 1994) five years after reservoir filling (Sobrinho et al., 2000). It is stated by Sobrinho et al. (2000) that maximum face deflection of CFRDs is usually around 0.4 to 0.5% of the dam height.

The leakage rate was initially 236 l/s shortly after reservoir impounding and gradually decreased with time as the reservoir level remained stable. In 1985, the measured leakage was around 70 l/s (Pinto et al., 1985). Joint movements were heavily affected by reservoir filling in the final stages when separation was recorded. The rate of reservoir filling was found to have no impact on the joint deformations. Overall, the deformations of the Foz do Areia dam were seen to be large; however, its performance considering the leakage rate is satisfying.

3.2.4 Tianshenqiao I Dam (China, 199)

The Tianshenqiao I dam (TSQ1), currently one of the highest CFRDs in China with the height of 178 m, is located on the Nanpan River, China. The concrete face slab of the TSQ1 is well instrumented to track the behavior of the slab at every stage of construction.

The rockfill material has been placed in seven stages and the concrete face slab has been built in 3 stages. The construction method of TSQ1 was unique as it was the first CFRD in which the rockfill, concrete face slab was built at the same time as reservoir impounding (Penman & Rocha-Filho, 2000). The details of the construction phases are shown in Figure 3.17. The aim of this unique construction sequence was to build first 6 stages, which were mainly focused on

upstream side up to an elevation of 768 m, to protect the construction site of the dam from the 500-year flood. The 7th stage of rockfill comprising the downstream of the dam, was placed starting from an elevation of 650 and continuing to the top. The downstream phase was raised with a high-speed rate of 1 m/day, which caused differential settlement between zones. As a result, the upstream slope of the 5th stage experienced tensile deformations before the 3rd stage of the face slab was placed at an elevation between 742 m and 768 m (Penman & Rocha-Filho, 2000). The crack on the cushion material is shown in Figure 3.18. The maximum width, depth and length of this crack were 5 cm, 1.5 m and 106 m, respectively (Keming & Zhogliang, 2001). After completion of the 3rd stage of the face slab, investigations were conducted on the concrete slab. It was found that the concrete face slab was cracked with openings mostly around 0.3 mm at elevations between 722 to 762 m. The measured initial leakage was 150 l/s (Keming & Zhogliang, 2001).

Figure 3.19 shows the deflection of the face slab at three cross sections. It can clearly be seen that the post-construction settlement has more impact on the bent line of the face slab where the concrete stages were separated. The progressive crack formation caused a rupture in the face slab in the 3rd year of operation (Cruz et al., 2009). This rupture was repaired, and the performance of the dam is satisfactory. This case study shows the importance of construction sequence on the stability of high CFRDs. Keming and Zhogliang (2001) claims that the cracks observed in TSQ1 dam could have been prevented if enough time was given for the rockfill phases to settle before constructing the concrete face slab.

3.3 Observed Seismic Performance of Some CFRDs

3.3.1 Zipingpu Dam (China, 2006)

The construction of Zipingpu dam (156 m-high) was completed in 2006. The maximum cross section of the dam is provided in Figure 3.20. The rockfill material of the dam mainly consisted of medium to hard limestones. High strength and low compressibility were achieved in the rockfill after effective process of compaction Zhang et al. (2015). The dam was subjected to the Wenchuan earthquake (M_s = 8.0) in 2008. It is the first case in which a high CFRD was shaken by a strong earthquake (Zhang et al., 2015). The earthquake caused a significant damage on the Zipingpu dam. The seismic-induced settlements across the dam are shown in Figure 3.21. The earthquake caused up to 1m of crest settlement and significant cracks on the concrete slab. The concrete slabs suffered from separations, cracking, arching bulging, and detaching Also, dislocations were seen in the horizontal and vertical joints connecting the slabs, with a maximum value of 170 mm in horizontal joints and 350 mm in vertical joints. The leakage rate raised from 17 l/s to 25 l/s due to shaking (Zhang et al., 2015). After necessary repairs were done, operation of the Zipingpu dam was reassured (Dakoulas 2012).

3.3.2 Cogoti Dam (Chile, 1938)

Cogoti dam is in north central Chile and has height of 82.7 m, with a crest length of 160 m (Arrau et al., 1985). There has not been compaction or sluicing of the rockfill during construction. The concrete face was constructed with individual slabs having an area of 10 x 10 m^2. The dam experienced four major earthquakes: Illapel (M_L = 7.9, 1943), La Ligua (M_L = 7.1, 1965), Papudo-Zapallar (M_L = 7.5, 1971), and Llolleo-Algarrobo (M_L = 7.7, 1985) earthquakes (Arrau et al., 1985). The first earthquake caused transversal and longitudinal cracks at the crest. Also, the

downstream slope and the concrete face experienced deformation, which urged the immediate repair measures (Verdugo and Peters, 2009). The maximum seismic crest settlement was observed after first earthquake with a value of 40 cm, while the others had lass impact on the behavior of the dam (Arrau et al., 1985). The leakage rate of 2600 l/s was measured in 1988 before the concrete face was repaired in 1988 (Verdugo and Peters, 2009).

3.4 Empirical Estimates for Dam Behavior

Fitzpatrick et al. (1985) introduced a method to assess deformation behavior of rockfill dams. The authors developed two moduli using measured displacement during construction and reservoir filling process. The configurations of deformation modulus of both cases are illustrated in Figure 3.22. This assessment is commonly used for evaluation of compressibility of rockfill. The advantage of observing the deformation modulus during construction is that the designers can take immediate measures if unfavorable behavior is observed during construction. The empirical relations were proposed as following:

$$E_{rc} = \gamma_r H d_1 / \delta_s \quad (3.1)$$

$$E_{rf} = \gamma_w h d_2 / \delta_n \quad (3.2)$$

in which,

E_{rc} is rockfill modulus during construction (in MPa),

E_{rf} is rockfill modulus during reservoir filling (in MPa),

γ_r and γ_w are the units weight of rockfill and water, respectively (in kN/m^3),

δ_s is settlement of rockfill thickness d_1 (δ_s in mm, d_1 in m),

H is the height of constructed rockfill above the location of measurement (in m),

δ_n is the face slab deflection at depth of h below water (δ_n in mm, h in m),

d_2 is the normal distance from the face slab to base (in m).

Three hydrostatic settlement cells are usually placed at different elevations on the central dam axis, which allows one to calculate Erc 6 times during construction only for the center of the dam. The average of these Erc values gives the secant modulus for the rockfill, as the settlement curves do not linearly increase with load. E_{rf} is an indication of rockfill modulus during reservoir impounding and is not calculated near the top of the upstream slope where the depth of water becomes zero, and the bottom of the upstream slope where d_2 becomes zero. It is also found that the rapid reservoir impounding causes E_{rf} to be significantly higher than E_{rc}. The creep deformation leads to a remarkable decrease in E_{rf} compared with the initial calculated modulus if the reservoir filling process is slow (Fitzpatrick et al., 1985).

As mentioned earlier, the particle size of rockfill materials used in the dams is highly large and does not allow laboratory tests to be performed in a full scale. Hence, the understanding of properties of rockfill, such as compressibility, becomes limited. The performance of precedents provides good opportunities to study the estimation of deformation behavior of rockfill properties (Hunter & Fell, 2003).

Figure 3.23 provides valuable information about the relationship between shape factor and the measured maximum deflection of 21 CFRDs normal to the face slab (D). Shape factor is defined as the ratio of concrete face area (A) to squared maximum height of the dam (H). The curved line illustrated in Figure 3.23 is the boundary between CFRDs showing either adequate or inadequate performance. The CFRDs that remained above the curve have suffered from severe face cracking, whereas those under the curve have performed well with no serious cracking incidents. The data obtained from observed behavior of CFRDs may result in practical and accurate predictions about behavior of face slabs.

Pinto and Marques Filho (1998) studied the influence of void and shape of valley on deformation modulus of 15 high CFRDs. The relation between those parameters is shown in Figure 3.24 in which two different trend curves are obtained. The first trend curve is obtained for dams that generally have a shape factor (A/H^2) lower than 3, while the second curve represents the dams that have a shape factor higher than 3. The shape factors lower than 3.5 are considered to represent the dams built narrow valleys (C. Marulanda & Marulanda, 2015). The CFRDs built in narrow valleys yield higher modulus of deformation than those having a shape factor higher than 3. Two dams (G and M) in the plot are not in accordance with the trends, which shows the possibility of uncertainties in the relation. It is also worth mentioning that the crest settlements take a longer time in narrow valleys due to arching effects, as stated by Sherard and Cooke (1987). Therefore, the modulus of deformation of the dams that have a shape factor less than 3 may decrease with time since the settlements is expected to increase.

Pinto and Marques Filho (1998) also developed an equation to estimate the maximum face slab deflection (D) under water load using deformation modulus and shape factor. The proposed equation of maximum face slab deflection is given as:

$$D = \frac{0.003}{e^{0.21(1+\frac{A}{H^2})}} \frac{H^2}{E_v} \tag{3.3}$$

in which, D and H are in m, E_v is in MPa, and A is m^2.

The authors indicate that the location of maximum face slab deflection (D) is around the mid-height of the dam. Figure 3.25 demonstrates the estimated face deflections of the dams by using Eq. (3.3), which takes the valley shape, rockfill modulus during construction, and height of the dam into consideration.

Hunter and Fell (2002) reports that the rockfill modulus estimation given in Eq. (3.1) overestimates the stresses, since it does not take the geometry of the dam into consideration. Thus, the calculated deformation modulus is different than the expected deformation modulus of the dam locations close to dam base. The authors analyzed the deformation behavior of CFRDs using a broad database range (35 CFRDs) from literature and proposed methods to estimate the deformation modulus and maximum deflection of face slab regarding the influences of particle size, geometry of the dam's longitudinal section, unconfined compressive strength (UCS), and rockfill and layer thickness of placement for compaction. Hunter and Fell (2002) created a two-dimensional (2D) model that presents longitudinal section of the valley, as shown in Figure 3.26, using a finite difference analysis model. The rockfill was modeled as linear elastic material. The authors conducted several analyses for different base widths (20, 50, and 100 m) and valley slopes to see the abutment impacts on the vertical stresses. Even though the authors were aware of the limitations of 2D analysis for analyzing arching effects, they concluded that the overall trend of abutment impacts on the stress values in the embankment were simulated. The reservoir was not included in the analysis. The results are presented in Figure 3.27. The main findings from these analyses were presented as follows:

- Evident arching effects were observed in longitudinal sections where the river width is 20 m along with steep slopes.
- The thickness of lifts built in stages is important and underestimates the stresses if the simulation is modeled with very thick layers.
- Insignificant arching effects is obtained for the models whose river width over height ratio is close to 1. Based on the geometries used in the analysis, the authors recommended applying some stress reduction factors for a more accurate estimation of deformation modulus.

Figure 3.28 and Figure 3.29 illustrate the proposed method by Hunter and Fell (2002) to estimate deformation modulus of CFRDs at the end of construction and the maximum face slab deflection during reservoir impounding. Some of the deformation moduli were modified considering the stress reduction factor obtained from the finite difference analysis. Figure 3.28 shows the particle size of D_{80}, where 80% of the sample diameter is less than this value and can be used in behavior of well-compacted rockfill dams whose strength varies from very high strength and medium to high strength. Hunter and Fell (2002) used the Australian Standard AS 1726-1993 classification system to classify the strength of rockfill. According to this classification system, the UCS of rockfills with very high strength is 70-240 MPa, high strength is 20-70 MPa, and medium strength is 6-20 MPa (Hunter & Fell, 2002). The dams that have very high and medium to high strength with different D_{80} particle size may yield different deformation modulus.

Hunter and Fell (2002) also developed an empirical method to estimate face slab deflection during first reservoir impounding, as shown in Figure 3.29. There are several components in this approach to estimate the deflection, such as E_{rf}, E_{rc}, upstream slopes, and dam height. E_{rc} is taken from Figure 3.28, which takes vertical stresses into consideration. The E_{rf}/E_{rc} ratio varies with upstream slopes and the height of the embankment. E_{rf} is the value presented in Eq. (3.2). After calculating representative E_{rf}/E_{rc} ratio from Figure 3.29, the maximum deflection of the face slab can be estimated by substituting E_{rf} in Eq. (3.2).

CFRDs are naturally free-drainage structures as the particle size increases from upstream to downstream and less compaction effort is made going from upstream to downstream (Pinto et al., 1982). Therefore, it can allow large leakage rates without threatening the safety of the dam. However, such large leakages require treatment. The flow rate resulted from a crack opening in

the concrete slab can be estimated using Eq. (3.4) which was derived from experiments (ICOLD, 2010).

$$q = \frac{g w^3 i}{12 v \left[1 + 8.8 \left({}^{m}/_{2w}\right)^{1.5}\right]} \tag{3.4}$$

in which,

q is unit flow rate ($m^3/s/m$),

g is acceleration of gravity (m/s^2),

w is crack width (m),

i is hydraulic gradient,

d is frictional head loss associated with flow through the crack (m),

v is kinematic viscosity of water, $1x10^{-6}$ m^2/s at 20 ℃,

m is the roughness parameter (m).

3.5 CFRDs Beyond Empiricism

Rigorous analyses using numerical tools are becoming popular in the design stages of CFRDs. Theses analyses include the determination of zoning and the addition of new materials between the walls of vertical panels (C. Marulanda & Marulanda, 2015). In numerical analyses, the determination of proper zoning and material selection along with well-gradation becomes more important if a rockfill with low strength is going to be used. The study of Marsal (1973) proves that more favorable deformation behavior can be observed in well-graded rockfills with low strength than poorly-graded rockfills with high strength.

Marulanda-Escobar and Marulanda-Posada (2008) described the fundamental considerations involved in numerically modeling a CFRD with a high degree of accuracy as follows:

- The CFRDs should be modeled with three-dimensional representation,
- Topography of terrain should be taken into consideration,
- The rockfill and reservoir should be modeled using a staged-construction feature,
- Proper stress-strain relationship of material should be considered,
- The concrete face should be modeled physically along with interfaces between panels, plinth, and rockfill.

The influence of the staged-construction feature in numerical analyses on deformation behavior of embankments was first addressed by Clough and Woodward (1967). The authors created a hypothetical earth dam model with a height of 30.48 m (100 ft) and upstream and downstream slopes of 1V:2.5H. The embankment material was modeled as linear elastic in two-dimensional plane strain conditions using the finite element method. The elasticity modulus of the rockfill was 9.6 MPa with a Poisson's ratio of 0.4 and the unit weight of rockfill was 21.2 kN/m^3. Two analyses were carried out. The first analysis was performed by modeling the embankment in single lift, whereas the second analysis was modeled in 10-lift increments. There was no difference between two analyses considering horizontal displacement. However, the vertical displacements in both analyses show different settlement magnitudes at different locations. The single-lift analysis yielded the maximum settlement at the crest with a magnitude of 48.8 cm (1.6 ft), whereas the maximum settlement of the 10-lift increments model occurred in the middle of the dam with a magnitude of 24.4 cm (0.8 ft), as seen in observed settlement of rockfill dams in the field (see

Figure 3.30). Therefore, it can be concluded that modeling the dams with multiple lift stages (similar to real dam construction) results in a more accurate estimation of the behavior of the dams.

The designers of Porce III dam (154 m high) have taken the advantage of detailed finite element analyses to finalize the design details of the dam. The maximum cross section of the dam is given in Figure 3.31. The modulus of materials of different zones were estimated after evaluating a series of field and laboratory test results, such as test embankments, odometer tests, plate load tests, and LA abrasion and absorption tests. It was determined that the materials of the upstream zone would have a modulus greater than 85 MPa (C. Marulanda & Marulanda, 2015). With these strength profiles a three-dimensional finite element analysis was conducted for several scenarios in which a variation of different rockfill modulus for different zones were considered. The summary of the calculated stresses in the concrete face slab for the cases of different scenarios of rockfill modulus in different zones is shown in Table 3.4. As a result of these analyses, the calculated compressive and tensile stresses in the concrete face were checked and it was found that the maximum compressive stress in the concrete face would be 20 MPa in a scenario where all zones have a modulus of 70 MPa. Figure 3.32 illustrates the location of predicted maximum compressive stresses in the concrete face. C. Marulanda and Marulanda (2015) stated that the maximum compressive stress in the concrete face was limited to 15 MPa or less for all scenarios presented in Table 3.4. This limitation was decided based on the recorded stress values of another CFRD whose concrete face was cracked at a stress value of approximately 18.5 MPa. The solution proposed to relieve the excessive stresses in the concrete face was to put compressible materials in compressible joints. The new scenarios with different configurations of compressible joints were defined (see Figure 3.33) and utilized in the finite element analysis. A configuration with five vertical compressible joints, as shown Figure 3.33a, was chosen as the best scenario for dissipation

of stresses in the concrete face. The results presented in the Figure 3.34 show significant mitigation from using compressible joints. The satisfying performance was observed in the dam behavior after construction (C. Marulanda & Marulanda, 2015).

Table 3.1: Miaojiaba dam materials (Wen et al., 2017).

Material	Classification	Placing	Compaction
Rockfill (3B, 3C)	Metamorphic tuff $Ø_{max}$ = 0.80 m	0.85 m layers	10 passes, 25 t towed vibratory roller
Transition	Processed Metamorphic tuff $Ø_{max}$ = 0.30 m	0.45 m layers	8 passes, 20 t self-propelled vibratory roller
Cushion	Blended sand and gravel $Ø_{max}$ = 0.15 m	0.45 m layers	8 passes, 20 t self-propelled vibratory roller

Table 3.2: Aguamilpa dam materials (Cruz et al., 2009).

Zone	Classification	Layer Thickness (cm)	Compaction Procedure
1A	Random	80	Not compacted, just placed
1B	Fine silty sand $Ø_{max}$ = 0.2 cm	30	Not compacted, just placed
2F	Alluvial gravel and silty sand mix. $Ø_{max}$ = 3.8 cm	30	4 passes, 100 kN smooth-drum vibratory roller (SDVR)
2B	Crushed alluvial gravel and sand mix. $Ø_{max}$ = 7.6 cm	30	Layer:4 passes, 100 kN SDVR Face: 6 passes, 40 kN SDVR
3B	Dredged alluvium $Ø_{max}$ = 40 cm	60	4 passes, 100 kN SDVR
T	Rockfill 3C with reduced $Ø_{max}$ $Ø_{max}$ = 50 cm	60	4 passes, 100 kN SDVR
3C	Rockfill (ignimbrite) $Ø_{max}$ = 100 cm	120	4 passes, 100 kN SDVR
NA	Natural alluvium	-	-
CF	Concrete face	-	-

Table 3.3: Deformation moduli of Aguamilpa dam zones measured from instrumentation readings (Macedo-Gomez et al., 2000).

Zones	Dam Instrumentation		
	Inclinometers	Hydraulic Settl. devices	Clusters of pressure cells
3B	221.71 MPa	259.96 MPa	122.62 MPa
T	145.12 MPa	129.49 MPa	-
3C	43.16 MPa	47.09 MPa	-

Table 3.4: Estimated stresses in concrete face of Porce III dam with different modulus of rockfill Marulanda-Escobar and Marulanda-Posada (2008).

Mod. of 3B (MPa)	Mod. of 3C (MPa)	Mod. of 3D (MPa)	Hor. Stress (MPa)	Vert. Stress (MPa)	Slab Deflection (m)
70	70	70	-19.92	-19.00	0.34
90	90	90	-16.16	-17.25	0.26
120	120	120	-11.85	-12.58	0.20
90	60	60	-15.37	-16.28	0.26
90	60	50	-15.39	-17.39	0.27

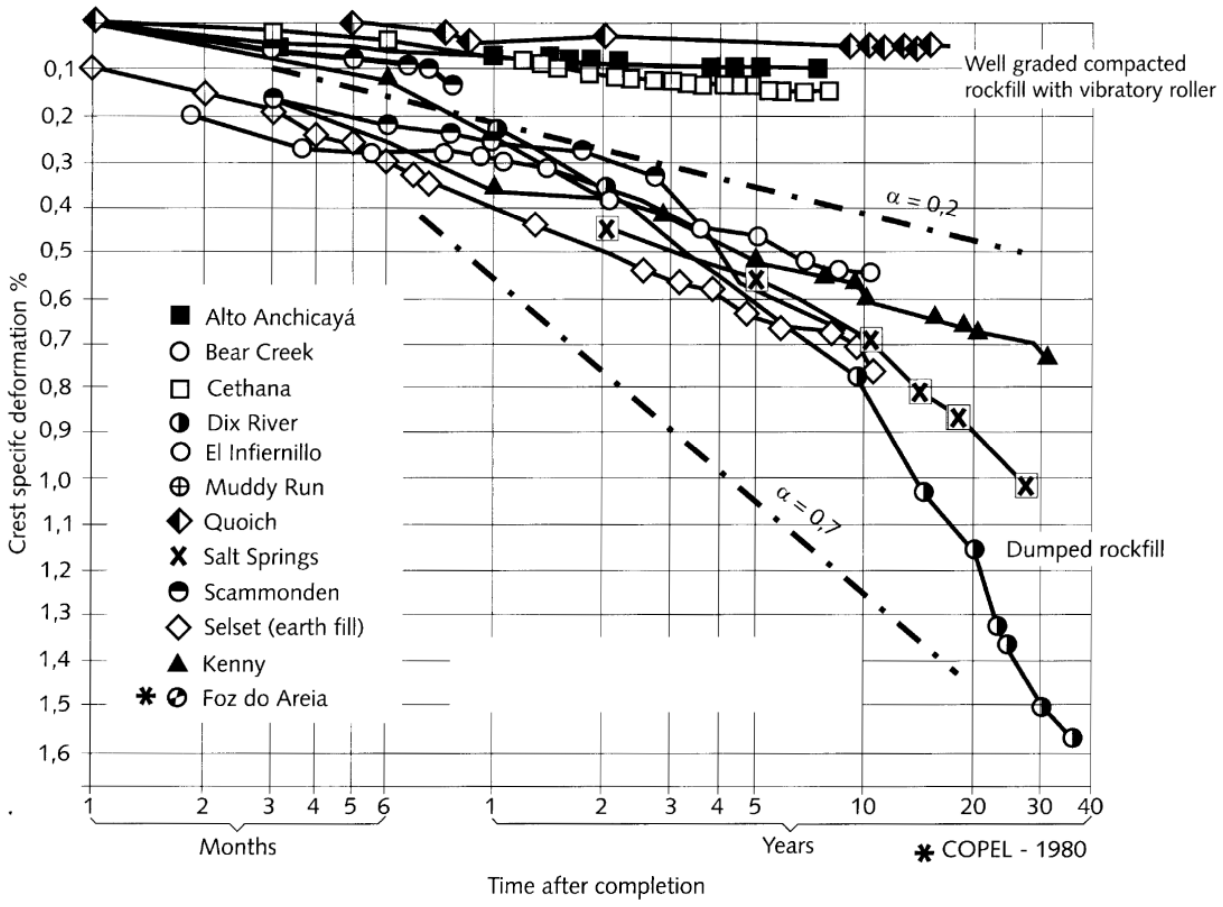

Figure 3.1: Long-term crest settlement of some rockfill dams (Cruz et al., 2009).

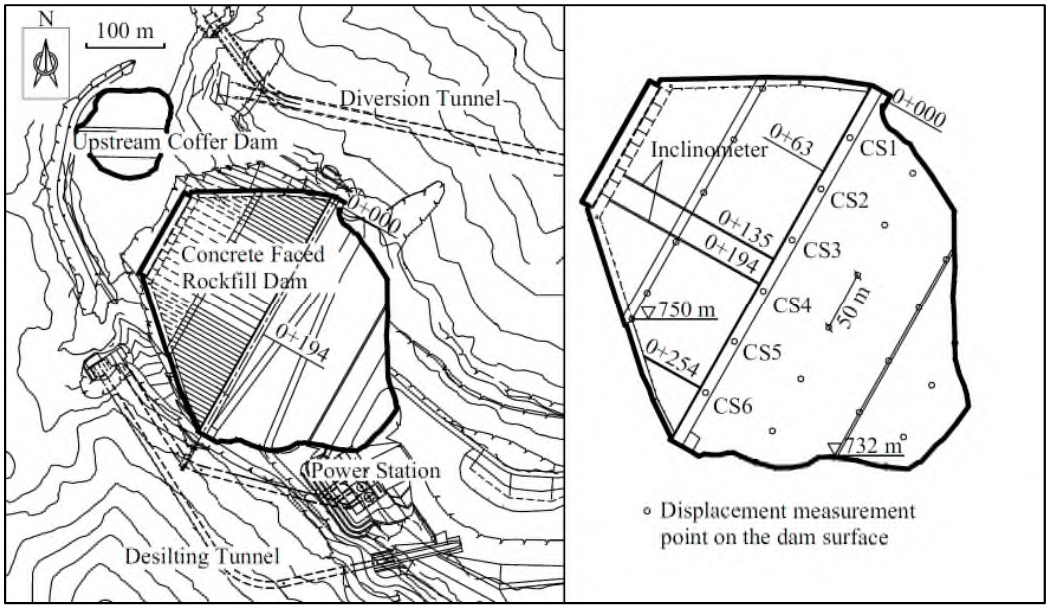

Figure 3.2: Plan view of Miaojiaba dam and displacement instruments on dam surface (Wen et al., 2017).

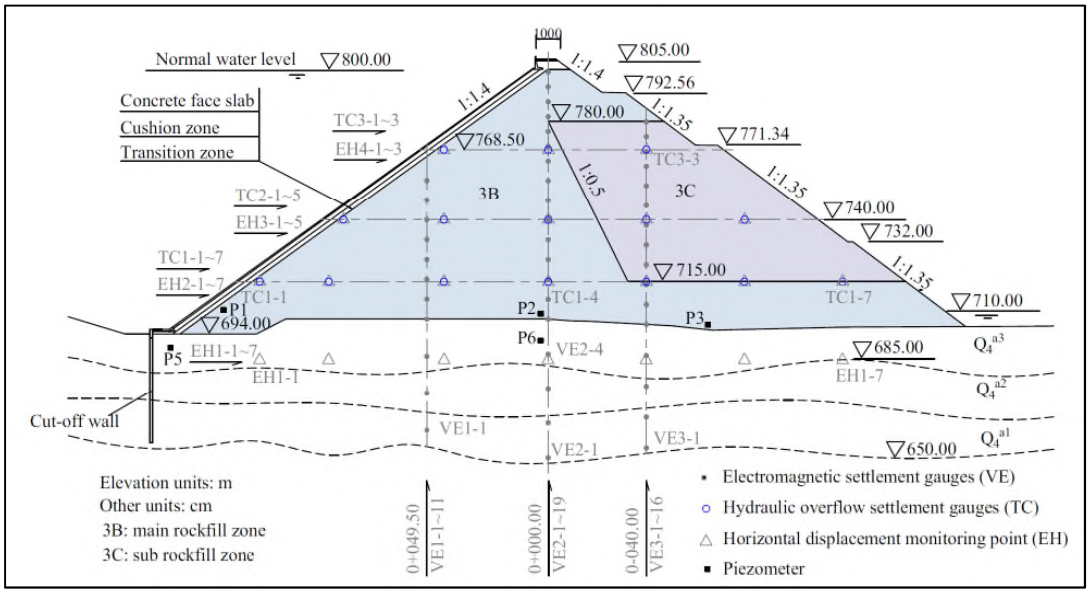

Figure 3.3: Cross section of Miaojiaba dam with instruments installed inside of the dam (Wen et al., 2017).

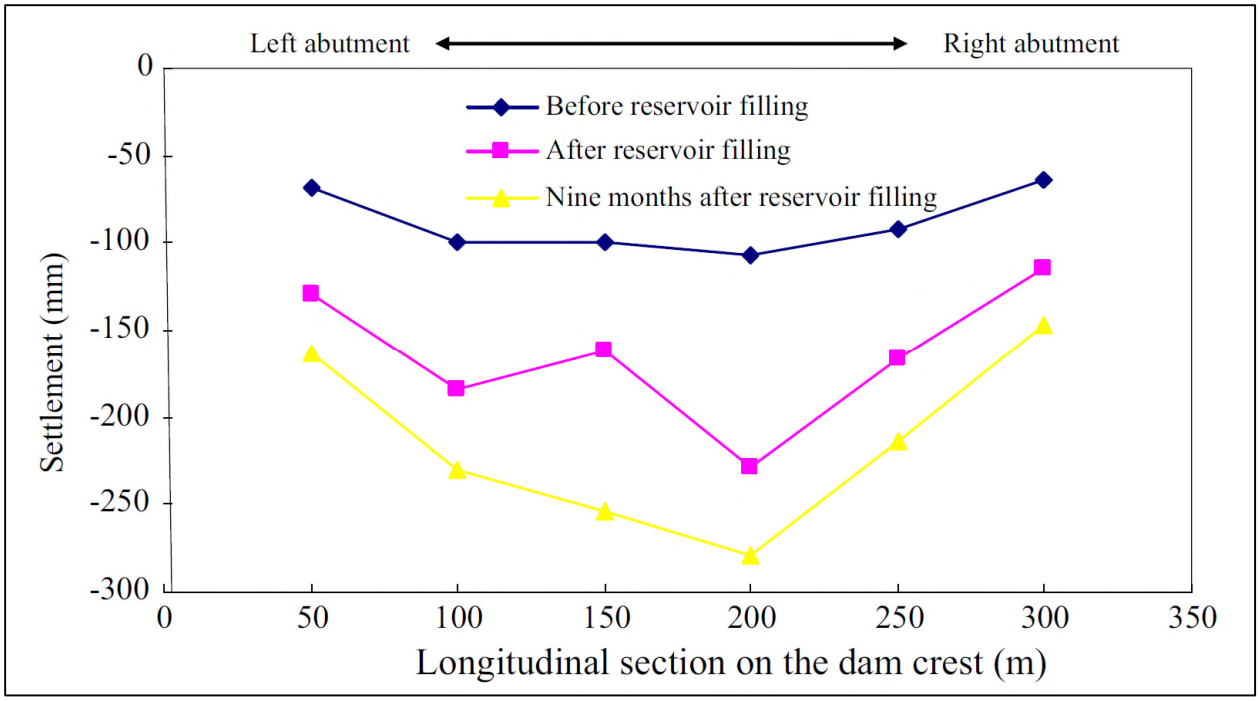

Figure 3.4: Crest settlement of Miaojiaba dam along dam axis (Wen et al., 2017).

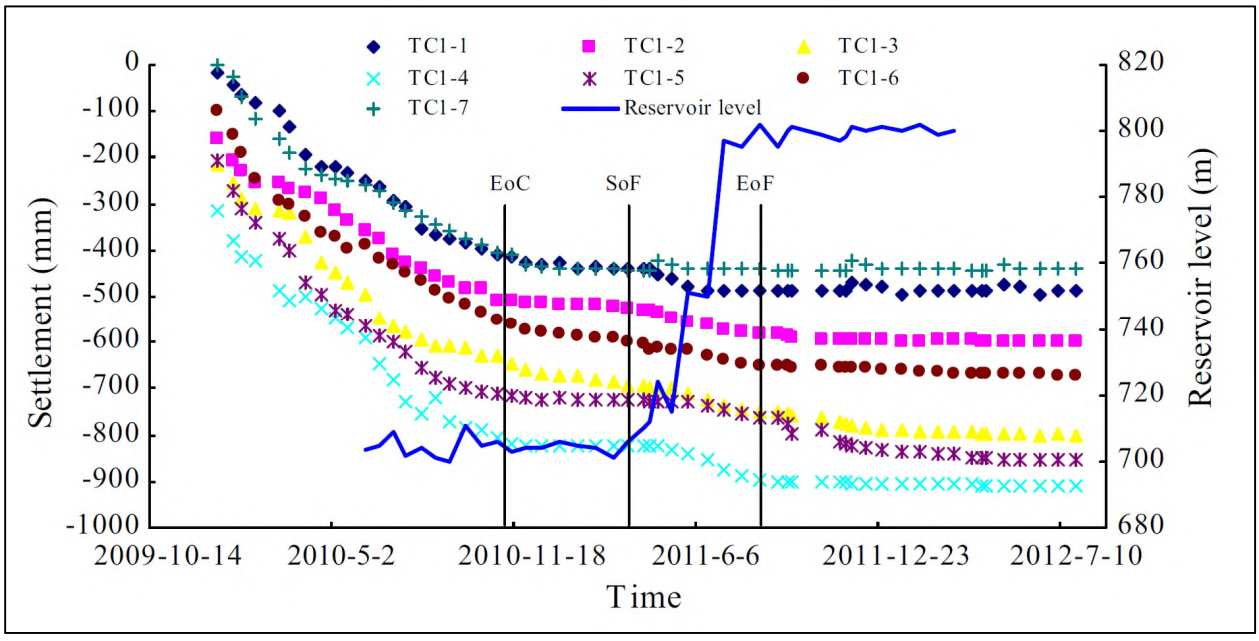

Figure 3.5: Internal settlement at elevation of 715.00 m (EoC: end of construction, SoF: start of reservoir filling, EoF: end of reservoir filling) (Wen et al., 2017).

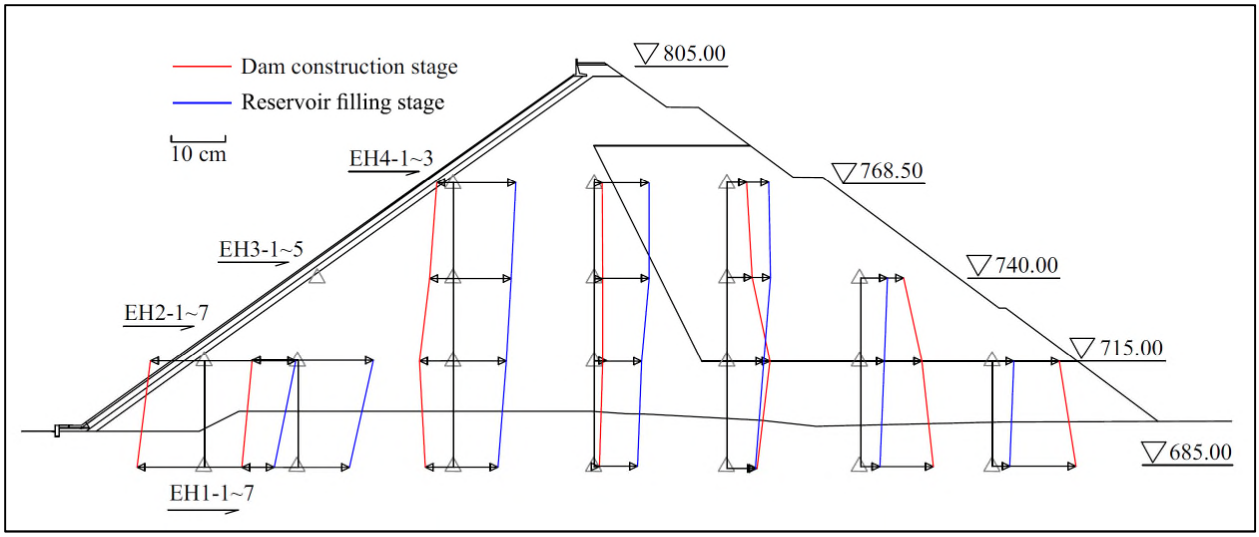

Figure 3.6: Observed lateral deformations of Miaojiaba dam before-after reservoir filling (Wen et al., 2017).

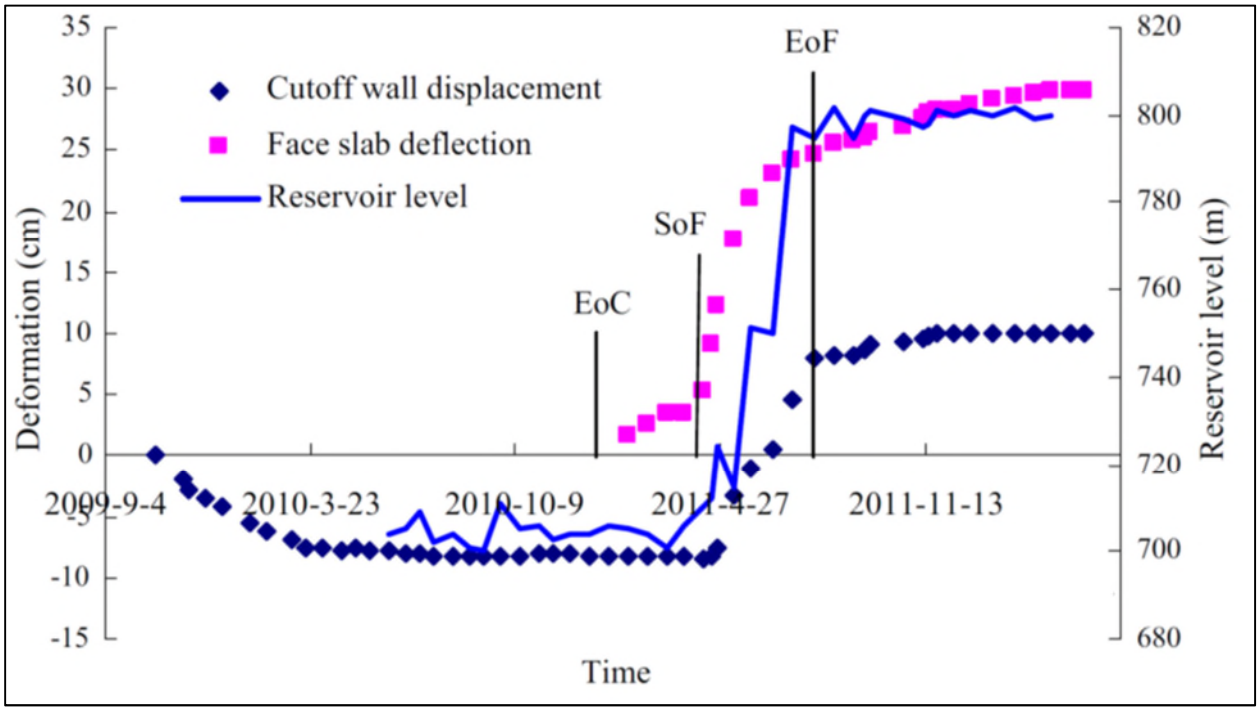

Figure 3.7: Observed displacement of cutoff wall and deflection of face slab (Wen et al., 2017).

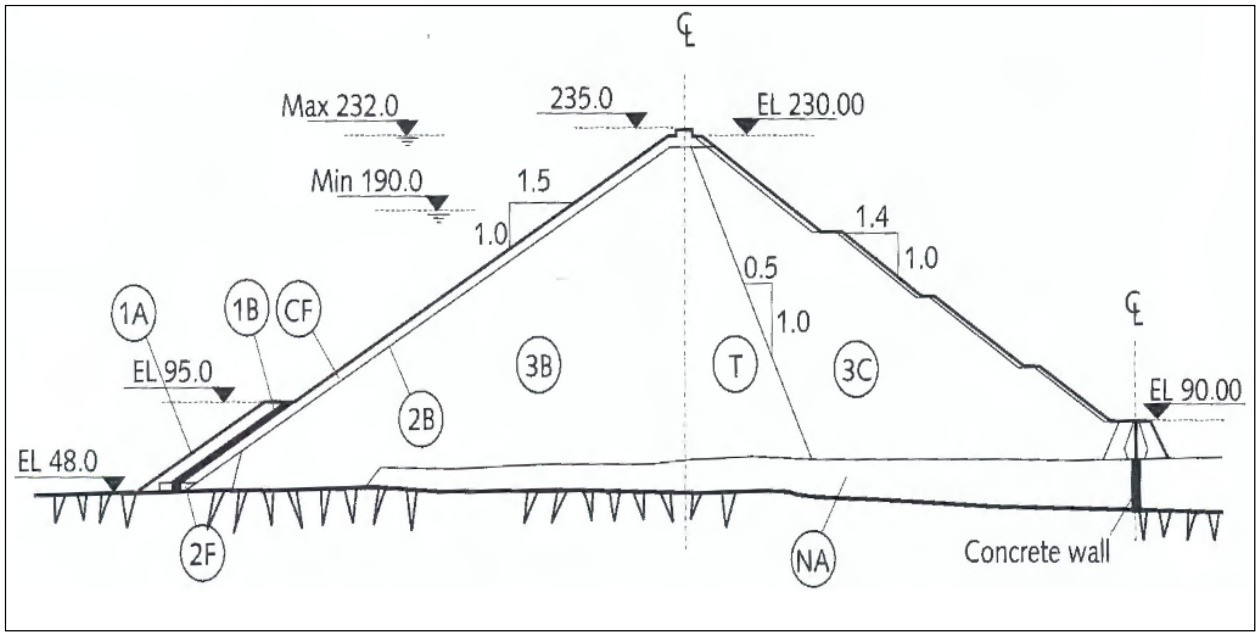

Figure 3.8: Maximum cross section of Aguamilpa dam (Cruz et al., 2009).

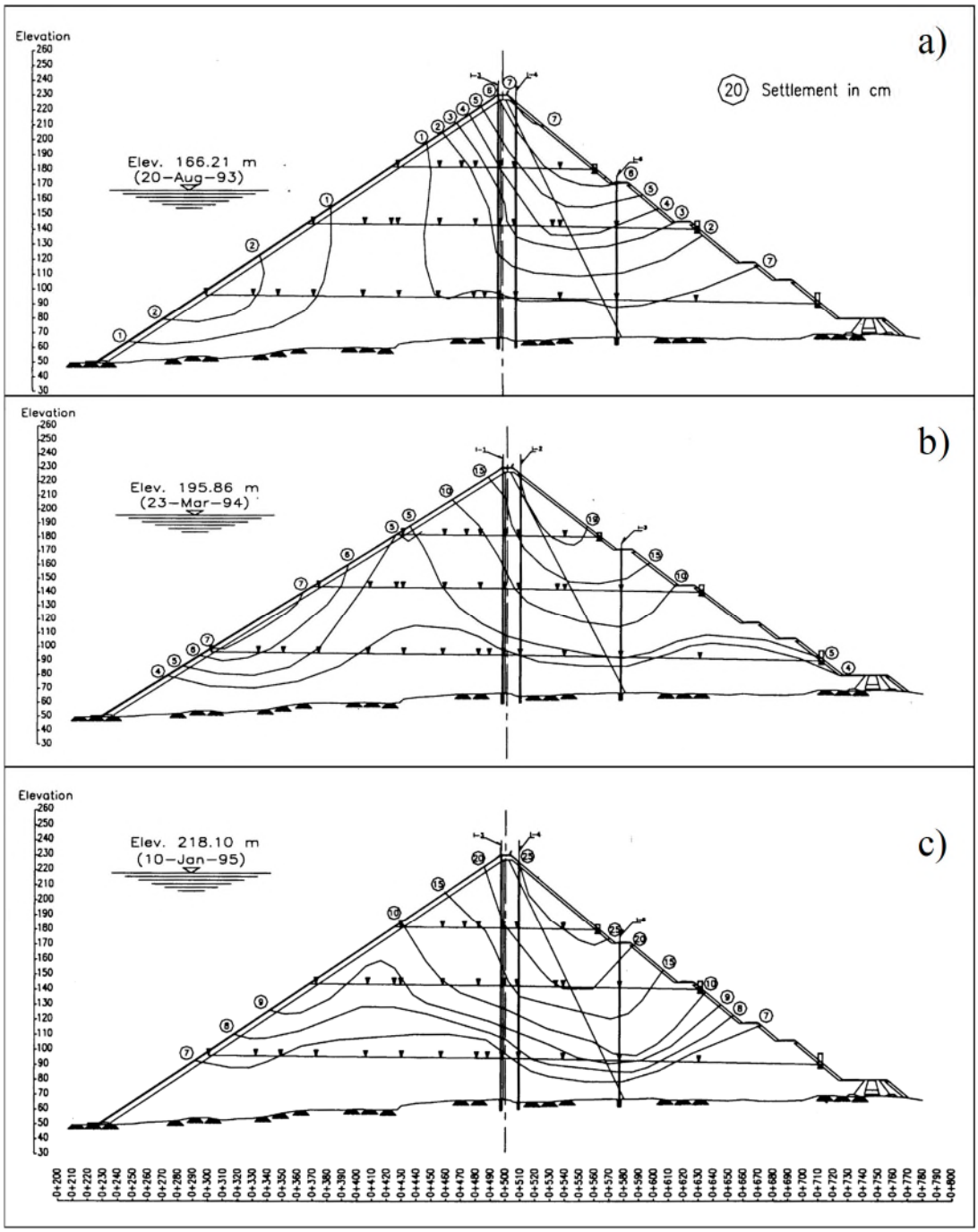

Figure 3.9: Settlement contours of Aguamilpa dam, three reservoir filling stages (Macedo-Gomez et al., 2000).

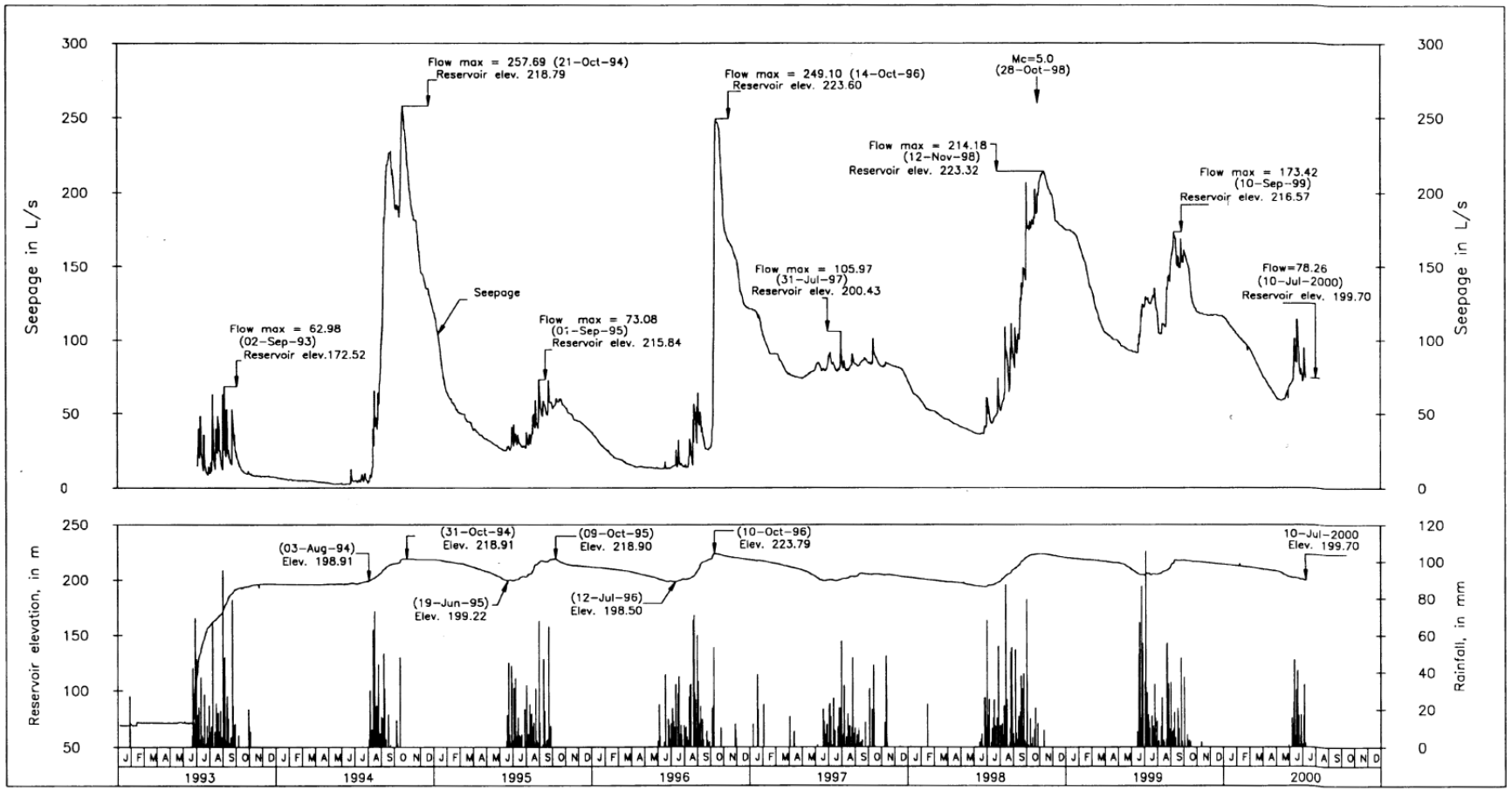

Figure 3.10: Leakage performance of Aguamilpa dam (Marulanda & Pinto, 2000).

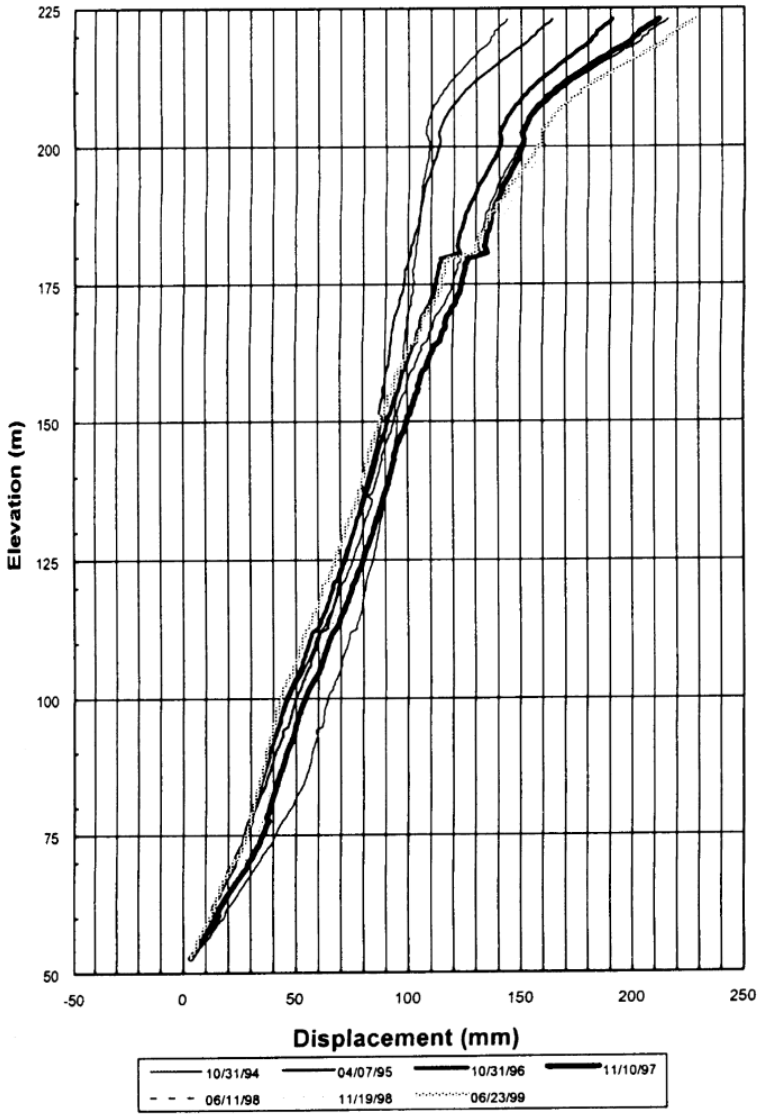

Figure 3.11: Deflection of face slab of Aguamilpa dam at maximum cross section (Macedo-Gomez et al., 2000).

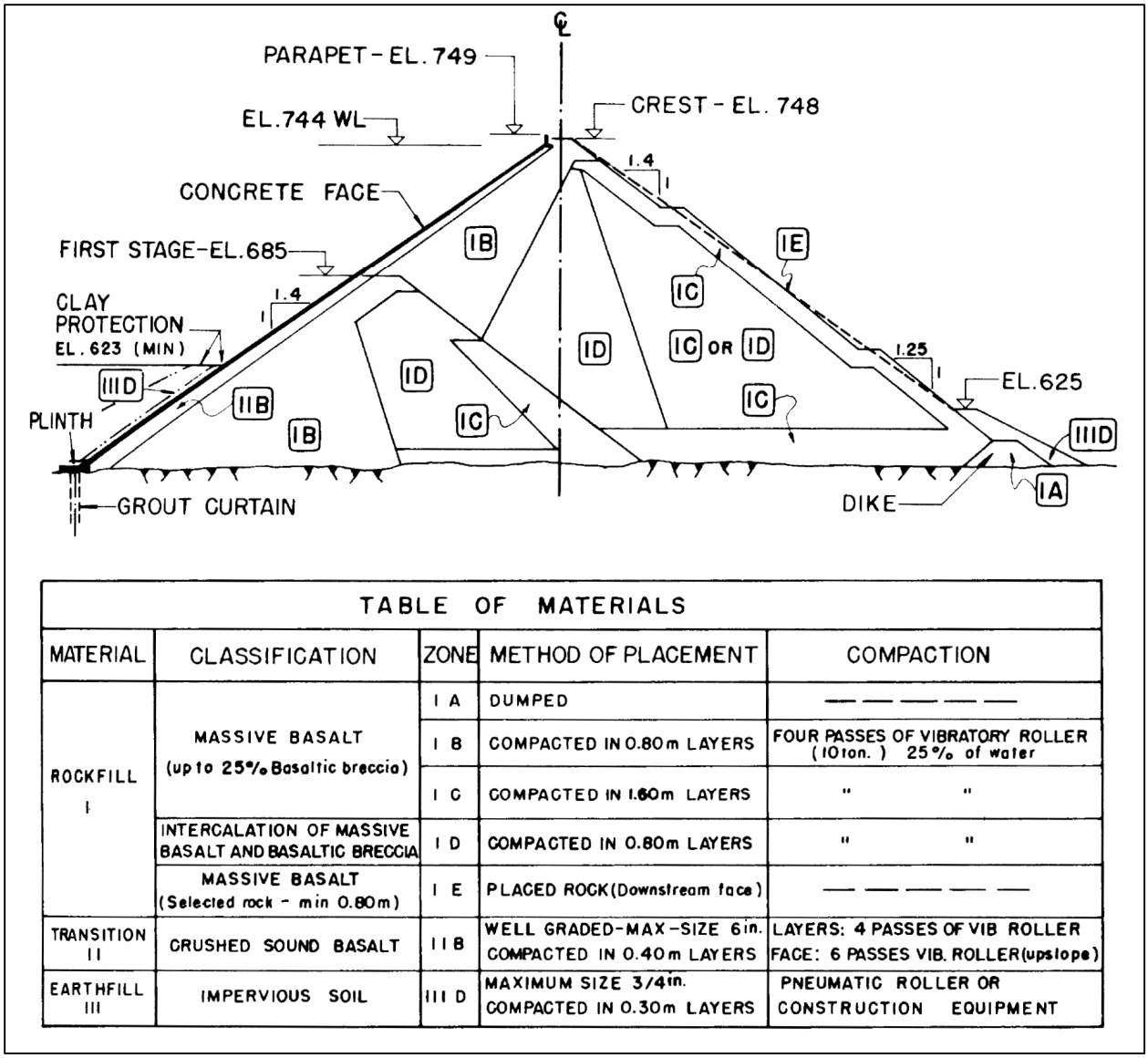

TABLE OF MATERIALS

MATERIAL	CLASSIFICATION	ZONE	METHOD OF PLACEMENT	COMPACTION
ROCKFILL I	MASSIVE BASALT (up to 25% Basaltic breccia)	I A	DUMPED	— — — — —
		I B	COMPACTED IN 0.80m LAYERS	FOUR PASSES OF VIBRATORY ROLLER (10ton.) 25% of water
		I C	COMPACTED IN 1.60m LAYERS	" "
	INTERCALATION OF MASSIVE BASALT AND BASALTIC BRECCIA	I D	COMPACTED IN 0.80m LAYERS	" "
	MASSIVE BASALT (Selected rock - min 0.80m)	I E	PLACED ROCK (Downstream face)	— — — — —
TRANSITION II	CRUSHED SOUND BASALT	II B	WELL GRADED-MAX-SIZE 6in. COMPACTED IN 0.40m LAYERS	LAYERS: 4 PASSES OF VIB ROLLER FACE: 6 PASSES VIB. ROLLER (upslope)
EARTHFILL III	IMPERVIOUS SOIL	III D	MAXIMUM SIZE 3/4in. COMPACTED IN 0.30m LAYERS	PNEUMATIC ROLLER OR CONSTRUCTION EQUIPMENT

Figure 3.12: Zoning and materials of Foz do Areia dam (Pinto et al., 1985).

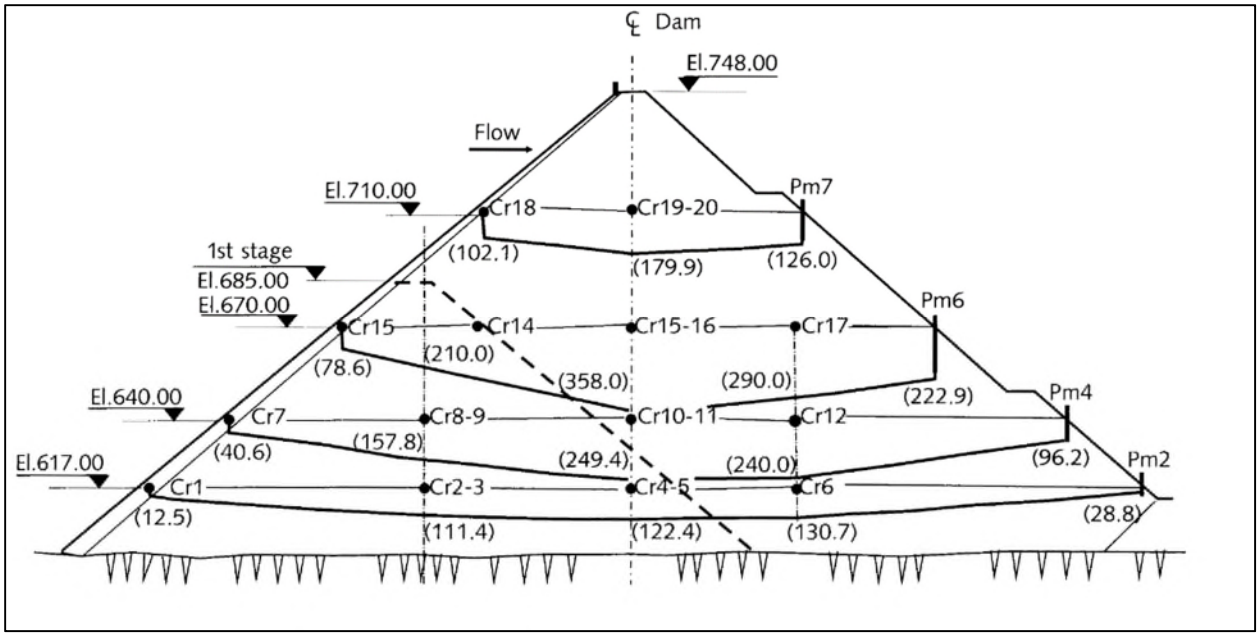

Figure 3.13: Settlement (in cm) of Foz do Areia dam at the end of construction (Pinto et al., 1982 adapted from Cruz et al., 2009).

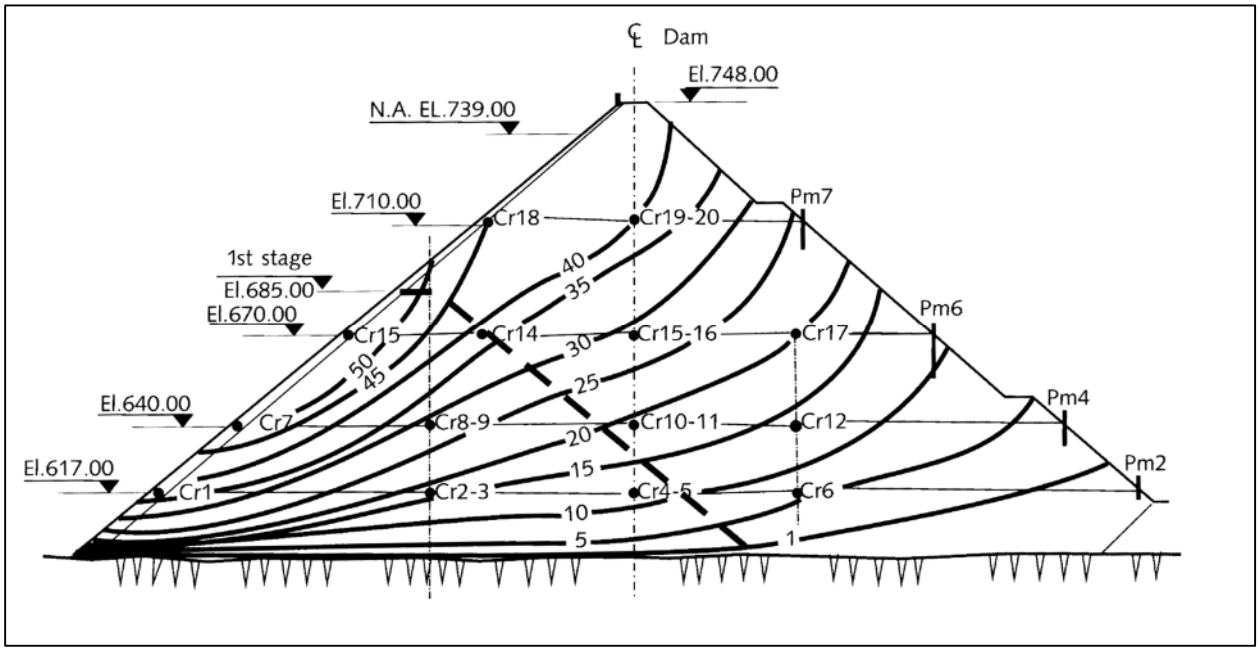

Figure 3.14: Equal settlement (in cm) contours of Foz do Areia dam after reservoir filling, September 1980 (Pinto et al., 1982 adapted from Cruz et al., 2009).

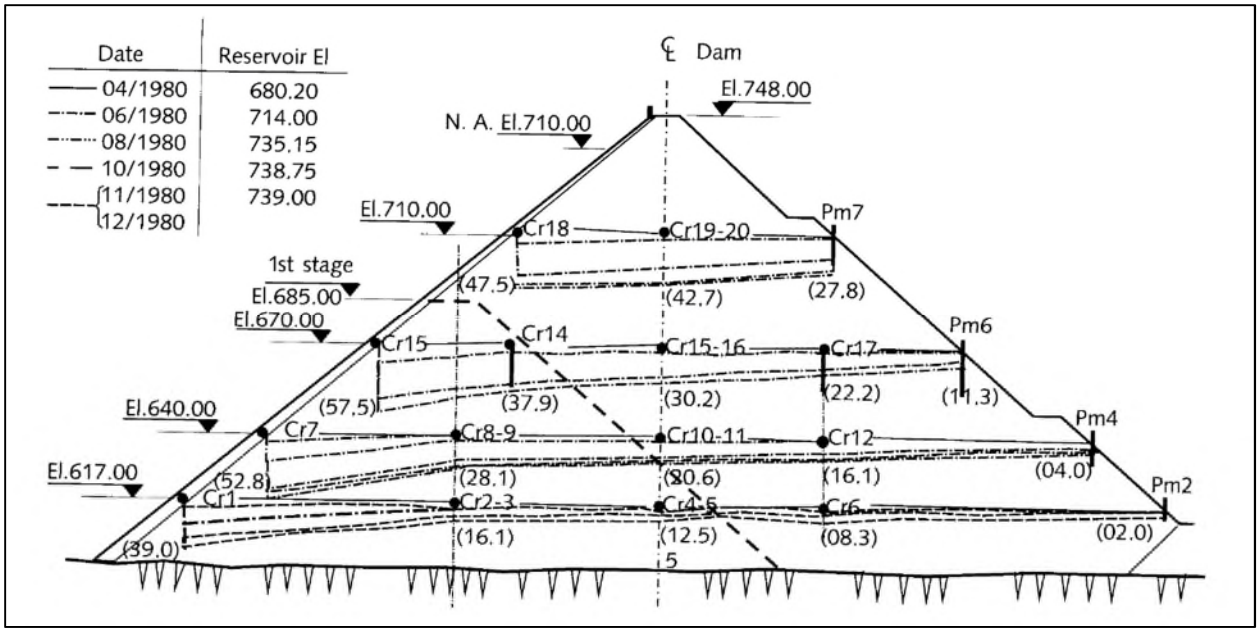

Figure 3.15: Settlement (in cm) of Foz do Areia dam after reservoir filling at the end of 1980 (Pinto et al., 1982 adapted from Cruz et al., 2009).

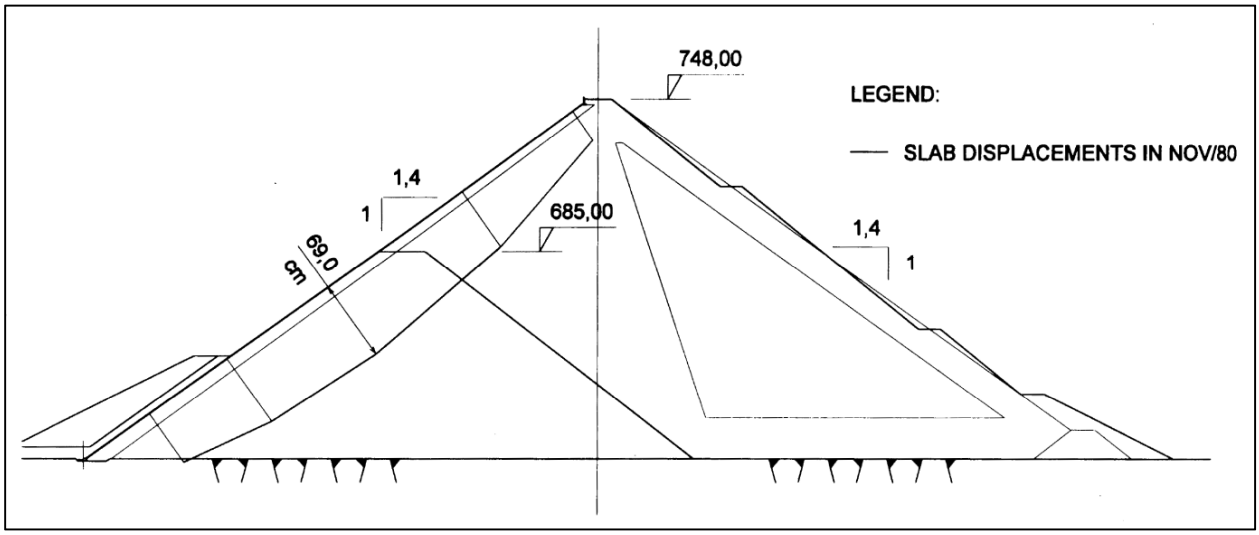

Figure 3.16: The face slab deflection of Foz do Areia dam at maximum cross section (Sobrinho et al., 2000).

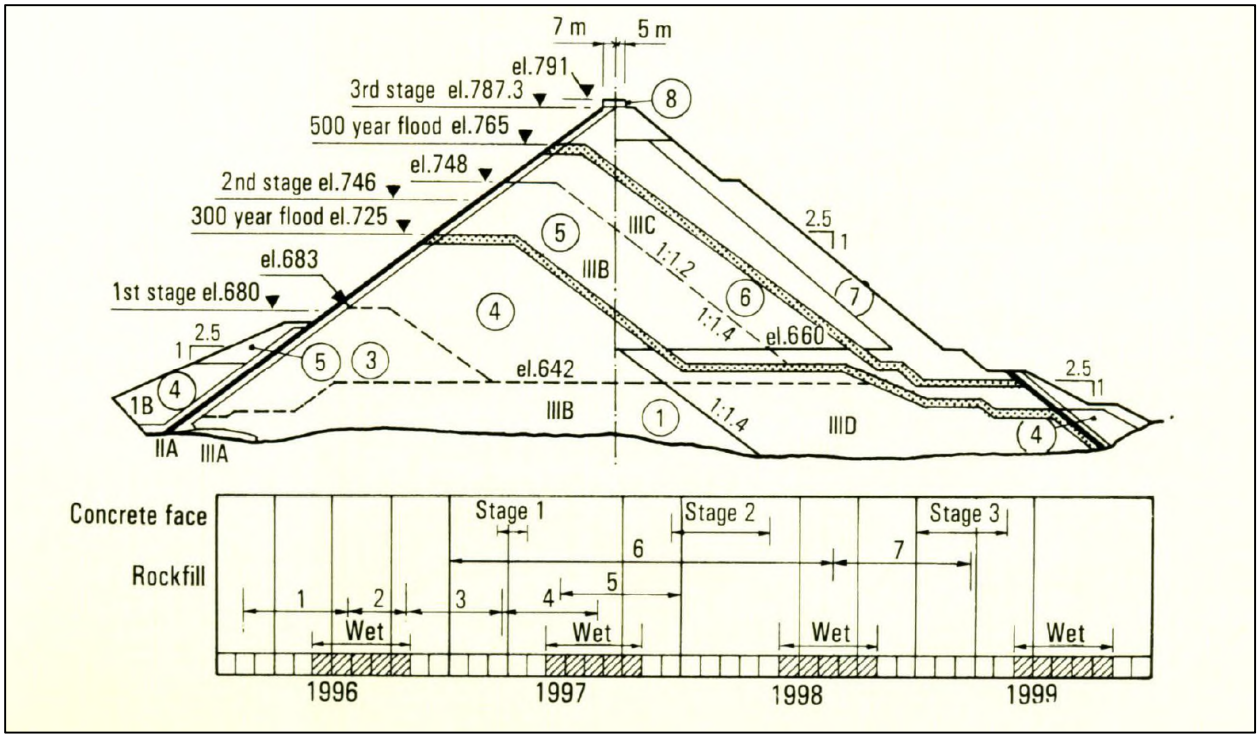

Figure 3.17: Stages of construction of TSQ1 dam (Keming & Zhogliang, 2001).

Figure 3.18: Crack occurred in cushion material of TSQ1 dam (Ma & Cao, 2007).

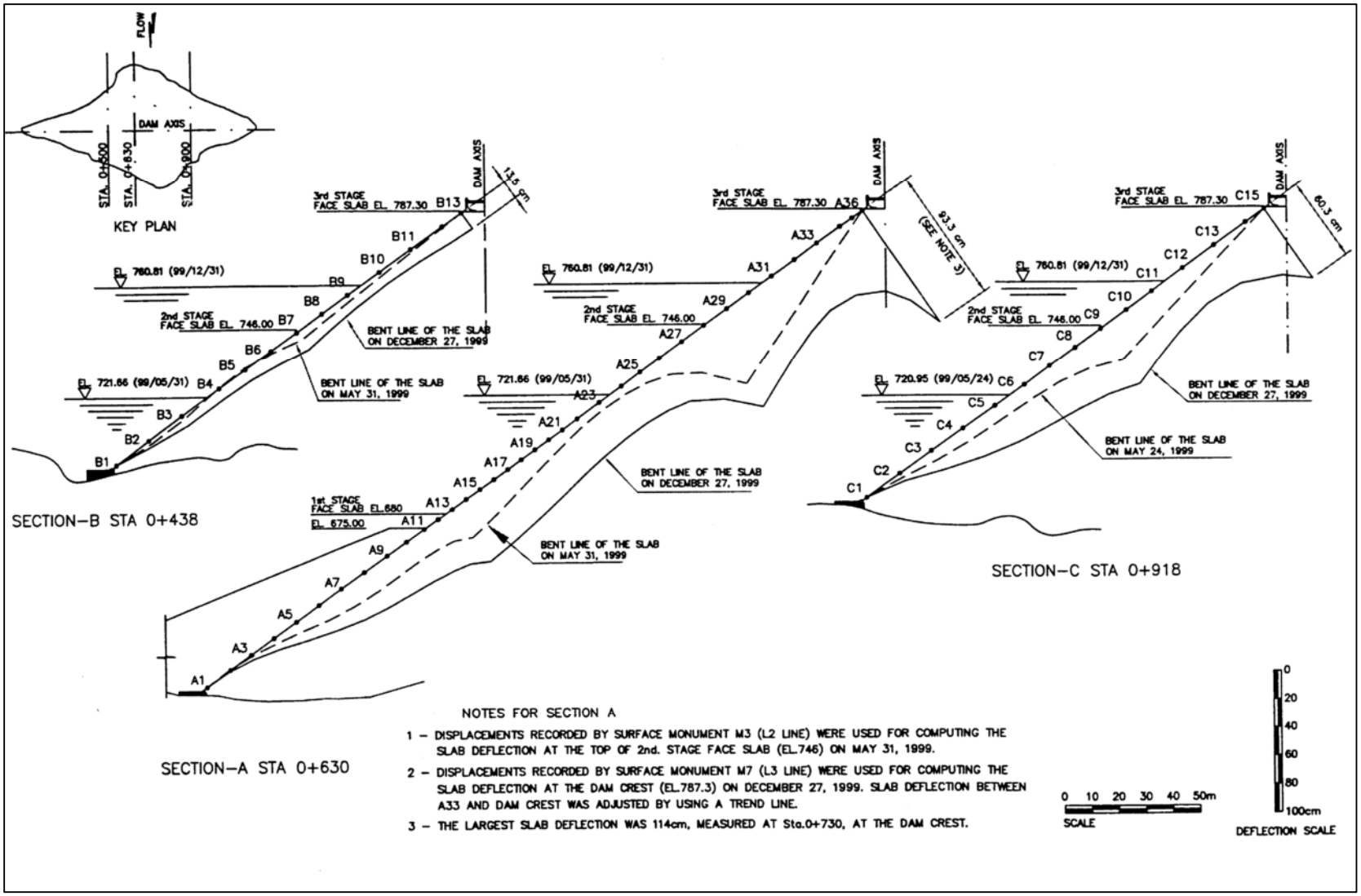

Figure 3.19: Face deflections of TSQ1 dam at three sections (Penman & Rocha-Filho, 2000).

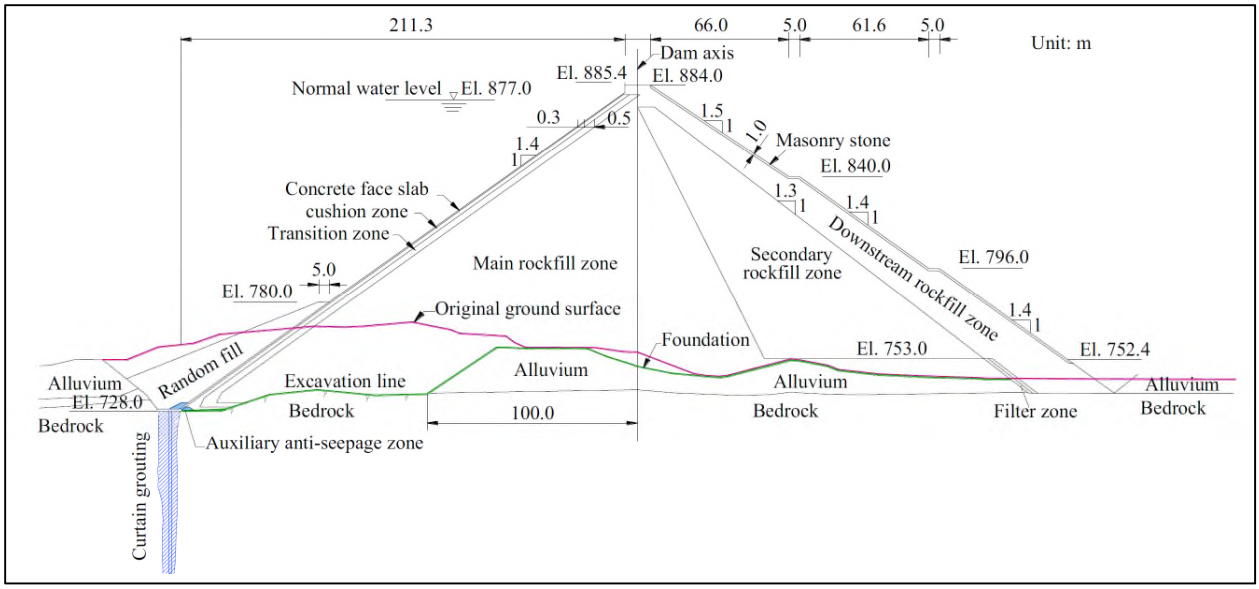

Figure 3.20: Maximum cross section of the Zipingpu dam (Zhang et al., 2015).

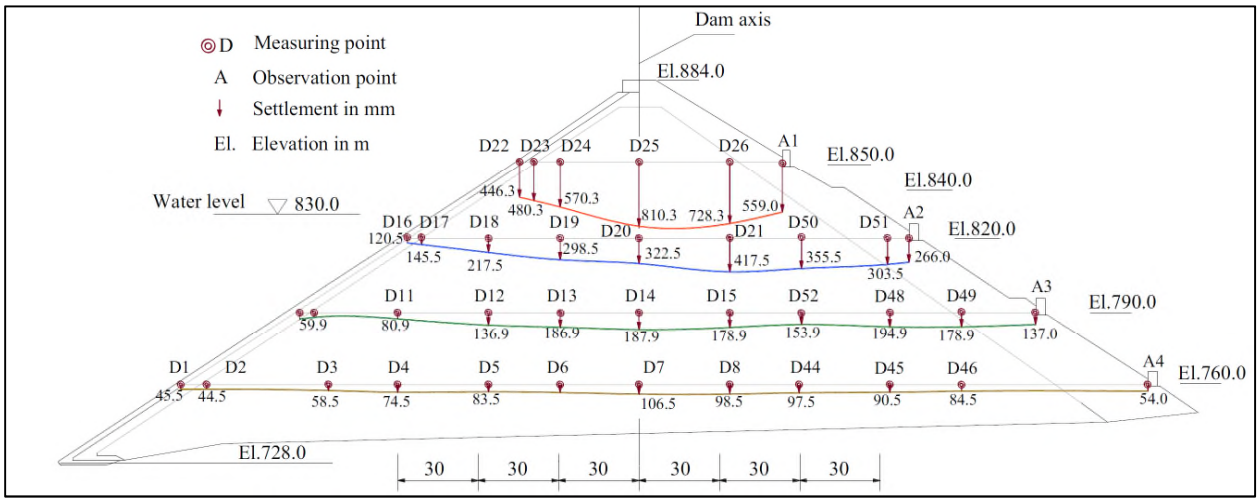

Figure 3.21: Seismic-induced settlements on the downstream slope of the Zipingpu dam (Zhang et al., 2015).

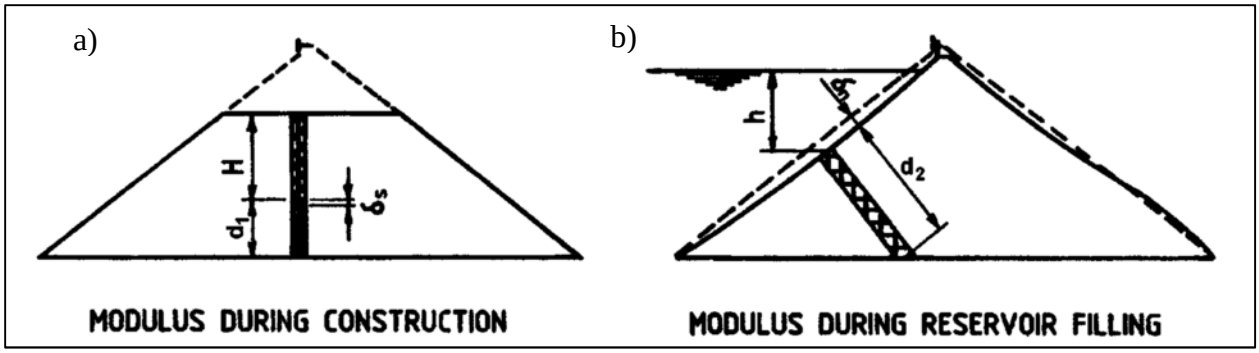

Figure 3.22: Determination of rockfill modulus (Fitzpatrick et al., 1985).

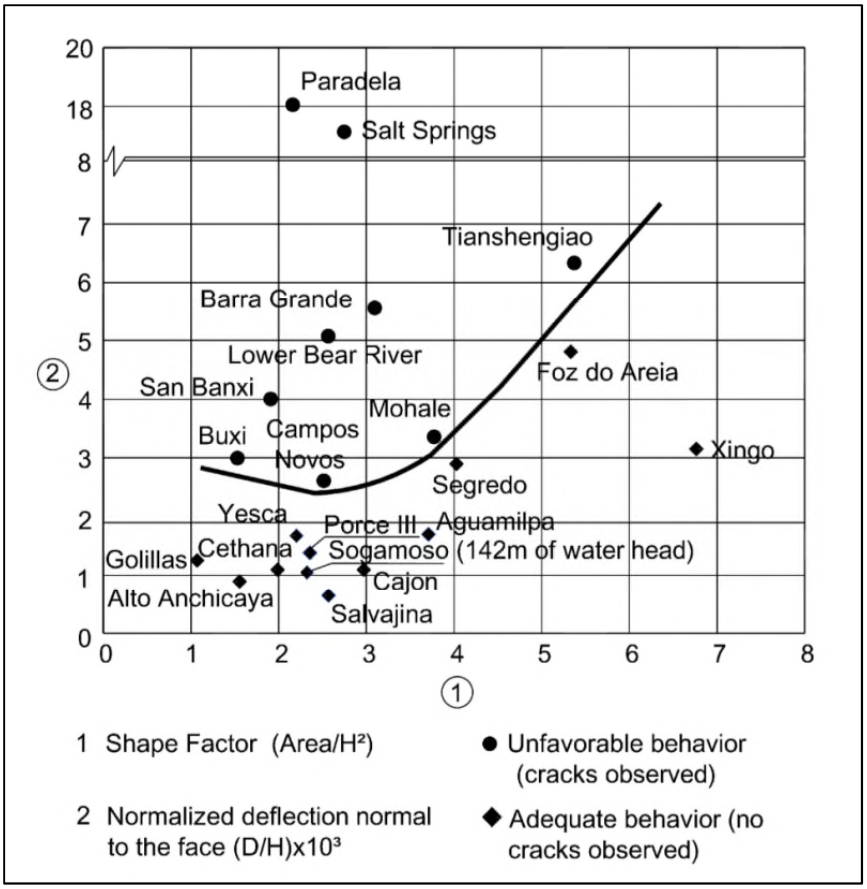

Figure 3.23: Normal deflection of the face as a function of the shape factor (C. Marulanda & Marulanda, 2015).

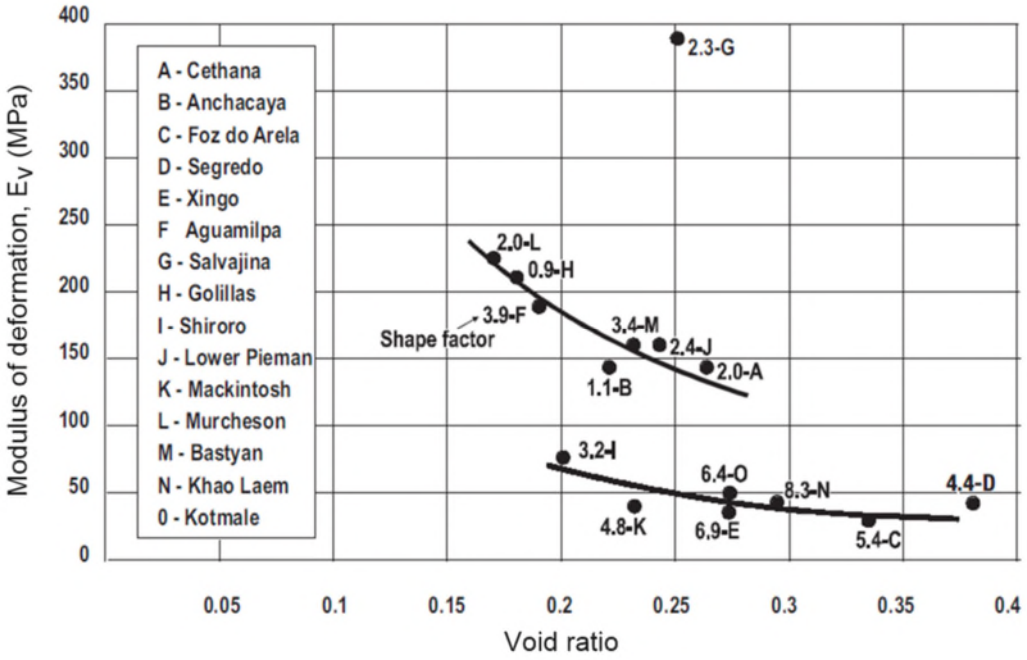

Figure 3.24: Relation between modulus of deformation and void ratio (Pinto & Marques Filho, 1998).

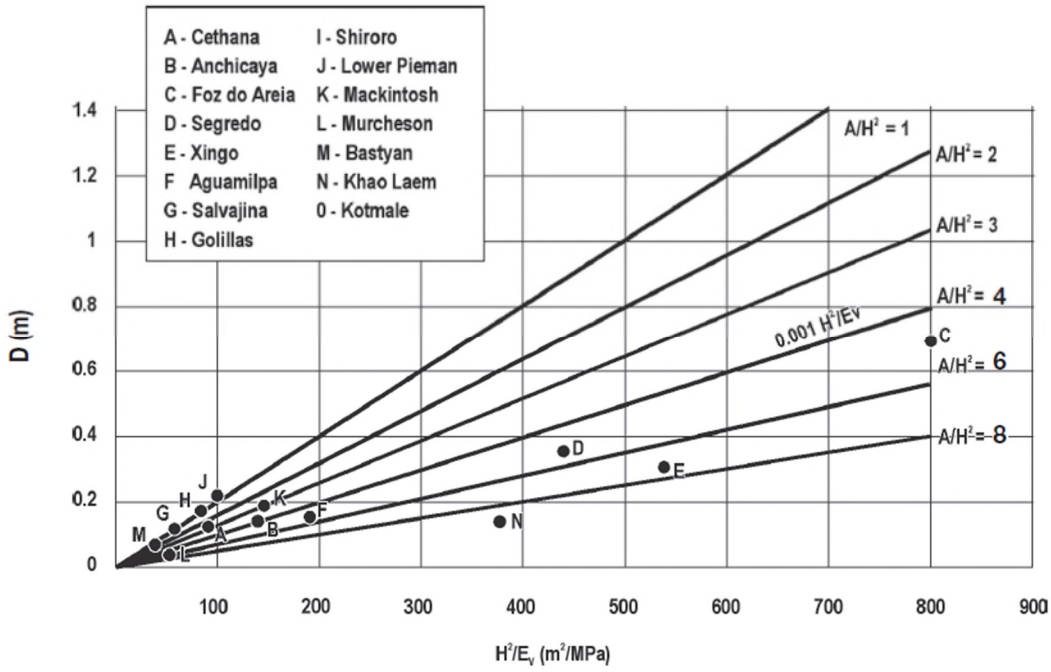

Figure 3.25: Estimation of maximum face deflection (Pinto & Marques Filho, 1998).

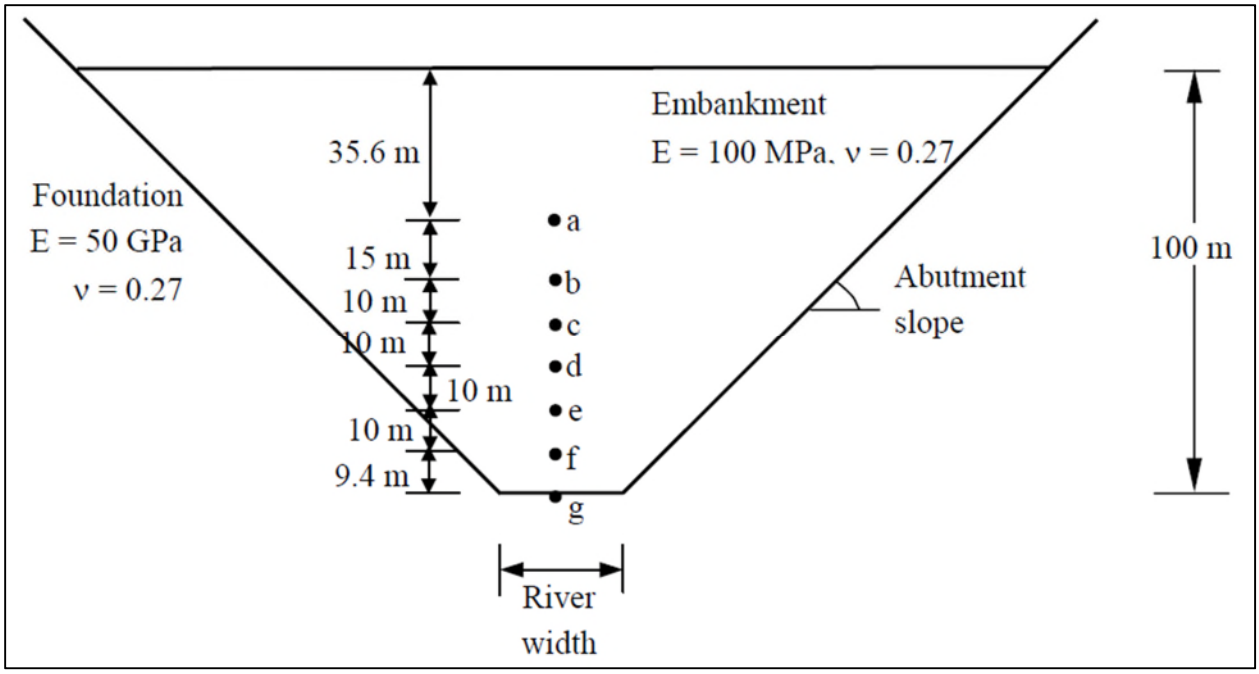

Figure 3.26: Two-dimensional model representing longitudinal section (Hunter & Fell, 2002).

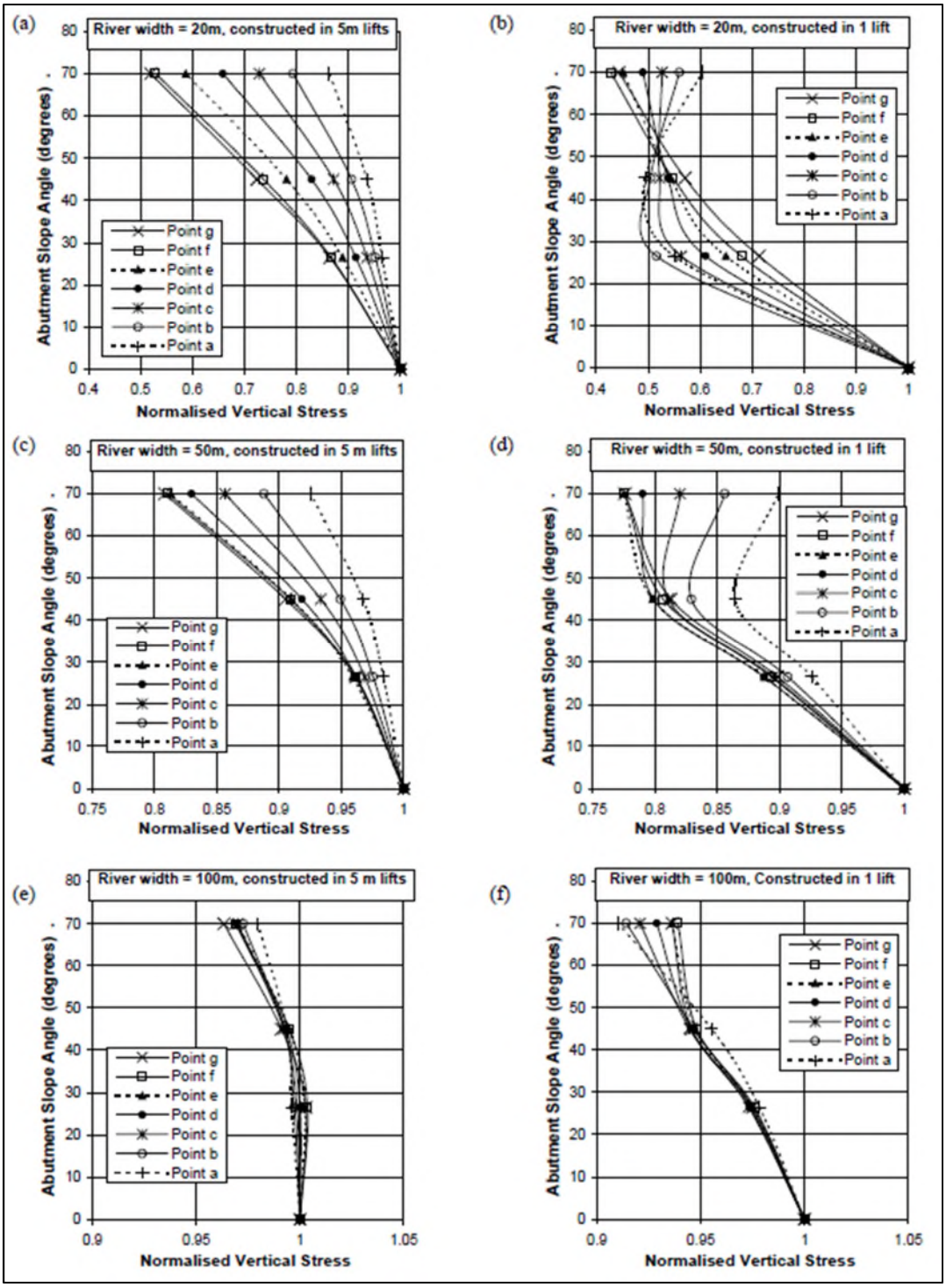

Figure 3.27: Finite difference analyses results at the end of construction in 5 m and 1 m lift rockfill placements: River width is 20 m in (a) and (b), 50 m in (c) and (d), 100 m in (d) and (e) (Hunter & Fell, 2002).

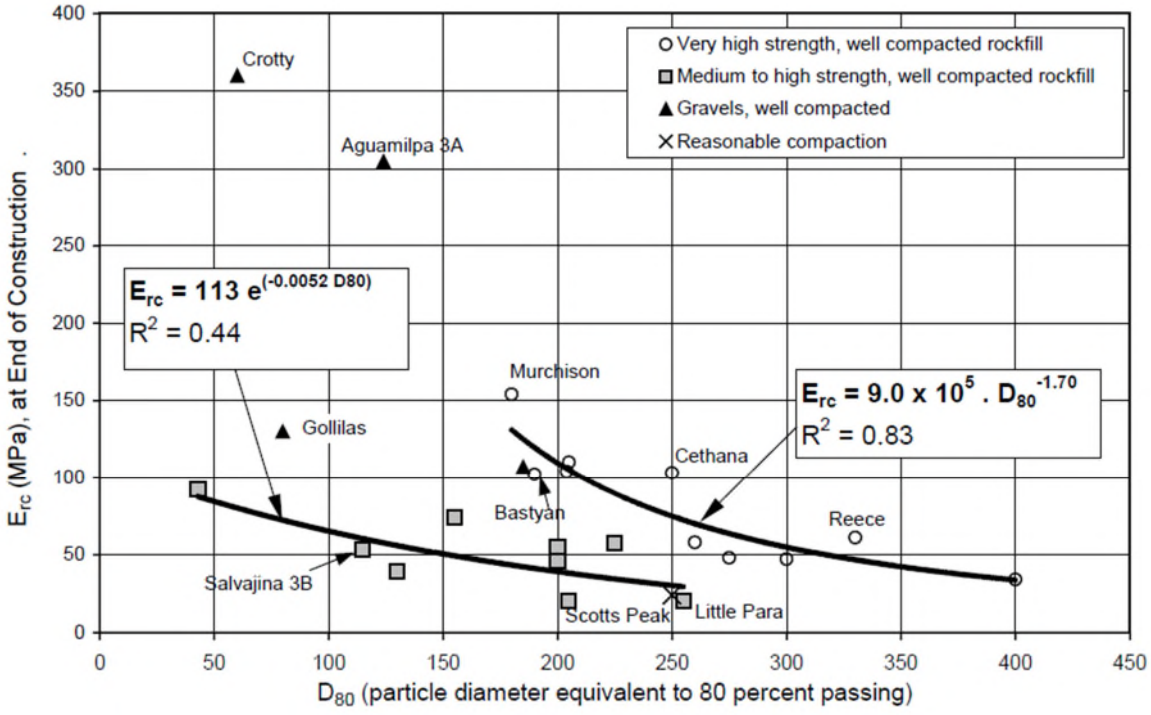

Figure 3.28: Correlation between secant modulus of compacted rockfill at the end of construction and D_{80} particle size (Hunter & Fell, 2002).

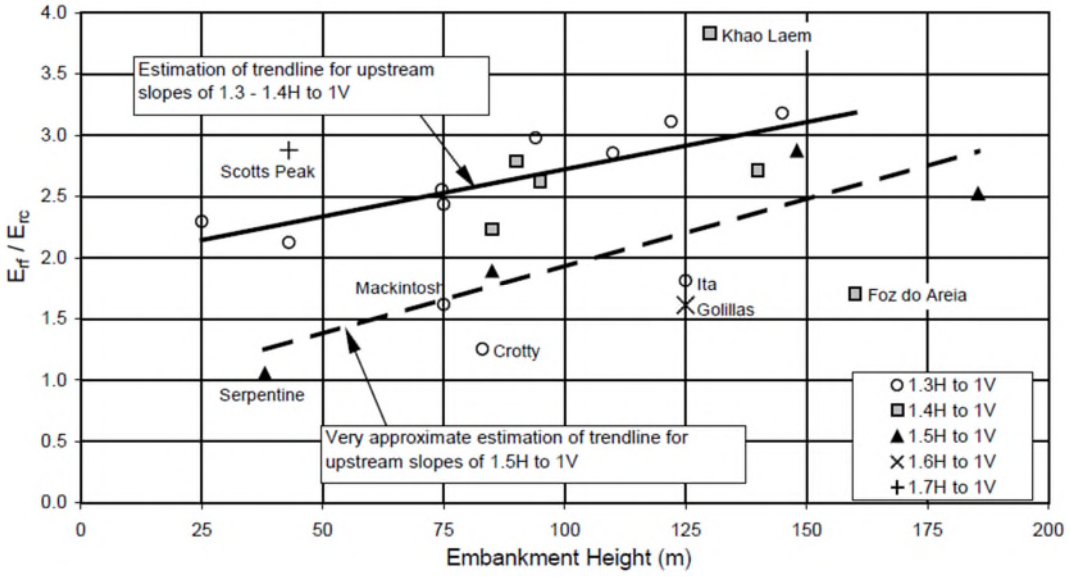

Figure 3.29: Correlation between E_{rf} /E_{rc} and dam height (Hunter & Fell, 2002).

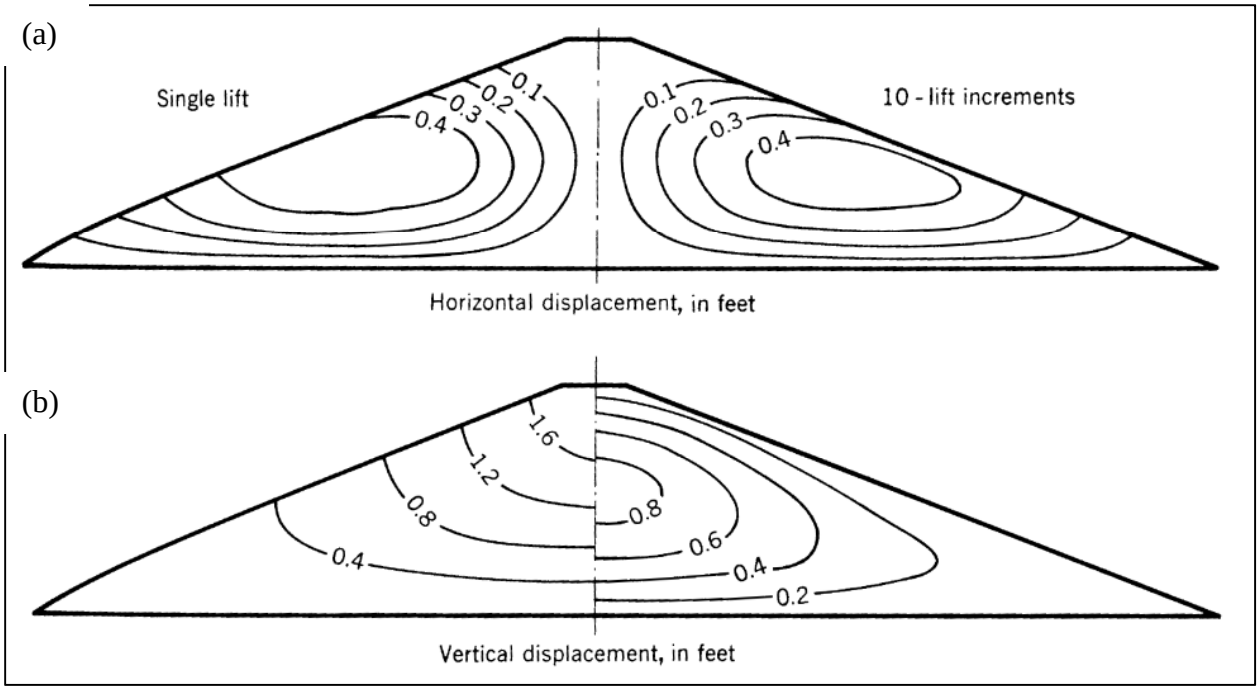

Figure 3.30: Calculated deformation contour comparison of single lift with 10-lift increments due to gravity for: (a) Horizontal and (b) vertical displacement (Clough & Woodward, 1967).

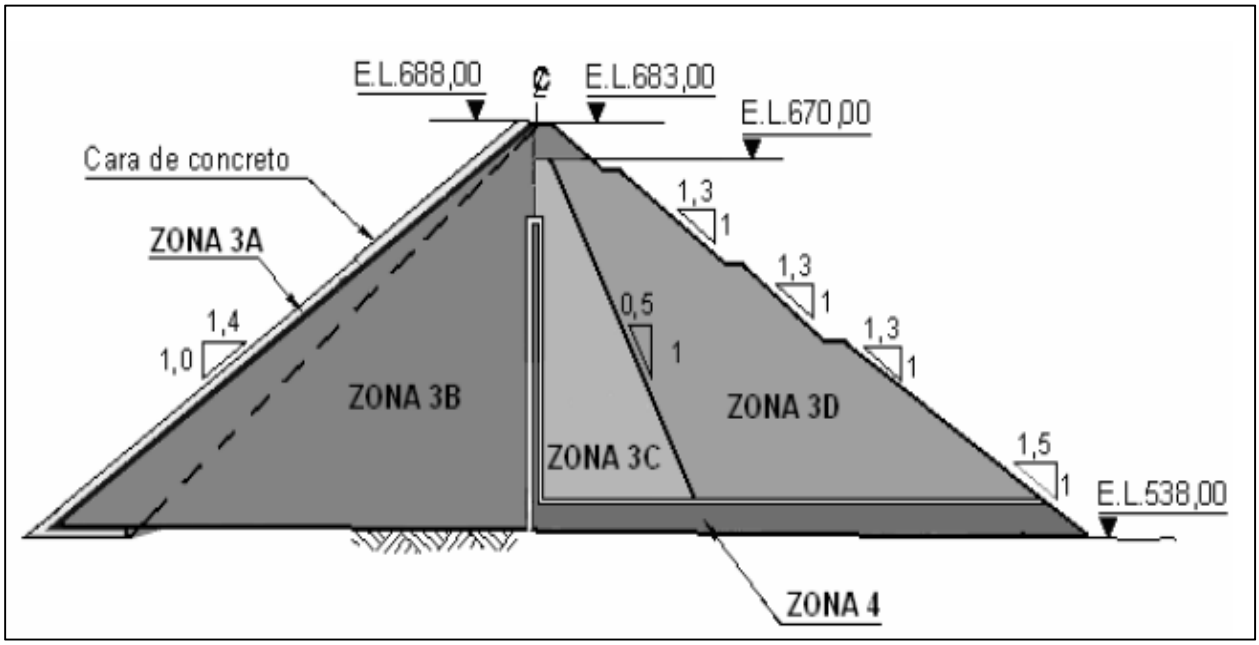

Figure 3.31: Cross Section of Porce III Dam (Marulanda-Escobar & Marulanda-Posada, 2008).

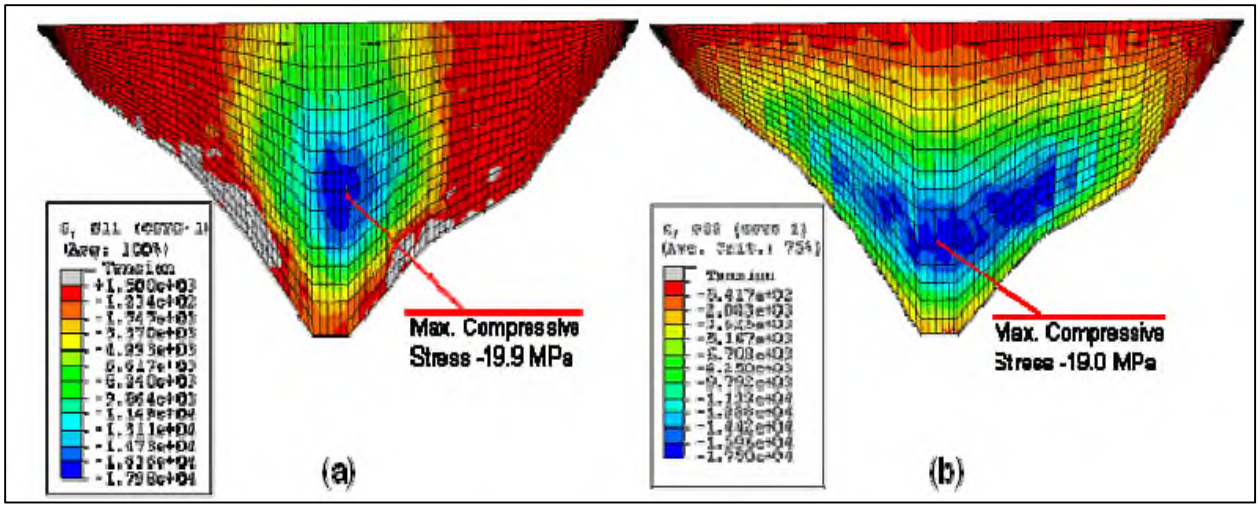

Figure 3.32: Predicted stresses in the concrete face of Porce III dam for rockfill modulus of 70 MPa: (a) Horizontal (b) Slope direction (Marulanda-Escobar & Marulanda-Posada, 2008).

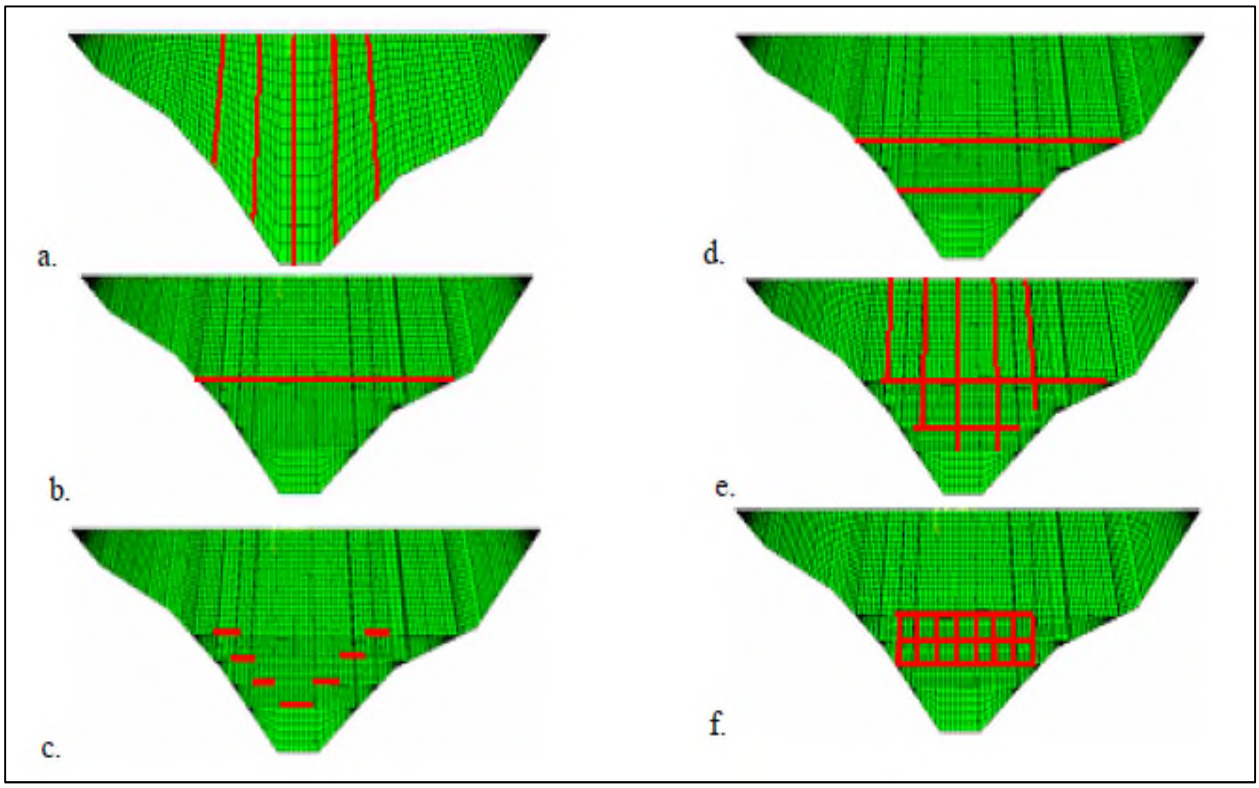

Figure 3.33: Different configurations of compressible joints in concrete face of Porce III dam (Marulanda-Escobar & Marulanda-Posada, 2008).

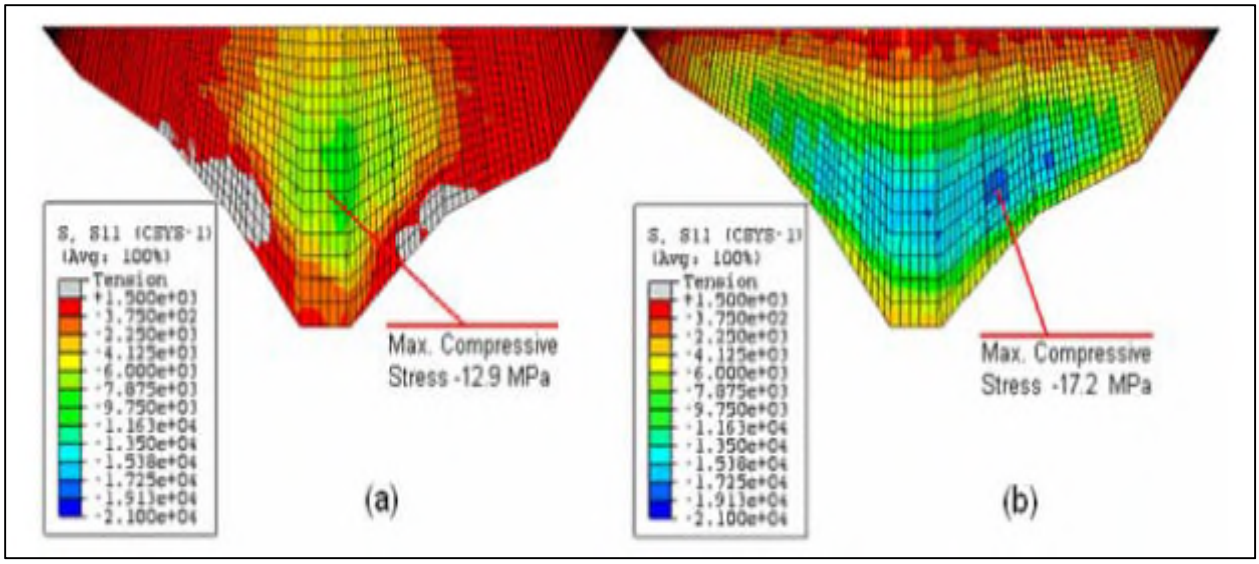

Figure 3.34: Predicted stresses in the concrete face of Porce III dam for rockfill modulus of 70 MPa with five vertical compressible joints: (a) Horizontal and (b) Slope direction (Marulanda-Escobar & Marulanda-Posada, 2008).

CHAPTER 4

NUMERICAL MODELING OF DYNAMIC CENTRIFUGE TEST OF CFRD

4.1 Introduction

The seismic response of the CFRDs have not sufficiently been investigated due to lack of field-measurements during earthquakes. The lack of knowledge about seismic response of the CFRDs urges the need for improving the design methods using numerical tools. Estimation of the seismic response of the CFRDs is necessary to understand the behavior of the CFRDs and take measures to increase the safety factor.

In this thesis, a series of numerical analyses were performed using finite element method on a CFRD model representing the prototype of a centrifuge model. The dynamic centrifuge tests conducted on a CFRD model, whose details were published by Kim et al. (2011), were chosen as a case study for this project. The effects of the hysteretic damping (Masing and non-Masing un/reloading rules) and the interface type (welded and friction contact) between rockfill and concrete face slab on the dynamic behavior of the CFRDs were investigated. The calculated results from the numerical simulations were compared with the results of dynamic centrifuge experiments.

4.2 Centrifuge Experiments

Centrifuge tests are useful in geotechnical engineering problems such as seismic response of soil deposits, soil-structure interaction and many more in the case of lack of real case histories. Such tests generate similar stress values with the prototype model vie application of increased gravitational field and help engineers and researchers to understand the mechanism of certain phenomenon. Several examples of complex soil-structure systems which were modeled using centrifuge are provided in Gillis et al. (2015), Cerna-Diaz (2018), and Numanoglu et al. (2017a).

Thus, similarly, centrifuge tests carried out on CFRD models can be important for studying the seismic response of structures in the case of the limited recorded data at a real site.

The centrifuge test has been conducted at the KAIST centrifuge and earthquake simulator in Korea, which has 5 m platform radius. The maximum payload of 2400 kg can be applied to a maximum 100 g of centrifugal acceleration. The shaking table of the earthquake simulator has a maximum horizontal acceleration of 20 g with a payload up to 700 kg and a maximum horizontal acceleration of 40 g without payload (Kim et al., 2011).

A series of dynamic centrifuge tests has been conducted on two dam models: earth-core rockfill dam (ECRD) and CFRD (Kim et al., 2011). This study investigated only the CFRD model. A cross section from the middle of the centrifuge model and the instrumentation details is shown in Figure 4.1. The height (H) of the CFRD model was chosen to be 160 mm and the upstream reservoir of the model was filled with water to a height of the 0.9H. Both upstream and downstream slopes were 1.4H:1V. The water has been isolated to keep the CFRD model dry as the actual CFRDs in the field are dry due to their concrete face. The inside walls of the container for this study have been greased to reduce the effect of friction between the soil and the container of the centrifuge (Kim et al., 2011).

A centrifugal acceleration of 40 g was employed on CFRD model, which made the height, crest width, and thickness of the concrete face of the prototype CFRD model to be 6.4 m, 0.9 m, and 0.042m, respectively. The concrete face in centrifuge model was represented by using a 3 mm-thick high-density polyethylene (HDPE) with an elastic modulus of 1.2 GPa (Kim et al., 2011). The thickness of the concrete face in the prototype was determined regarding the scaling law equation as illustrated in Eq. (4.1):

$$t_m = \sqrt[3]{\frac{E_p}{E_m}} \frac{t_p}{N} \tag{4.1}$$

in which, E_p is the elastic modulus of the prototype, t_p is the thickness of the prototype, E_m is the elastic modulus of model, t_m is the thickness of model, and N is the scale factor. E_p, the elastic modulus of the concrete in the prototype, is 28 GPa (Kim et al., 2011).

Kim et al. (2011) reported that the friction angle (φ), cohesion (c) and density of the rockfill material used in the centrifuge experiments to be 43˚, 8 kPa and 2100 (kg/m^3), respectively. The rockfill material has been uniformly placed to build the main body of the centrifuge model. For the centrifuge tests, the rockfill samples have been gathered from a dam site to represent the similar material properties of actual dams in Korea. The rockfill materials used in the construction of real CFRDs normally consist of large-size particles, but it is impossible to use those large-size particles in the centrifuge tests. Therefore, parallel gradation technique has been employed to reduce the size of the sample (Kim et al., 2011). Figure 4.2 shows the particle size distribution of both the rockfill used in the model and the in-situ rockfill in Korea. The coefficient of uniformity (C_u) and the median particle size (D_{50}) of the model rockfill was determined to be 17.25 and 2.54 mm, respectively. The particle size distribution of the rockfill used in the centrifuge experiments were compared with some specimens (C33D1, C50D2, and C50D3) used in Menq (2003), which was developed to determine dynamic properties of granular materials, It was concluded that the rockfill material used in the centrifuge tests had a similar particle size distribution curve to the granular materials studied by Menq (2003), as illustrated in Figure 4.3.

The rockfill material used in the model has also been used in resonant column tests to define dynamic properties of the rockfill. The shear wave velocity (Vs) of the rockfill used in the

model was determined using resonant column test results and the equation of $V_S = 100.4\ (\sigma'_{mean})^{0.24}$ was derived, as shown in Figure 4.4 (Kim et al., 2011). Using this derived equation, the effective mean stress (σ'_{mean}) dependent Vs profile from the crest to the base of the dam at maximum cross section in prototype scale is plotted in Figure 4.5.

4.2.1 Instrumentation

The locations of the installed instrumentations shown in Figure 4.1 are presented in Table 4.1. The instruments installed to record the response of CFRD model during tests are 7 accelerometers (A), 8 strain gages (SG), and 2 laser displacement sensors (LDS). Kim et al. (2011) reported that 4 strain gages (SG2, SG3, SG5, and SG6) did not provide data during the centrifuge experiments because of a problem occurred in data acquisition system. As a result, the data from these 4 strain gages could not be obtained.

4.2.2 Input Motions

All nine tests were performed using Ofunato earthquake record (M_S=7.4, 1978), one of the most commonly used motion in Korea (Park et al. 2009), but with different peak ground accelerations (PGAs). The PGAs of the motions ranged from 0.092 g (Test 01) to 0.570 g (Test 09). The motions recorded at the base of the container (accelerometer of A00) for each test were used as the input motions in the numerical analyses. The input motions were applied to bottom nodes of the numerical model. The properties the motions recorded at the base of the container are shown in Table 4.2. Baseline correction has been applied to the input motions, as their displacement-time histories were non-zero at the end of the motion. The input motions of 9 nine tests with and without baseline correction are plotted from Figure 4.6 to Figure 4.14.

4.3 Numerical Model

The numerical model was developed using the finite element analysis program LS-DYNA (LSTC, 2009). The details of finite element mesh are shown in Figure 4.15 and Figure 4.16. The materials that exist in the numerical model are rockfill, concrete face, water, and container. The mid-cross section of the experimental model is simulated using 3-D brick elements. The model consisted of 1957 solid elements, and 32 shell elements. The rockfill, water, and container were created using eight-node brick elements with single point integration, while the concrete-face slab was modeled using shell elements with 2 integration points (see Figure 4.16). Linear elastic material was used to model the concrete-face and container, whereas water was modeled with elastic-fluid material. The material properties of elastic materials are presented in Table 4.3.

The maximum frequency of soil (f_{max}) was taken into consideration using Eq. (4.2) while choosing the element size of the mesh. Hashash et al. (2010) recommends that the minimum value of f_{max} be 25-30 Hz. An element size of 0.2 m was selected for the mesh elements, with nodes on the locations corresponding to the coordinates of accelerometers placed in the centrifuge model. Considering the smallest Vs was 150 m/s (see Figure 4.5), the f_{max} becomes 187.5 Hz for the layer thickness of 0.2 m.

$$f_{max} = {Vs}/{4(\Delta l)} \tag{4.2}$$

where, Δl is the layer thickness.

The bottom nodes of the model were vertically fixed and laterally allowed to move. Periodic boundary conditions were applied to the outermost nodes in two degrees of freedom (in X and Z directions). All the nodes in the numerical model were fixed in Y directions.

4.3.1 Constitutive Model

The numerical simulations use a three-dimensional effective stress soil model (I-soil) (Numanoglu, 2018) to describe important aspects of granular materials including small-strain nonlinearity, hysteretic damping, shear induced volumetric (contraction - dilation) behavior in terms of strains and excess porewater pressures, and effective mean stress dependency of the stress – strain behavior. The model uses distributed element modeling framework (Iwan 1967, Chiang and Beck 1994) whereby n number of nested elasto-plastic components are superimposed to obtain piecewise linearized shear stress – shear strain relation. The model provides flexible control over representing hysteretic behavior including Masing type and non-Masing type un/reloading via generalized hysteresis modeling formulation in three-dimensional stress space (Numanoglu et al. 2017b). The 3D formulation model closely follows the un/reloading rules developed by Phillips and Hashash (2009) in which Masing un/reloading rules are modified using a reduction factor (MRDF model) of:

$$F(\gamma_m) = p_1 - p_2\left(1 - \frac{G_{\gamma_m}}{G_{max}}\right)^{p_3} \tag{4.3}$$

where p_1, p_2 and p_3 are non-dimensional parameters to provide best fit with the target damping curve. Numanoglu et al. 2017b extends the MRDF model to 3D and eliminates any framework dependent derivation of un/reloading rules to better represent hysteretic damping. I-soil utilizes this generalized framework, and the model reproduces any type of normalized modulus reduction and damping curves defined by the user. The effective mean stress dependency of the mobilized shear strength is achieved using 3D Drucker – Prager yield surfaces for nested components. On the other hand, the shear modulus is dependent on effective means stress via:

$$G_{max} = G_{max}^{\sigma'_{ref}} \left[\frac{\sigma'_{mean} - \sigma'_{cut-off}}{\sigma'_{ref}} \right]^b \quad (4.4)$$

where $G_{max}^{\sigma'_{ref}}$ = small strain shear modulus at a given reference effective mean stress (σ'_{ref}), $\sigma'_{cut-off}$ = tension cut-off value below which stiffness vanishes, and b = model coefficient characterizing the effective mean stress dependence of the shear modulus. The relation between volumetric and shear strains is defined as:

$$d\varepsilon_v^p = A_0(\eta_{pt} - \eta)d\varepsilon_q^p \quad (4.5)$$

where A_0 = coefficient determining the rate of shear induced volumetric strains, η is tress ratio, η_{pt} is phase transformation stress ratio, $d\varepsilon_v^p$ is plastic volumetric strain increment, and $d\varepsilon_q^p$ is platic shear strain increment. The model induces contractive behavior (decrease in void ratio) if ($\eta_{pt} - \eta > 0$) or dilatant behavior (increase in void ratio) if ($\eta_{pt} - \eta < 0$). The implementation of the I-soil model is achieved by introducing it as a user defined material in LS-DYNA, along with a stress-strain backbone curve and initial shear modulus as input (Numanoglu et al., 2017a).

Several examples for the application of I-soil model in nonlinear site response analyses and 3-D soil-structure interaction analyses can be found in Baltaji et al. (2017) and Coleman et al. (2017). The next section describes the selection of dynamic properties of the rockfill and input parameters and curves for I-soil.

4.3.2 Dynamic Properties of the Rockfill Material

The normalized modulus reduction (G/G_{max}) and damping curves from two different reference dynamic curves were used to define the backbone curve of the rockfill, which required for I-soil model as input parameter. First, G/G_{max} and damping curves from Menq (2003) were used. Menq (2003) performed large-scale resonant column tests on 59 samples of sandy and

gravelly soils to define the dynamic properties of granular soils. Second, G/G_{max} and damping curves involved from Darendeli (2001) were used in this study. The normalized modulus reduction (G/G_{max}) and damping curves used as reference curves in this study were compared with the dynamic curves obtained from resonant column test results under a confining pressure of 25 kPa, as shown in Figure 4.17. The modulus reduction curve of Menq (2003) was found to relatively better capture the resonant column test results than that of Darendeli (2001) compared to the resonant column test results. Overall, a good agreement between selected target dynamic soil curves and measured G/G_{max} and damping curves was obtained. The at-rest coefficient of lateral earth pressure which is required to obtain reference normalized G/G_{max} and damping curves of Menq (2003) and Darendeli (2001) were obtained using Jakey's equation of $K_0 = (1 - sin\varphi')$ (Jaky, 1948).

The hysteretic damping of the rockfill were represented by utilizing both Masing and non-Masing type un/reloading rules. The Masing type un/reloading is known to overestimate the damping of the soil at large strains (Philips and Hashash, 2009). Philips and Hashash (2009) developed a new procedure that modifies the Masing un/reloading by introducing a reduction factor (MRDF) to overcome this overestimation of the damping at large strains. The non-Masing un/reloading that is generated with MRDF reduction factor estimates the hysteretic damping of soils better than Masing rules at large strains. Figure 4.18 shows the dynamic curves used in the I-soil constitutive model under a vertical stress of 63.9 kPa. Figure 4.18b shows the difference in hysteretic damping generated by Masing and non-Masing type un/reloading rules. The Masing type un/reloading overestimated the damping of the soil at large strains, whereas the non-Masing type un/reloading captured well the damping behavior of the soil generated by Menq (2003) and Darendeli (2001).

The resultant backbone curves (see Figure 4.18c) are used for I-soil as an input curve at corresponding effective mean stresses. The backbone curve is obtained with the generalized quadratic/hyperbolic model (GQ/H) model (Groholski et al. 2016) using DEEPSOIL v7.0 (Hashash et al. 2017), a 1-D nonlinear site response analysis software, to represent proper shear stress – shear strain relationship. The GQ/H model has the advantage of providing small-strain shear modulus (G_{max}), maximum shear strength at large stains (τ_{max}), and a flexible control between G_{max} and τ_{max} (Groholski et al. 2016). The small-strain shear modulus was calculated using $G_{max} = \rho V_s^2$, whereas the large-strain target shear strength was adapted from Eq. (4.6).

$$\tau_{max} = c + \sigma_v' \tan(\varphi') \tag{4.6}$$

where, σ_v is the vertical stress. The maximum target shear strength of 43º is used at 3% shear strain level following the procedure described in Numanoglu et al. (2017a).

Monotonic constant volume shear response of three gravel materials was studied by Hubler et al. (2017). It was reported that phase transformation angle (φ_{pt}) was dependent on the particle angularity. The gravel material having friction angle of 42˚ (ultimate state) had a phase transformation angle of 32˚, which was used to calculate the phase transformation stress ratio using tan (φ_{pt}) for the rockfill material considering the friction angle of rockfill material used in the centrifuge was 43˚.

The mean stresses of each element were calculated performing an elastic analysis with initial stiffnesses. Then, the elements that had mean stresses close to the ones in the middle layers which were used to obtain backbone curves were assigned the same material properties.

4.3.3 Interface Types between Rockfill and Concrete Face

Two different approaches were used in modeling of the interface between rockfill and concrete-face slab, as detailed in Figure 4.19. The first approach was to use welded contact, meaning that elements of the rockfill on the upstream slope and the elements of the concrete-face slab share the same nodes. This first approach does not take the interface into consideration in the simulation. The welded contact type was defined as unrealistic connection type by Uddin and Gazetas (1995). The second approach was to introduce an interface that allows slippage between rockfill and concrete-face slab. The interface formulation is based on a penalty method in which the software roughly estimates the magnitude of contact stiffness from the stiffness of interface elements that are normal to the interface. The interface obeys the Coulomb friction formulation (LSTC, 2009). The coefficient of friction (tanδ) implemented in frictional contact is calculated using Eq. (4.7) (Bowles, 1996).

$$tan\delta = \tan({}^{2}/_{3}\,\varphi') \tag{4.7}$$

4.3.4 Limitations and Assumptions in the Analyses

The centrifuge tests are a valuable laboratory testing method. However, the centrifuge tests investigated for this study has a small centrifugal acceleration of 40 g, which allows one to model a prototype that has a height of only 6.4 m and base width of 18.8 m. These dimensions are considerably smaller than the dimensions of CFRDs constructed in the field. Nonetheless, this centrifuge experiment was chosen as a case study despite the small scale, because it was one of the few dynamic centrifuge tests carried out on CFRDs. The rockfill was modeled as a dry material as it was isolated from the water in the centrifuge test. The numerical model was created with a single lift, meaning that it was not modeled with the staged-construction feature. The initialization

of stresses was achieved by activating the dynamic relaxation phase module of LS-DYNA (LSTC, 2009), which minimizes the effects of initial dynamic oscillation at beginning of the analyses.

The schematic configuration of performed analyses in this study is shown in Figure 4.20. In total, the number of performed analyses including nine motions is 72, in which Masing type un/reloading rules, non-Masing type un/reloading rules, welded contact, and friction contact were included with referenced dynamic soil curves of Menq (2003) and Darendeli (2001). A detailed comparison of the measured and calculated acceleration time histories and spectral accelerations are provided in the APPENDIX (as summarized in the analysis tree in Figure 4.20).

4.4 Comparison of Measured and Computed Results

After the prototype model was built, the dynamic analyses were performed for each test conducted on the centrifuge model from Test 01 to Test 09. The numerical results were compared to centrifugal measurements corresponding to acceleration time histories, %5-damped spectral accelerations, bending moment increments of the concrete face slab, and lateral deformations.

4.4.1 Spectral Accelerations

The first comparison of the results was done by examining each analysis separately. The measured and calculated acceleration-time histories and the associated spectral accelerations (Sa) for all nine tests were compared and shown between Figure 4.21 through Figure 4.29 for the case in which the numerical model was developed using dynamic curves of Menq (2003) with non-Masing un/reloading and the friction contact between rockfill and concrete face. Figure 4.21 shows the results of Test 01 in which the weakest motion is used as input motion. The computed response form Test 01 was in good agreement with centrifugal measurement between in periods between

0.2 to 10 s, whereas an overestimation in the response spectra at a period of approximately 0.09 s was observed at locations A14 and A13. In Test 02, good estimation was observed in response spectra at all locations except the A14 where the numerical model overestimated the response between periods of 0.01 s and 0.1 s at the crest (see Figure 4.22e). The computed responses from Test 03 to Test 07 were greatly consistent with the centrifuge measurements in terms of both acceleration and spectral responses. In Test 08 and Test 09, a good agreement between computed and measured response spectra was achieved since these two motions were the strongest two motions in the tests. Numerical analysis reasonably captured the response spectra at the crest in both Test 04 and Test 09 (Figure 4.28e and Figure 4.29e). A slight overestimation was seen in the lower part of the dam (A11, A12, A31, and A32) in the period ranges between 0.01 to 0.2 s in both Test 08 and Test 09 (see Figure 4.28 and Figure 4.29).

4.4.2 Mean Residual Spectral Accelerations and PGA Profiles

The mean residual spectral accelerations and peak ground accelerations, including all nine tests, were calculated to better demonstrate the overall differences between centrifugal measurements and numerical estimations. The residuals were calculated using Eq. (4.8) (Hashash et al., 2015):

$$Residual\ X = \log\left(\frac{X_{measured}}{X_{calculated}}\right) \tag{4.8}$$

where, X is the compared parameter (Sa, PGA, etc.). According to this equation, the calculated response underestimates the measured response when X is greater than 0, while overestimation is seen when X is smaller than 0. The mean residuals of spectral accelerations and peak ground accelerations for Menq (2003) dynamic curves are illustrated in Figure 4.30 and Figure 4.31, respectively. Overall, Masing un/reloading and welded contact caused overestimation in spectral

accelerations in periods between 0.03 to 0.1 s with a maximum mean residual of -0.28 (90% overestimation) and underestimation in periods between 0.1 to 1 s with a maximum mean residual of 0.16 (31% underestimation), as the height of the dam increased. The mean residual PGAs showed that Masing un/reloading were slightly better than non-Masing un/reloading in capturing PGAs, as shown in Figure 4.31.

The closest estimation of mean residual spectral accelerations and peak ground accelerations referenced dynamic curves by Menq (2003) was also obtained with non-Masing un/reloading along with friction contact, particularly at the crest (A14). Good estimation of response spectra was achieved in periods between 0.1 to 1 s at almost all the locations. An overestimation was observed in periods ranging from 0.01 to 0.03 s in response spectra, with an average mean residual difference of about -0.07 (17% overestimation). The average overestimation of -0.11 (29% overestimation) was seen in periods between 0.03 to 0.09 s, with a maximum difference of -0.22, which means 1.65 times higher than measured S_a, at location of A32 (see Figure 4.30e). In periods between 1 to 10 s, the maximum underestimation of 0.12 and maximum overestimation of -0.28 were observed; however, it can be considered as insignificant as the measured and computed spectral accelerations are small in these periods. As for the mean residual PGAs, a small amount of overestimation of mean residual PGA was observed, with a maximum mean residual PGA of -0.08 (20 % overestimation) at location of A32 (see Figure 4.31). Overall, mean residuals showed that the predictions were close to the centrifugal measurements considering the response spectra and PGAs. A similar trend was seen when dynamic curves of Darendeli (2001) was used for the reference dynamic curves (see Figure 4.32 and Figure 4.33). A close relationship was observed in computed spectral accelerations for the referenced dynamic soil curves of Menq (2003) and Darendeli (2001). However, the results obtained using Menq (2003) dynamic curves

were slightly better than those from Darendeli (2001) in capturing the measured response spectra at the crest.

4.4.3 Bending Moment Increments

Another comparison between the results of centrifugal measurements and numerical analyses was done over maximum and minimum bending moment increments. For this comparison, the numerical results were presented for the case where Menq (2003) dynamic curves were used as reference along with non-Masing un/reloading rules and friction contact utilization, which yielded the best estimation in capturing measured spectral accelerations. The strain gages provided data were SG1, SG4, SG7, and SG8 (see Figure 4.1 for the locations). Kim et al. (2011) stated that the bending moments were calculated using Eq. (4.9).

$$M_p = -(\epsilon_o - \epsilon_i)\frac{(Et^2N^2)}{12(1-\nu^2)} \tag{4.9}$$

where, ϵ_o is the strain on the outer face, ϵ_i is the strain on the inner face E is Young's modulus, ν is Poisson's ratio, N is scale factor. The comparison of bending moment increments is presented in Figure 4.34. The bending moment increments obtained by numerical results of Test 09, Test 08, and Test 07 showed a good agreement with centrifugal measurements. A reasonable estimation of bending moment increments was achieved in other tests (from Test 06 to Test 01). Overall, the bending moment increments obtained from the simulations were close to centrifugal measurements.

4.4.4 Lateral Deformations

As for the lateral deformations, the numerical model could not capture the horizontal deformations measured in the centrifuge test. According to Kim et al. (2011), the lateral

displacements and settlements at the crest and on the downstream slope were measured using an image-processing technique with laser displacement sensor (LDS). The measured and calculated lateral displacements during Test 09 are shown in Figure 4.35 and Figure 4.36, respectively. The measured residual deformation at the crest was stated to be 51.2 mm (Kim et al., 2011), while 15 mm of lateral deformation was calculated in the numerical analysis. On the slope, the measured residual lateral deformation was 14.1 mm, whereas a lateral movement of 1.2 mm through upstream direction was calculated. The displacement-time histories recorded by LDS were differentiated two times. It was found that the acceleration-time histories from the differentiations showed differences with acceleration-time histories recorded by accelerometers that were installed below the LSDs. With the same data obtaining technique, heave behavior at the crest of the model was reported during the centrifuge experiments Kim et al. (2011).

The results presented in the APPENDIX showed that the hysteretic damping type had a key role on the response of the dam as the level of shaking increased. Non-Masing type un/reloading captured the spectral accelerations better than Masing type un/reloading. This finding can be attributed to the difference between those damping formulations at large strains. The analyses with Masing type un/reloading considerably underestimated the response in periods between 0.1 – 1 s due to overestimation of damping at large strains, as the level of shaking increases. Furthermore, the response of the dam is strongly influenced by the connection type, particularly at the crest. The welded contact caused significant overestimation between periods of 0.01 – 0.1 s and underestimation between periods of 0.1 – 1 s was observed, particularly at the crest (A14), as the level of shaking increased, whereas friction contact resulted in good agreement with centrifugal measurements.

4.5 Summary

The response of a 6.4 m-height CFRD model, which was the prototype of a centrifuge model, was studied. A series of nonlinear dynamic analyses were performed using finite element method to study the impact of the hysteretic damping of the rockfill and the interface type on the dynamic response of the CFRDs. The hysteretic damping of the rockfill was represented with both Masing and non-Masing un/reloading rules, while the interface was modeled with both welded and friction contact. The dynamic soil curves by Menq (2003) and Darendeli (2001) were used as reference curves. In total, 72 nonlinear dynamic finite element analysis simulations were carried out using I-soil constitutive model. It was concluded from the comparisons that the closest estimation of measured response was obtained when non-Masing type un/reloading rules were used along with accounting for friction contact between rockfill and the concrete face in terms of spectral accelerations and bending moment increments, but not lateral deformations. The Masing un/reloading rules and welded contact caused underestimation, particularly at the crest of the dam. These observations show that better characterization of hysteretic damping and interaction between rockfill and concrete face significantly improves the predictive capabilities of numerical tools to estimate the seismic response of CFRDs.

Table 4.1: Locations of accelerometers (A), strain gages (SG) and laser displacement sensors (LDS) installed on centrifuge model (Kim et al., 2011).

Instrumentation	**Coordinates**		
	X (mm)	**Y(mm)**	**Z(mm)**
A00	Attached to the base of rigid container		
A11	245	245	35
A12	245	245	75
A13	245	245	115
A14	245	245	155
A31	345	245	35
A32	345	245	75
LDS1	245	245	160
LDS2	345	245	89
SG1	12	245	9
SG2	41	245	29
SG3	69	245	49
SG4	98	245	70
SG5	126	245	90
SG6	155	245	110
SG7	183	245	131
SG8	212	245	151

Table 4.2: Properties of the baseline corrected motions recorded at the base of the container.

Test Number	**Peak Ground Accelerations (g)**	**Arias Intensity, I_A (m/s)**
Test 01	0.09	0.06
Test 02	0.13	0.18
Test 03	0.17	0.31
Test 04	0.21	0.50
Test 05	0.28	0.83
Test 06	0.37	1.29
Test 07	0.42	2.51
Test 08	0.44	2.99
Test 09	0.55	3.63

Table 4.3: Material properties of concrete, container and water.

Property	**Concrete-face**	**Container[1]**	**Water[2]**
Density, ρ, (kg/m^3)	2400	2700	1000
Elastic modulus, E, (GPa)	28	69	-
Bulk modulus, K, (GPa)	-	-	2.2
Poisson's ratio, ν	0.2	0.33	0.499
Damping Ratio, ξ, (%)	1	1	-

References: 1. Tsinidis et al. (2016), 2. Bernier et al. (2016)

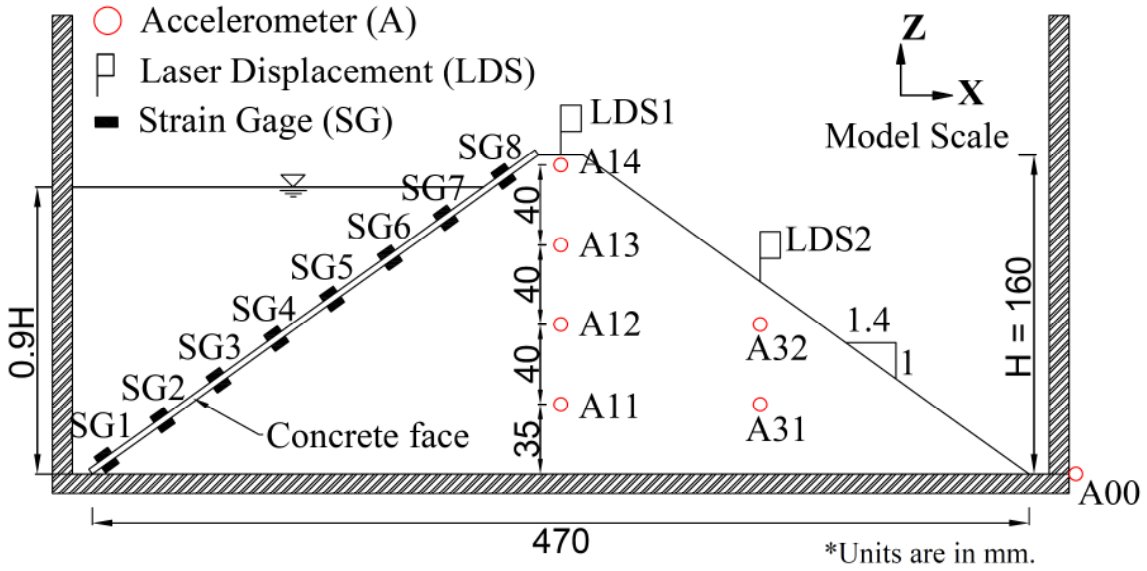

Figure 4.1: Cross section and instrumentation installed in the CFRD centrifuge model (reprinted from Kim et al., 2011).

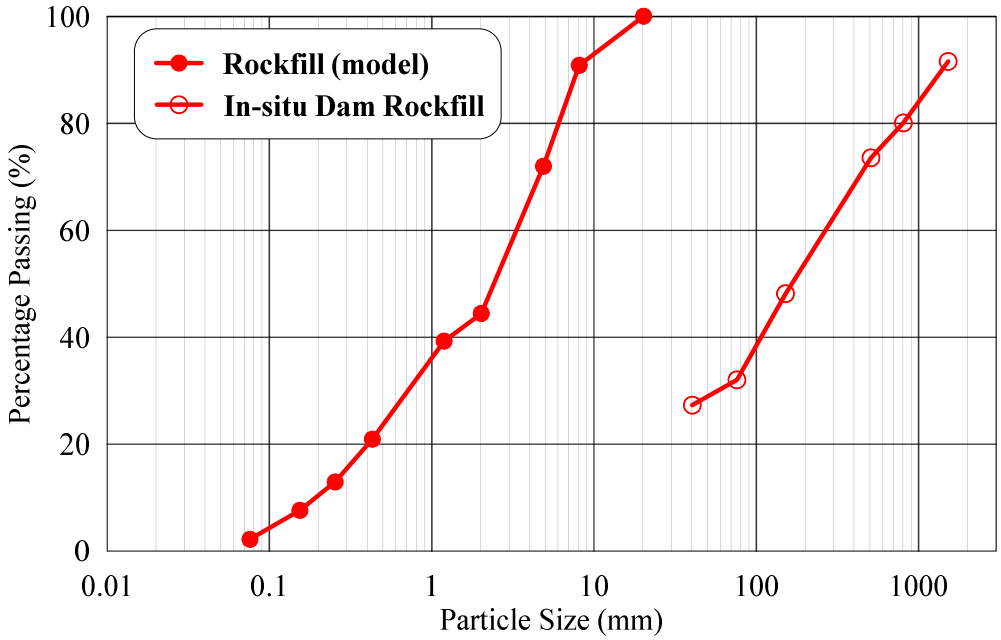

Figure 4.2: Particle size distribution of in-situ rockfill and the rockfill material used in the centrifuge model (reprinted from Kim et al., 2011).

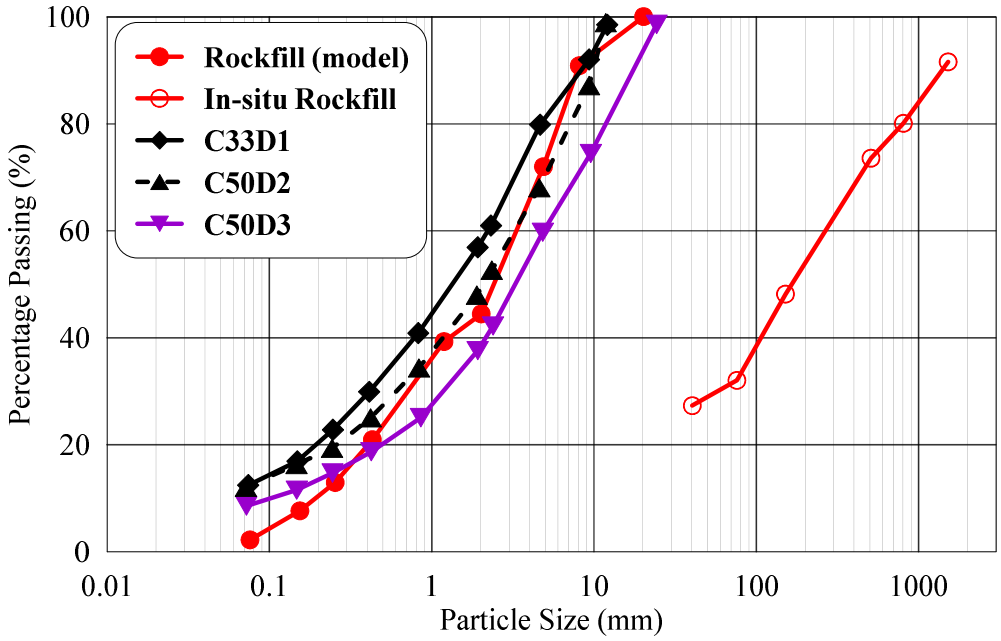

Figure 4.3: Evaluation of particle size distribution of rockfill and several specimens used in Menq (2003).

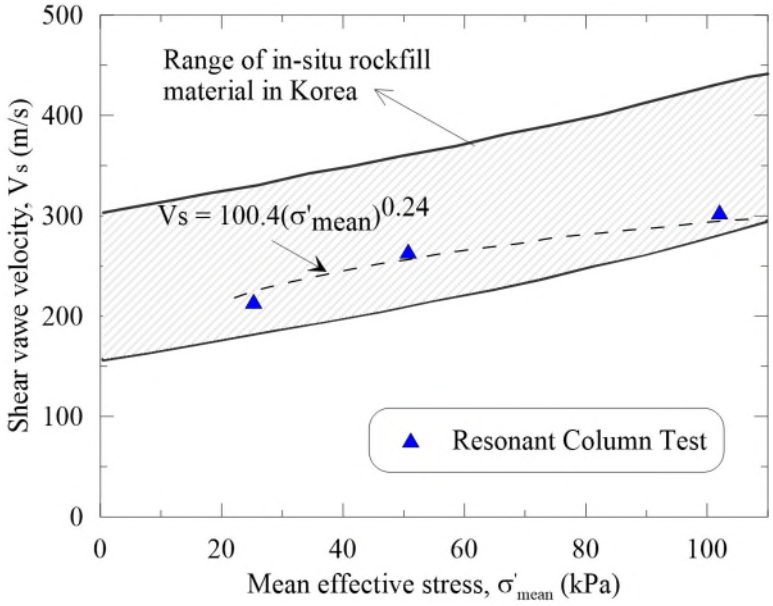

Figure 4.4: Vs of the rockfill measured by the resonant column test (reprinted from Kim et al., 2011).

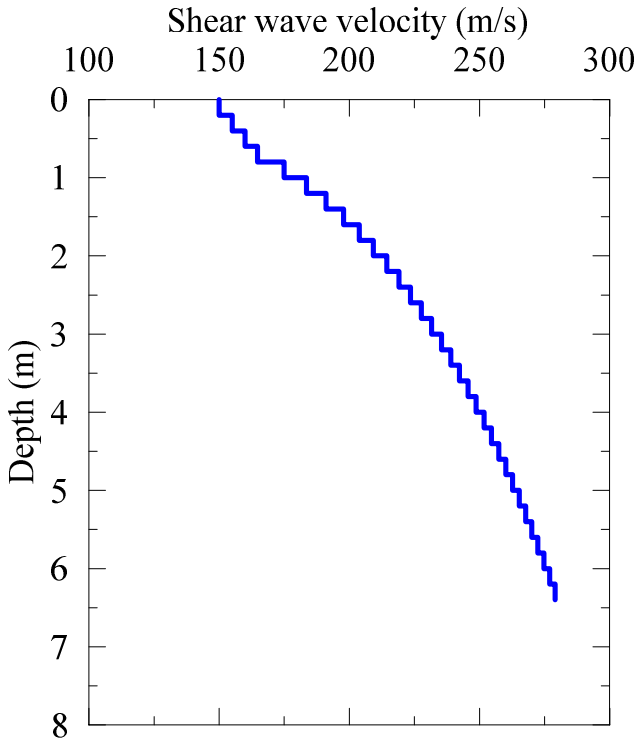

Figure 4.5: Shear wave velocity vs depth from the crest to the base in prototype.

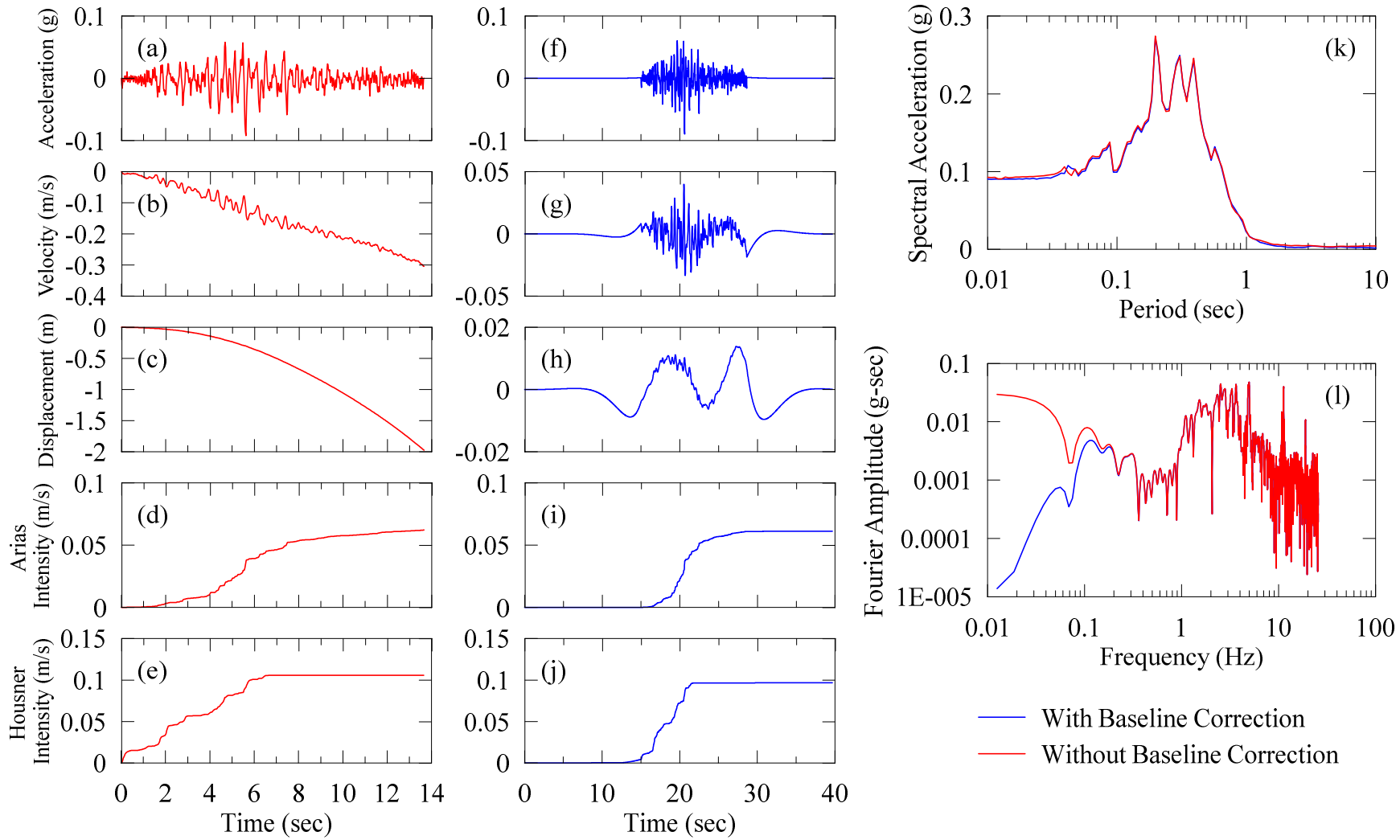

Figure 4.6: Baseline corrected motion recorded at the base of container (A00) of Test 01: (a) Acceleration, (b) Velocity, (c) Displacement, (d) Arias intensity, (e) Housner intensity time histories, (f) Response spectrum, and (g) Fourier amplitude spectrum.

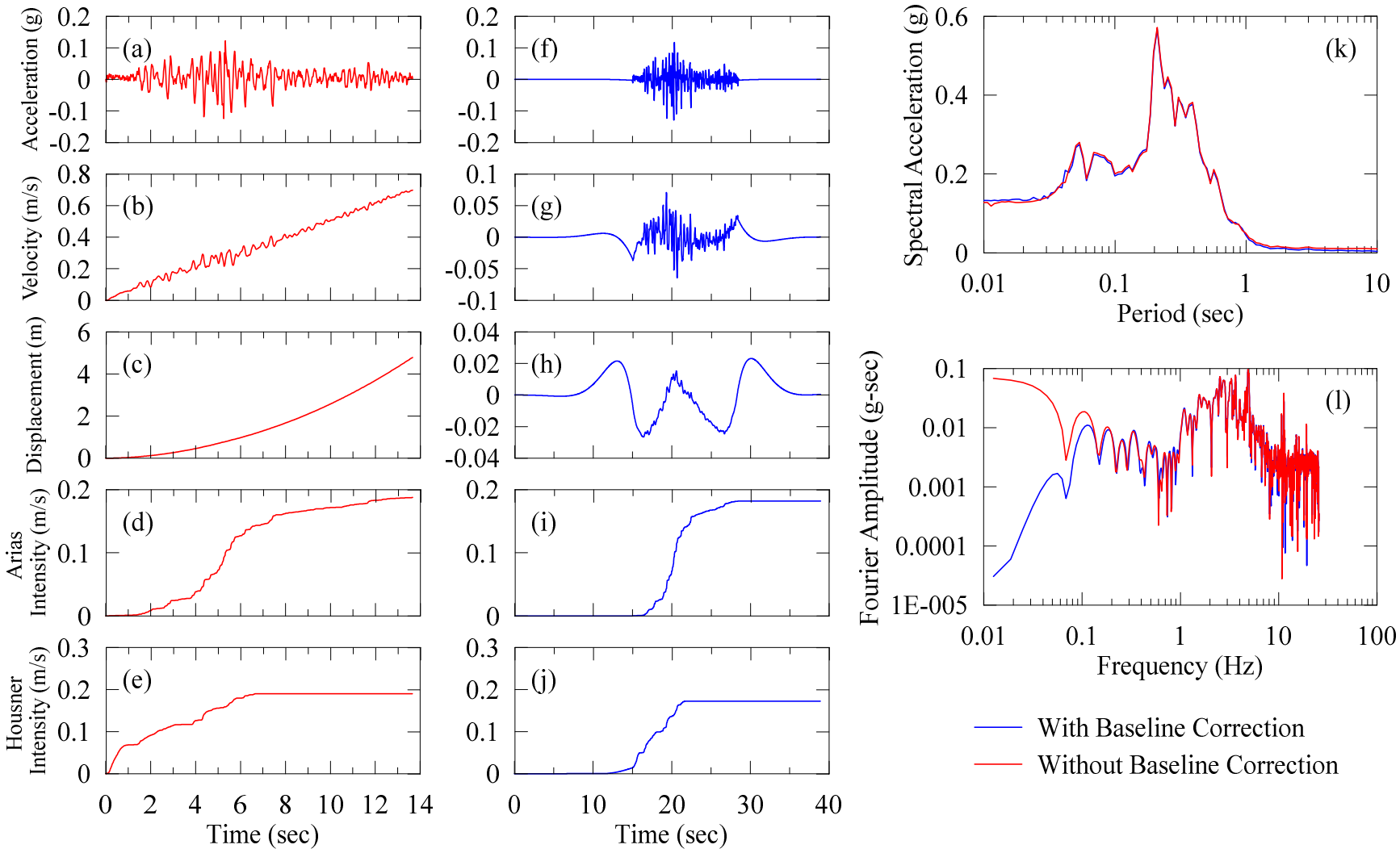

Figure 4.7: Baseline corrected motion recorded at the base of container (A00) of Test 02: (a) Acceleration, (b) Velocity, (c) Displacement, (d) Arias intensity, (e) Housner intensity time histories, (f) Response spectrum, and (g) Fourier amplitude spectrum.

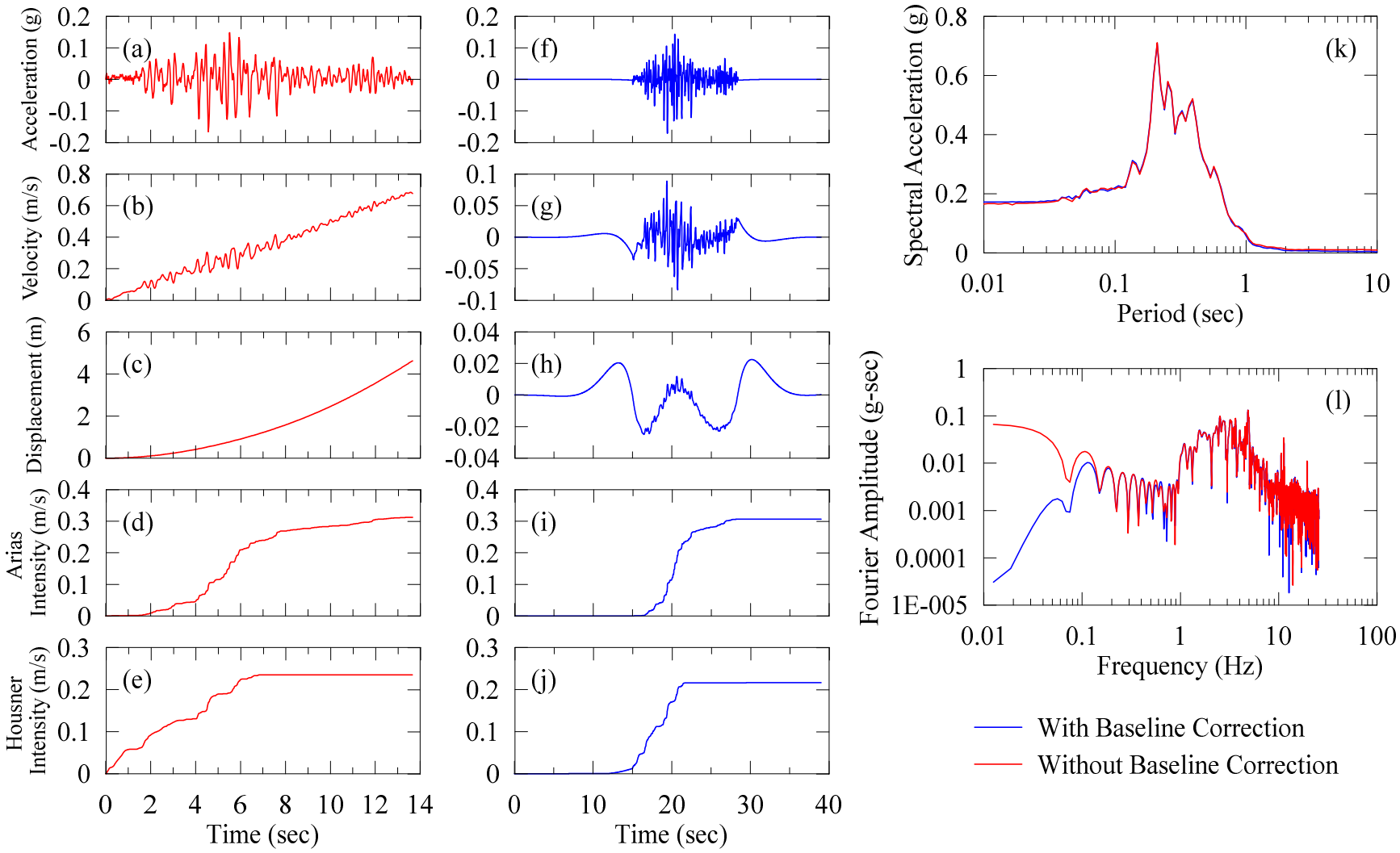

Figure 4.8: Baseline corrected motion recorded at the base of container (A00) of Test 03: (a) Acceleration, (b) Velocity, (c) Displacement, (d) Arias intensity, (e) Housner intensity time histories, (f) Response spectrum, and (g) Fourier amplitude spectrum.

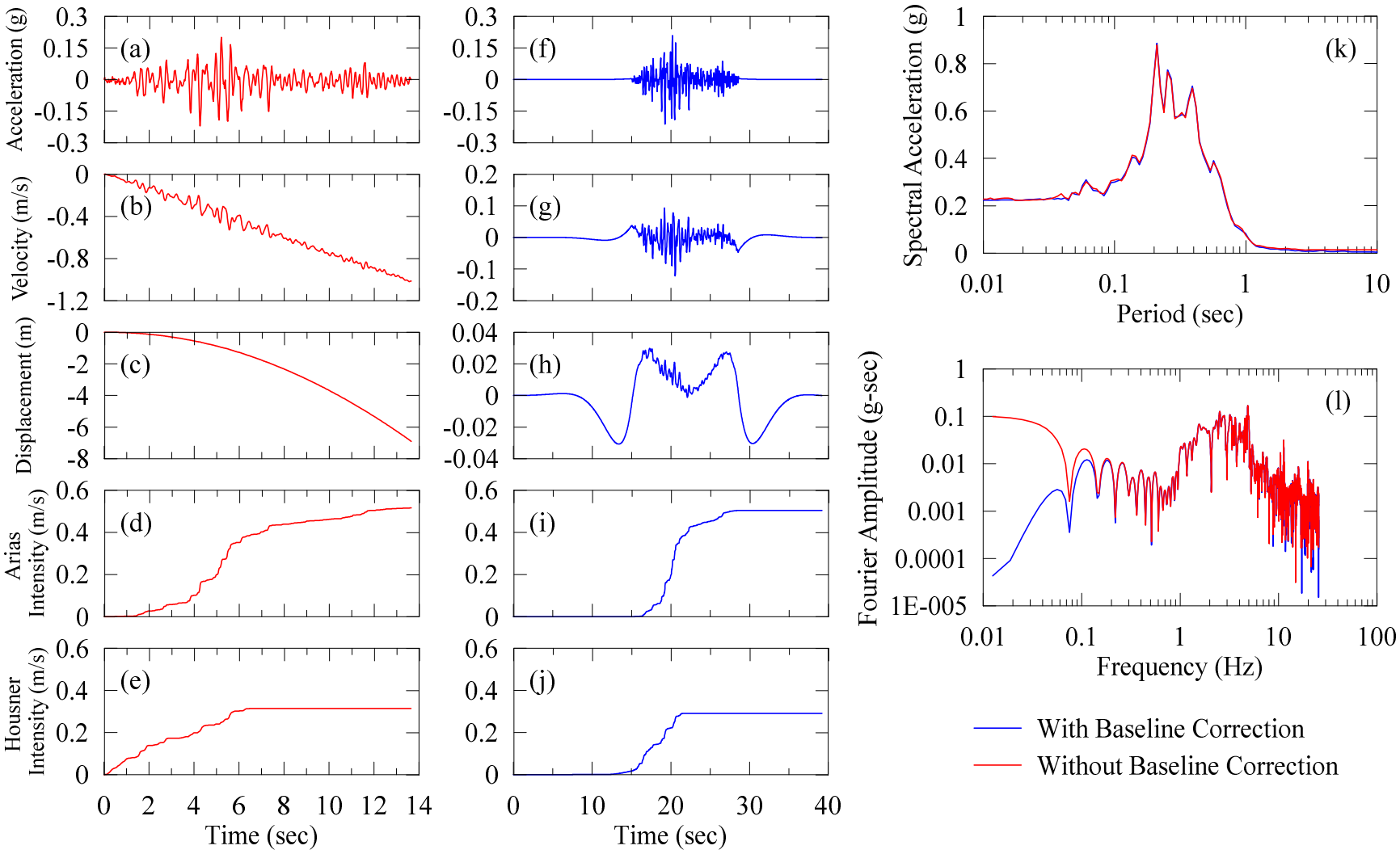

Figure 4.9: Baseline corrected motion recorded at the base of container (A00) of Test 04: (a) Acceleration, (b) Velocity, (c) Displacement, (d) Arias intensity, (e) Housner intensity time histories, (f) Response spectrum, and (g) Fourier amplitude spectrum.

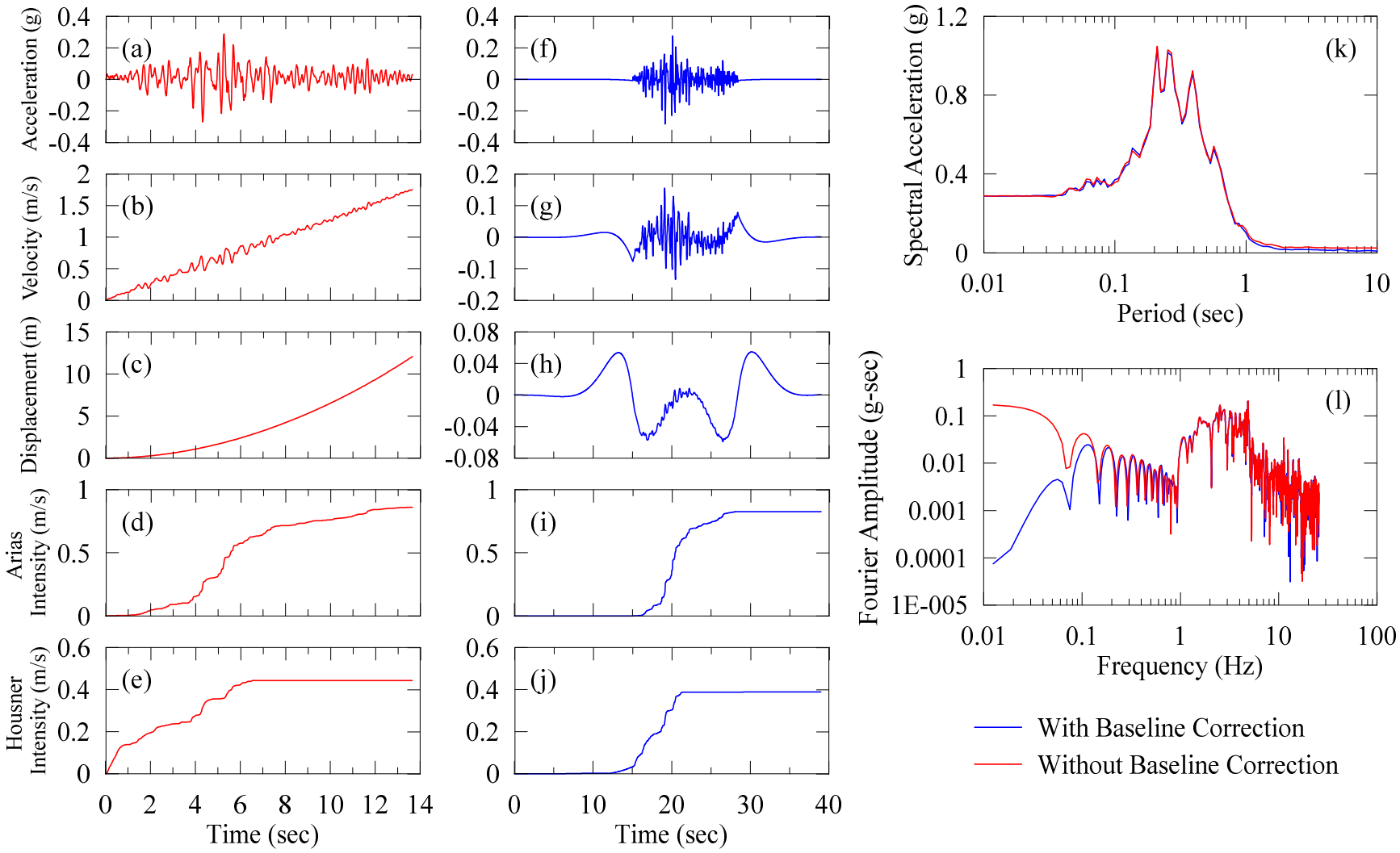

Figure 4.10: Baseline corrected motion recorded at the base of container (A00) of Test 05: (a) Acceleration, (b) Velocity, (c) Displacement, (d) Arias intensity, (e) Housner intensity time histories, (f) Response spectrum, and (g) Fourier amplitude spectrum.

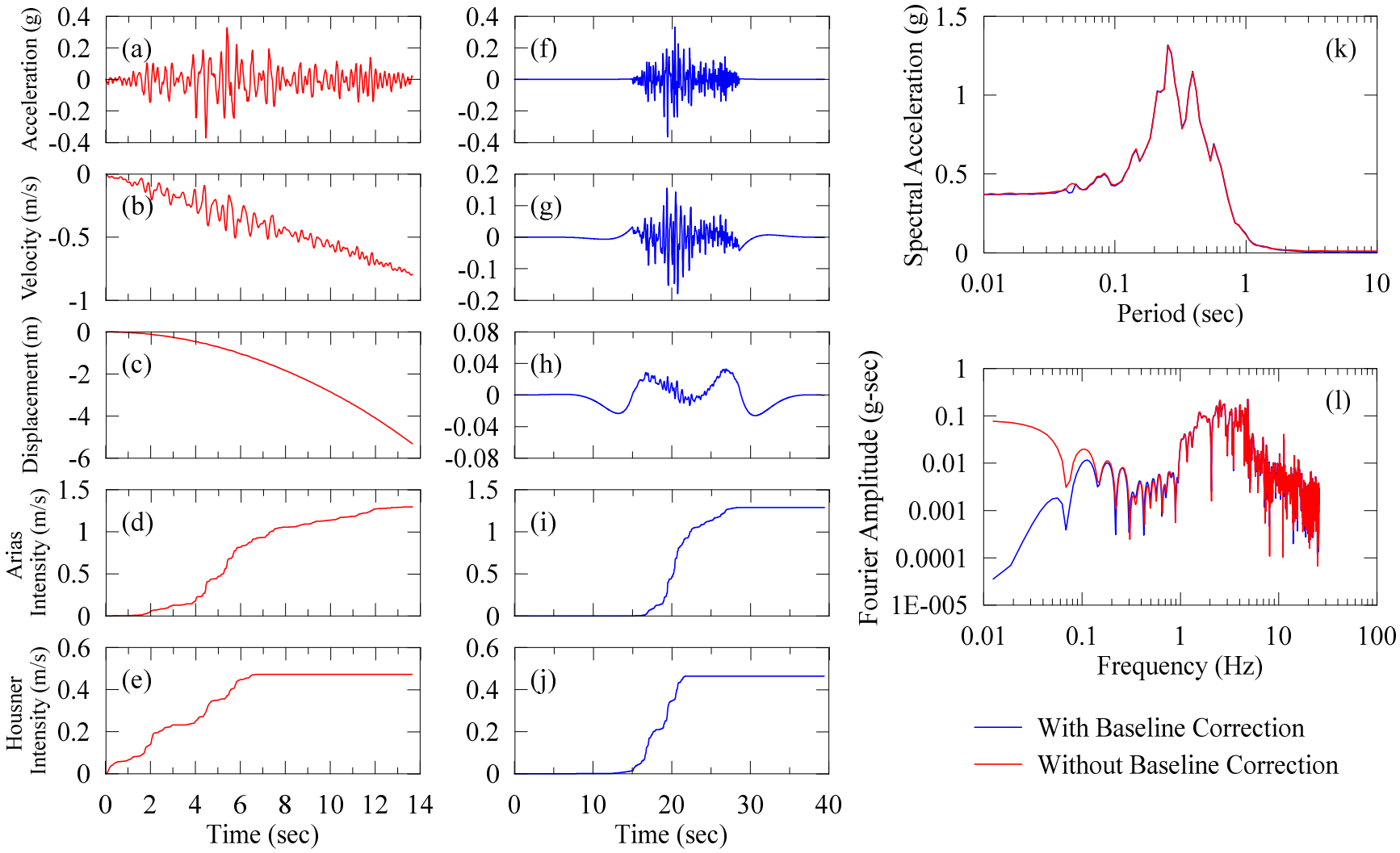

Figure 4.11: Baseline corrected motion recorded at the base of container (A00) of Test 06: (a) Acceleration, (b) Velocity, (c) Displacement, (d) Arias intensity, (e) Housner intensity time histories, (f) Response spectrum, and (g) Fourier amplitude spectrum.

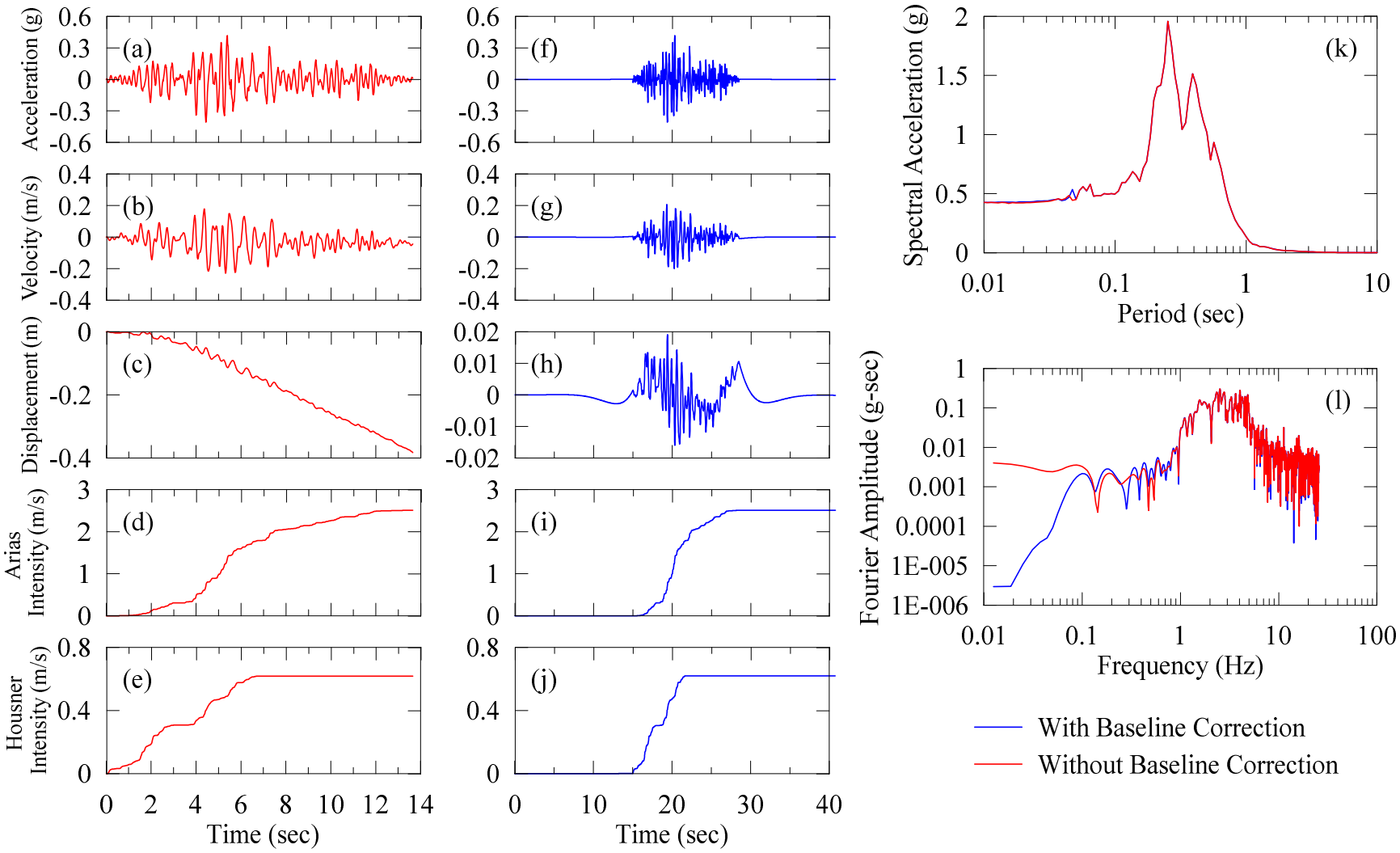

Figure 4.12: Baseline corrected motion recorded at the base of container (A00) of Test 07: (a) Acceleration, (b) Velocity, (c) Displacement, (d) Arias intensity, (e) Housner intensity time histories, (f) Response spectrum, and (g) Fourier amplitude spectrum.

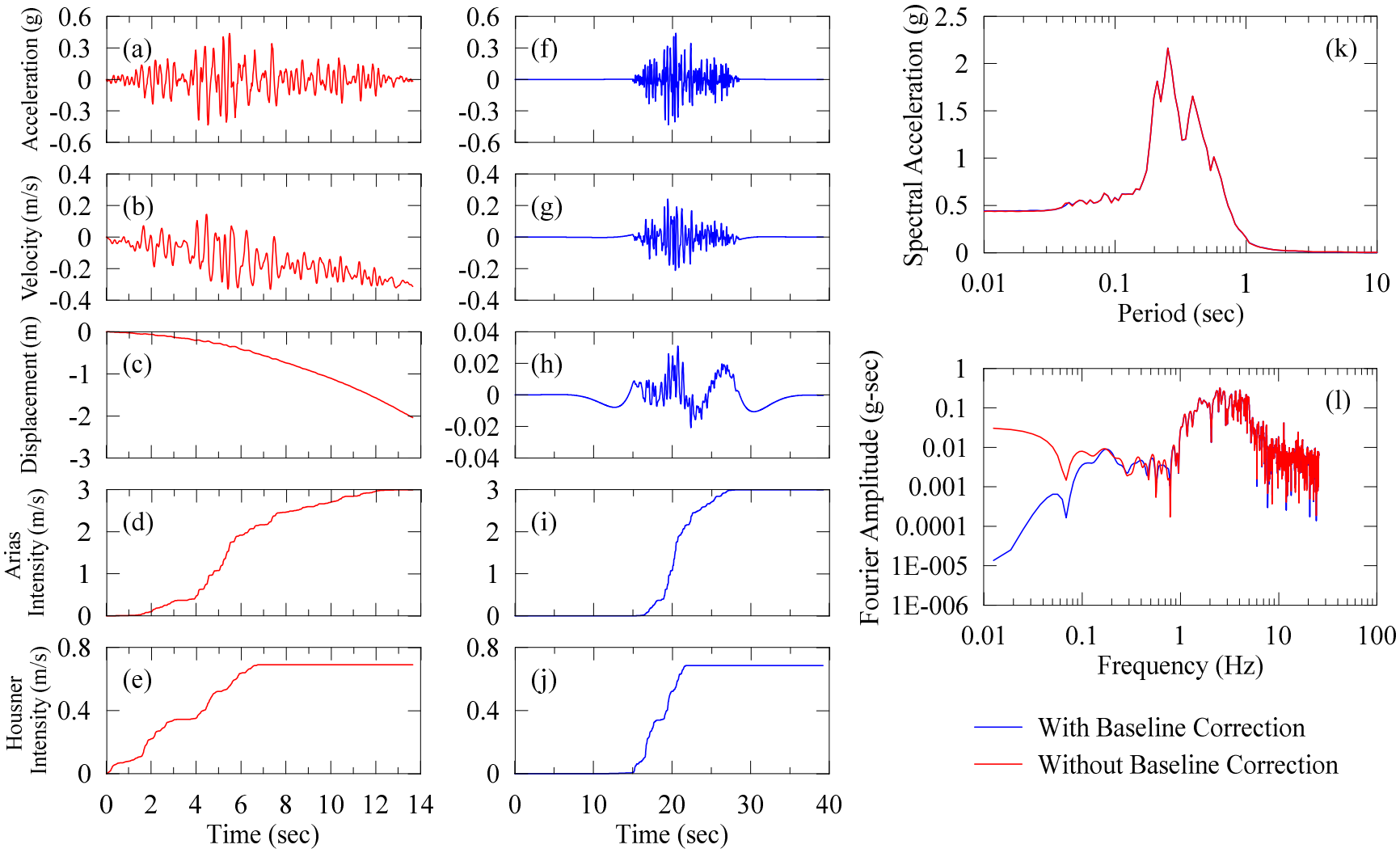

Figure 4.13: Baseline corrected motion recorded at the base of container (A00) of Test 08: (a) Acceleration, (b) Velocity, (c) Displacement, (d) Arias intensity, (e) Housner intensity time histories, (f) Response spectrum, and (g) Fourier amplitude spectrum.

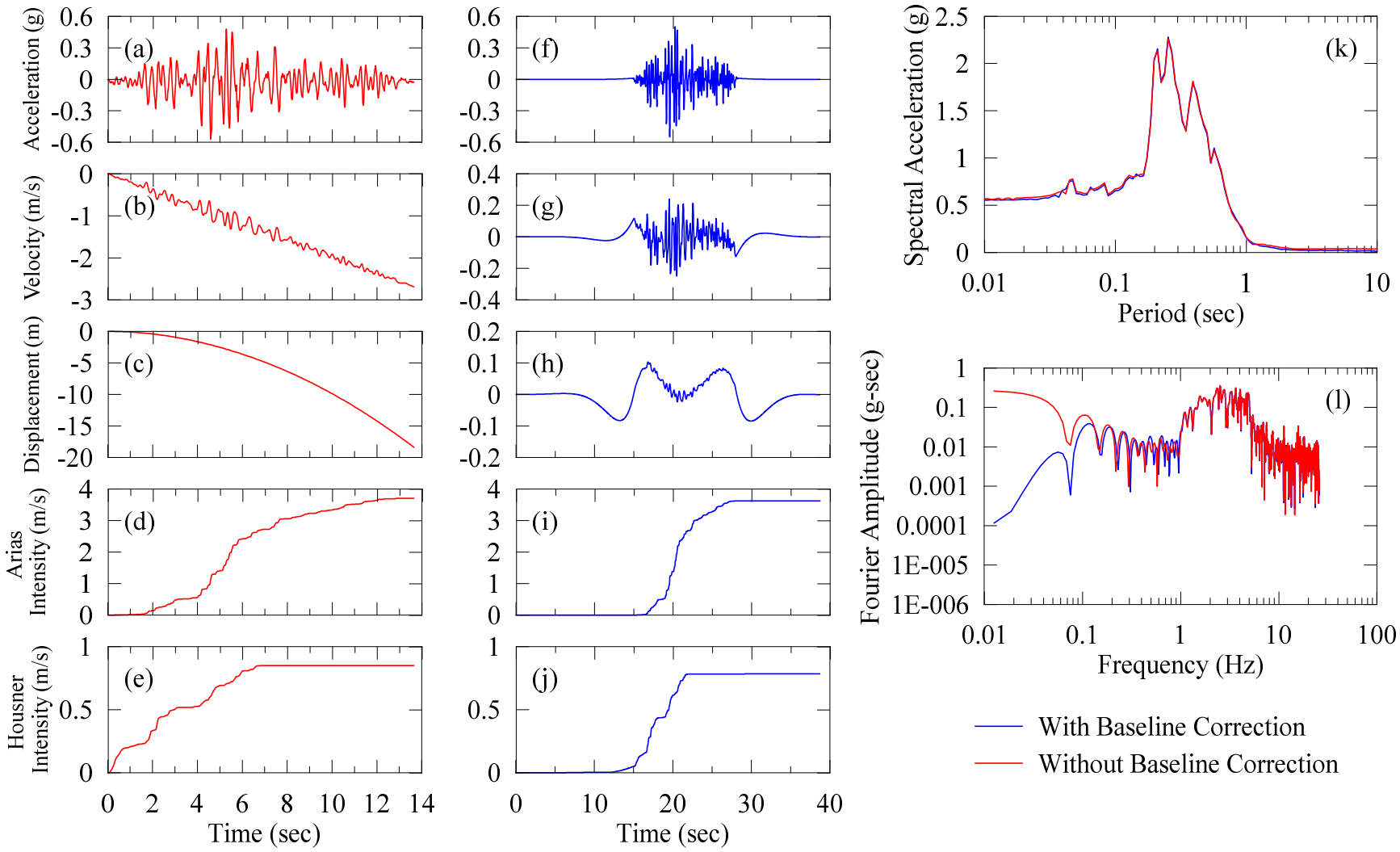

Figure 4.14: Baseline corrected motion recorded at the base of container (A00) of Test 09: (a) Acceleration, (b) Velocity, (c) Displacement, (d) Arias intensity, (e) Housner intensity time histories, (f) Response spectrum, and (g) Fourier amplitude spectrum.

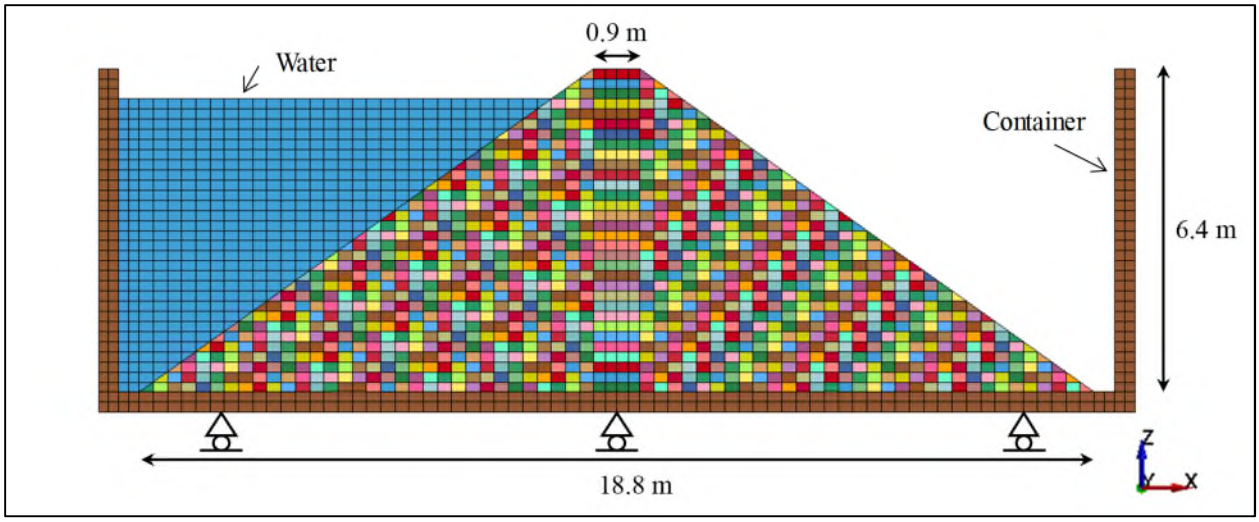

Figure 4.15: Finite element mesh used for the analyses of prototype.

.

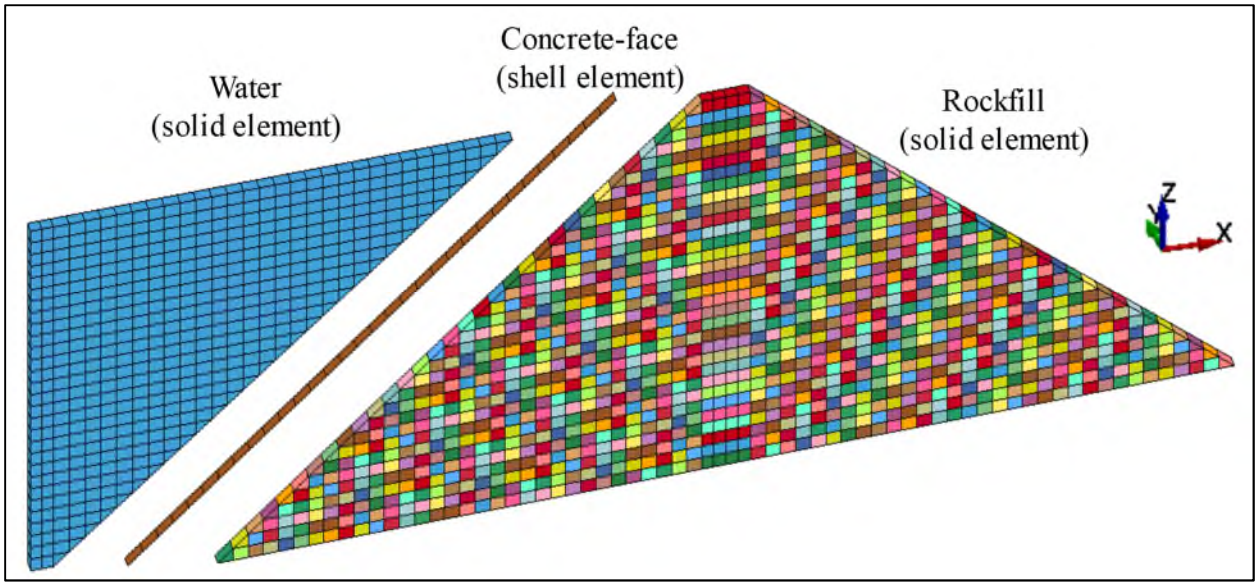

Figure 4.16: Element types used in the FEM.

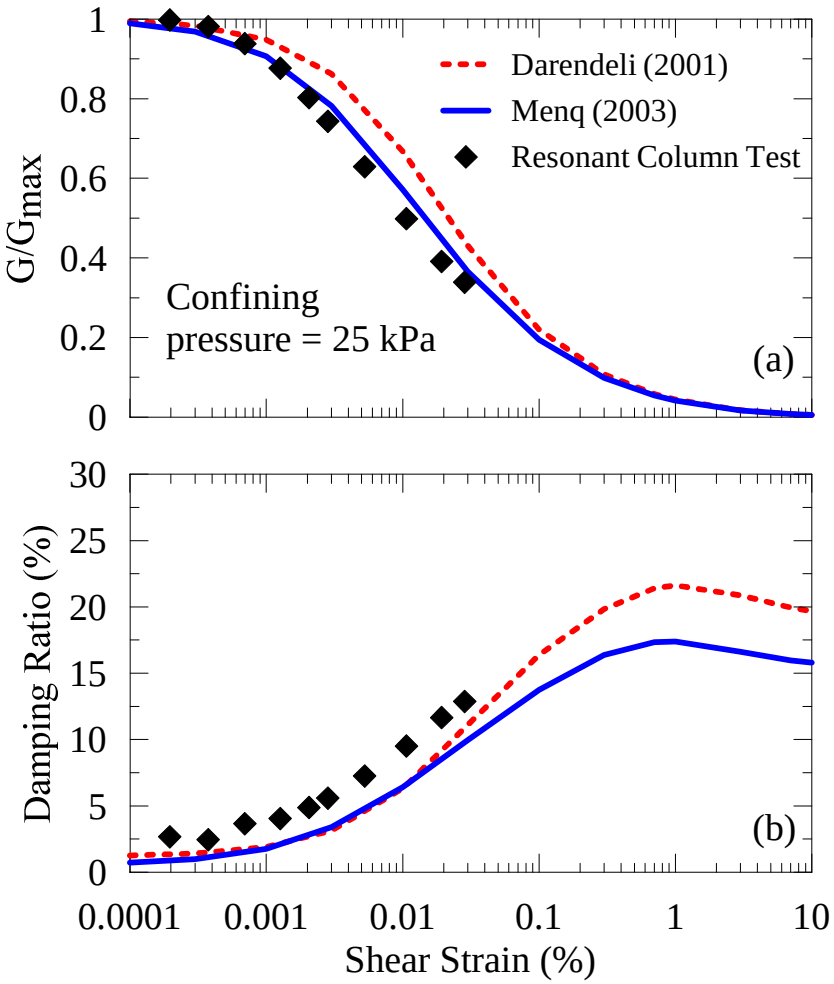

Figure 4.17: Modulus reduction and damping curves from Menq (2003), Darendeli (2001) and resonant coulmn test results under a confining pressure of 25 kPa.

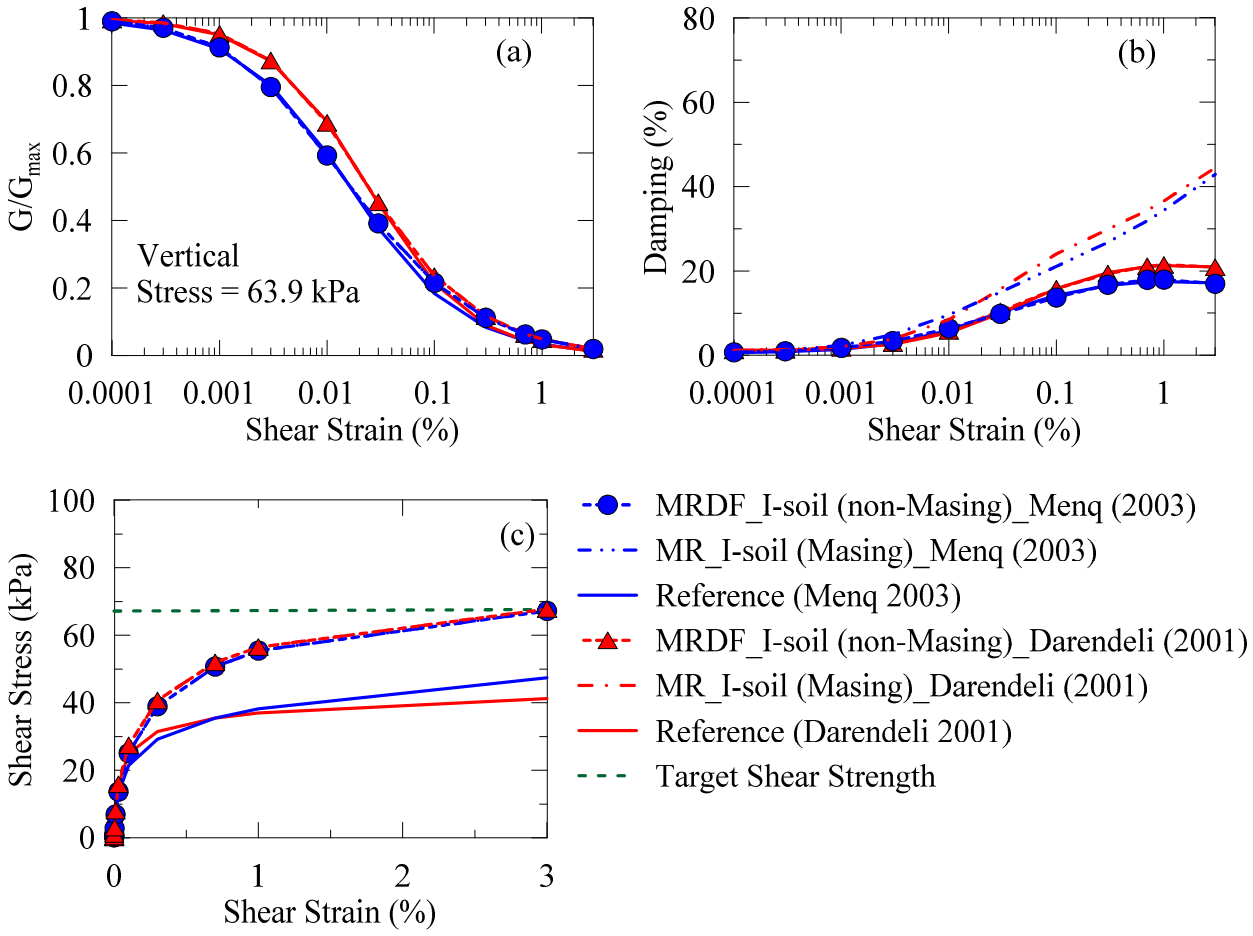

Figure 4.18: Dynamic curves used in I-soil: (a) Normalized modulus reduction, (b) Damping, and (c) Backbone curves.

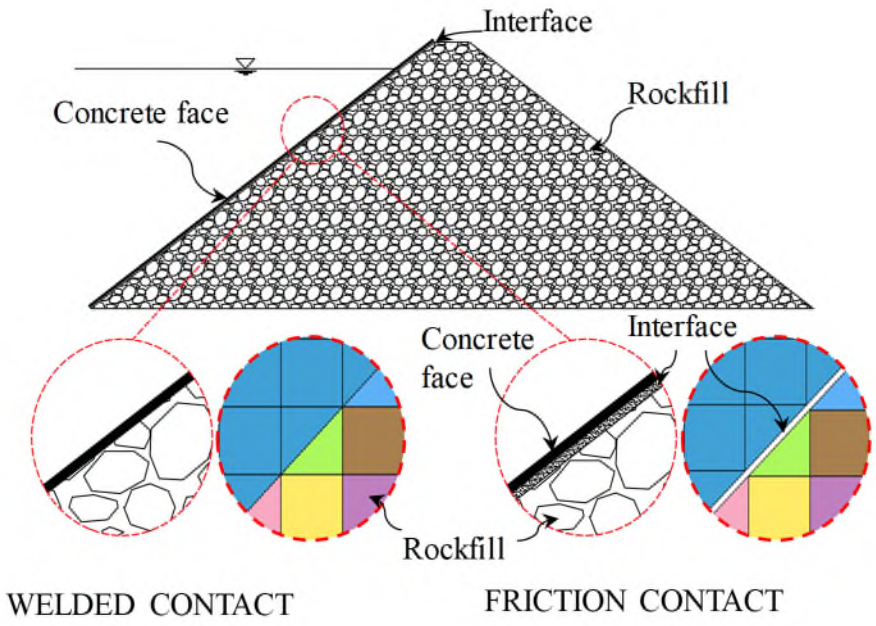

Figure 4.19: Interface types between rockfill and concrete face slab.

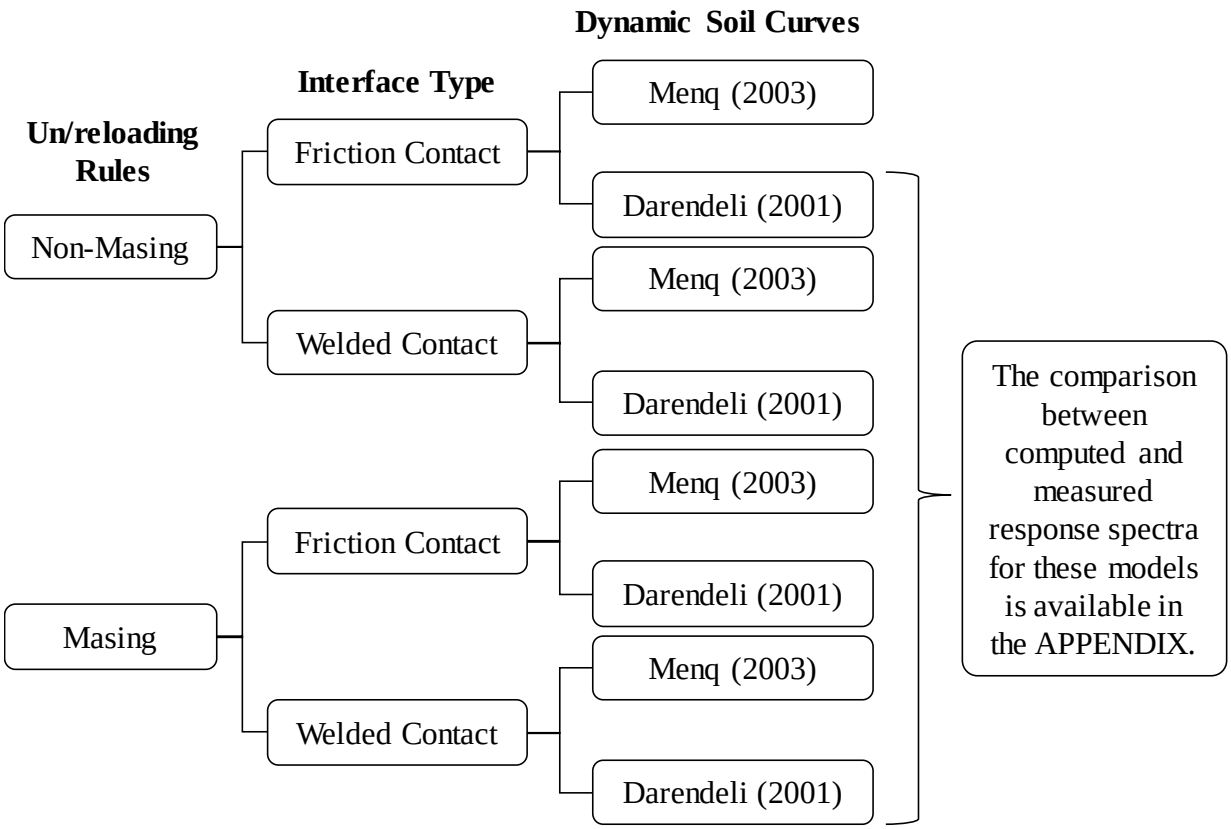

Figure 4.20: Analysis tree for simulated nine motions.

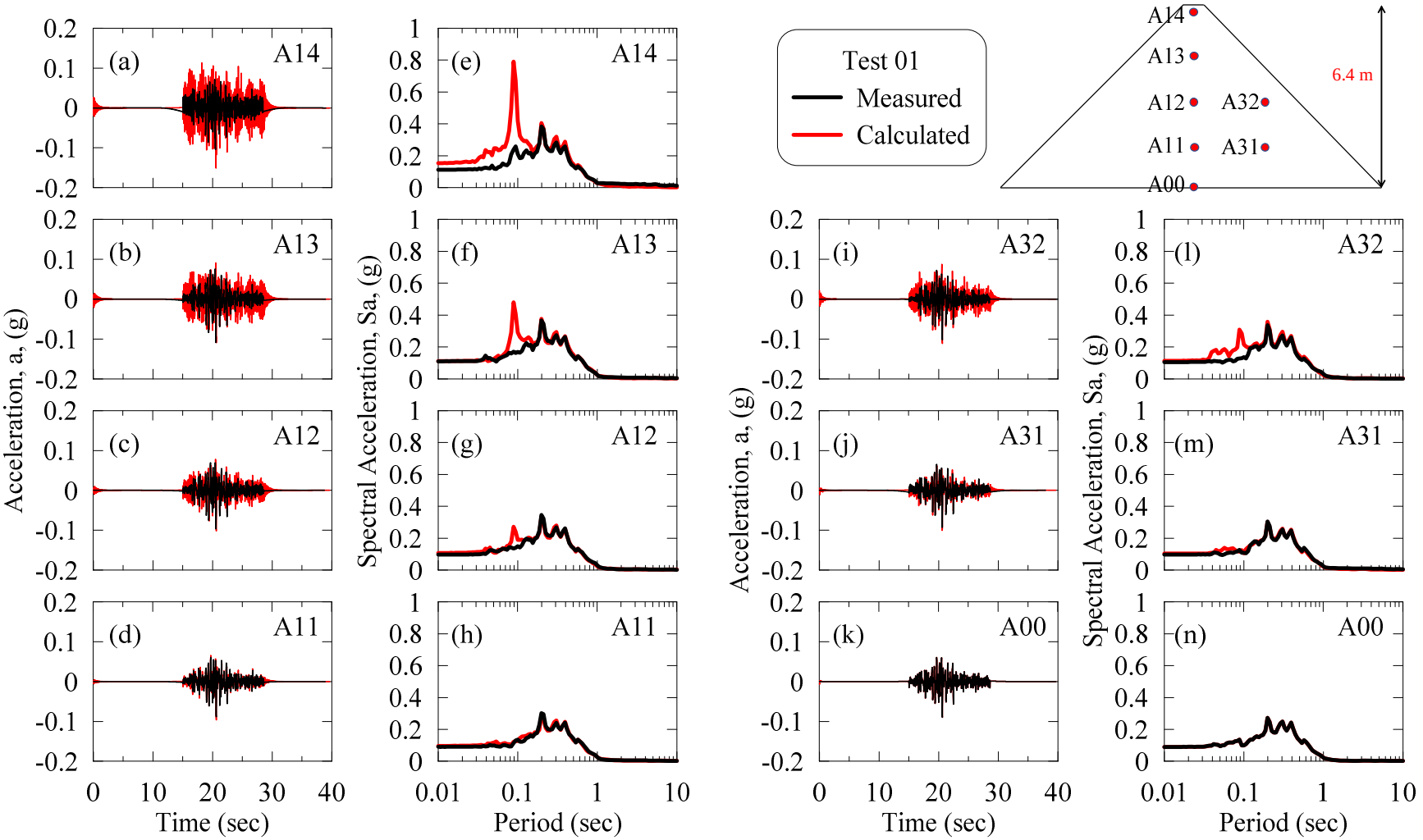

Figure 4.21: Acceleration time histories and response spectra at different depths of dam during Test 01 for friction contact and the dynamic soil curves of Menq (2003) with non-Masing un/reloading.

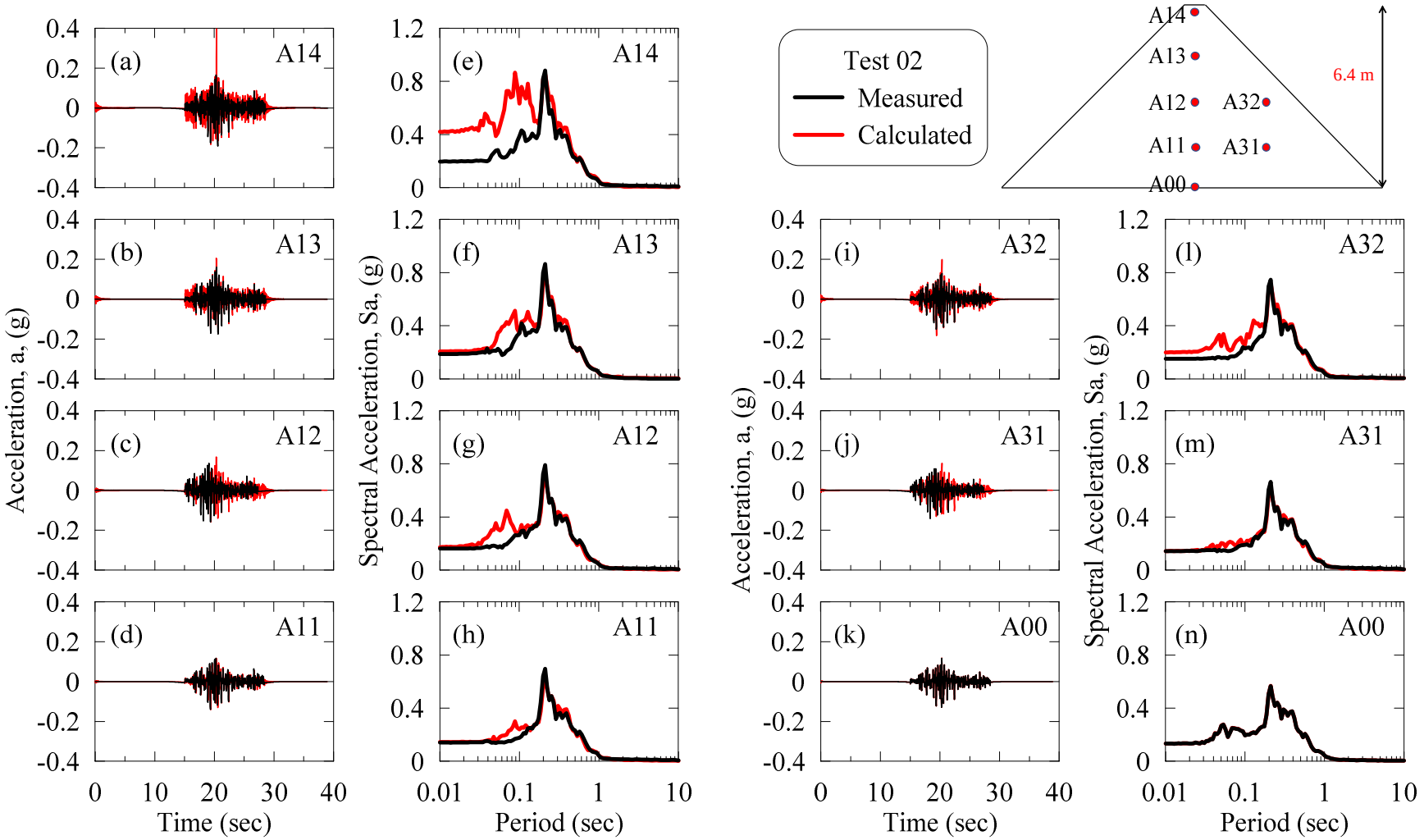

Figure 4.22: Acceleration time histories and response spectra at different depths of dam during Test 02 for friction contact and the dynamic soil curves of Menq (2003) with non-Masing un/reloading.

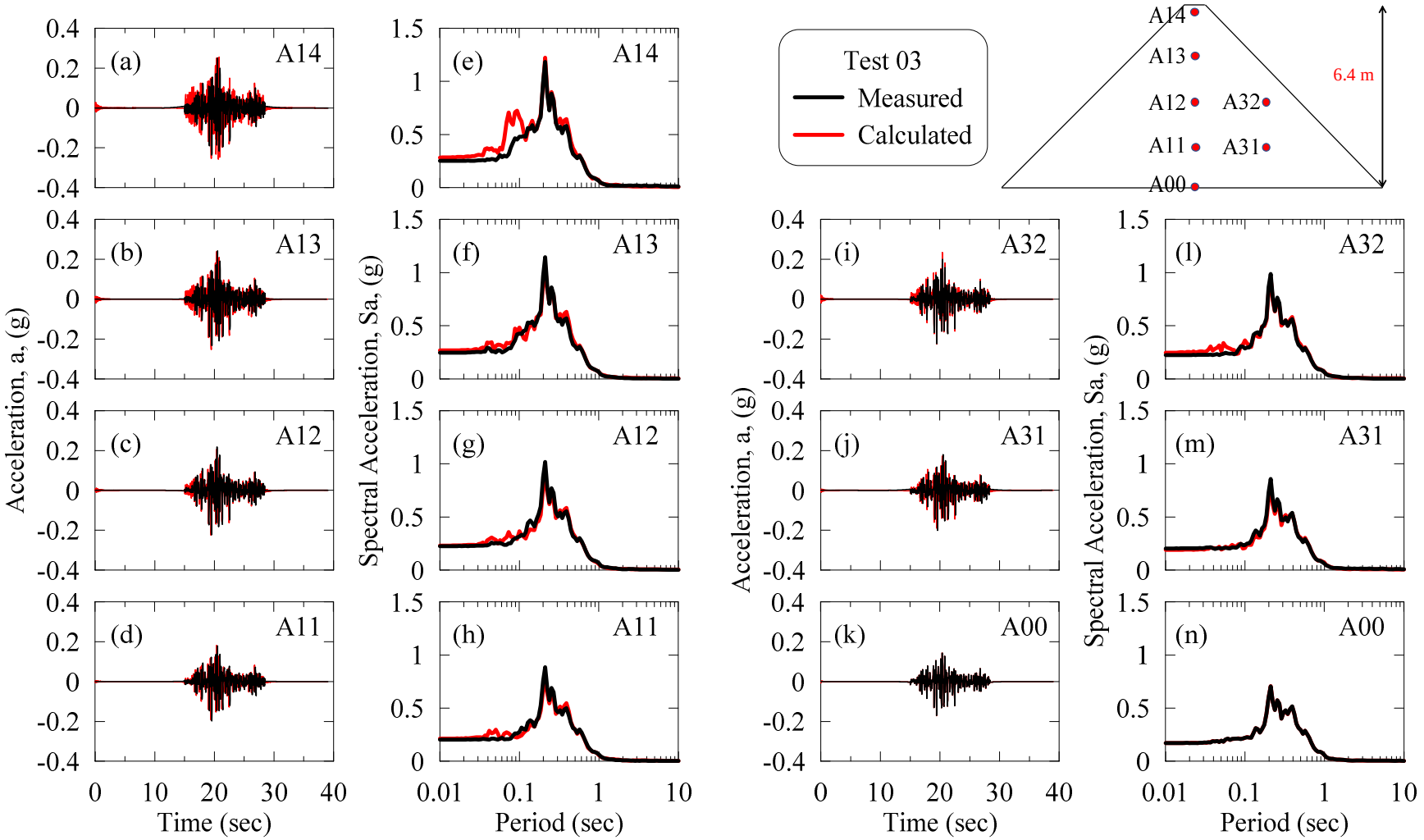

Figure 4.23: Acceleration time histories and response spectra at different depths of dam during Test 03 for friction contact and the dynamic soil curves of Menq (2003) with non-Masing un/reloading.

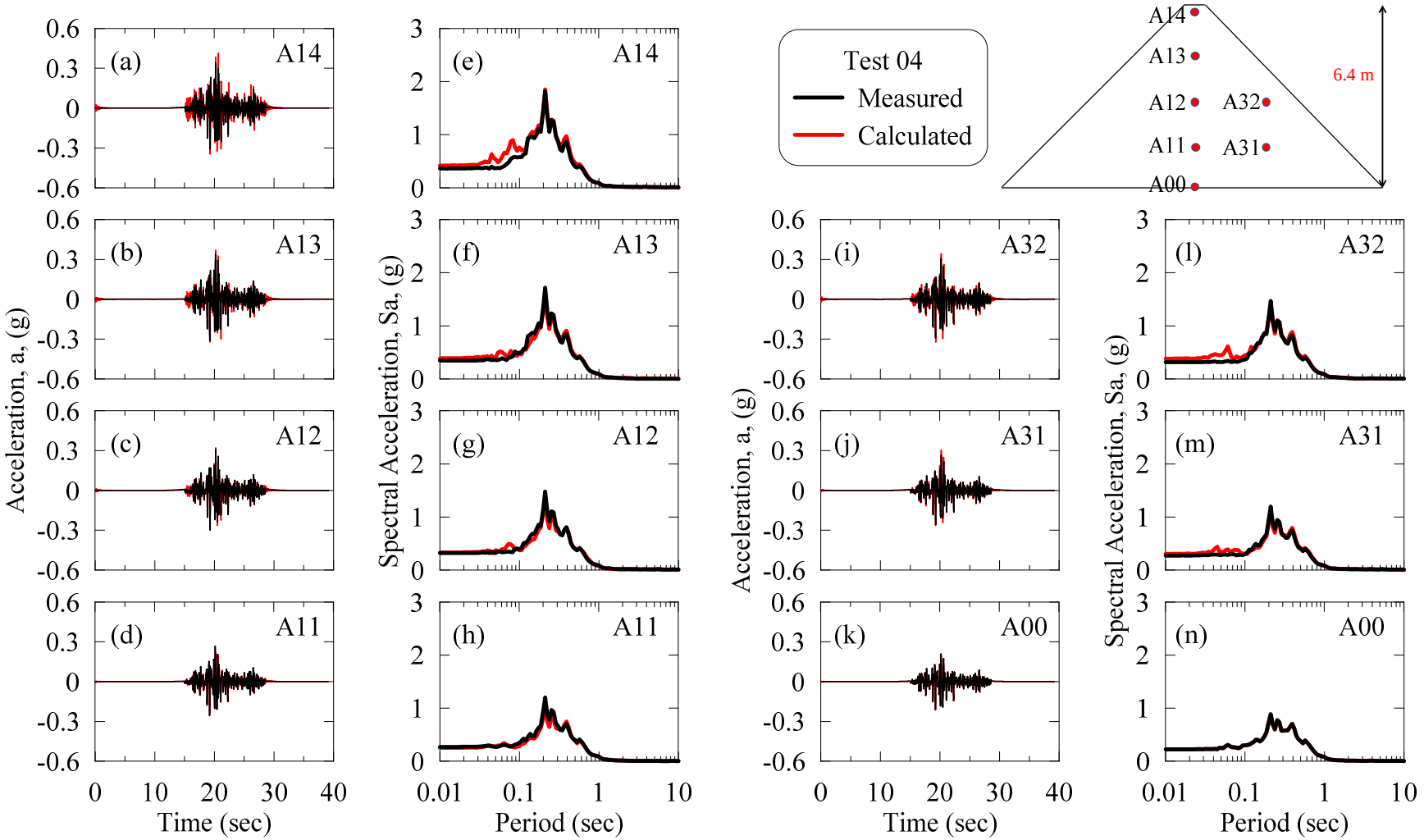

Figure 4.24: Acceleration time histories and response spectra at different depths of dam during Test 04 for friction contact and the dynamic soil curves of Menq (2003) with non-Masing un/reloading.

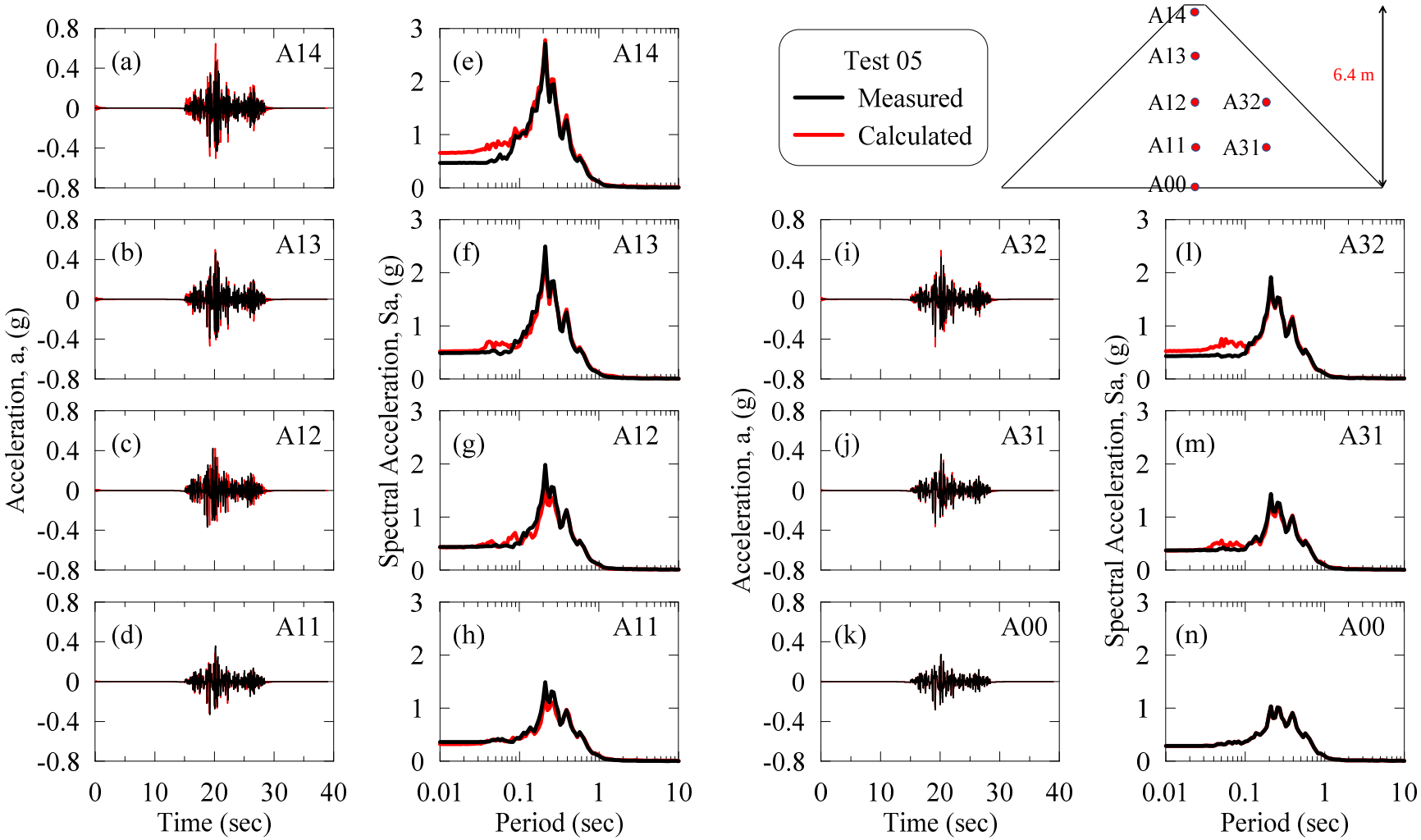

Figure 4.25: Acceleration time histories and response spectra at different depths of dam during Test 05 for friction contact and the dynamic soil curves of Menq (2003) with non-Masing un/reloading.

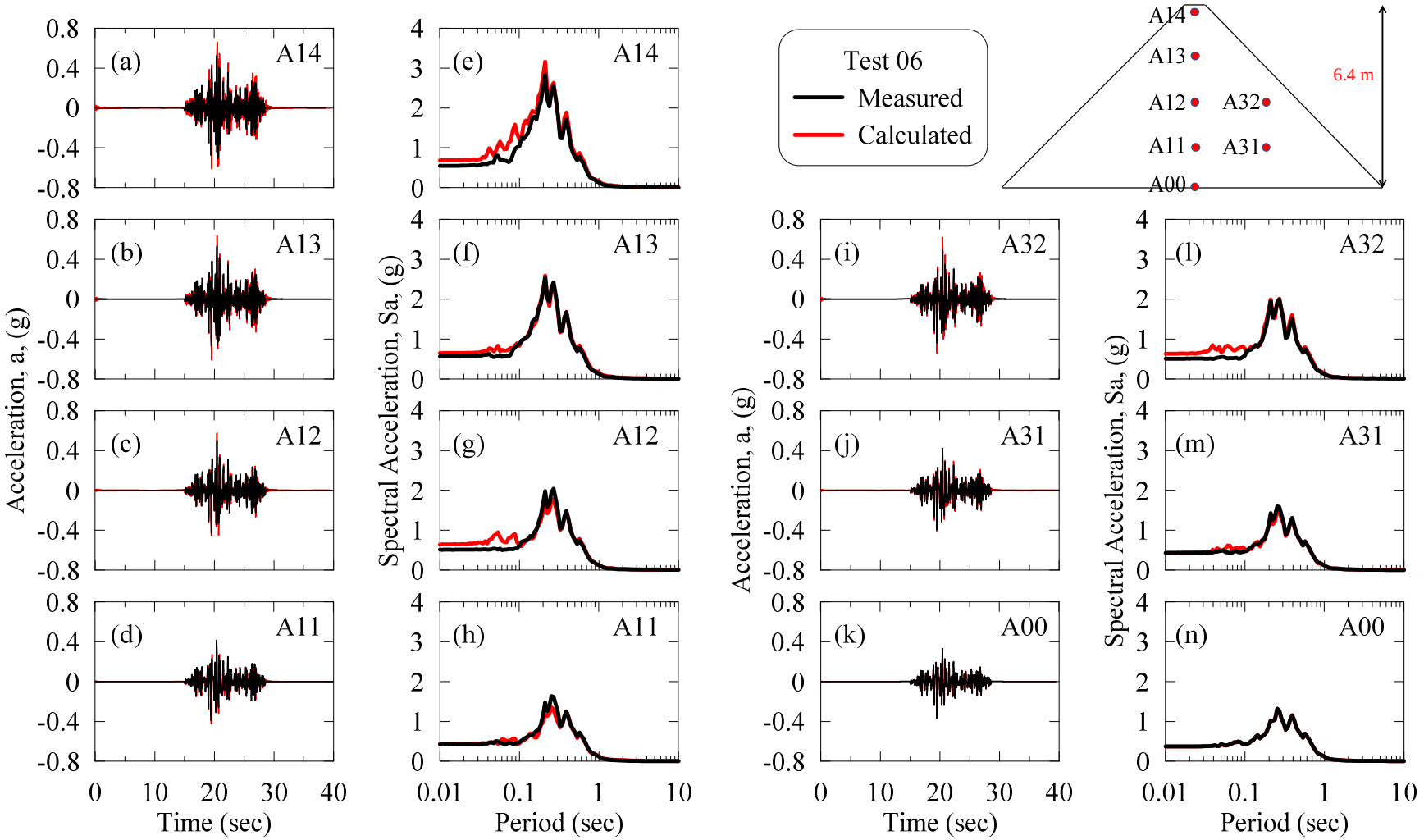

Figure 4.26: Acceleration time histories and response spectra at different depths of dam during Test 06 for friction contact and the dynamic soil curves of Menq (2003) with non-Masing un/reloading.

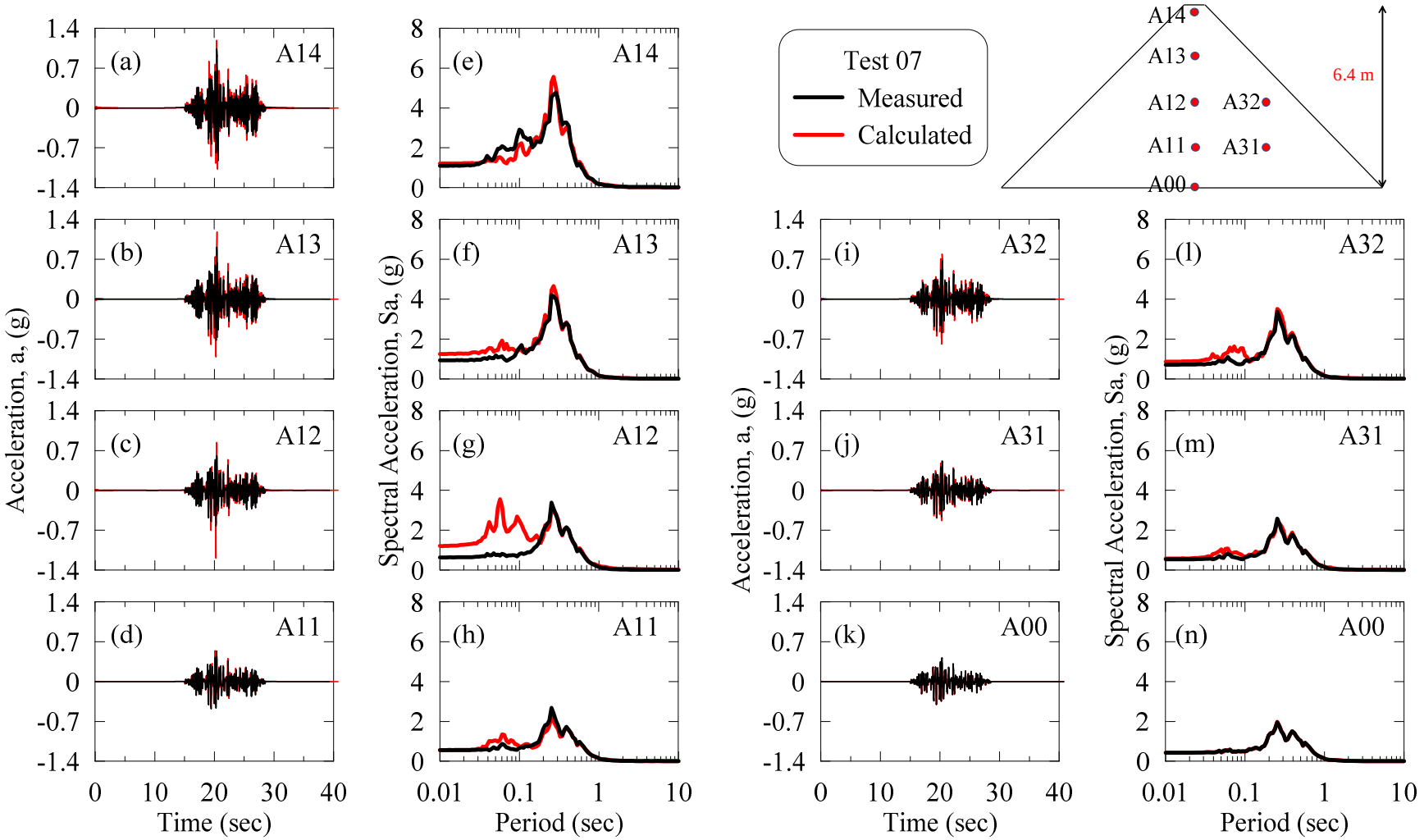

Figure 4.27: Acceleration time histories and response spectra at different depths of dam during Test 07 for friction contact and the dynamic soil curves of Menq (2003) with non-Masing un/reloading.

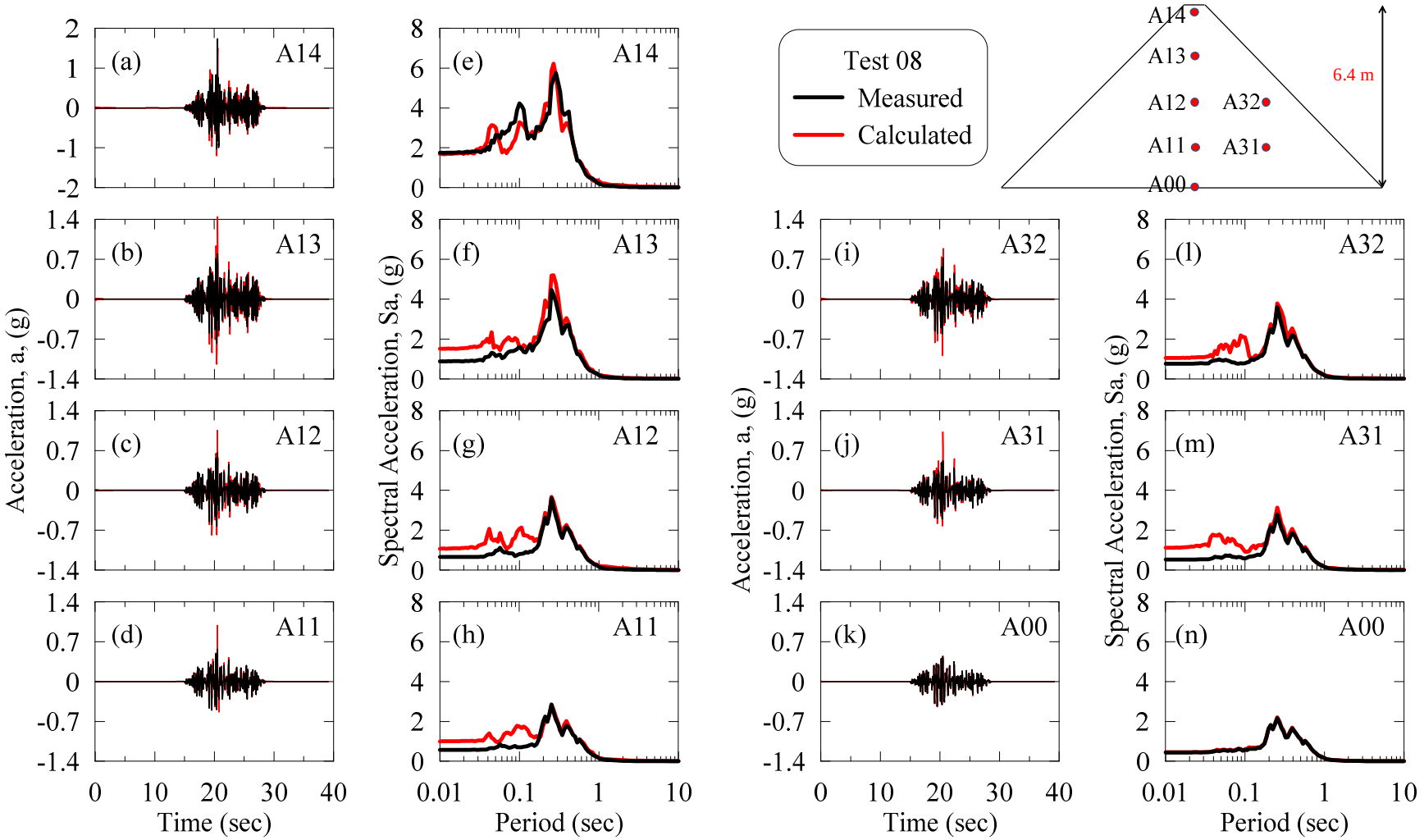

Figure 4.28: Acceleration time histories and response spectra at different depths of dam during Test 08 for friction contact and the dynamic soil curves of Menq (2003) with non-Masing un/reloading.

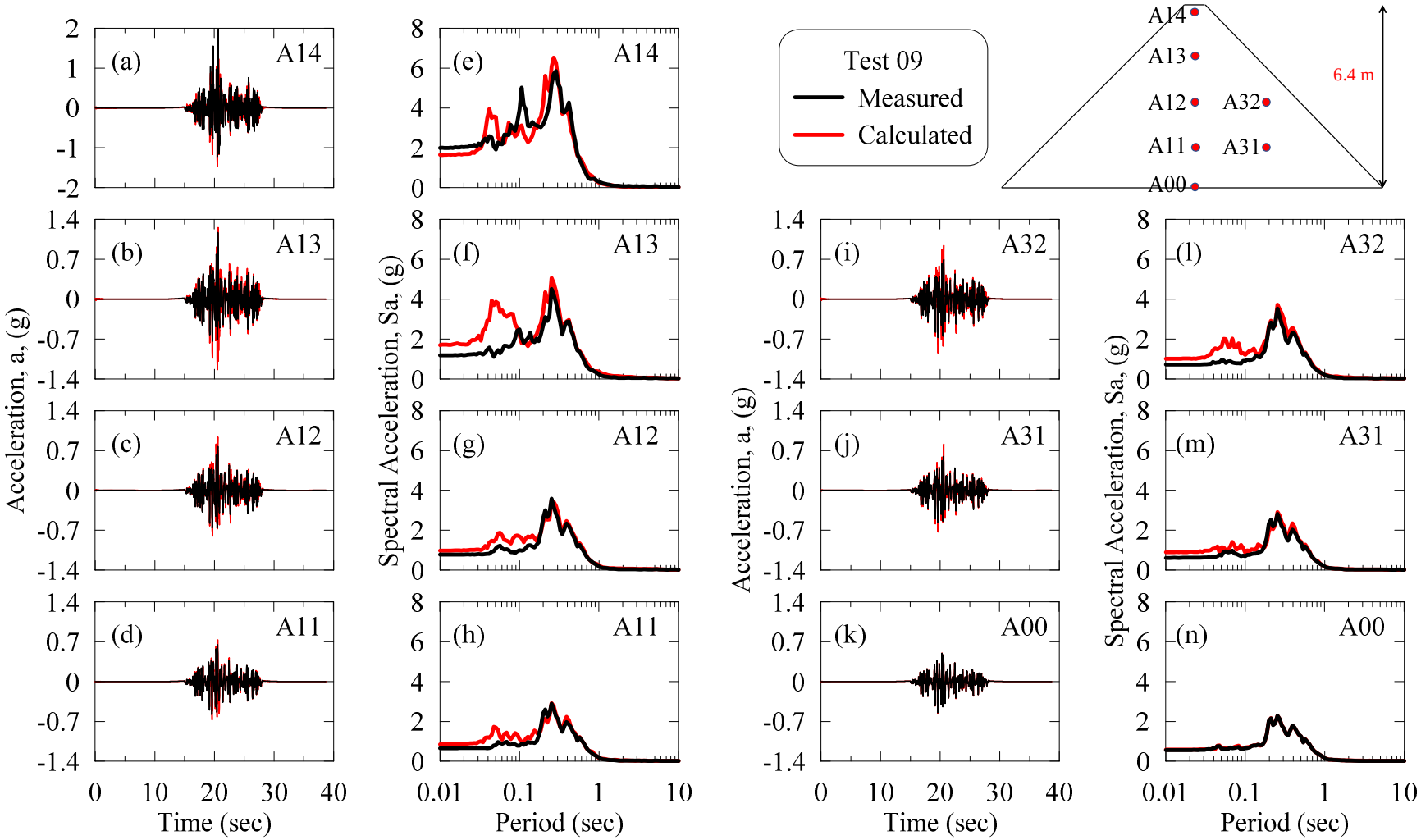

Figure 4.29: Acceleration time histories and response spectra at different depths of dam during Test 09 for friction contact and the dynamic soil curves of Menq (2003) with non-Masing un/reloading.

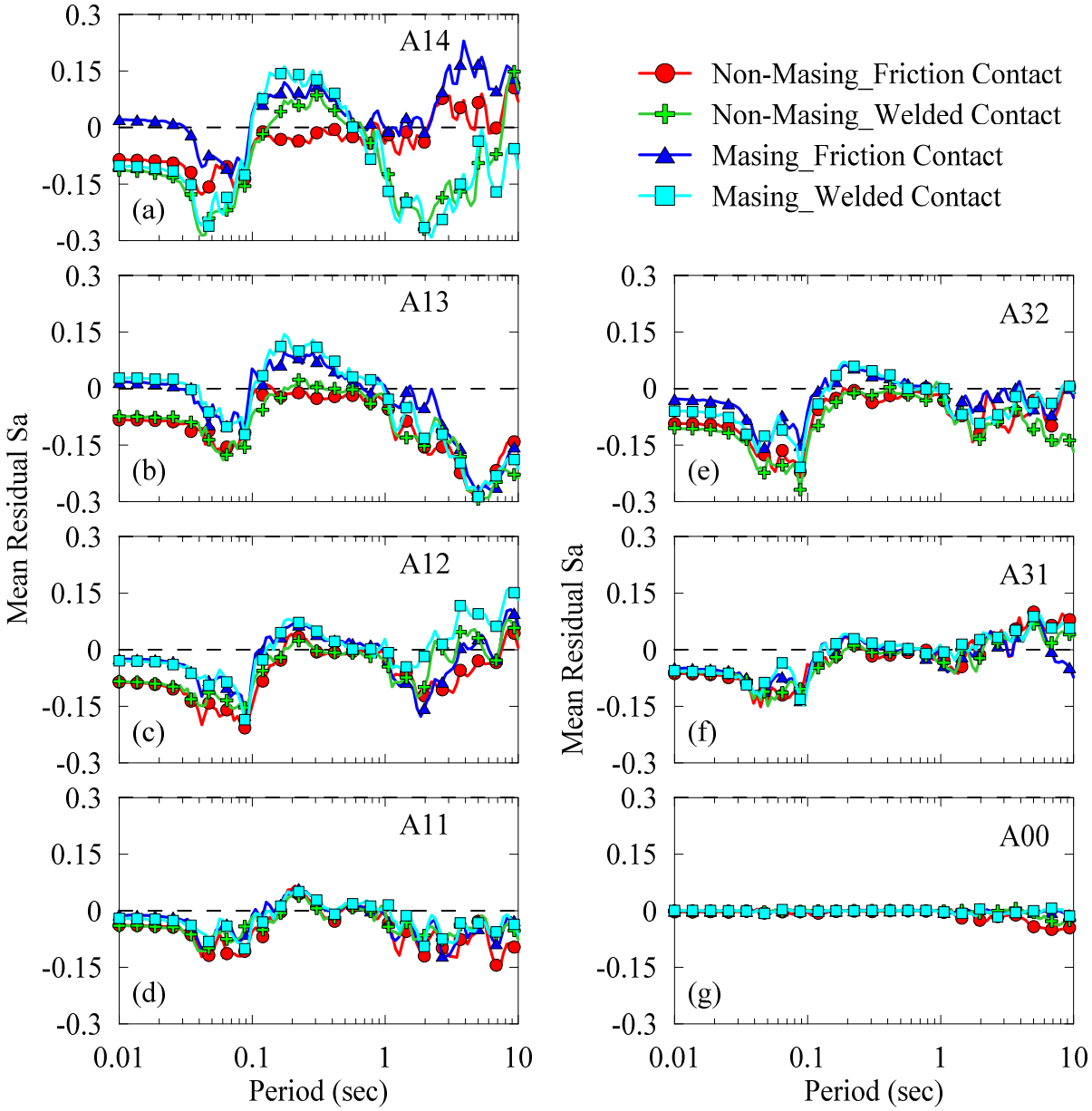

Figure 4.30: Mean residual spectral accelerations during all motions (Test 01 – Test 09) for dynamic curves from Menq (2003).

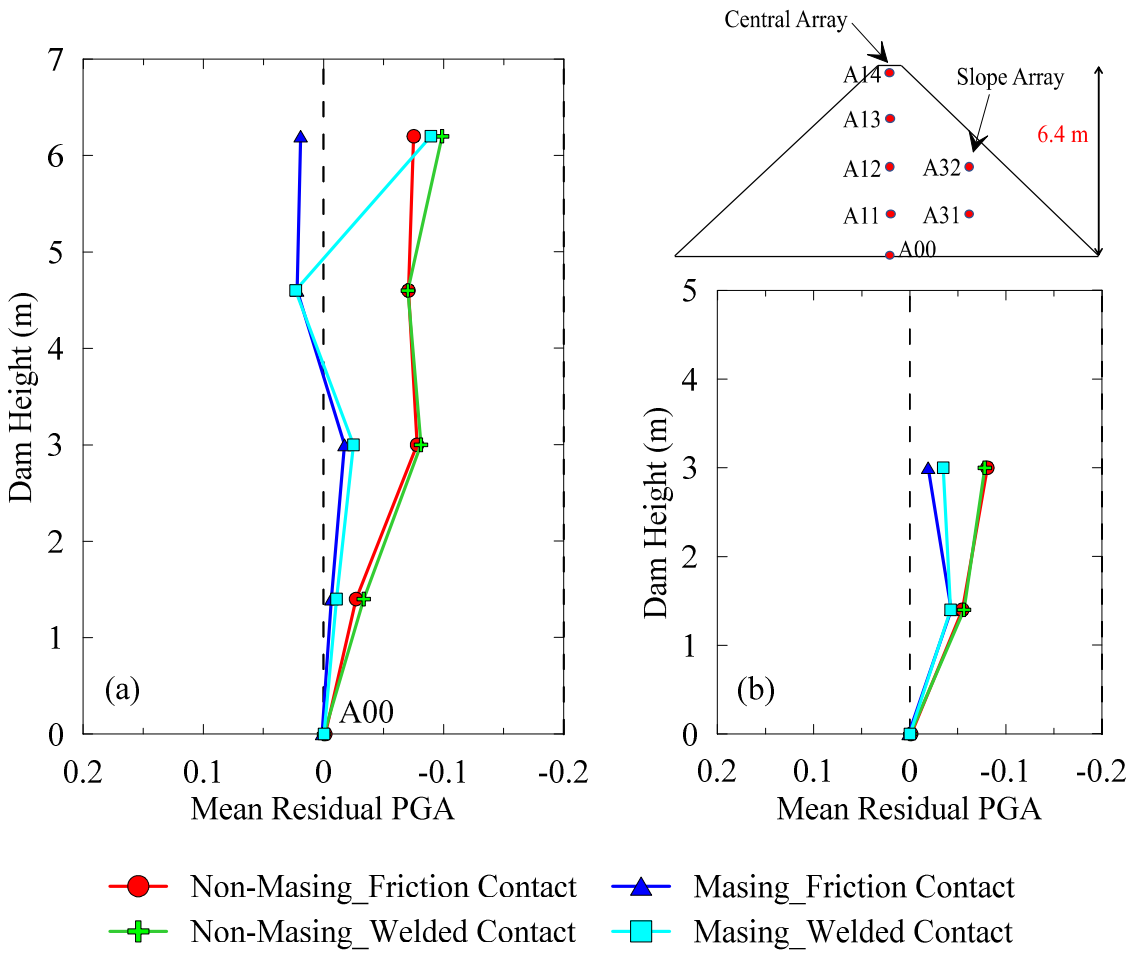

Figure 4.31: Mean residual peak ground accelerations during all motions (Test 01 – Test 09) for dynamic curves from Menq (2003): (a) Central array and (b) Slope array.

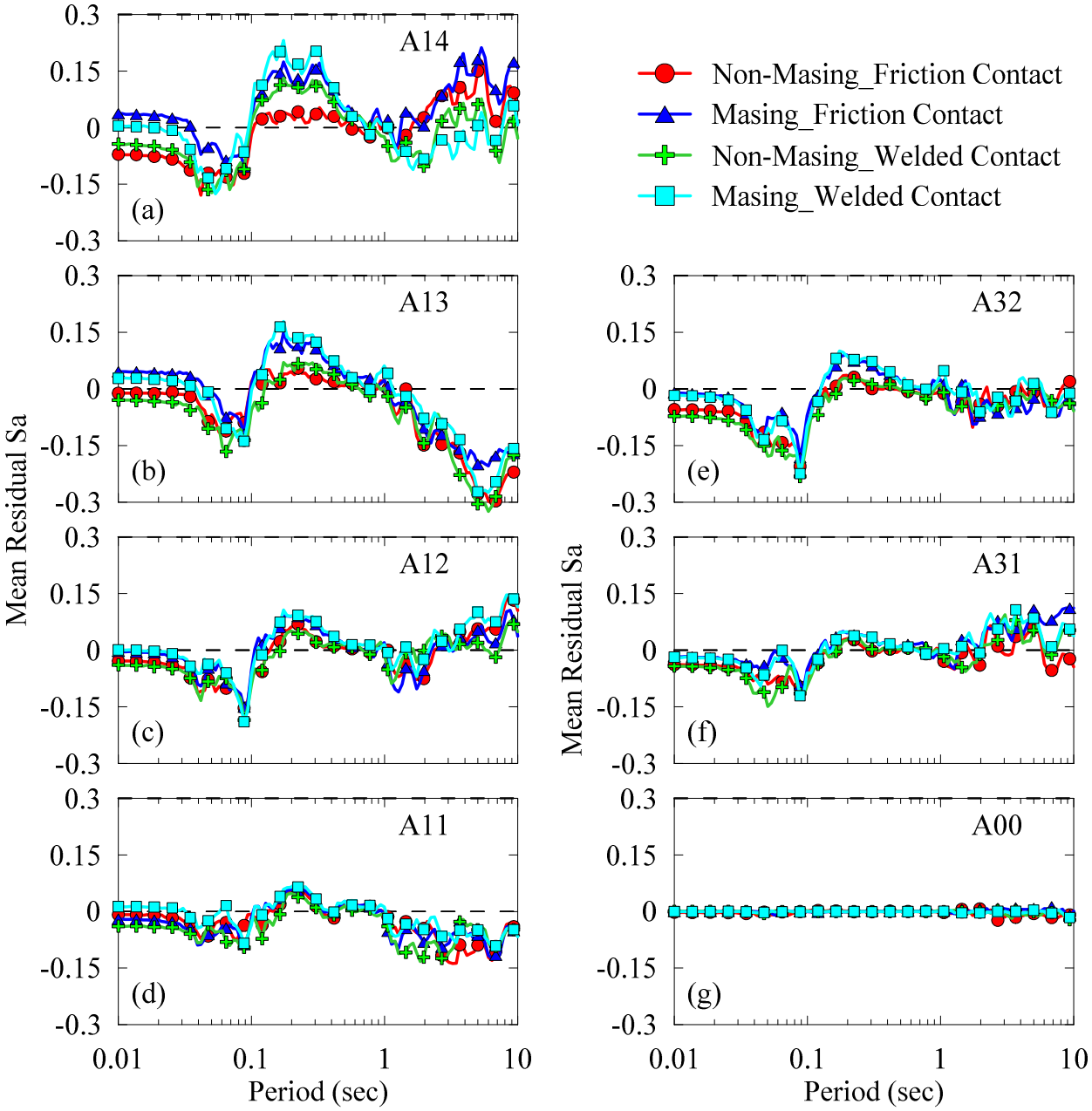

Figure 4.32: Mean residual spectral accelerations during all motions (Test 01 – Test 09) for dynamic curves from Darendeli (2001).

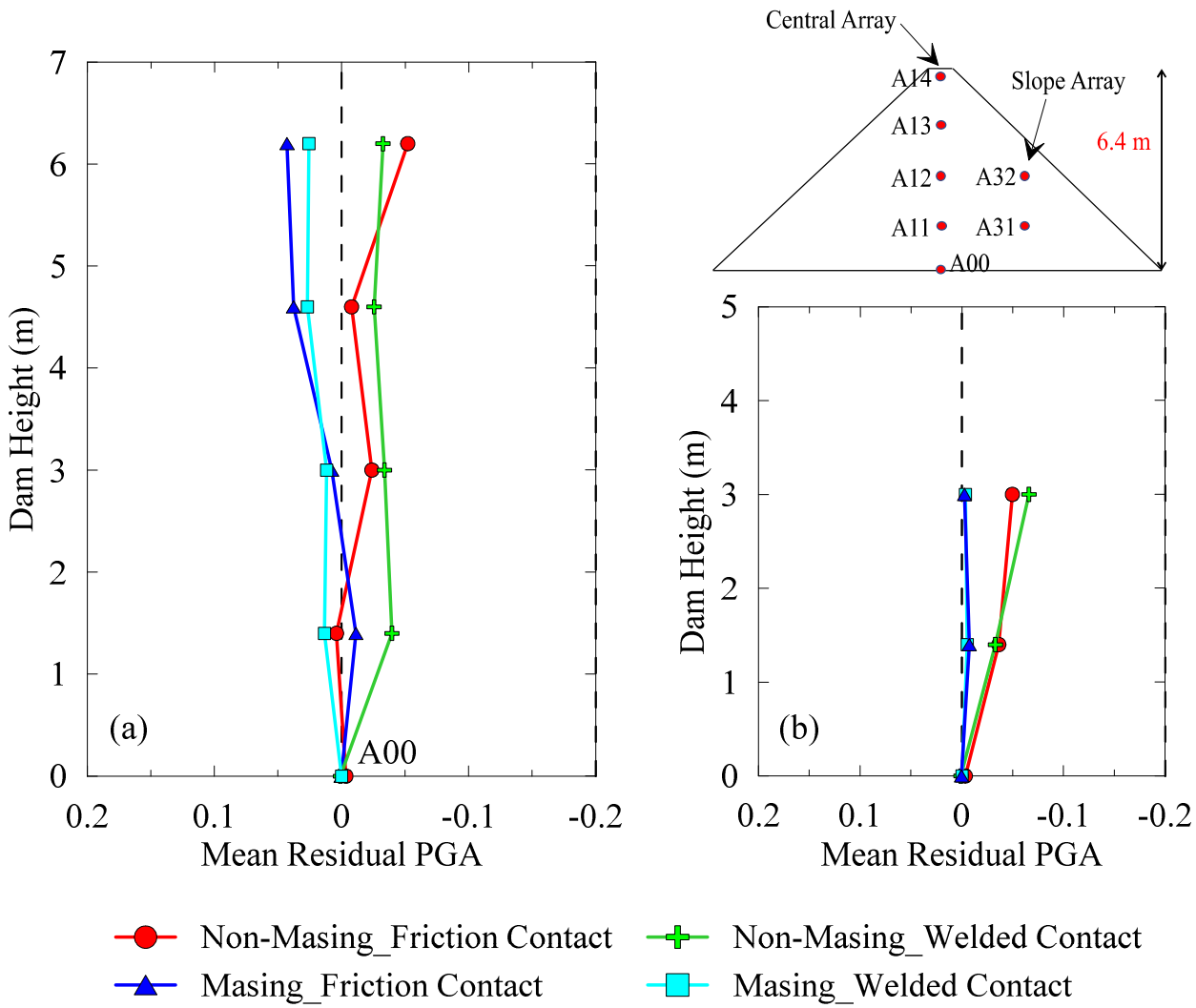

Figure 4.33: Mean residual peak ground accelerations during all motions (Test 01 – Test 09) for dynamic curves from Darendeli (2001): (a) Central array and (b) Slope array.

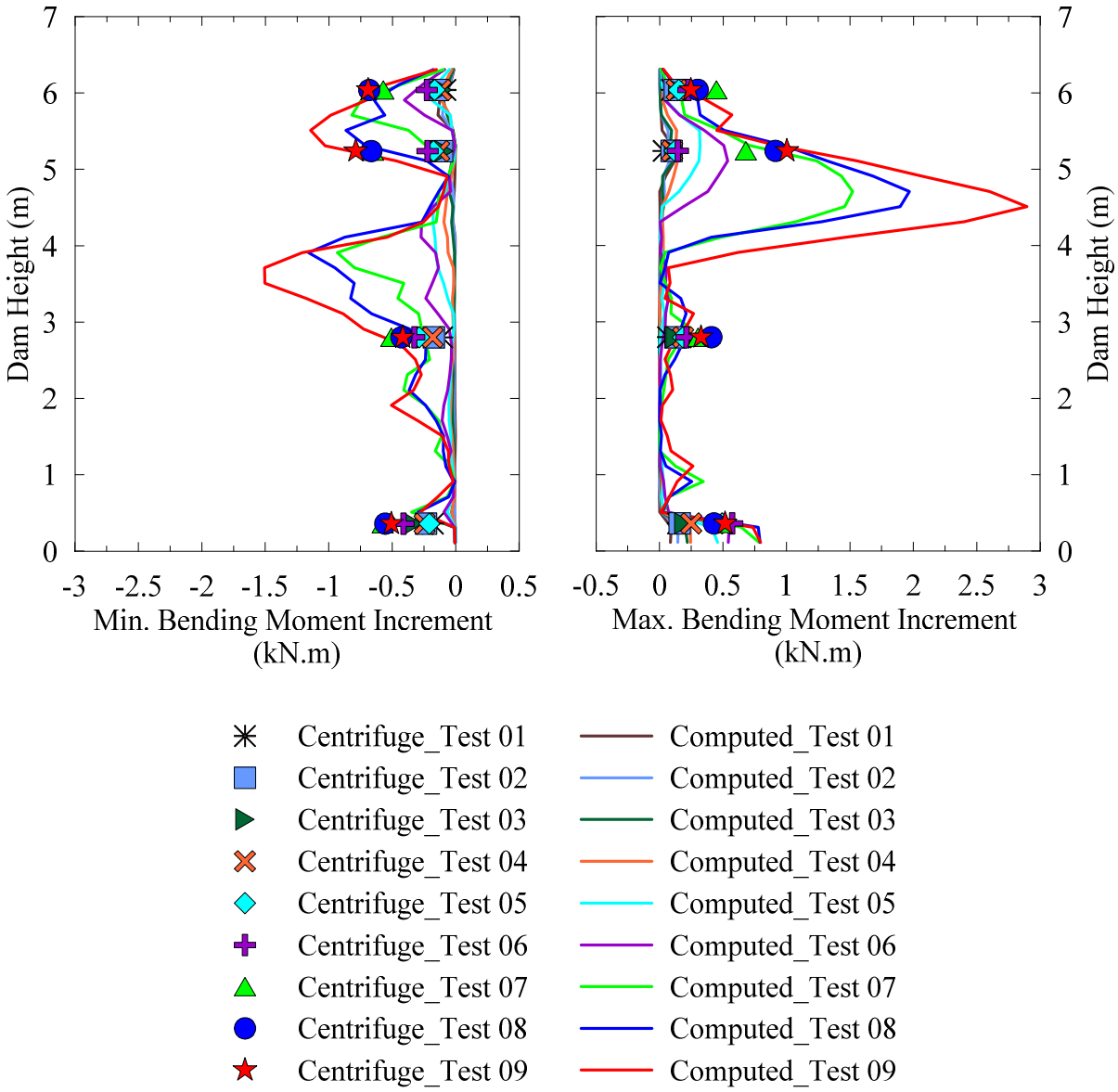

Figure 4.34: Comparison of computed and measured maximum and minimum bending moment increments on the concrete face slab for the numerical model with non-Masing un/reloading and friction contact.

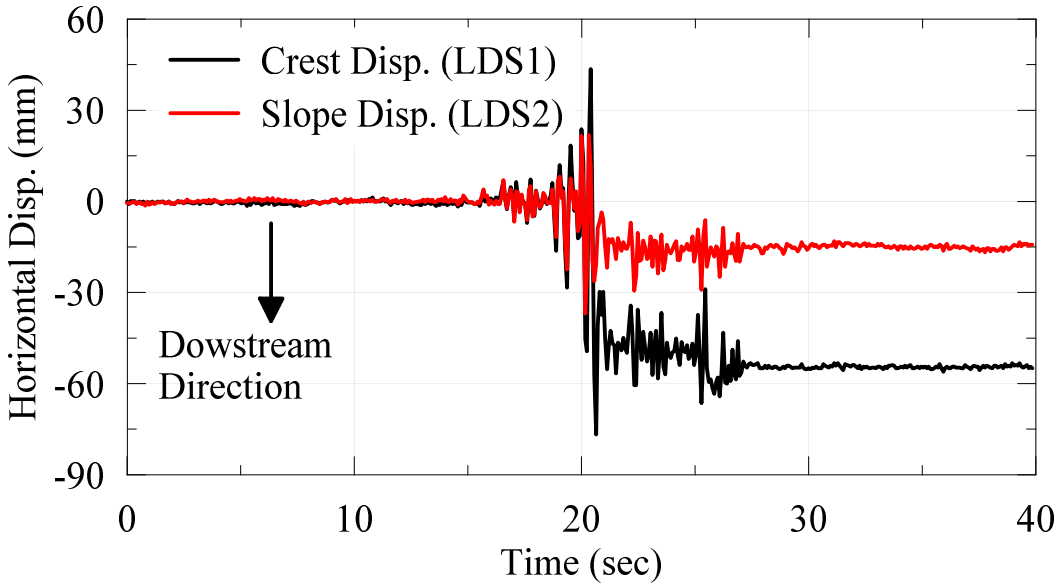

Figure 4.35: Lateral displacement measured in the centrifuge test during Test 09.

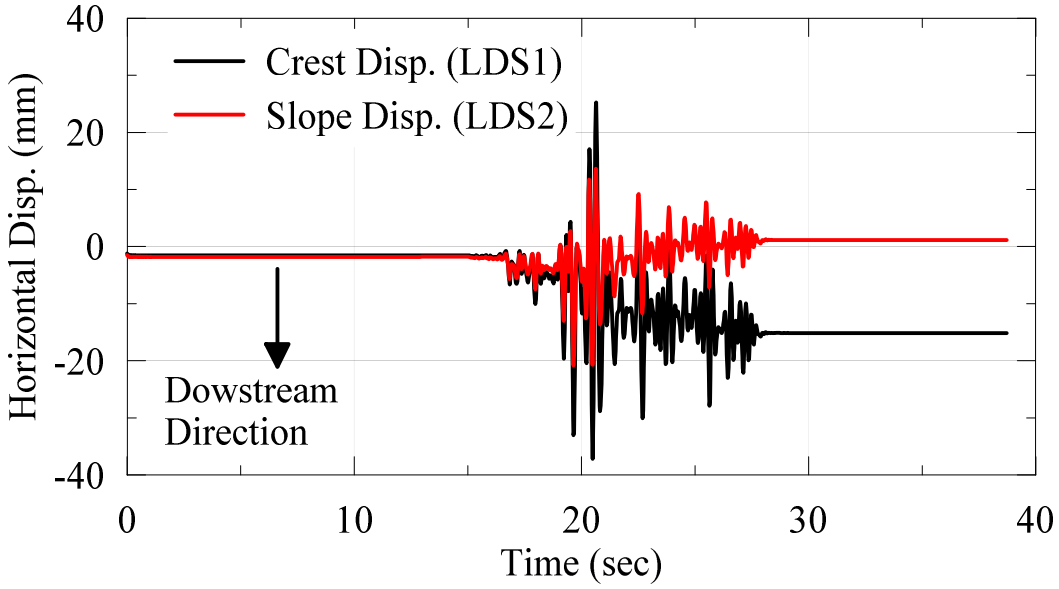

Figure 4.36: Calculated lateral displacement during Test 09 for the numerical model with non-Masing un/reloading rules and friction contact.

CHAPTER 5

SUMMARY, CONCLUSIONS AND FUTURE WORK

Two main goals of this study are: (1) investigating the effects of hysteretic damping of the rockfill, and (2) investigating the effects of the contact type defined for modeling the interface between rockfill and concrete face on the seismic response of the CFRDs. A series of nonlinear dynamic analyses were performed on a CFRD model using finite element method. The development and available design details of CFRDs are summarized in Chapter 2. The static performance of four CFRDs which are well-documented were briefly presented in Chapter 3. In Chapter 4, the seismic response of a CFRD prototype representing a centrifuge CFRD model was studied using finite element method. The effects of two factors that were investigated in the numerical simulations can be presented as follows:

- Masing and non-Masing un/reloading were utilized to represent the hysteretic damping of the rockfill. The Masing un/reloading is known to overestimate the hysteretic damping at large strains, while non-Masing un/reloading can represent the damping of the soil with a high degree of accuracy.
- The interface between rockfill and concrete face was modeled based on two approaches: (1) welded contact, and (2) friction contact. In the welded contact, the separation of concrete face from the rockfill was not allowed. In friction contact, the slippage between rockfill and concrete face was allowed with a certain amount of friction. The predicted response was compared to centrifugal measurements in terms of acceleration time histories, spectral accelerations, bending moment increments of the concrete face, and lateral deformations.

The main findings of the nonlinear dynamic finite element analyses of the prototype model can be summarized as follows:

- The hysteretic damping of the rockfill was found to have significant effects on the seismic response of the dam as the magnitude of earthquake motions increased. The Masing type un/reloading dramatically underestimated the response spectra between certain periods (0.1 – 1 s), particularly at the crest, while it led to good agreement with measured PGA profile. The Non-Masing type un/reloading, however, was found to result in good agreement with measured response in terms of acceleration time histories and associated response spectra. It is demonstrated that better characterization of hysteretic damping of the soil material successfully captures the measured behavior in the centrifuge test.
- The contact type between rockfill and concrete face had a great impact on the response spectra at the crest of the dam. The analyses with friction contact yielded closer predictions than welded contact in terms of spectral acceleration and bending moment increments.
- Even though a good agreement between computed and measured accelerations and bending moment increments was obtained, the lateral movements at the crest and on the slope of the model, which were recorded with image processing technique, could not be captured in the numerical simulations.

Properly selected dynamic properties of the rockfill and the connection type between rockfill and concrete face is necessary for a reliable dynamic simulation of CFRDs. Possible future work in the continuation of this study includes:

- The numerical approaches used in this study can be expanded to either a real CFRD or a dynamic centrifuge experiment performed on a CFRD with a larger dimensions and centrifugal acceleration. The simulations in this study represented a prototype CFRD of a small-scale centrifuge model in which a centrifugal acceleration of 40 g was used. The prototype scales were considerably smaller than a real CFRD constructed in the fields.
- This study can be further expanded to incorporate the topographical and/or other three-dimensional factors to better estimate the observed behavior of CFRDS. Three dimensional and topographic effects were not investigated in this study.
- Further experimental and numerical studies are required to investigate the effect of staged construction as well as static and dynamic crest settlements on the overall seismic response of both rockfill and concrete face.

REFERENCES

Arrau, L., Ibarra, I., & Noguera, G. (1985, October). Performance of Cogoti dam under seismic loading. In *Concrete Face Rockfill Dams-Design, Construction, and Performance* (pp. 1–13). ASCE.

Baltaji, O., Numanoglu, O. A., Veeraraghavan, S., Hashash, Y. M. A., Coleman, J. L., & Bolisetti C. (2017). Non-linear time domain site response and soil structure analysis for nuclear facilities using MOOSE. *Transactions, 24th International Conference on Structural Mechanics in Reactor Technology (SMiRT 24), Busan, South Korea, August 2017.*

Bernier, C., Padgett, J. E., Proulx, J., & Paultre, P. (2016). Seismic fragility of concrete gravity dams with spatial variation of angle of friction: case study. *Journal of Structural Engineering*, *142*(5), 05015002.

Bowles, J. E. (1996). *Foundation analysis and design*. New York: McGraw-Hill.

Cerna-Diaz, A.A. (2018). *Evaluation of cyclic behavior of dense sands under multidirectional loading using centrifuge tests*. Ph. D., University of Illinois at Urbana-Champaign.

Chiang, D. Y., & Beck, J. L. (1994). "A new class of distributed-element models for cyclic plasticity—I. Theory and application." *International journal of solids and structures*, 31(4), 469-484.

Clough, R. W., & Woodward, R. J. (1967). Analysis of embankment stresses and deformations. *Journal of the Soil Mechanics and Foundations Division*, *93*(4), 529–549.

Coleman, J., Slaughter, A., Veeraraghavan, S., Bolisetti, C., Numanoglu, O. A., Spears, R., Hoffman, W., & Kurt, E. (2017). *MASTODON Theory Manual* (No. INL/EXT-17-41930). Idaho National Laboratory, Idaho Falls, ID (United States).

Cooke, J. B., & Sherard, J. L. (1987). Concrete-Face rockfill dam: II. design. *Journal of Geotechnical Engineering*, *113*(10), 1113–1132.

Cooke, J. B. (1984). Progress in rockfill dams. *Journal of Geotechnical Engineering*, *110*(10), 1381–1414. https://doi.org/10.1061/(ASCE)0733-9410(1984)110:10(1381)

Cooke, J. B. (2000). The high CFRD dams. *J. Barry Cooke volume: Concrete Face Rockfill Dams*, Beijing, 1-4.

Cruz, P. T., Materón, B., & Freitas, M. (2009). *Concrete face rockfill dams*. Leiden, The Netherlands: CRC Press/Balkema.

Dakoulas, P. (2012). Nonlinear seismic response of tall concrete-faced rockfill dams in narrow canyons. *Soil Dynamics and Earthquake Engineering*, *34*(1), 11-24.

Darendeli, M. B. (2001*). Development of a new family of normalized modulus reduction and material damping curves*. Ph. D., University of Texas at Austin.

Fitzpatrick, M. D., Cole, B. A., Kinstler, F. L., & Knoop, B. P. (1985). Design of concrete-faced rockfill dams. In *Concrete Face Rockfill Dams-Design, Construction, and Performance* (pp. 410–434). ASCE.

Fu, Z., Chen, S., & Han, H. (2017). Experimental investigations on the residual strain behavior of a rockfill material subjected to dynamic loading. *Journal of Materials in Civil Engineering*, *29*(5). https://doi.org/10.1061/(ASCE)MT.1943-5533.0001816

Gillis, K., Dashti, S., & Hashash, Y. M. A. (2015). Dynamic calibration of tactile sensors for measurement of soil pressures in centrifuge. *Geotechnical Testing Journal*, *38*(3), 261-274.

Groholski, D. R., Hashash, Y. M. A., Kim, B., Musgrove, M., Harmon, J., & Stewart, J. P. (2016). Simplified model for small-strain nonlinearity and strength in 1D seismic site response analysis. *Journal of Geotechnical and Geoenvironmental Engineering*, *142*(9). https://doi.org/10.1061/(ASCE)GT.1943-5606.0001496

Hashash, Y.M.A., Musgrove, M.I., Harmon, J.A., Ilhan, O., Groholski, D.R., Phillips, C.A., and Park, D. (2017) "DEEPSOIL 7.0, User Manual".

Hashash, Y. M. A., Phillips, C., & Groholski, D. R. (2010). Recent advances in non-Linear site response analysis. In *5th International Conference on Recent Advances in Geotechnical Earthquake Engineering and Soil Dynamics*, Missouri Univ. of Science and Technology, Rolla, MO.

Hashash, Y. M. A., Dashti, S., Romero, M. I., Ghayoomi, M., & Musgrove, M. (2015). Evaluation of 1-D seismic site response modeling of sand using centrifuge experiments. *Soil Dynamics and Earthquake Engineering, 78*, 19-31.

Hubler, J. F., Athanasopoulos-Zekkos, A., & Zekkos, D. (2017). Monotonic, Cyclic, and Postcyclic Simple Shear Response of Three Uniform Gravels in Constant Volume Conditions. *Journal of Geotechnical and Geoenvironmental Engineering*, *143*(9), 04017043.

Hunter, G., & Fell, R. (2002). *The deformation behaviour of rockfill* (UNICIV report no. r-405). Sydney, Australia: University of New South Wales, School of Civil and Environmental Engineering.

Hunter, G., & Fell, R. (2003). Rockfill modulus and settlement of concrete face rockfill dams. *Journal of Geotechnical and Geoenvironmental Engineering*, *129*(10), 909–917. https://doi.org/10.1061/(ASCE)1090-0241(2003)129:10(909)

ICOLD (2010). Concrete face Rockfill Dams: Concepts for design and construction. *International Commission on Large Dams,* Bulletin 141.

ICOLD (1989). Rockfill dams with concrete facing - State of art. *International Commission on Large Dams*, Bulletin 70.

Iwan, W. D. (1967). "On a class of models for the yielding behavior of continuous and composite systems." *Journal of Applied Mechanics*, 34(3): 612-617.

Jaky, J. (1948). "Pressure in silos." ICSMFE, London 1: 103-107.

Keming, C., & Zhogliang, Z. (2001). Performance of the Tianshengqiao 1 CFRD. *International Journal on Hydropower & Dams*, *8*(5), 78–83.

Kim, M.-K., Lee, S.-H., Choo, Y. W., & Kim, D.-S. (2011). Seismic behaviors of earth-core and concrete-faced rock-fill dams by dynamic centrifuge tests. *Soil Dynamics and Earthquake Engineering*, *31*(11), 1579–1593. https://doi.org/10.1016/j.soildyn.2011.06.010

Lambe, T. W., & Whitman, R. V. (1969). *Soil Mechanics*. New York: John Wiley.

Leps, T. M. (1970). Review of shearing strength of rockfill. *Journal of the Soil Mechanics and Foundations Division*, *96*(4), 1159–1170.

Lowe, J. (1964). Shear strength of coarse embankment dam materials. In *Proc. 8th Int. Congress on Large Dams* (Vol. 3, pp. 745–761). Paris: International Commission on Large Dams.

LSTC (2009). LS DYNA Keyword User's Manual - Release 971 R4. L. Corporation. Livermore, California.

Ma, H., & Cao, K. (2007). Key technical problems of extra-high concrete faced rock-fill dam. *Science in China Series E: Technological Sciences*, *50*(1), 20–33.

Macedo-Gomez, G., Castro-Abonce, J., & Montanez-Cartaxo, L. (2000). Behavior of Aguamilpa dam. *J. Barry Cooke volume: Concrete Face Rockfill Dams*, Beijing, 117–151.

Marsal, R. J. (1973). Mechanical properties of rockfill. In *Embankment-dam engineering; Casagrande volume* (pp. 271–354). New York: Wiley.

Marulanda, A., & Pinto, N. L. de S. (2000). Recent experience on design, construction, and performance of CFRD dams. *J. Barry Cooke volume: Concrete Face Rockfill Dams*, Beijing, 279-315.

Marulanda, C., & Marulanda, A. (2015). CFRD: past and present (*). In *25th international congress on large dams*. Stavanger, Norway: International Commission on Large Dams.

Marulanda-Escobar, C., & Marulanda-Posada, A. (2008). Recent experience on design, construction and performance of CFRD dams. In *International Conference on Case Histories in Geotechnical Engineering*. Missouri University of Science and Technology.

Masing G. Eignespannungen und verfestigung beim messing. *In: Second International Congress on Applied Mechanics*, Zurich, Switzerland, 1926, (pp. 332–335).

Menq, F. Y. (2003). *Dynamic properties of sandy and gravelly soils.* Ph.D., University of Texas at Austin.

Montanez-Cartaxo, L. E. (1992). The perimetric joint design for Aguamilpa dam. *International Water Power and Dam Construction*, *44*(4), 22–28.

Numanoglu, O. A. (2018). Ph.D. Thesis in progress. University of Illinois at Urbana Champaign.

Numanoglu, O. A., Hashash, Y. M. A., Cerna-Diaz, A., Olson, S. M., Bhaumik, L., Rutherford, C. J., & Weaver, T. (2017a). Nonlinear 3-D modeling of dense sand and the simulation of a soil-structure system under multi-directional loading. In *Geotechnical Frontiers 2017*. https://doi.org/10.1061/9780784480489.038

Numanoglu, O. A., Musgrove, M., Harmon, J. A., & Hashash, Y. M. A. (2017b). Generalized Non-Masing Hysteresis Model for Cyclic Loading. *Journal of Geotechnical and Geoenvironmental Engineering*, *144*(1), 06017015.

Park, D., Kwak, D. Y., Cho, C. K., & Chun, B. S. (2009). Evaluation of liquefaction potential of port structures with earthquake magnitude adjustment. *Journal of Coastal Research*, 1035-1039.

Penman, A., & Rocho-Filho, P. (2000). Instrumentation for CFRD dams. *J. Barry Cooke volume: Concrete Face Rockfill Dams*, Beijing, 221-278.

Phillips, C., & Hashash, Y. M. A. (2009). Damping formulation for nonlinear 1D site response analyses. *Soil Dynamics and Earthquake Engineering*, *29*(7), 1143–1158. https://doi.org/10.1016/j.soildyn.2009.01.004

Pinto, N. L. de S., & Marques Filho, P. L. (1998). Estimating the maximum face deflection in CFRDs. *International Journal on Hydropower and Dams*, *5*(6), 28–32.

Pinto, N. L. de S., Marques Filho, P. L., & Maurer, E. (1985). Foz do Areia dam-design, construction, and behaviour. In *Concrete Face Rockfill Dams-Design, Construction, and Performance* (pp. 173–191). ASCE.

Pinto, N. L. de S., Materon, B., & Marques Filho, P. L. (1982). Design and performance of Foz do Areia concrete membrane as related basalt properties. In *14th international congress on large dams* (Vol. 4, pp. 873–905). Rio de Janeiro: International Commission on Large Dams.

Romana, M. (2015). The plinth foundation of CFRD dams. In *25th international congress on large dams*. Stavanger, Norway: International Commission on Large Dams.

Seed, H. B., Seed, R. B., Lai, S. S., & Khamenehpour, B. (1985). Seismic design of concrete faced rockfill dams. In *Concrete Face Rockfill Dams—Design, Construction, and Performance* (pp. 459-478). ASCE.

Sherard, J. L. (1985). The upstream zone in concrete-face rockfill dams. In *Concrete Face Rockfill Dams-Design, Construction, and Performance* (pp. 618–641). ASCE.

Sherard, J. L., & Cooke, J. B. (1987). Concrete-Face rockfill dam: I. Assessment. *Journal of Geotechnical Engineering*, *113*(10), 1096–1112. https://doi.org/10.1061/(ASCE)0733-9410(1987)113:10(1096)

Sierra, J. M., Ramirez, C. A., & Hacelas, J. E. (1985). Design features of Salvajina dam. In *Concrete Face Rockfill Dams-Design, Construction, and Performance* (pp. 266–285). ASCE.

Sobrinho, J. A., Sardinha, A. E., Albertoni, S. C., & Dijkstra, H. H. (2000). Development aspects of CFRD in Brazil. *J. Barry Cooke volume: Concrete Face Rockfill Dams*, Beijing, 153-176.

Tsinidis, G., Pitilakis, K., & Madabhushi, G. (2016). On the dynamic response of square tunnels in sand. *Engineering Structures*, *125*, 419-437.

Uddin, N., & Gazetas, G. (1995). Dynamic response of concrete-faced rockfill dams to strong seismic excitation. *Journal of Geotechnical Engineering*, *121*(2), 185–197. https://doi.org/10.1061/(ASCE)0733-9410(1995)121:2(185)

Varadarajan, A., Sharma, K. G., Venkatachalam, K., & Gupta, A. K. (2003). Testing and modeling two rockfill materials. *Journal of Geotechnical and Geoenvironmental Engineering*, *129*(3), 206–218. https://doi.org/10.1061/(ASCE)1090-0241(2003)129:3(206)

Verdugo, R., & Peters, G. (2009). Observed seismic behavior of three Chilean large dams. *Earthquake geotechnical case histories for performance-based design*, 409-430.

Wen, L., Chai, J., Xu, Z., Qin, Y., & Li, Y. (2017). Monitoring and numerical analysis of behaviour of Miaojiaba concrete-face rockfill dam built on river gravel foundation in China. *Computers and Geotechnics*, *85*, 230–248. https://doi.org/10.1016/j.compgeo.2016.12.018

Xiao, Y., Liu, H., Chen, Y., & Jiang, J. (2014). Strength and deformation of rockfill material based on large-scale triaxial compression tests. I: Influences of density and pressure. *Journal of Geotechnical and Geoenvironmental Engineering, 140*(12). https://doi.org/10.1061/(ASCE)GT.1943-5606.0001176

XU, Z. (2015). *Embankment and tailings dams* (General Report Q 98). Stavanger, Norway: International Commission on Large Dams (ICOLD).

Zhang, J. M., Yang, Z., Gao, X., & Zhang, J. (2015). Geotechnical aspects and seismic damage of the 156-m-high Zipingpu concrete-faced rockfill dam following the Ms 8.0 Wenchuan earthquake. *Soil Dynamics and Earthquake Engineering, 76*, 145-156.

APPENDIX A: DETAILED ANALYSES RESULTS

This APPENDIX provides detailed comparison of the centrifugal measurements with the numerical predictions of nine tests for the cases where hysteretic soil damping (Masing and non-Masing un/reloading rules), the different interface types (welded and friction contacts), and different referenced dynamic soil curves (Menq, 2003 and Darendeli, 2001) were attempted in creating the model. The comparison of acceleration time histories and spectral accelerations were presented.

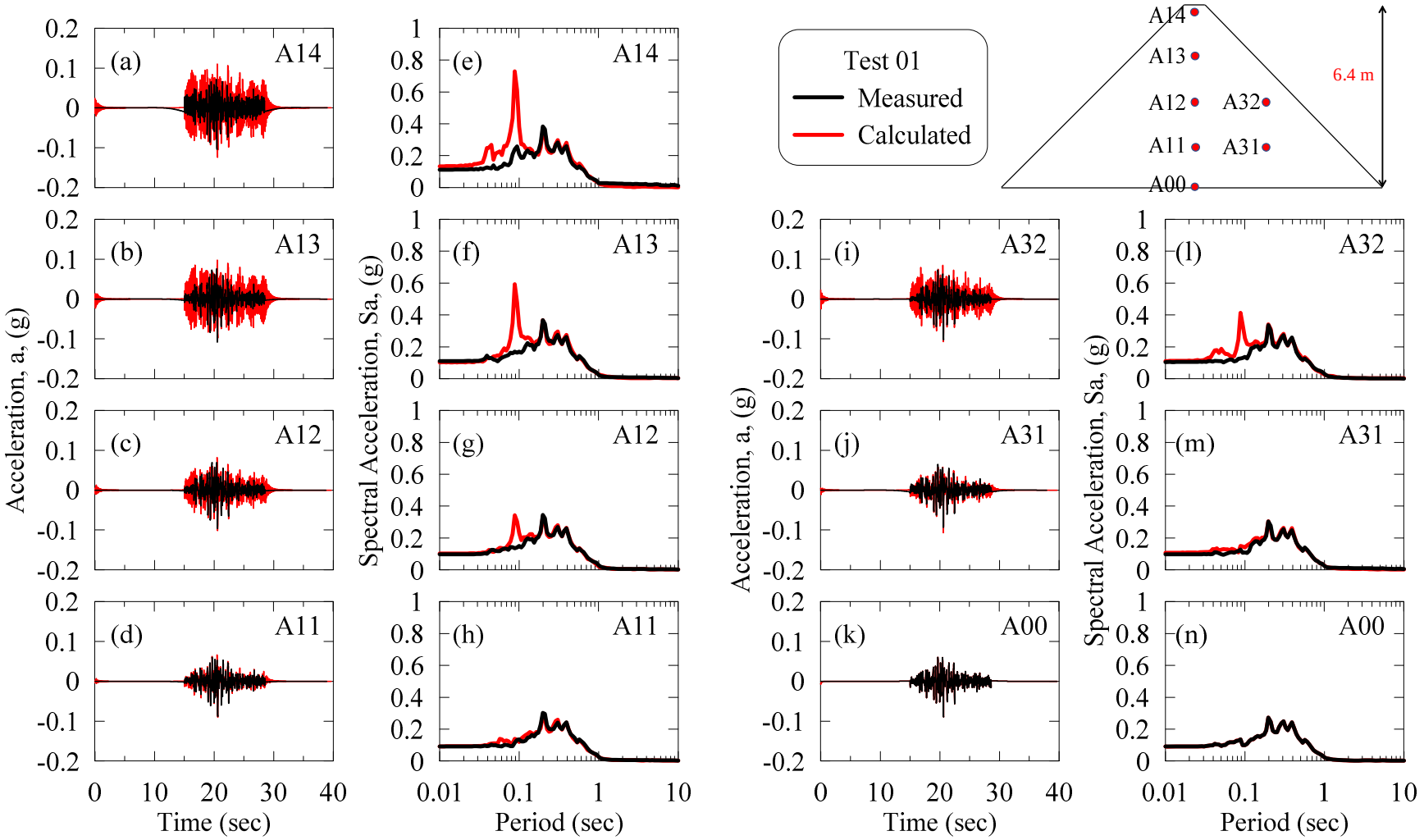

Figure A.1: Acceleration time histories and response spectra at different depths of dam during Test 01 for welded contact and the dynamic soil curves of Menq (2003) with non-Masing un/reloading.

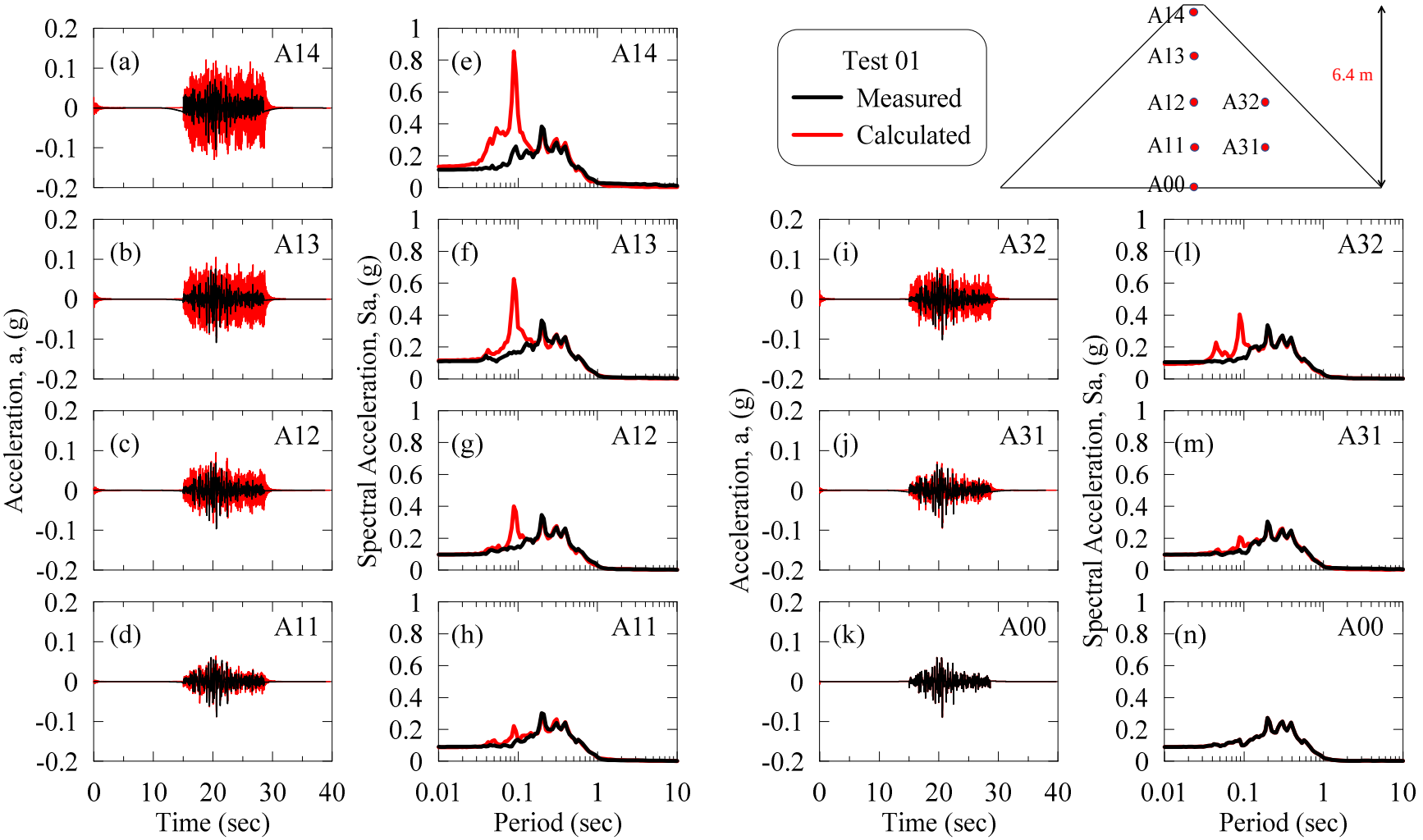

Figure A.2: Acceleration time histories and response spectra at different depths of dam during Test 01 for friction contact and the dynamic soil curves of Menq (2003) with Masing un/reloading.

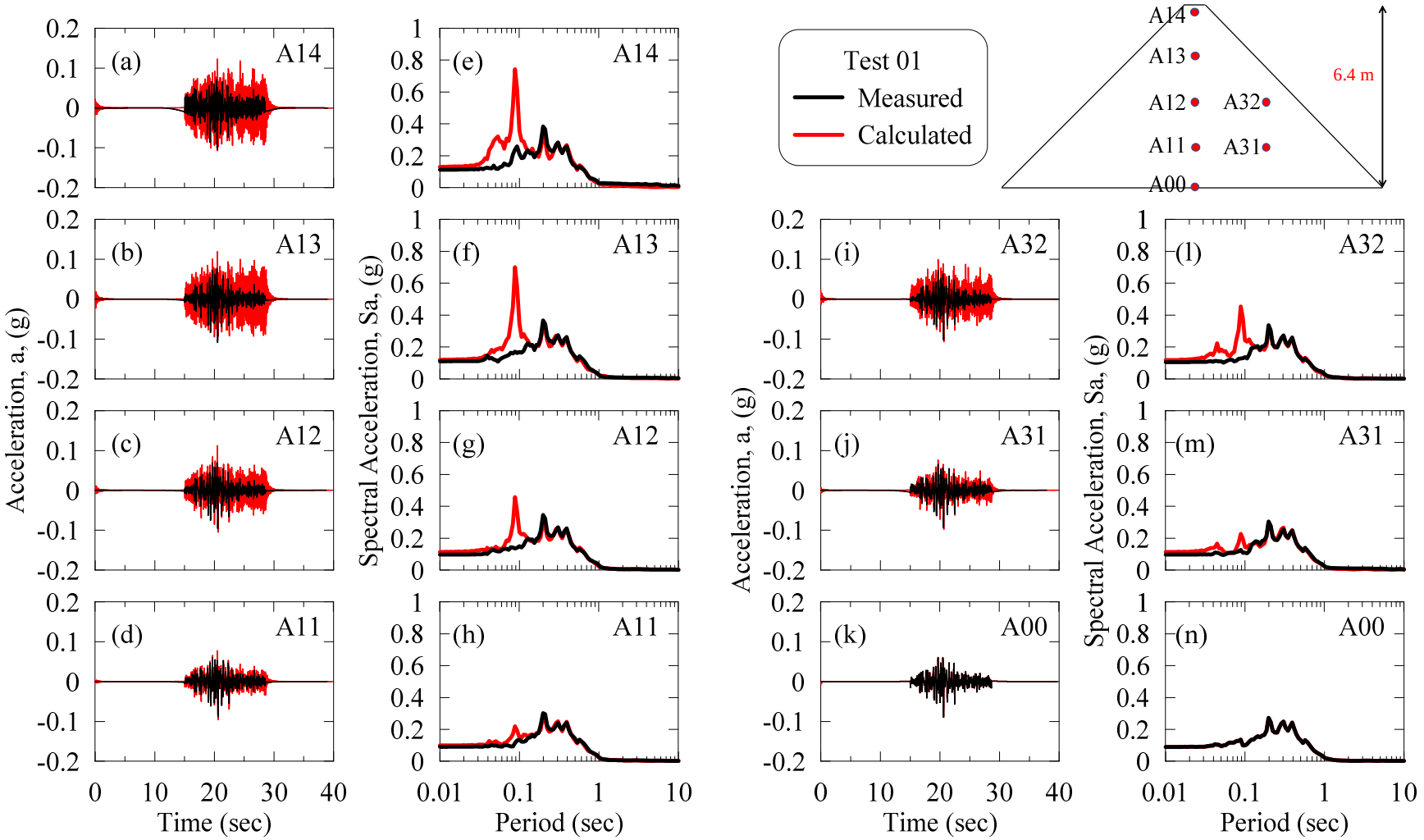

Figure A.3: Acceleration time histories and response spectra at different depths of dam during Test 01 for welded contact and the dynamic soil curves of Menq (2003) with Masing un/reloading.

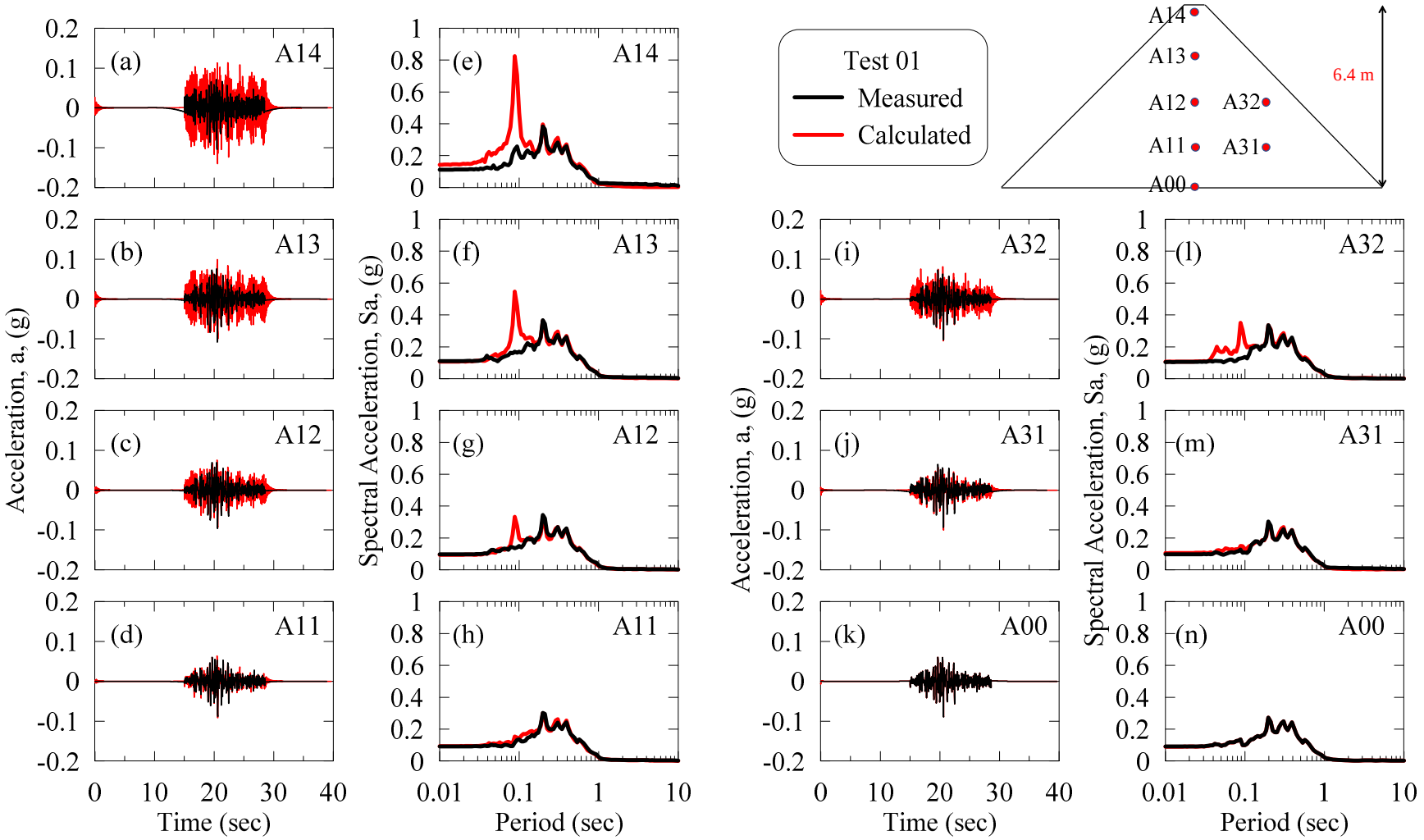

Figure A.4: Acceleration time histories and response spectra at different depths of dam during Test 01 for friction contact and the dynamic soil curves of Darendeli (2001) with non-Masing un/reloading.

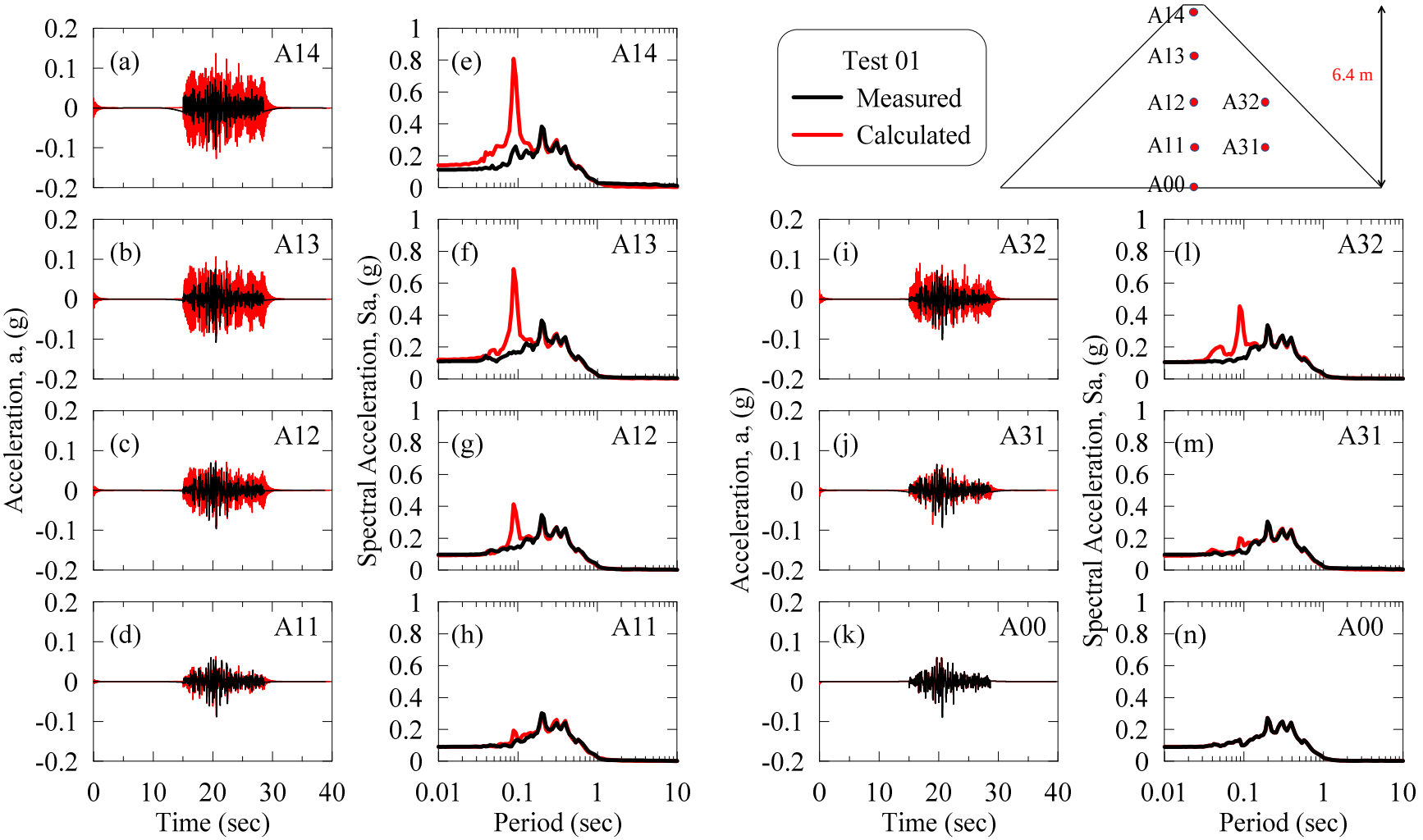

Figure A.5: Acceleration time histories and response spectra at different depths of dam during Test 01 for welded contact and the dynamic soil curves of Darendeli (2001) with non-Masing un/reloading.

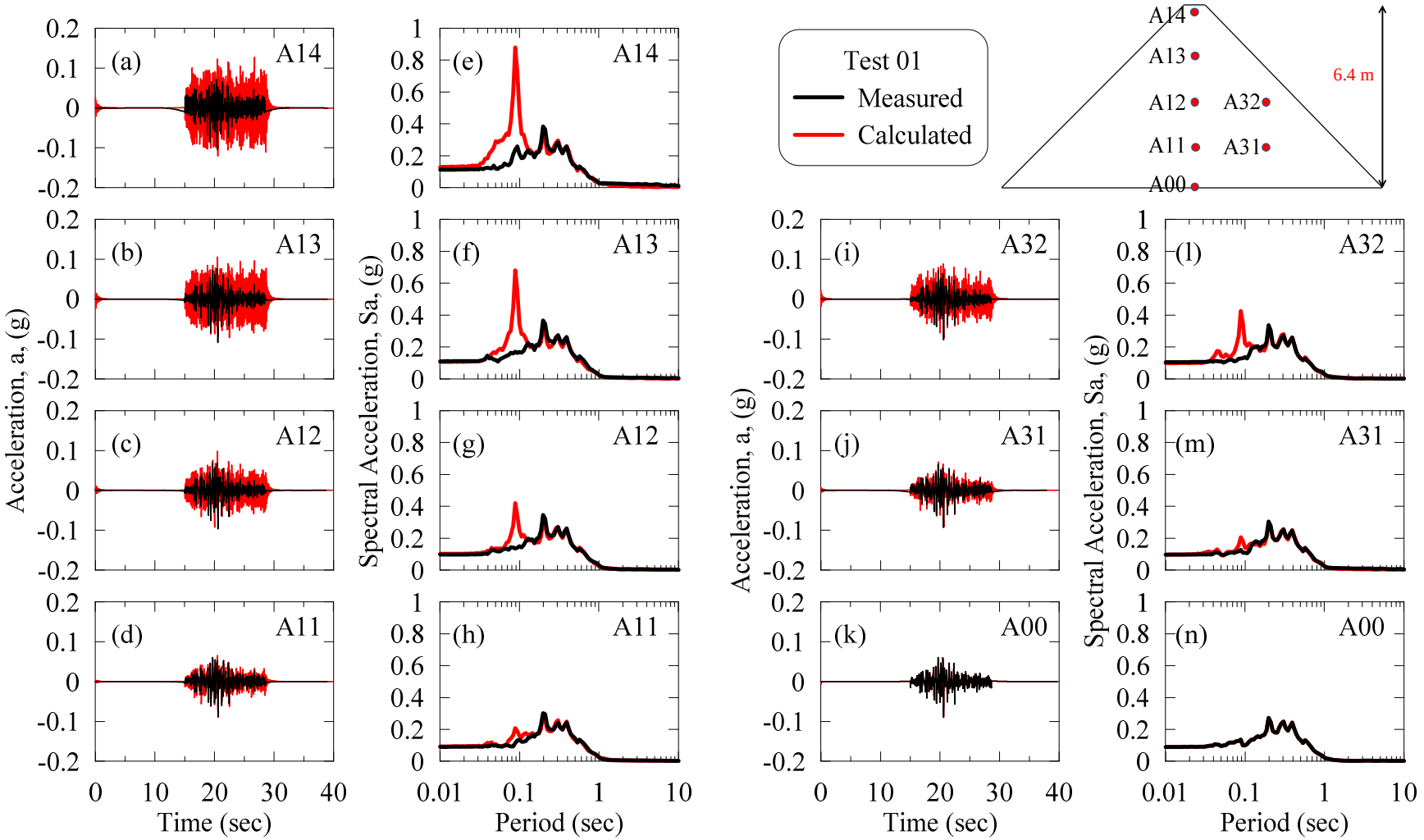

Figure A.6: Acceleration time histories and response spectra at different depths of dam during Test 01 for friction contact and the dynamic soil curves of Darendeli (2001) with Masing un/reloading.

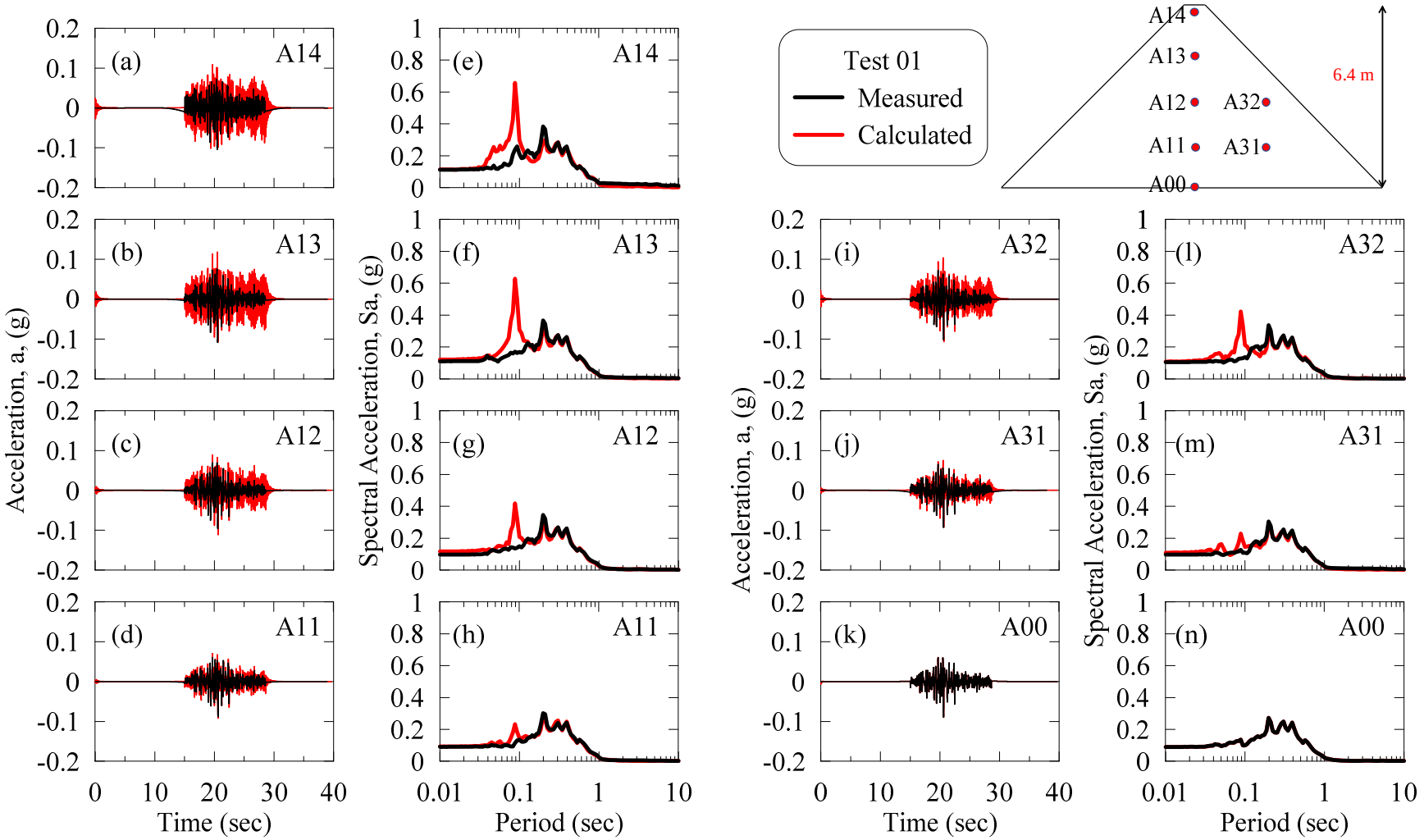

Figure A.7: Acceleration time histories and response spectra at different depths of dam during Test 01 for welded contact and the dynamic soil curves of Darendeli (2001) with Masing un/reloading.

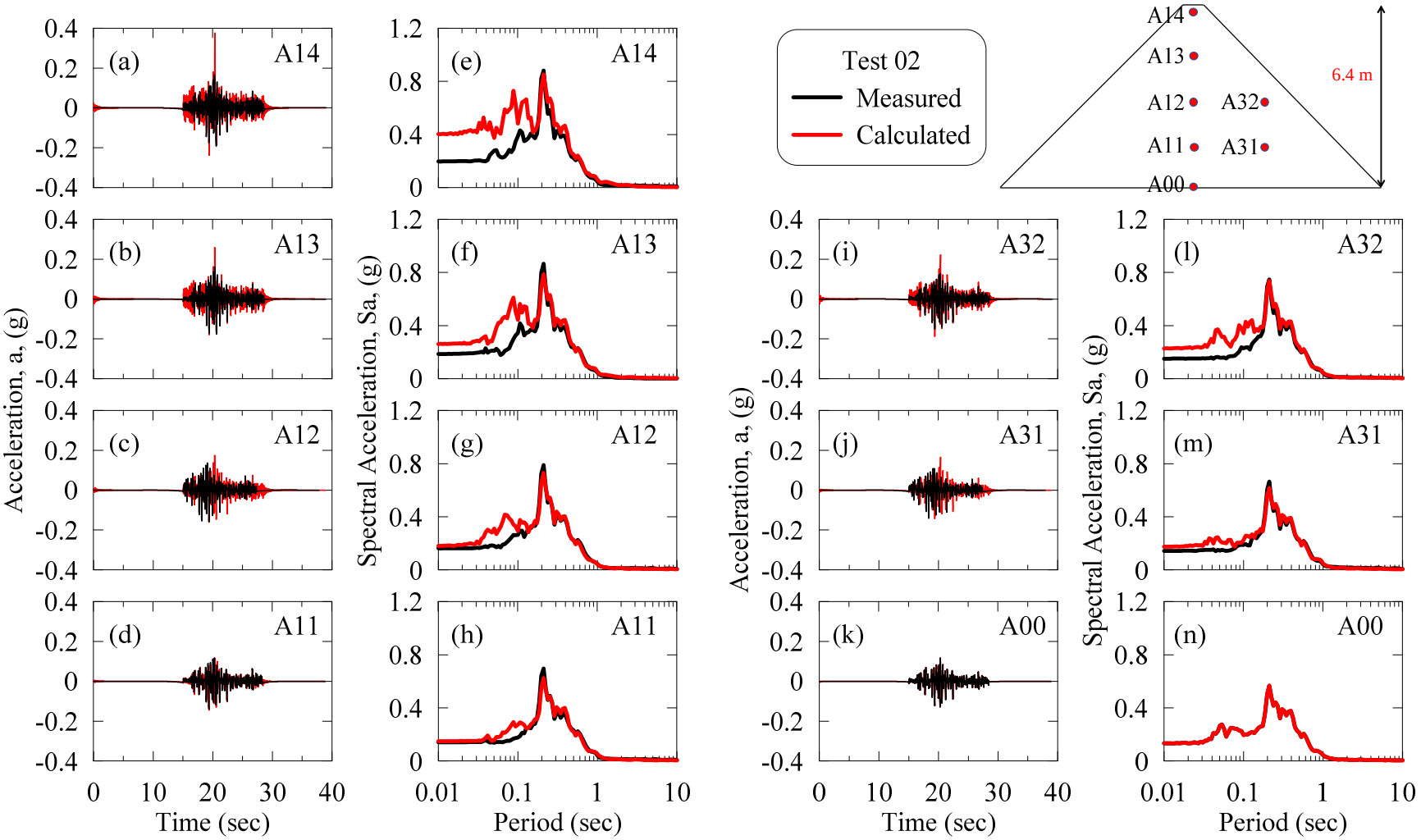

Figure A.8: Acceleration time histories and response spectra at different depths of dam during Test 02 for welded contact and the dynamic soil curves of Menq (2003) with non-Masing un/reloading.

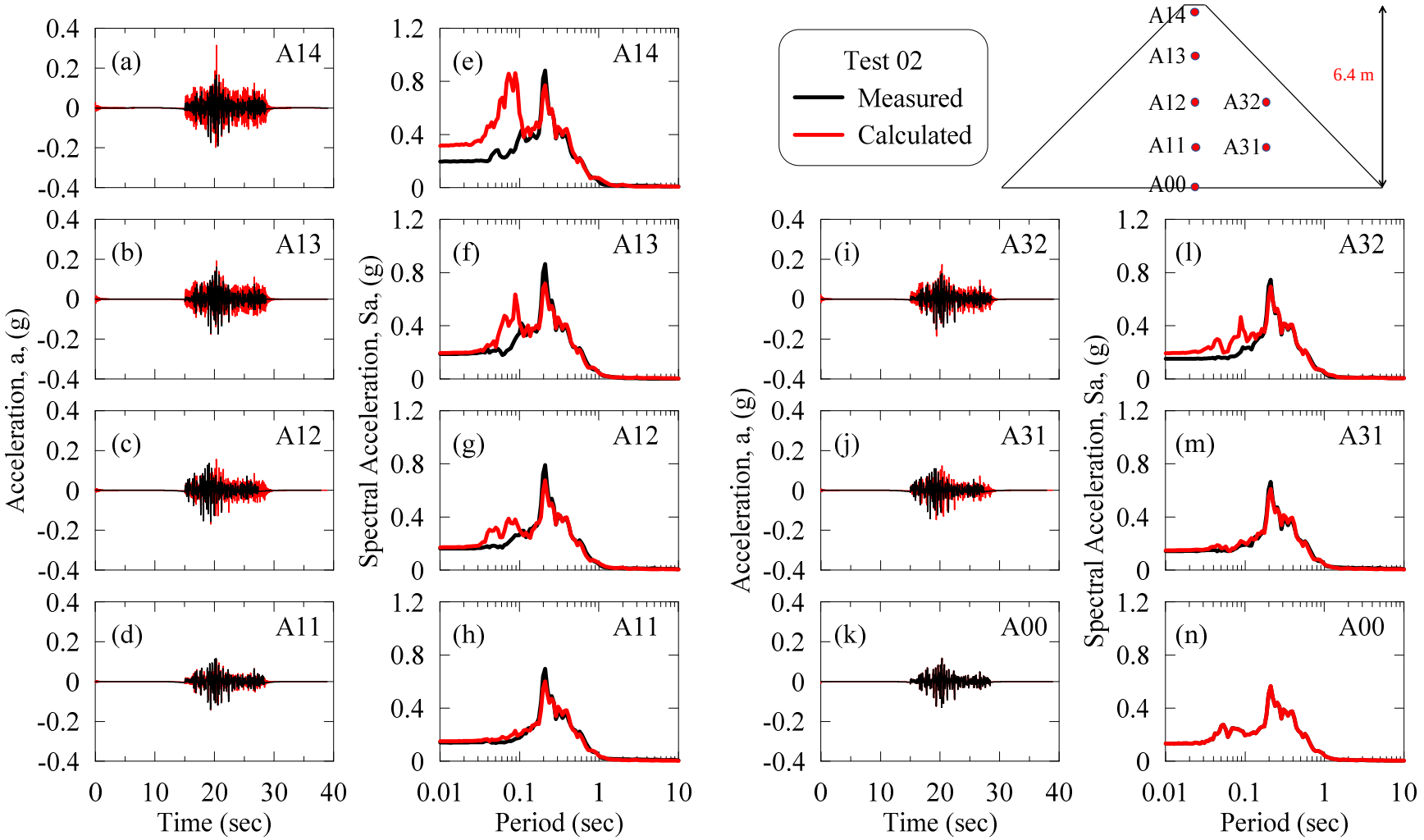

Figure A.9: Acceleration time histories and response spectra at different depths of dam during Test 02 for friction contact and the dynamic soil curves of Menq (2003) with Masing un/reloading.

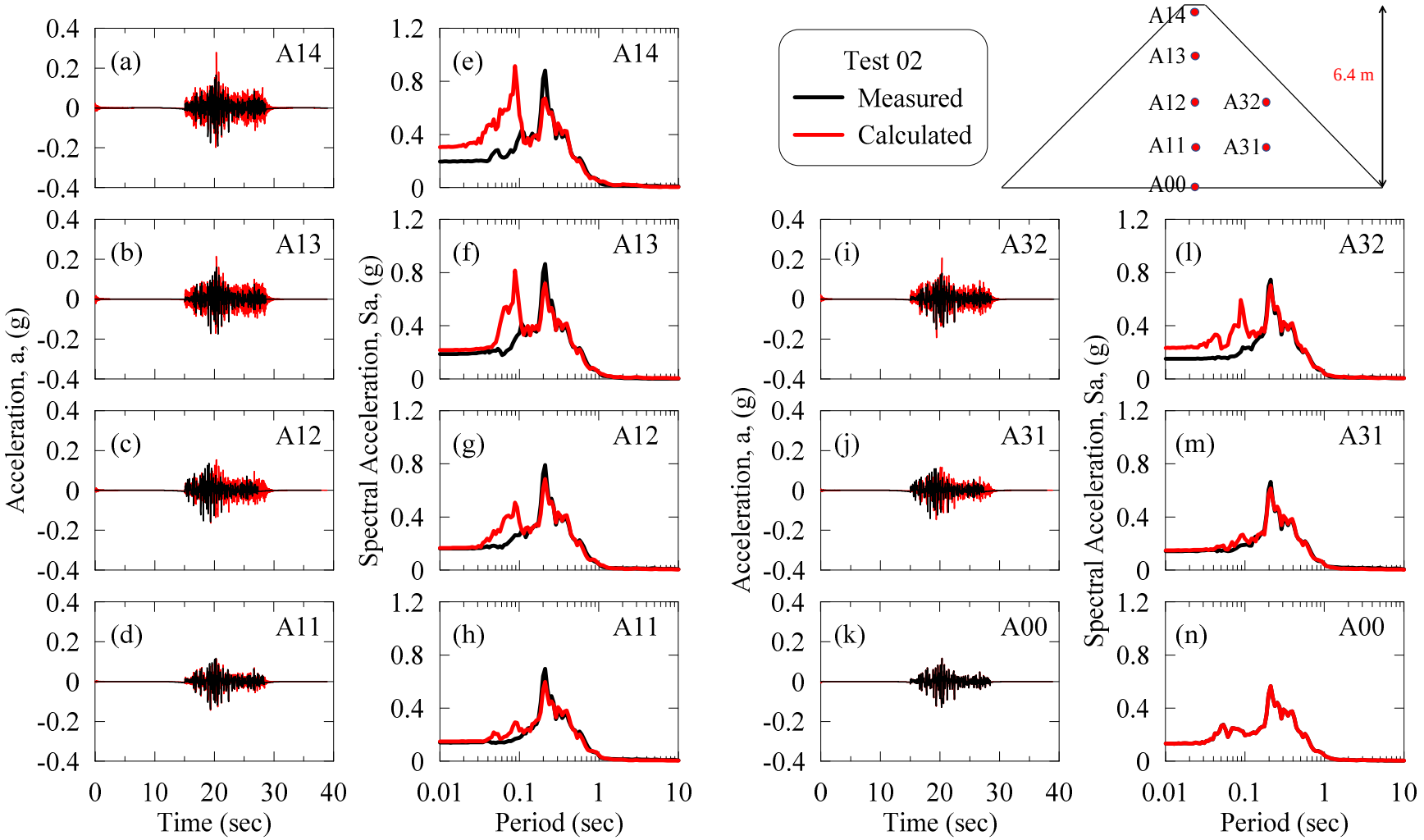

Figure A.10: Acceleration time histories and response spectra at different depths of dam during Test 02 for welded contact and the dynamic soil curves of Menq (2003) with Masing un/reloading.

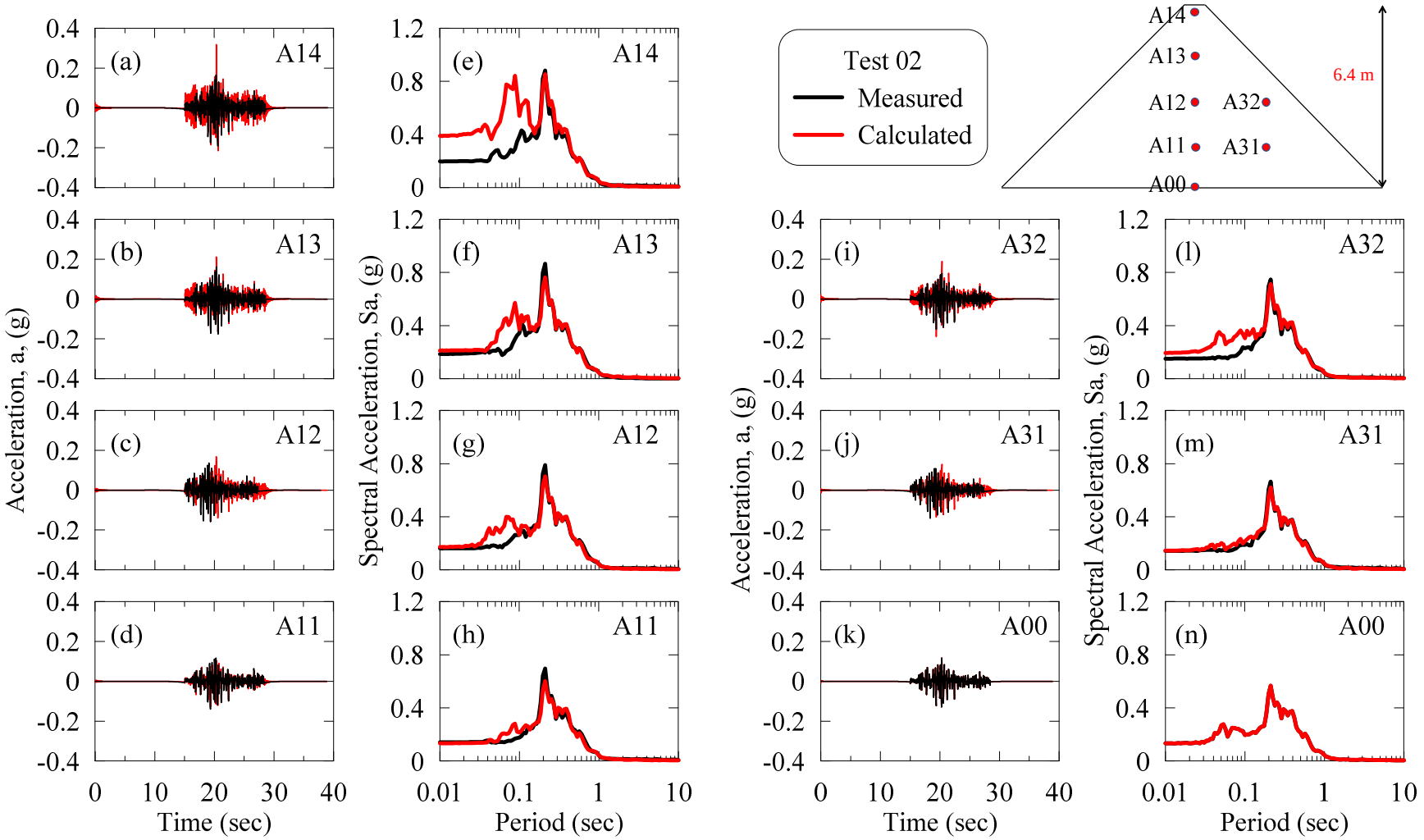

Figure A.11: Acceleration time histories and response spectra at different depths of dam during Test 02 for friction contact and the dynamic soil curves of Darendeli (2001) with non-Masing un/reloading.

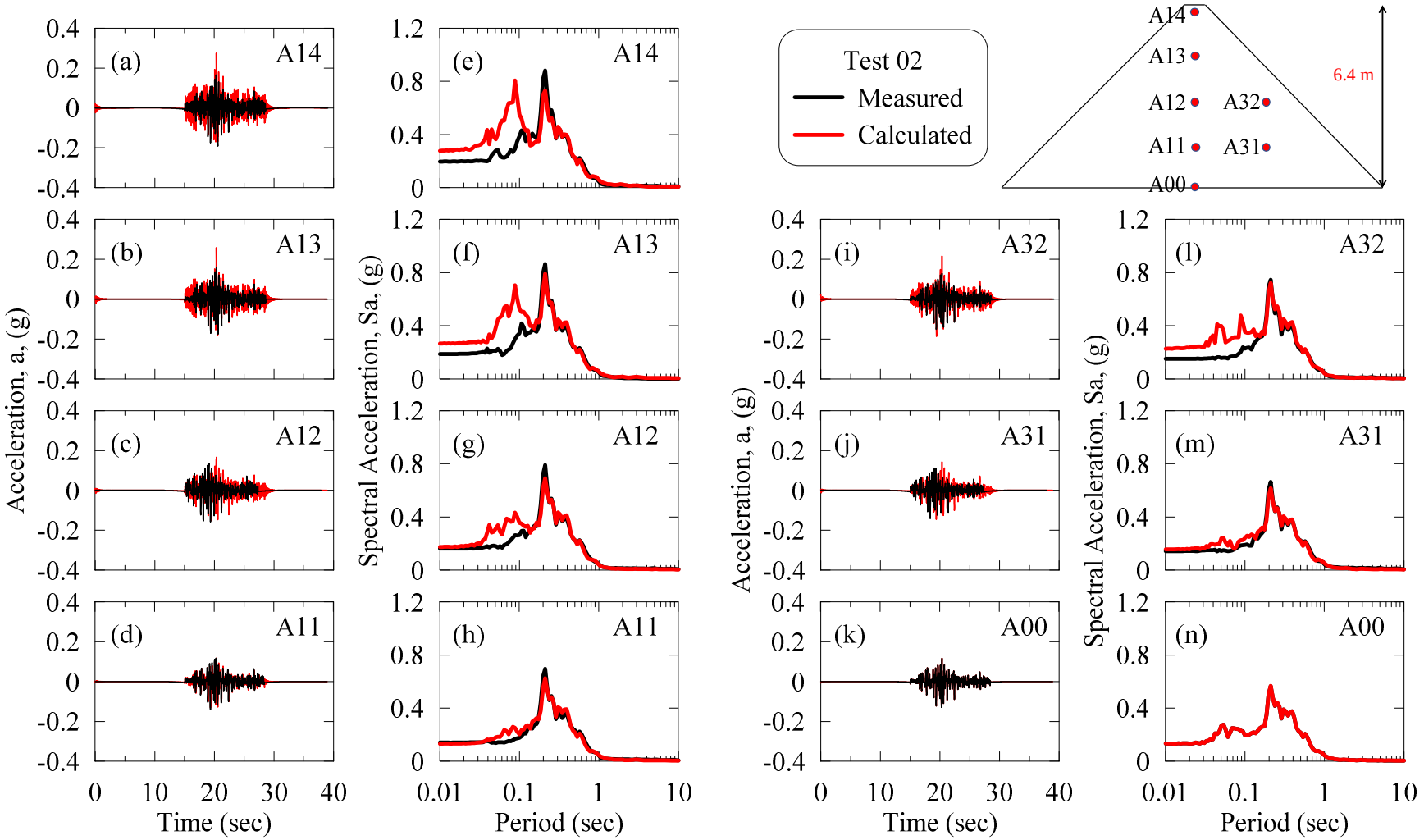

Figure A.12: Acceleration time histories and response spectra at different depths of dam during Test 02 for welded contact and the dynamic soil curves of Darendeli (2001) with non-Masing un/reloading.

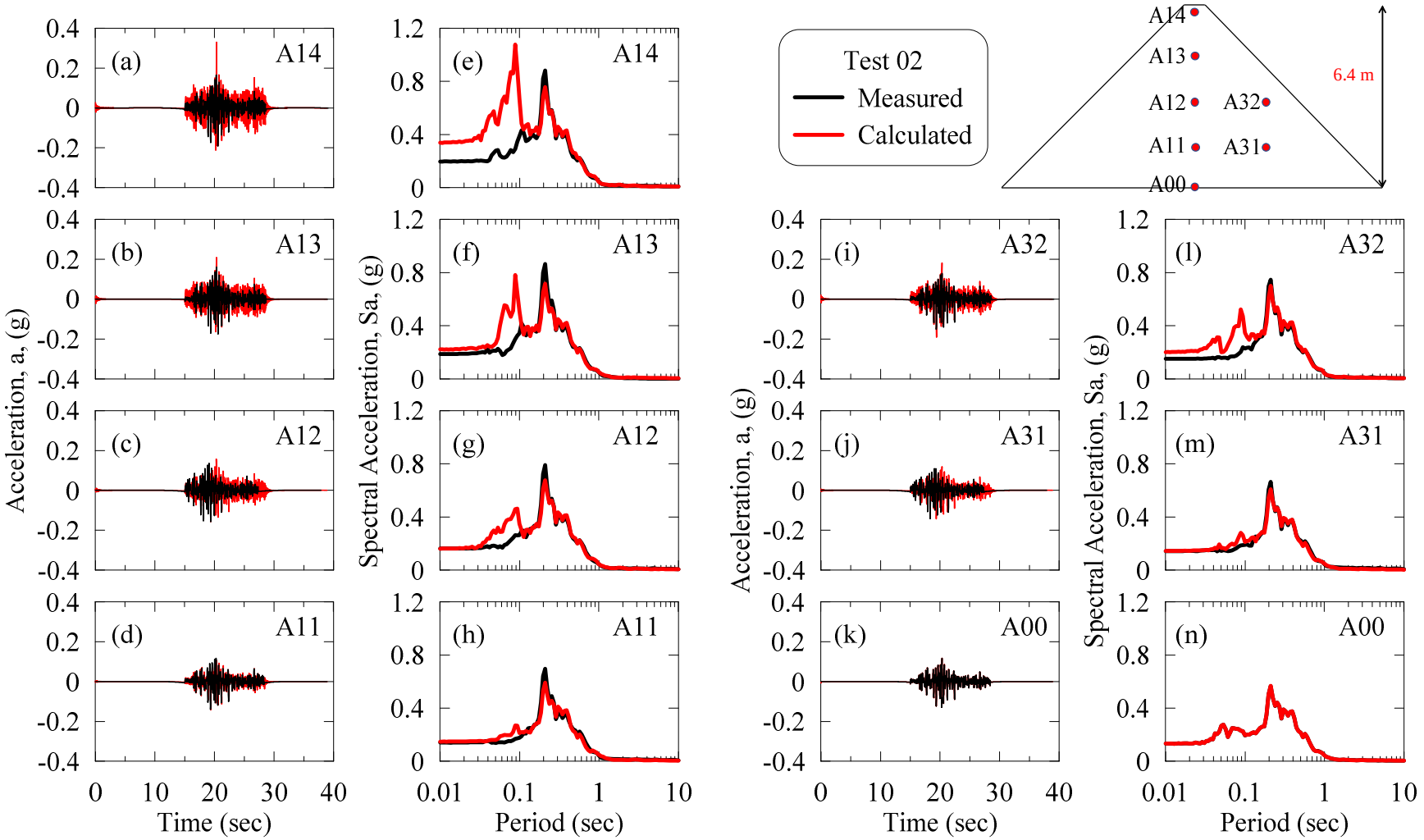

Figure A.13: Acceleration time histories and response spectra at different depths of dam during Test 02 for friction contact and the dynamic soil curves of Darendeli (2001) with Masing un/reloading.

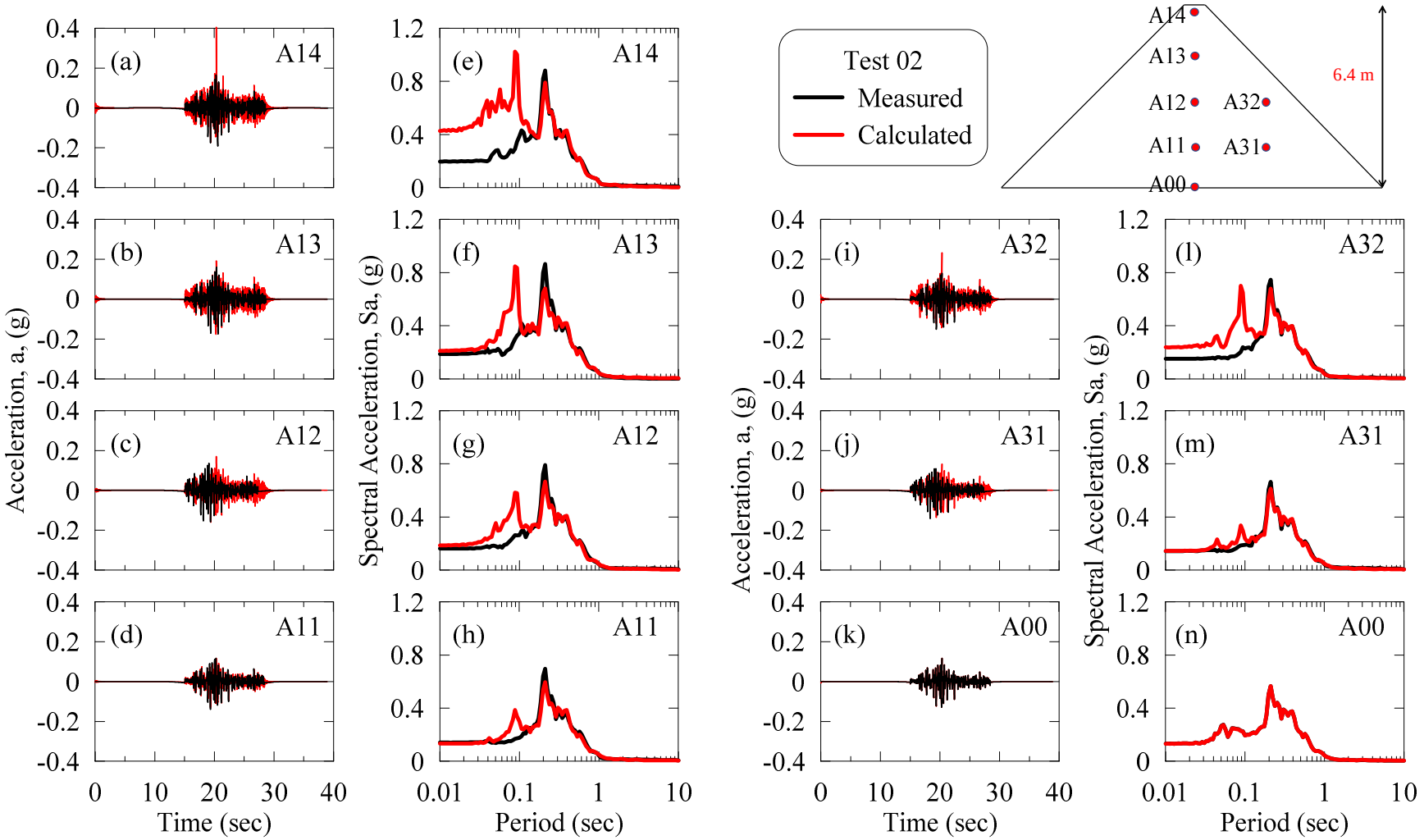

Figure A.14: Acceleration time histories and response spectra at different depths of dam during Test 02 for welded contact and the dynamic soil curves of Darendeli (2001) with Masing un/reloading.

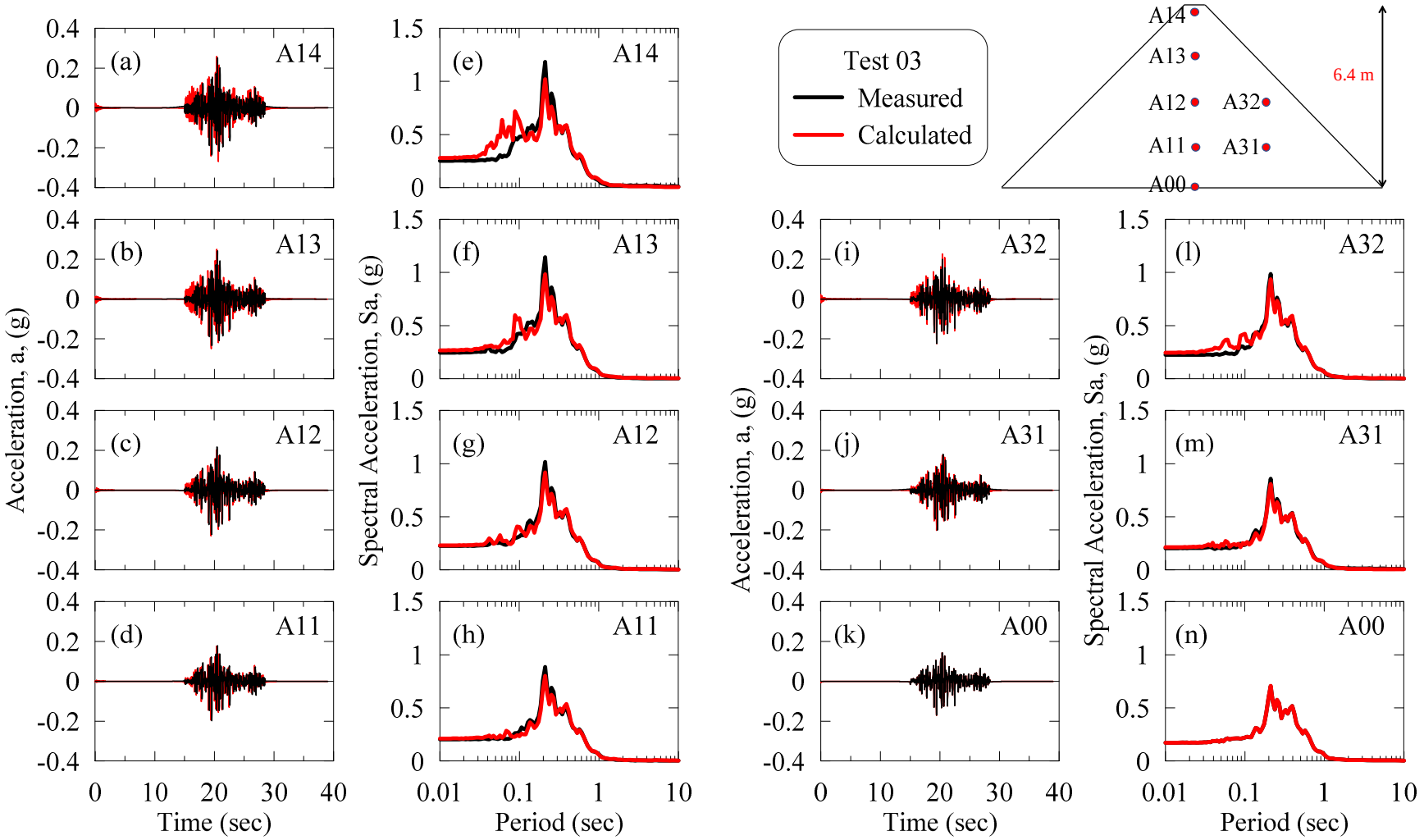

Figure A.15: Acceleration time histories and response spectra at different depths of dam during Test 03 for welded contact and the dynamic soil curves of Menq (2003) with non-Masing un/reloading.

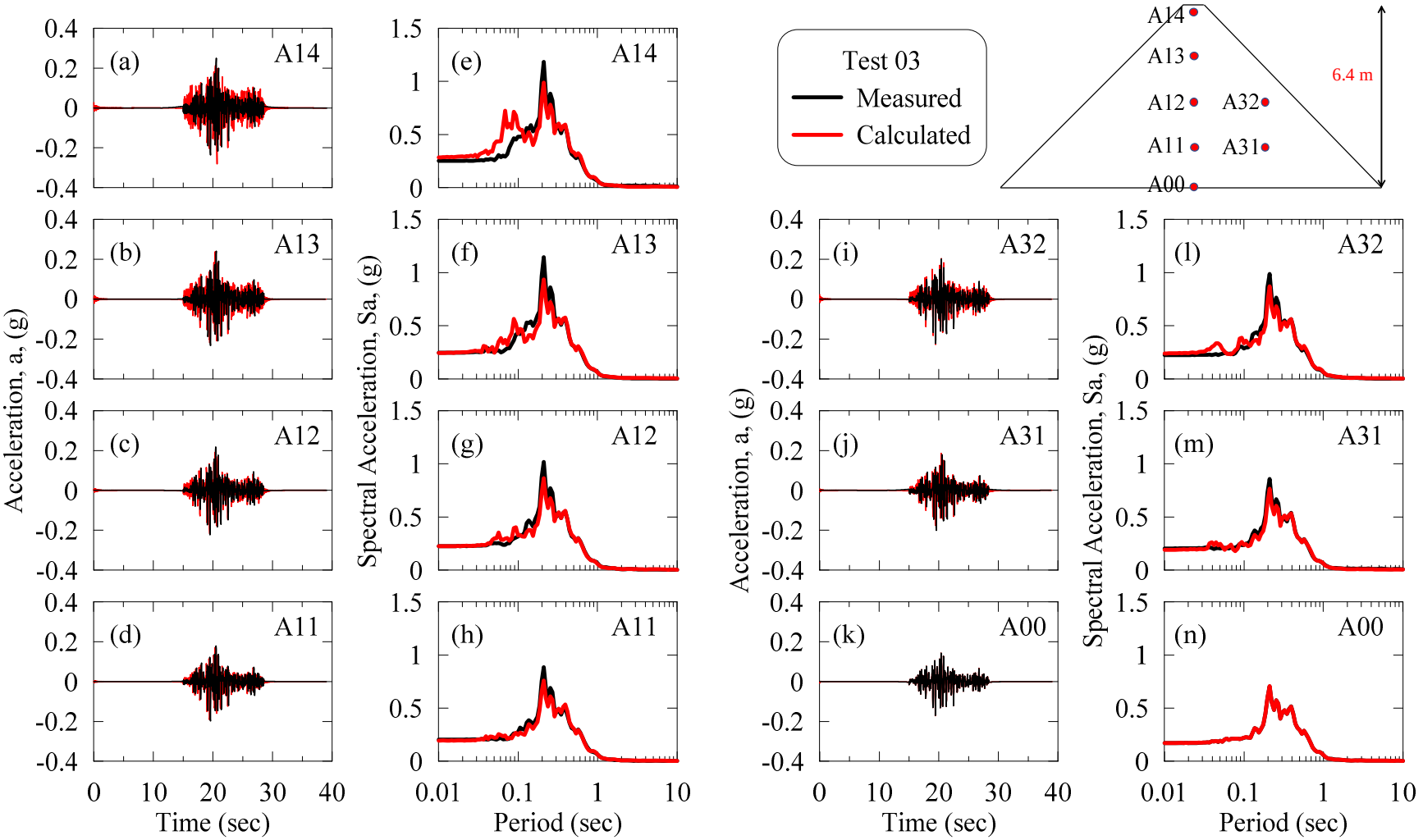

Figure A.16: Acceleration time histories and response spectra at different depths of dam during Test 03 for friction contact and the dynamic soil curves of Menq (2003) with Masing un/reloading.

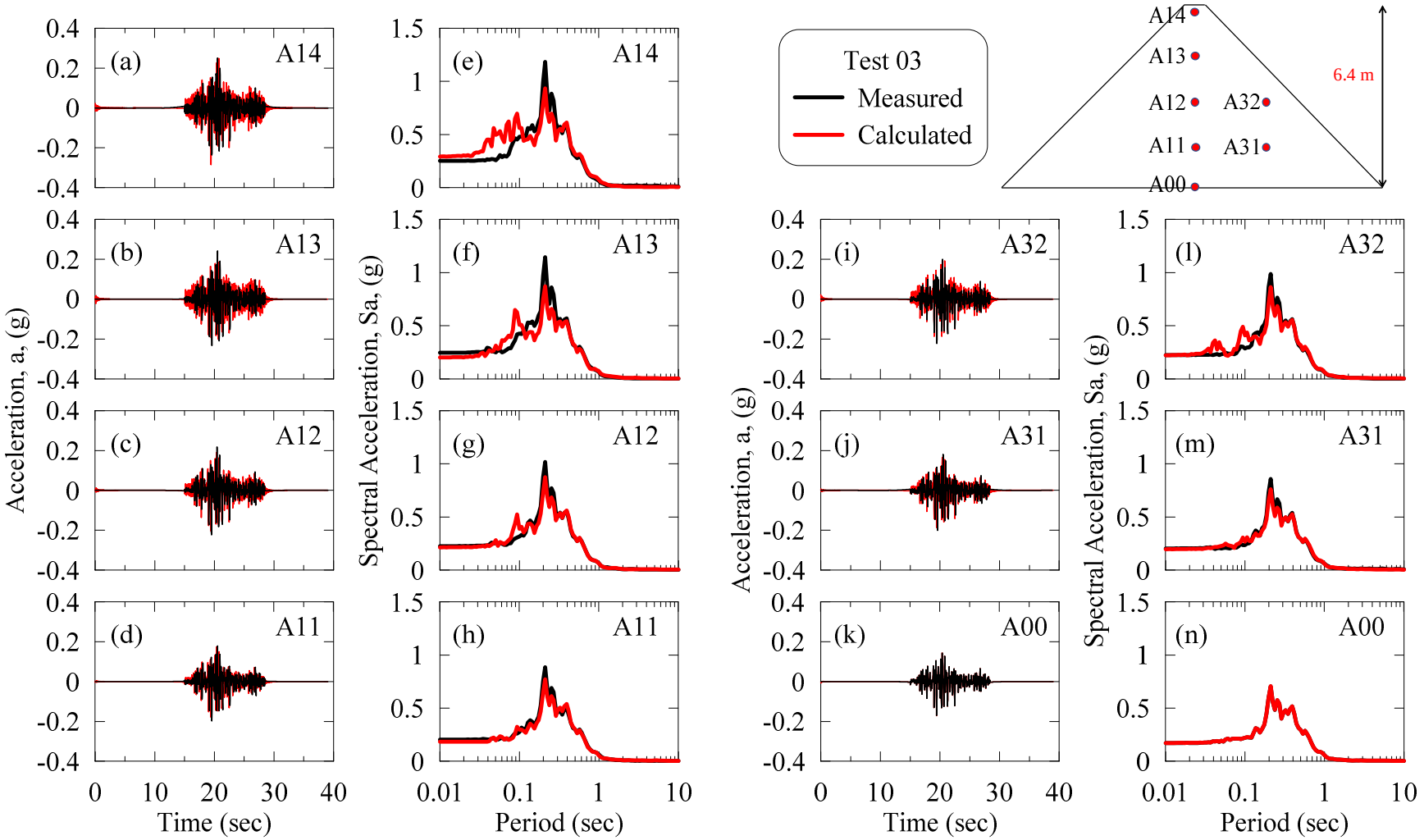

Figure A.17: Acceleration time histories and response spectra at different depths of dam during Test 03 for welded contact and the dynamic soil curves of Menq (2003) with Masing un/reloading.

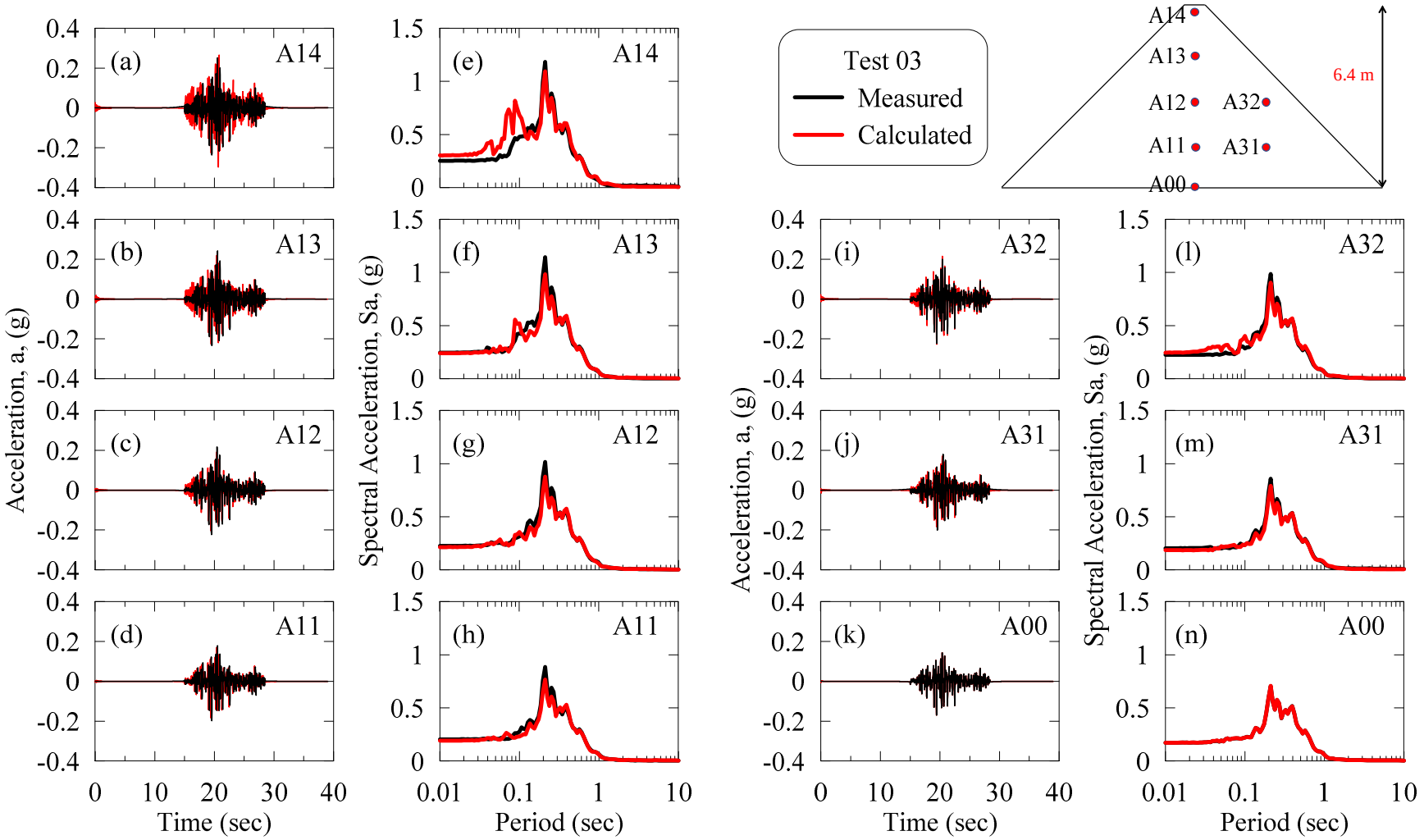

Figure A.18: Acceleration time histories and response spectra at different depths of dam during Test 03 for friction contact and the dynamic soil curves of Darendeli (2001) with non-Masing un/reloading.

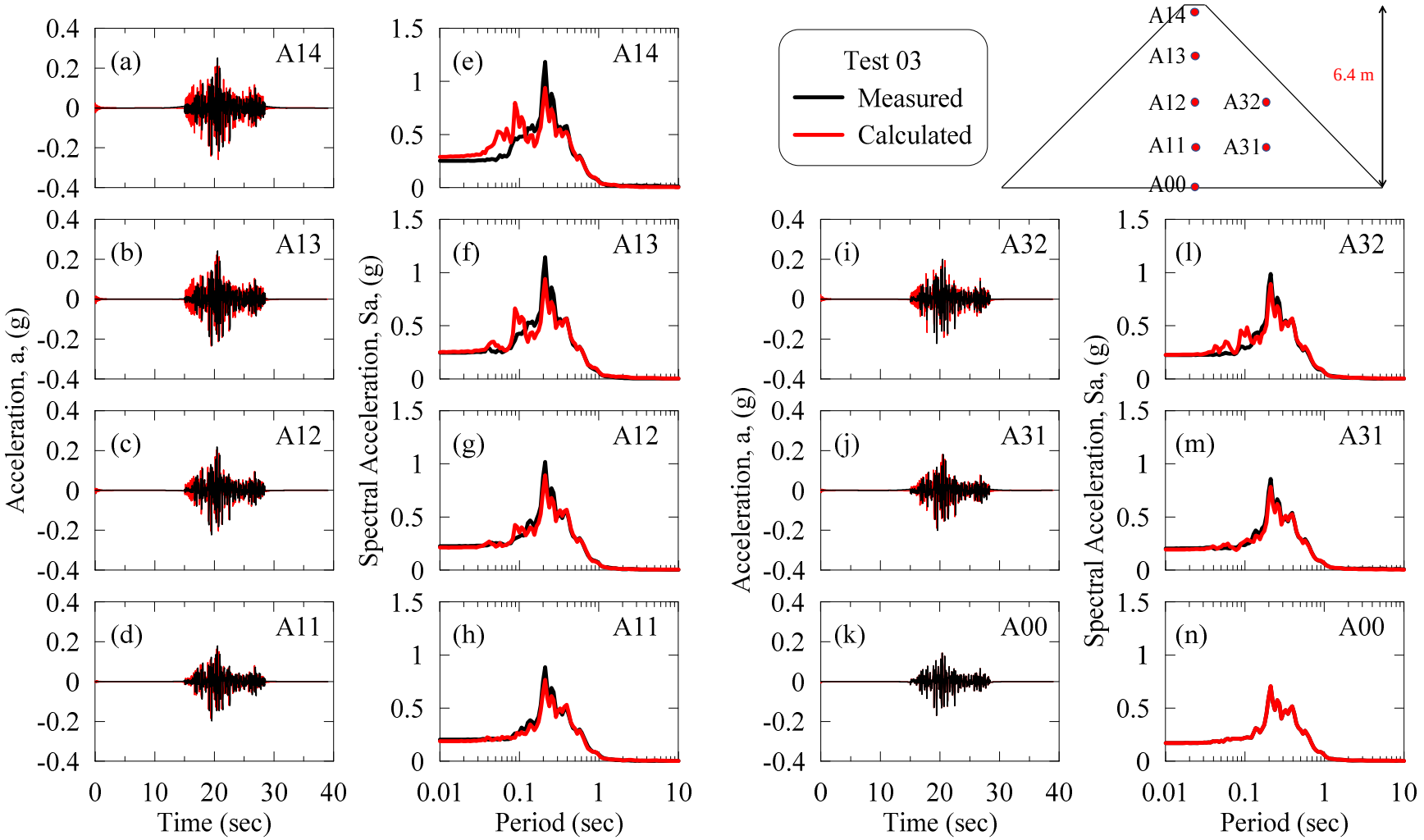

Figure A.19: Acceleration time histories and response spectra at different depths of dam during Test 03 for welded contact and the dynamic soil curves of Darendeli (2001) with non-Masing un/reloading.

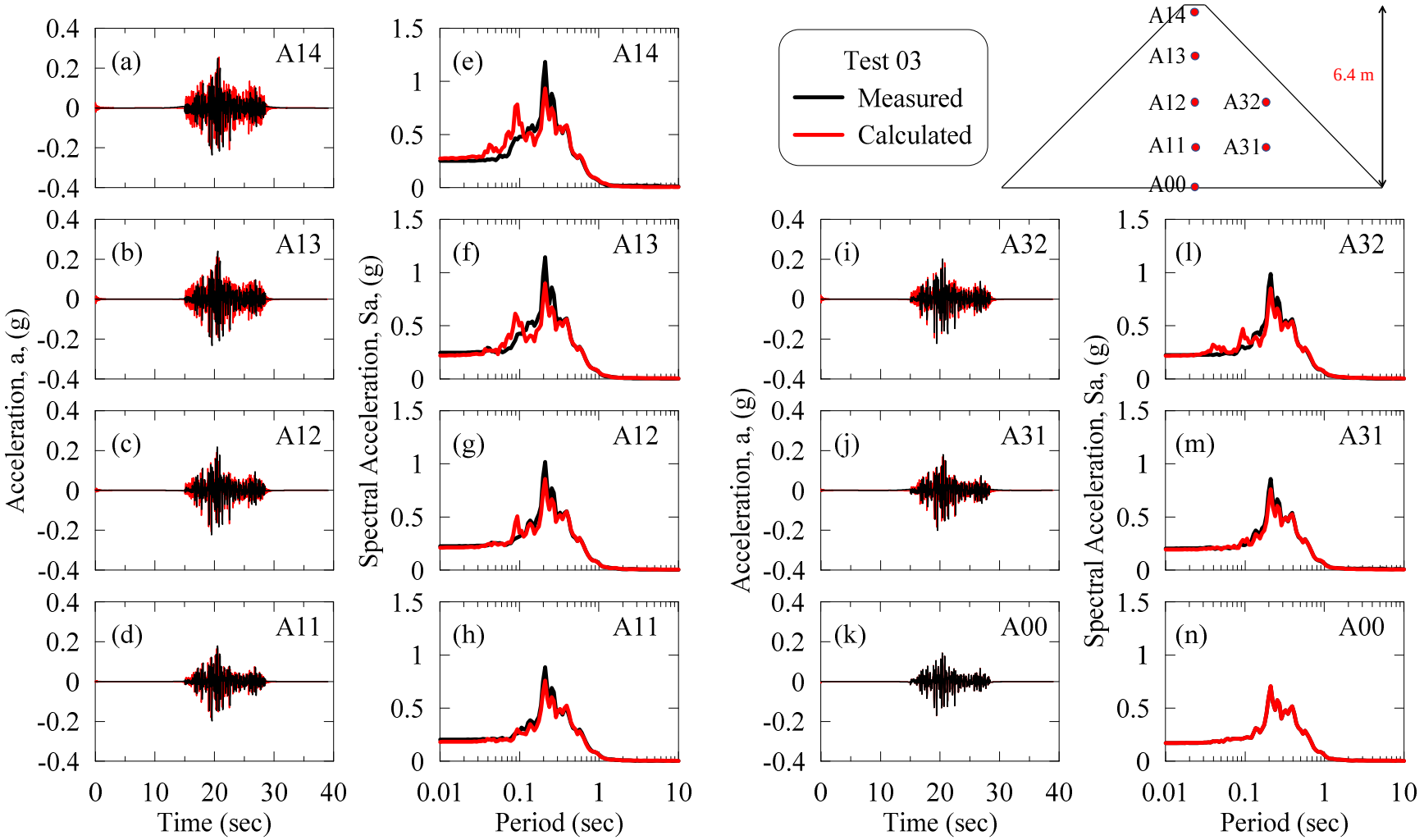

Figure A.20: Acceleration time histories and response spectra at different depths of dam during Test 03 for friction contact and the dynamic soil curves of Darendeli (2001) with Masing un/reloading.

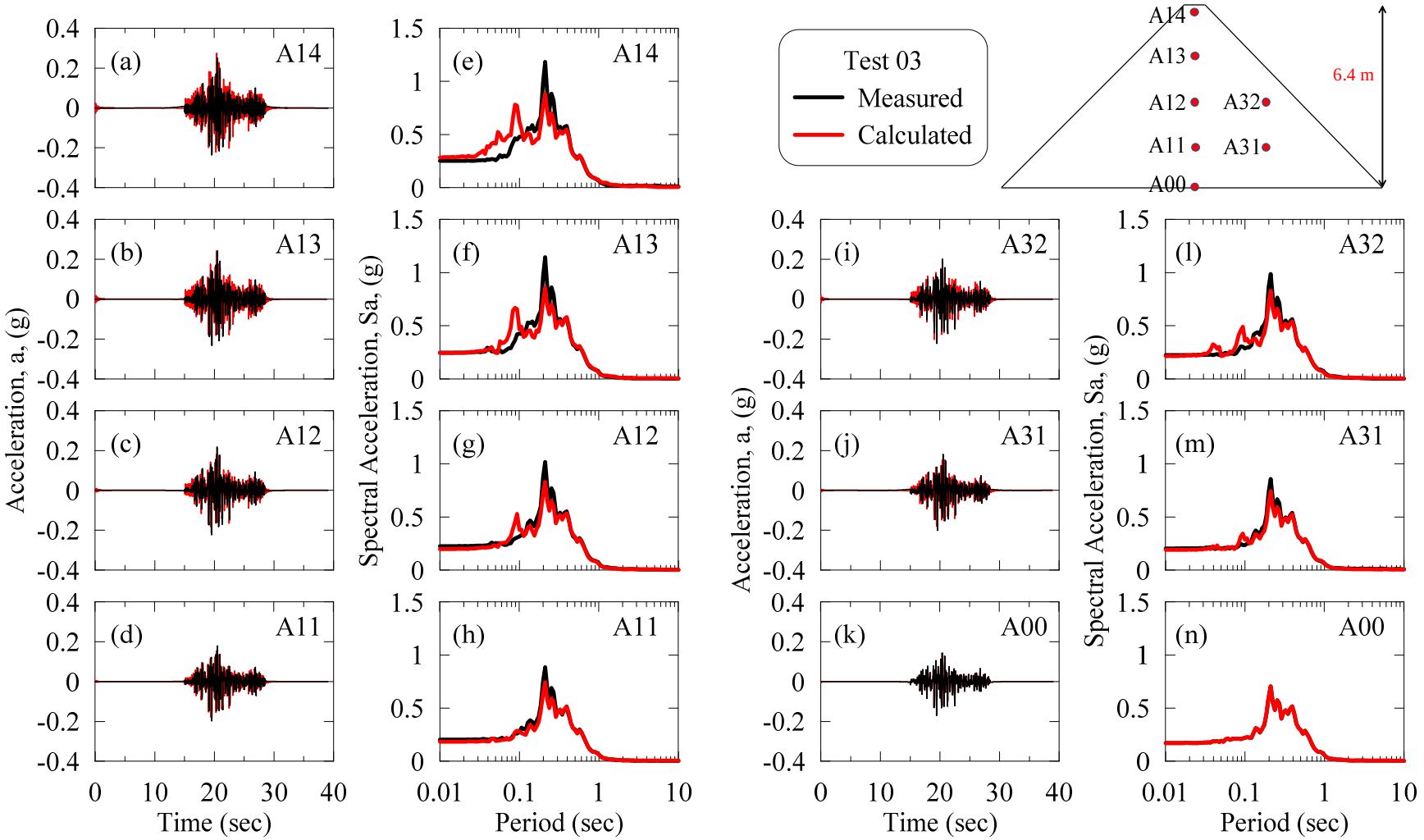

Figure A.21: Acceleration time histories and response spectra at different depths of dam during Test 03 for welded contact and the dynamic soil curves of Darendeli (2001) with Masing un/reloading.

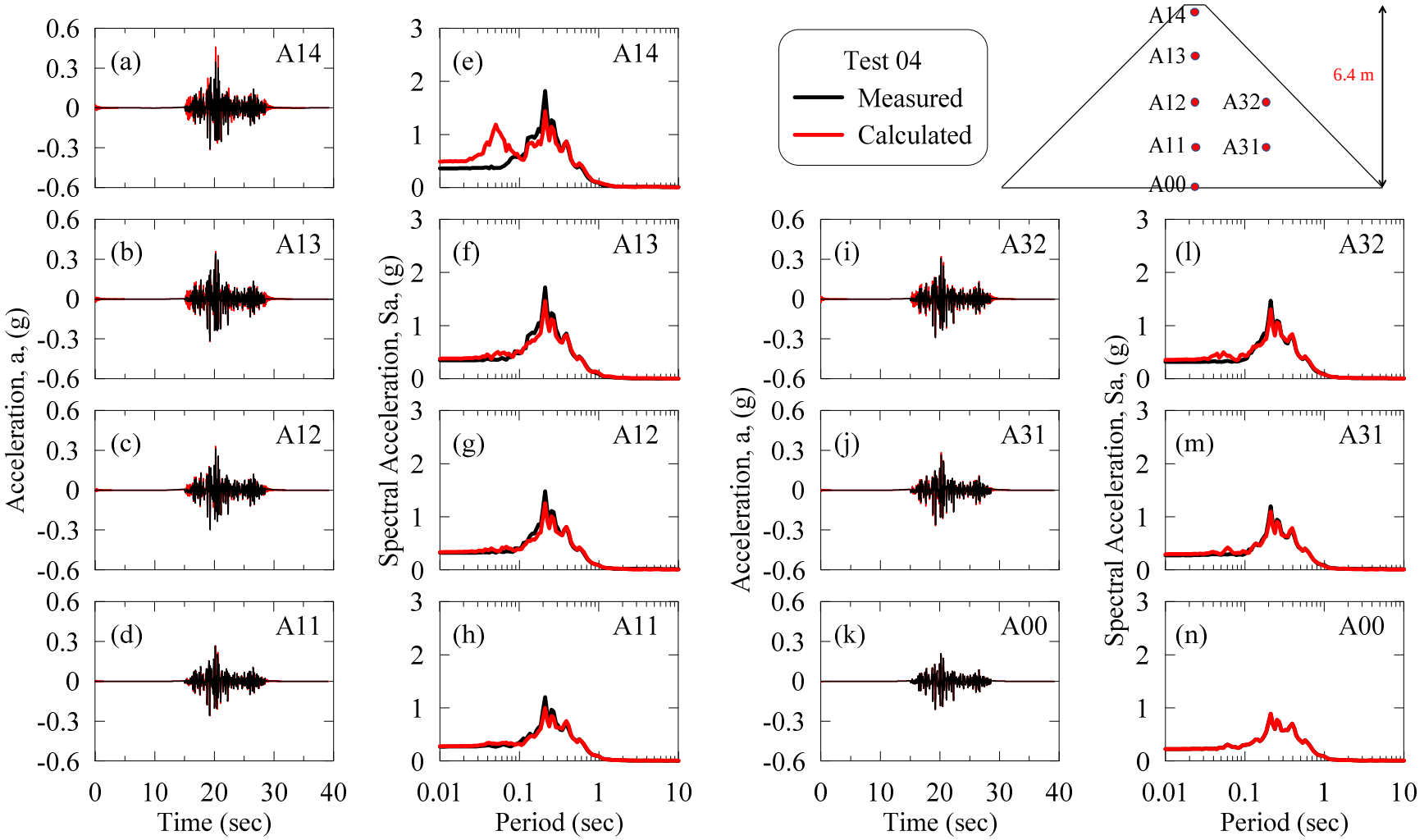

Figure A.22: Acceleration time histories and response spectra at different depths of dam during Test 04 for welded contact and the dynamic soil curves of Menq (2003) with non-Masing un/reloading.

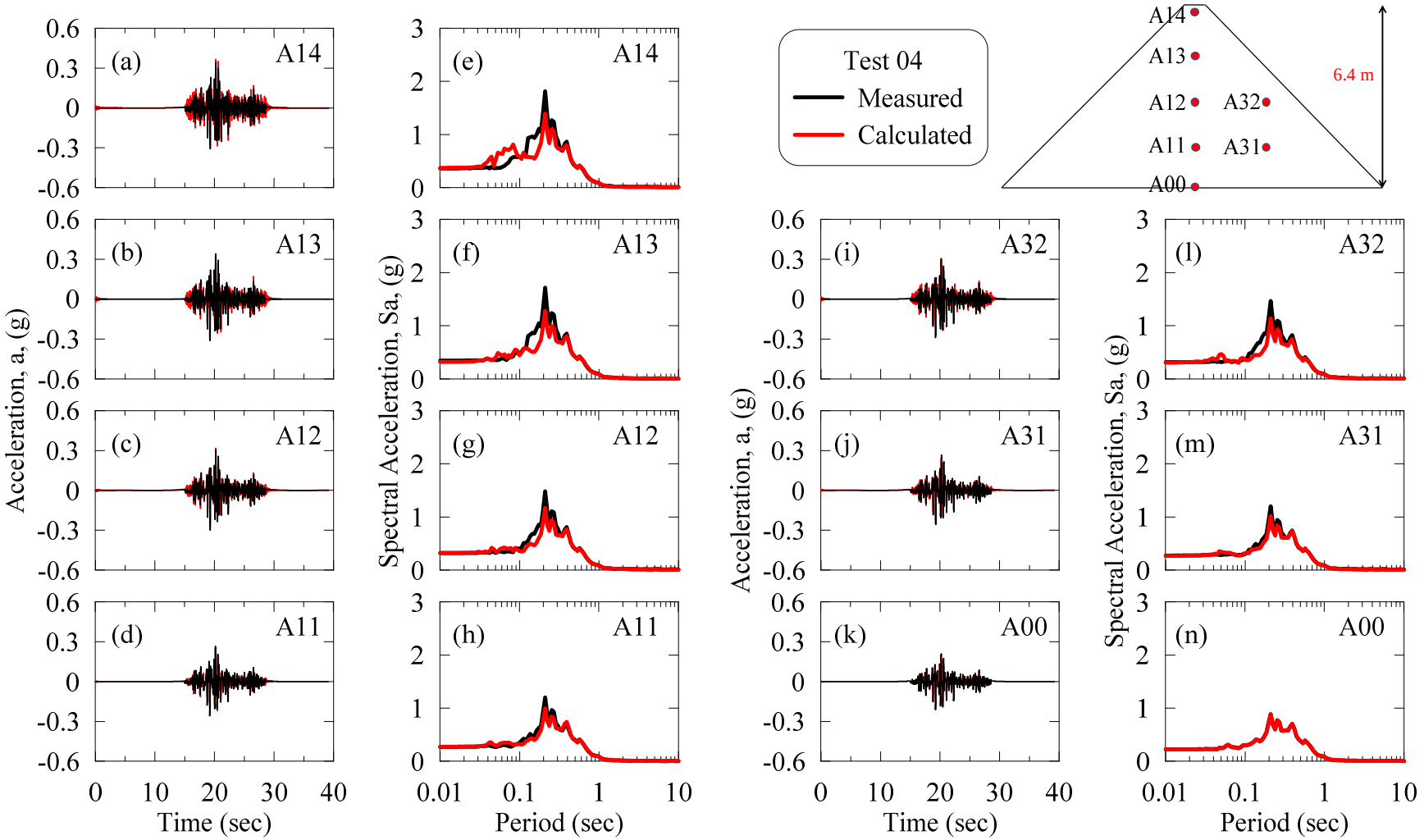

Figure A.23: Acceleration time histories and response spectra at different depths of dam during Test 04 for friction contact and the dynamic soil curves of Menq (2003) with Masing un/reloading.

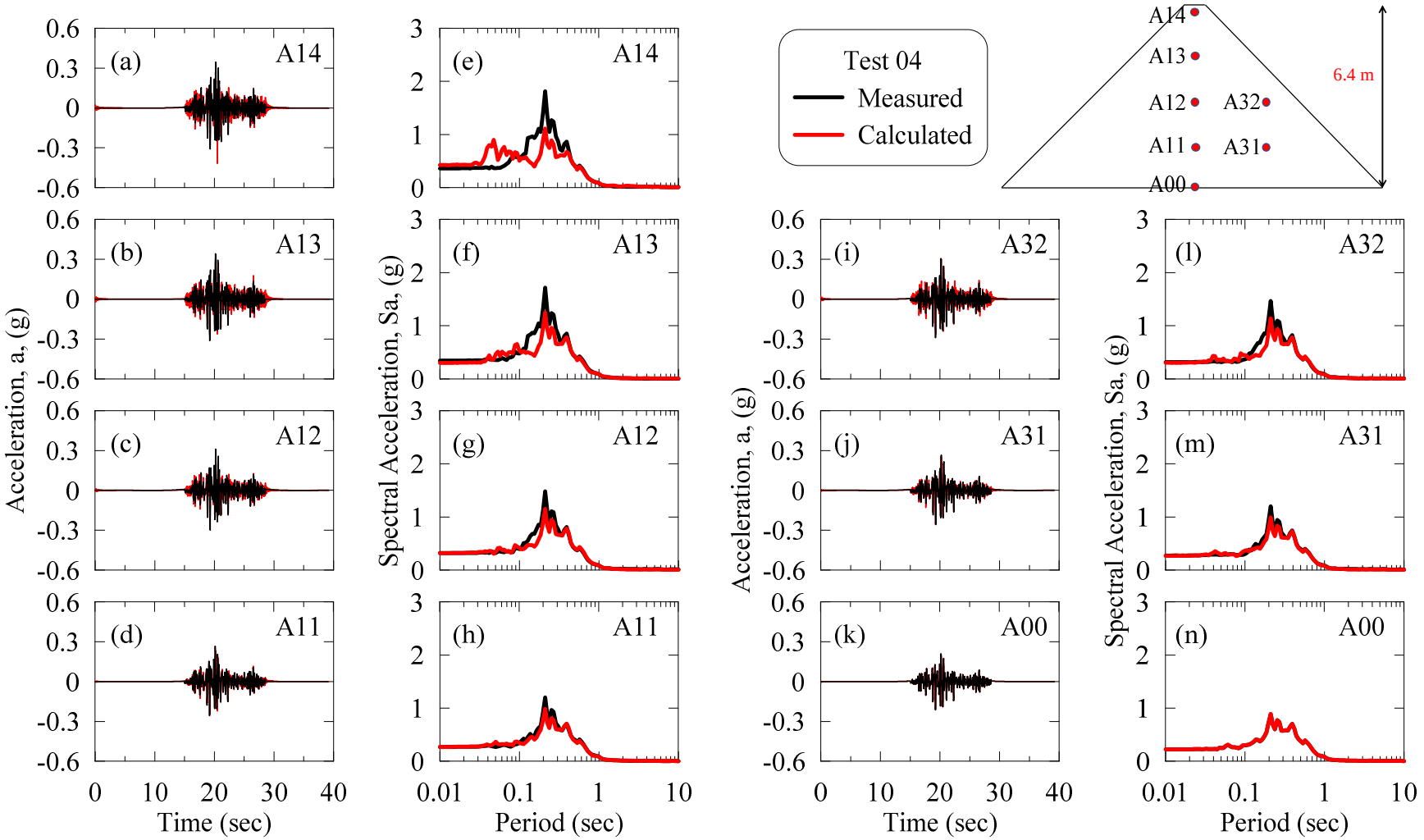

Figure A.24: Acceleration time histories and response spectra at different depths of dam during Test 04 for welded contact and the dynamic soil curves of Menq (2003) with Masing un/reloading.

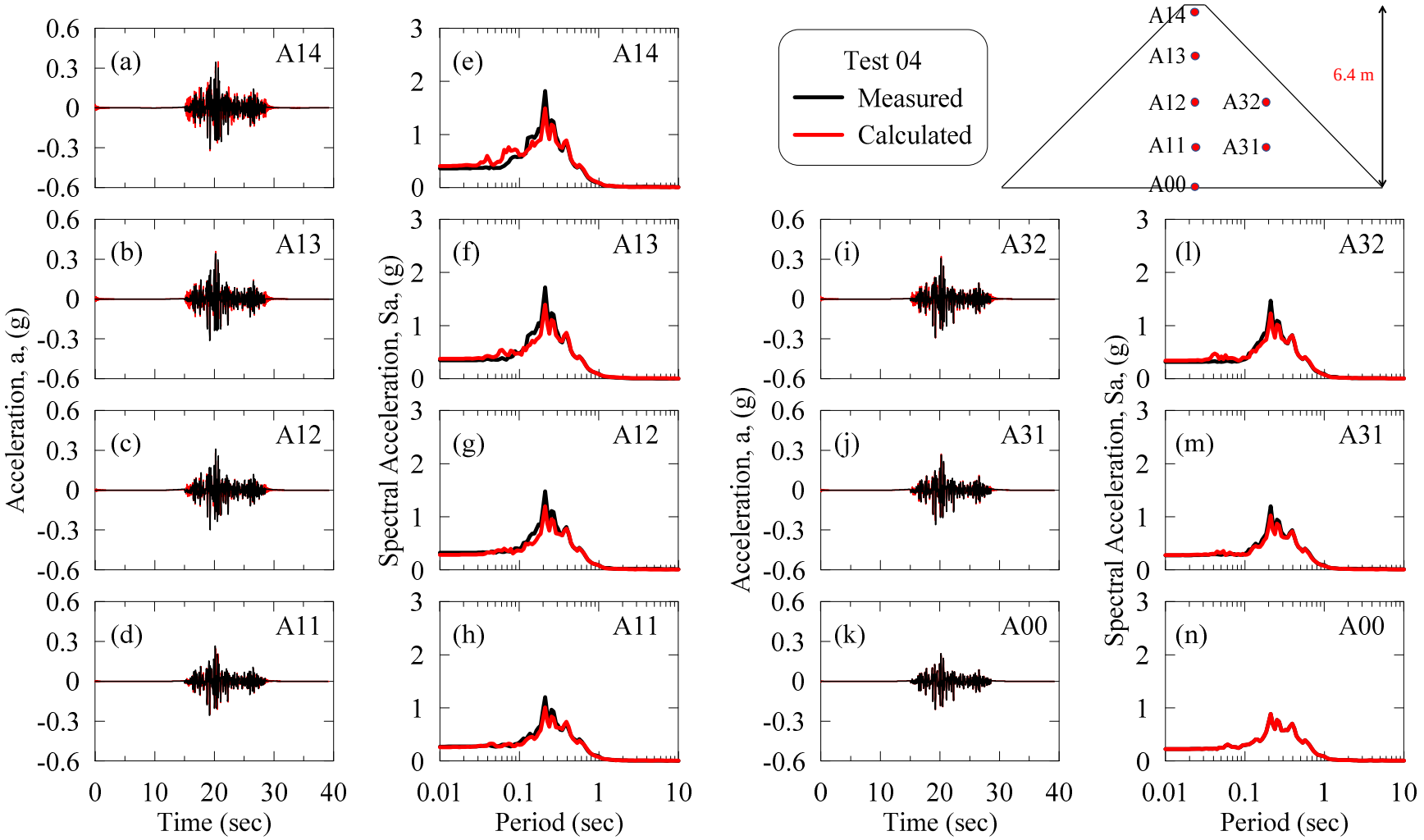

Figure A.25: Acceleration time histories and response spectra at different depths of dam during Test 04 for friction contact and the dynamic soil curves of Darendeli (2001) with non-Masing un/reloading.

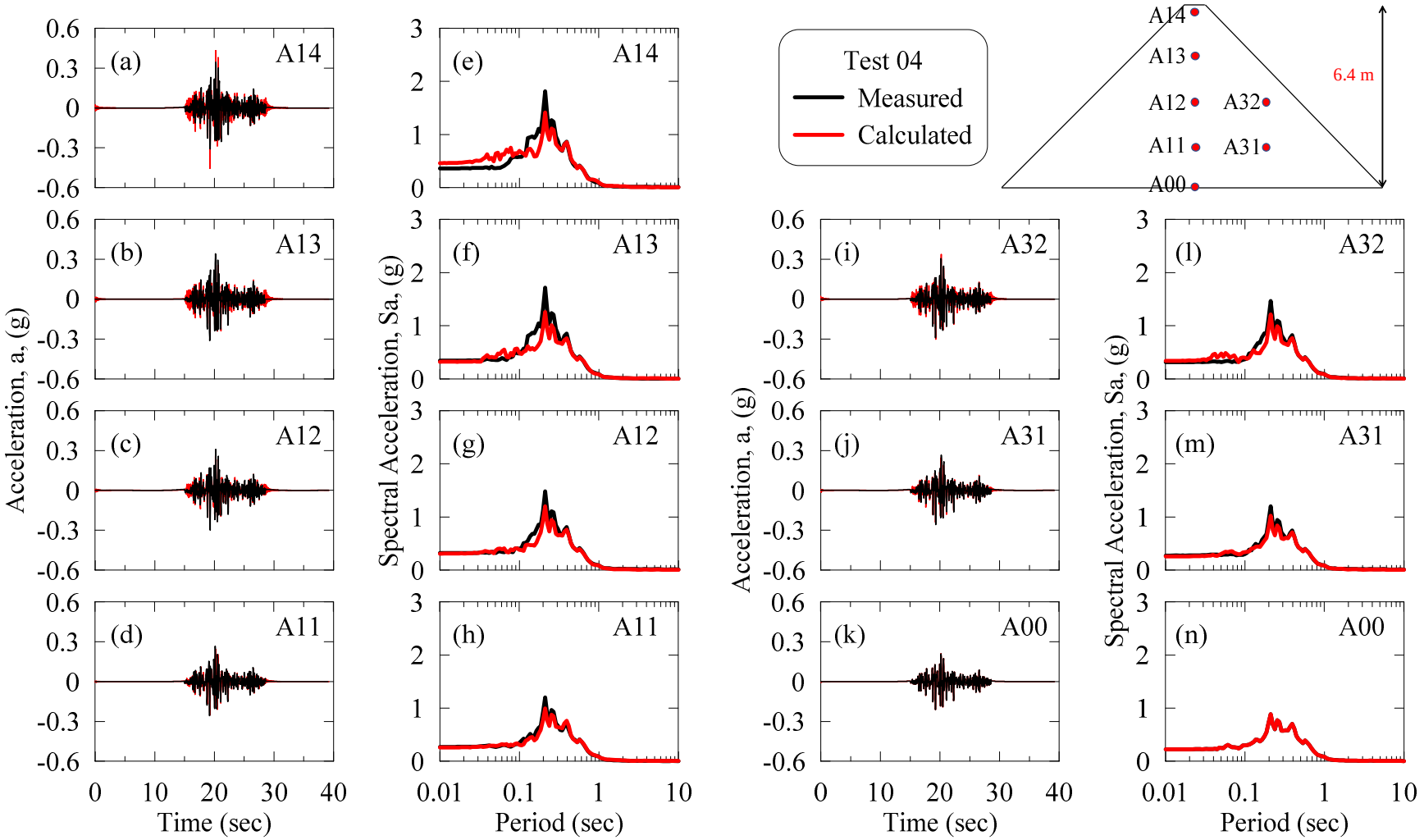

Figure A.26: Acceleration time histories and response spectra at different depths of dam during Test 04 for welded contact and the dynamic soil curves of Darendeli (2001) with non-Masing un/reloading.

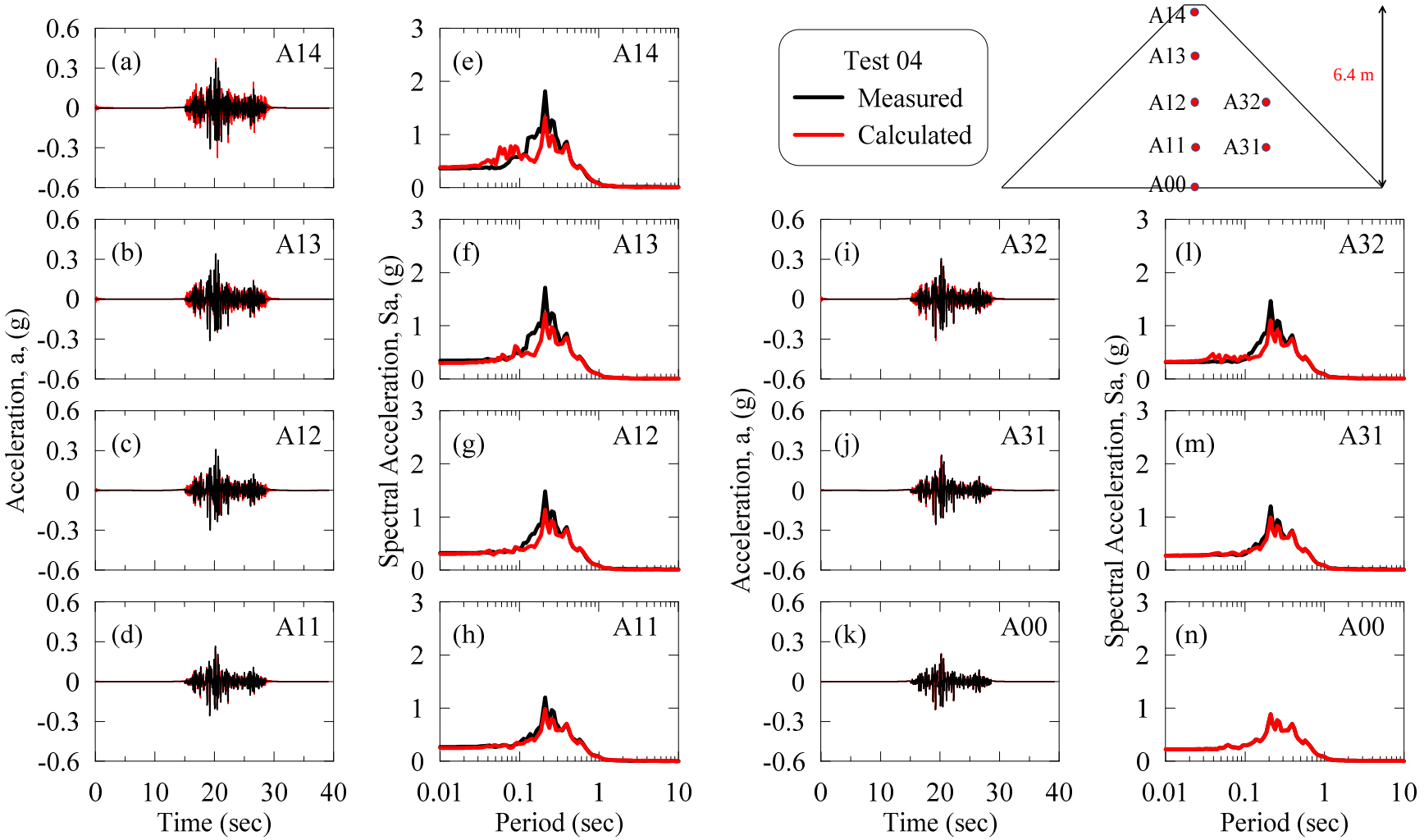

Figure A.27: Acceleration time histories and response spectra at different depths of dam during Test 04 for friction contact and the dynamic soil curves of Darendeli (2001) with Masing un/reloading.

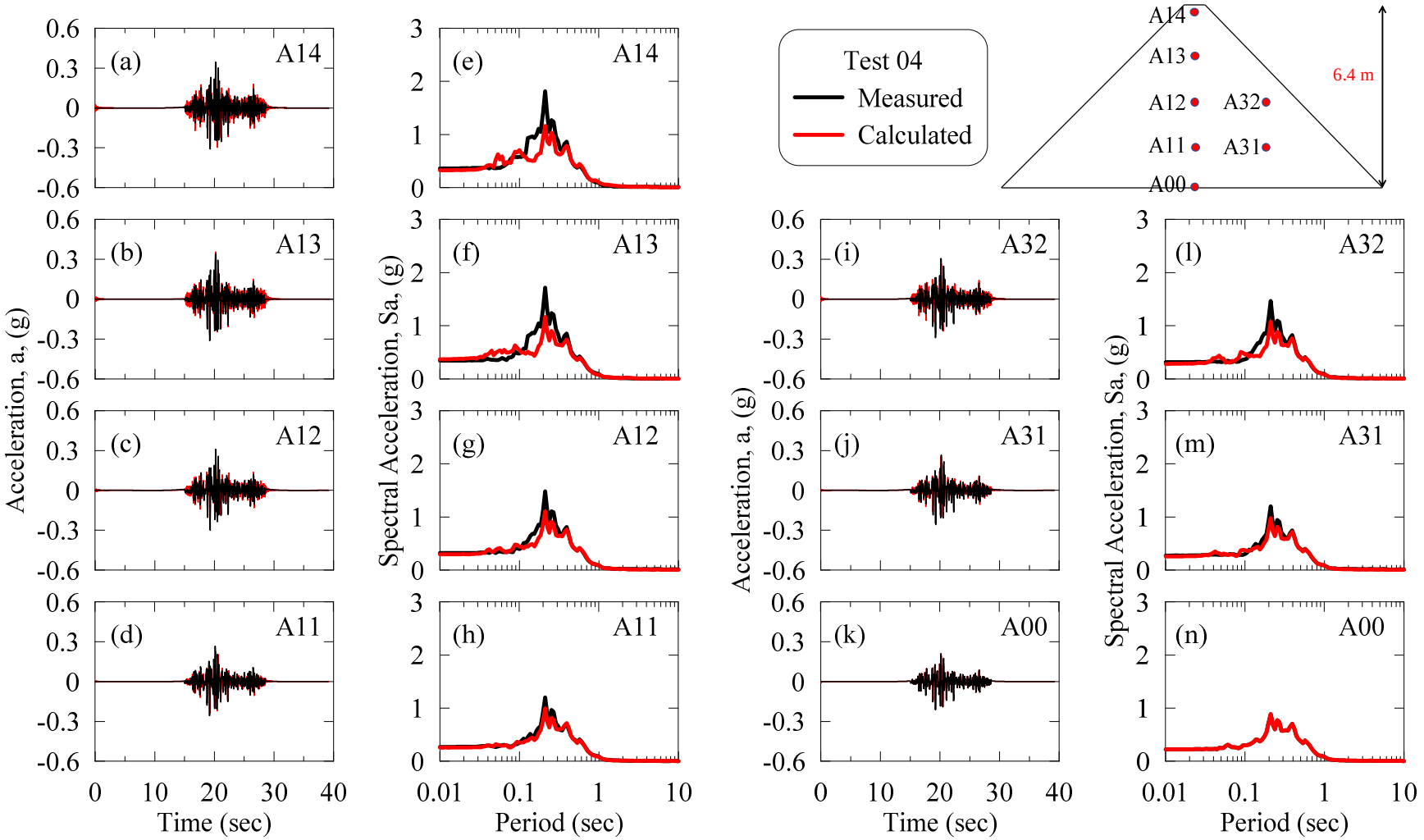

Figure A.28: Acceleration time histories and response spectra at different depths of dam during Test 04 for welded contact and the dynamic soil curves of Darendeli (2001) with Masing un/reloading.

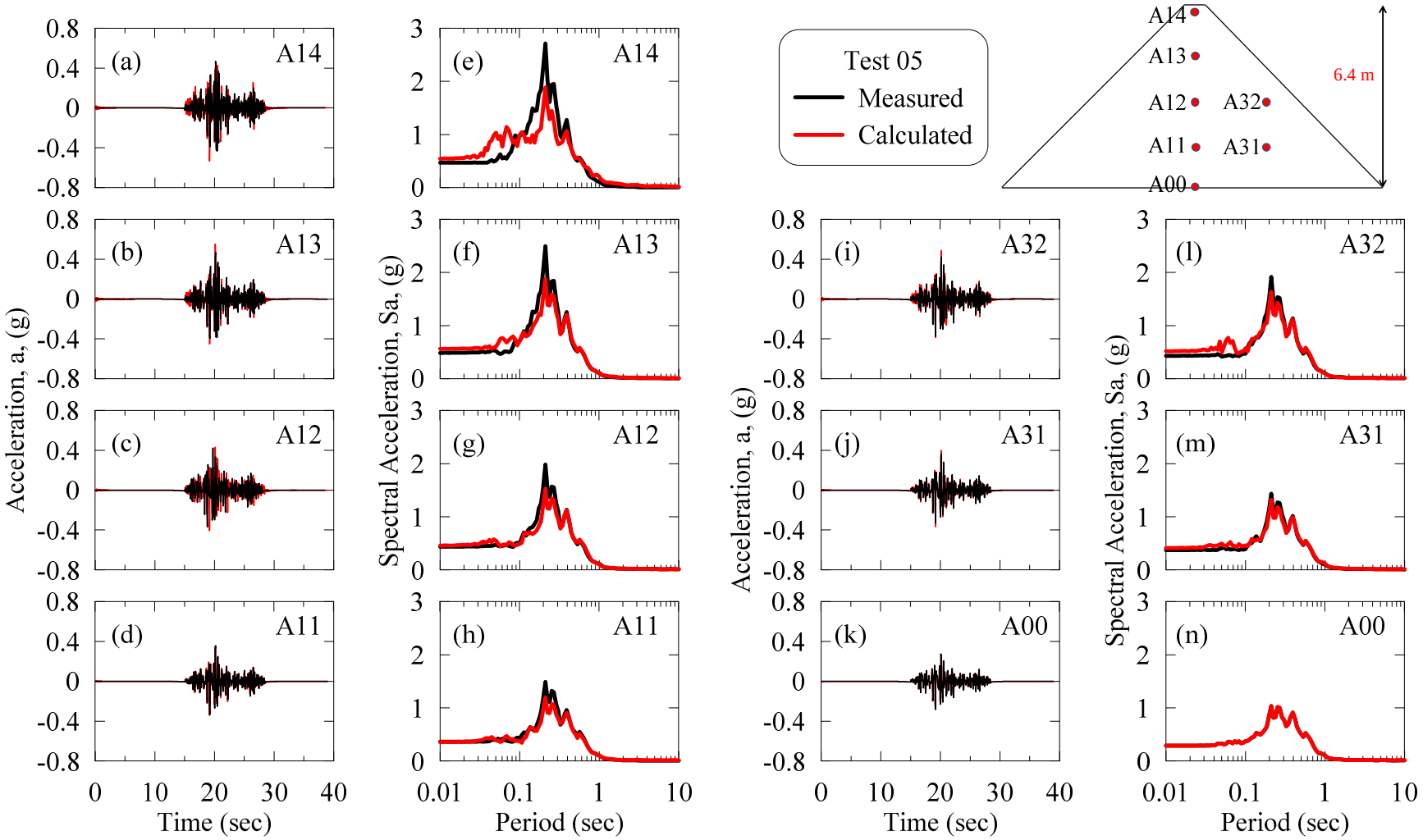

Figure A.29: Acceleration time histories and response spectra at different depths of dam during Test 05 for welded contact and the dynamic soil curves of Menq (2003) with non-Masing un/reloading.

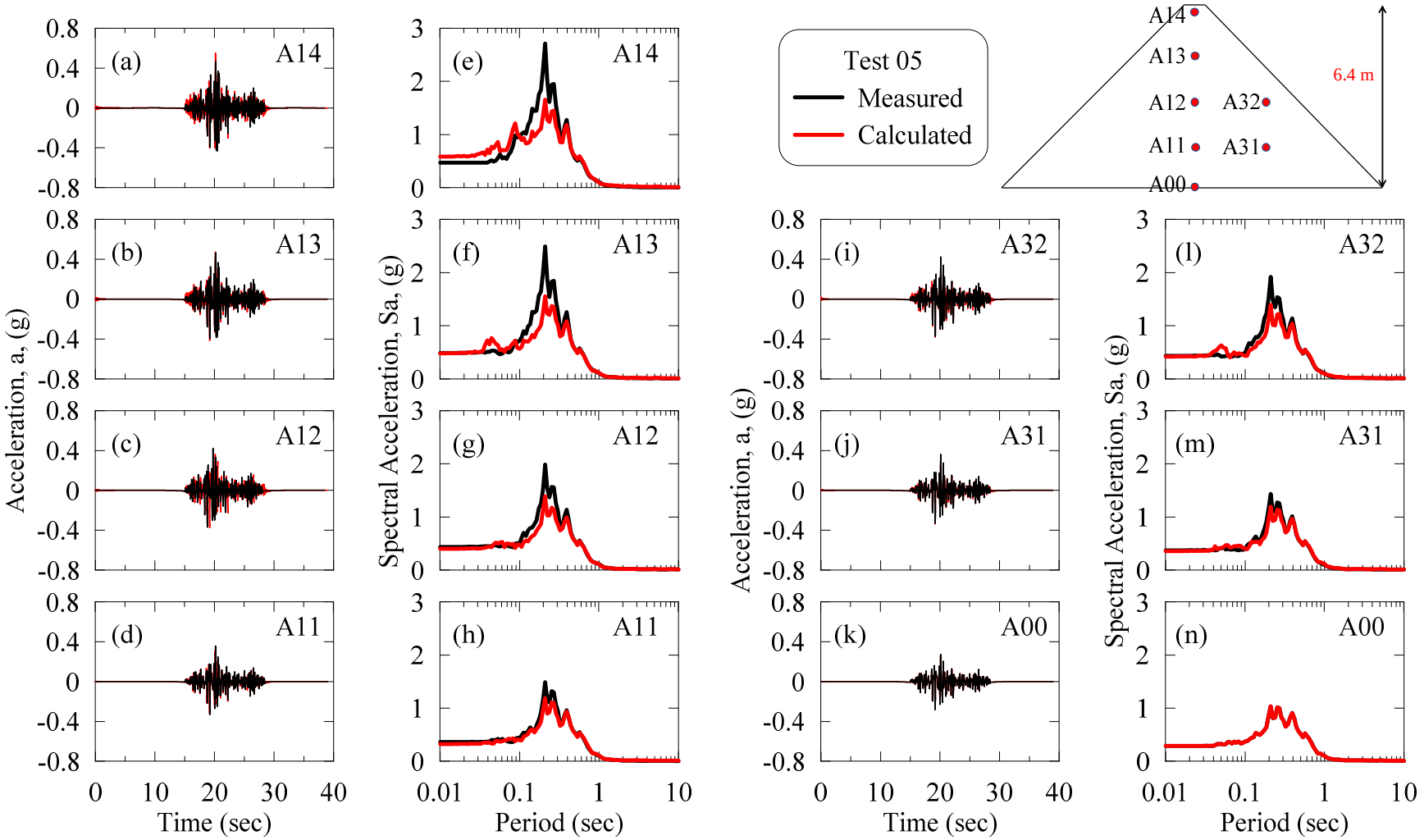

Figure A.30: Acceleration time histories and response spectra at different depths of dam during Test 05 for friction contact and the dynamic soil curves of Menq (2003) with Masing un/reloading.

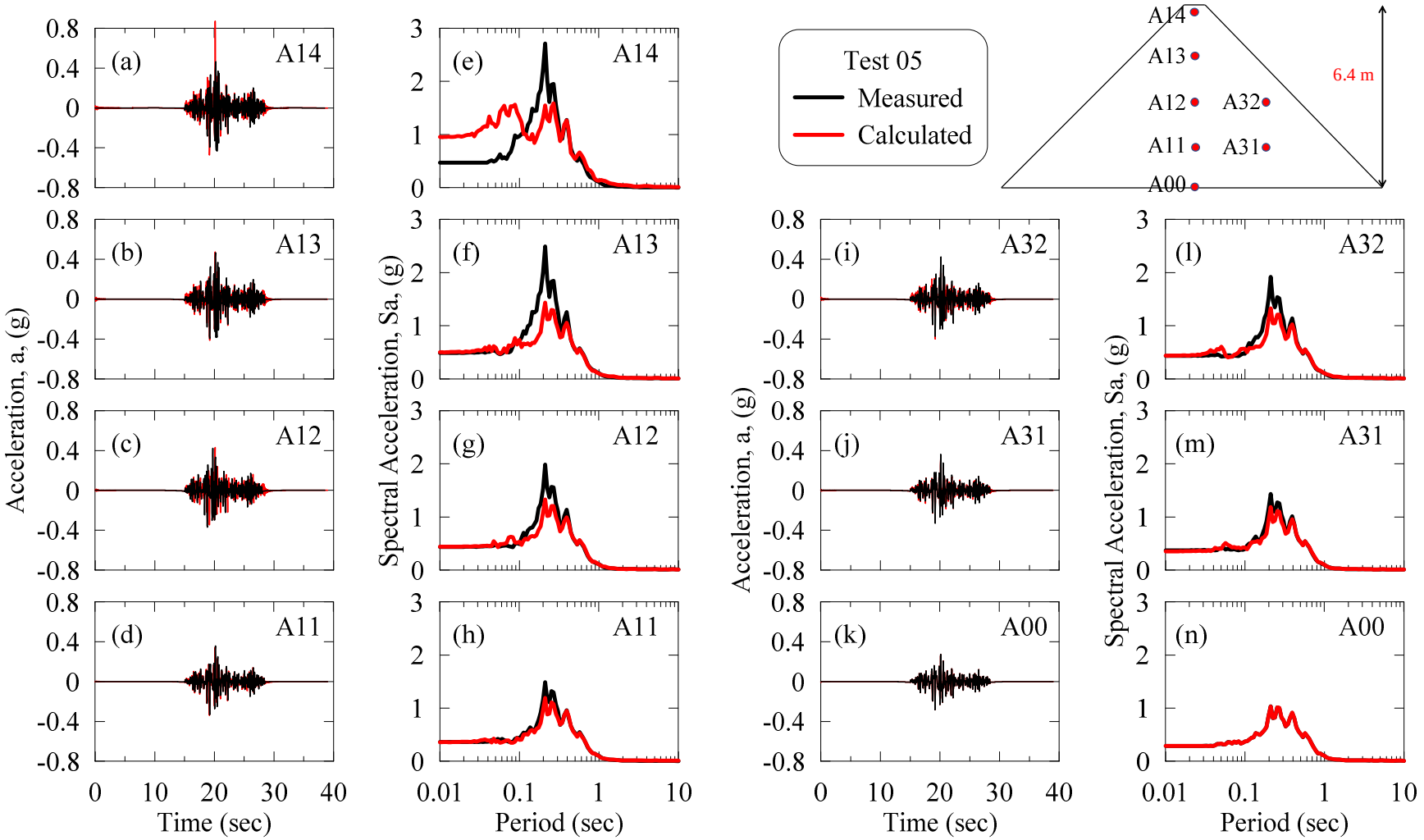

Figure A.31: Acceleration time histories and response spectra at different depths of dam during Test 05 for welded contact and the dynamic soil curves of Menq (2003) with Masing un/reloading.

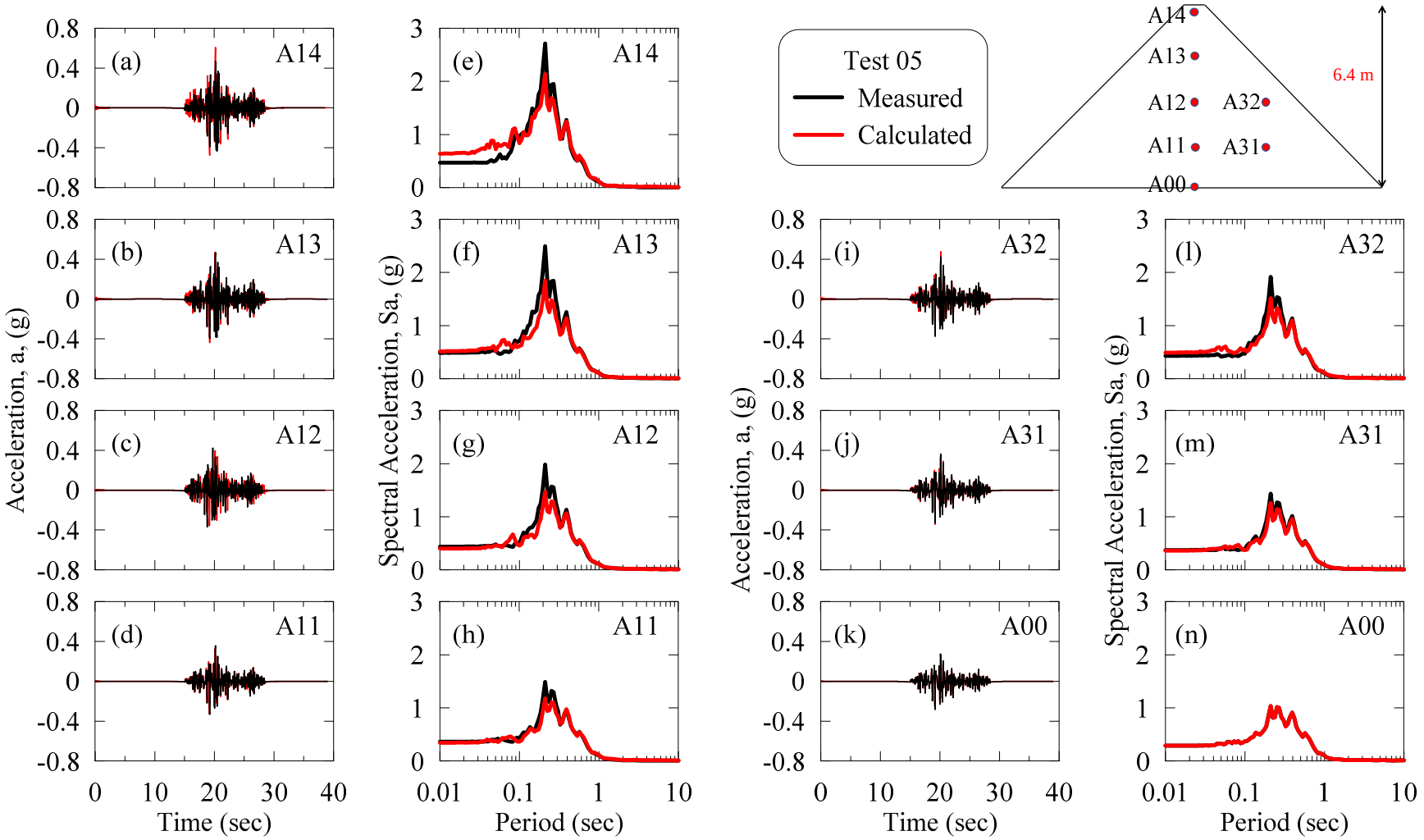

Figure A.32: Acceleration time histories and response spectra at different depths of dam during Test 05 for friction contact and the dynamic soil curves of Darendeli (2001) with non-Masing un/reloading.

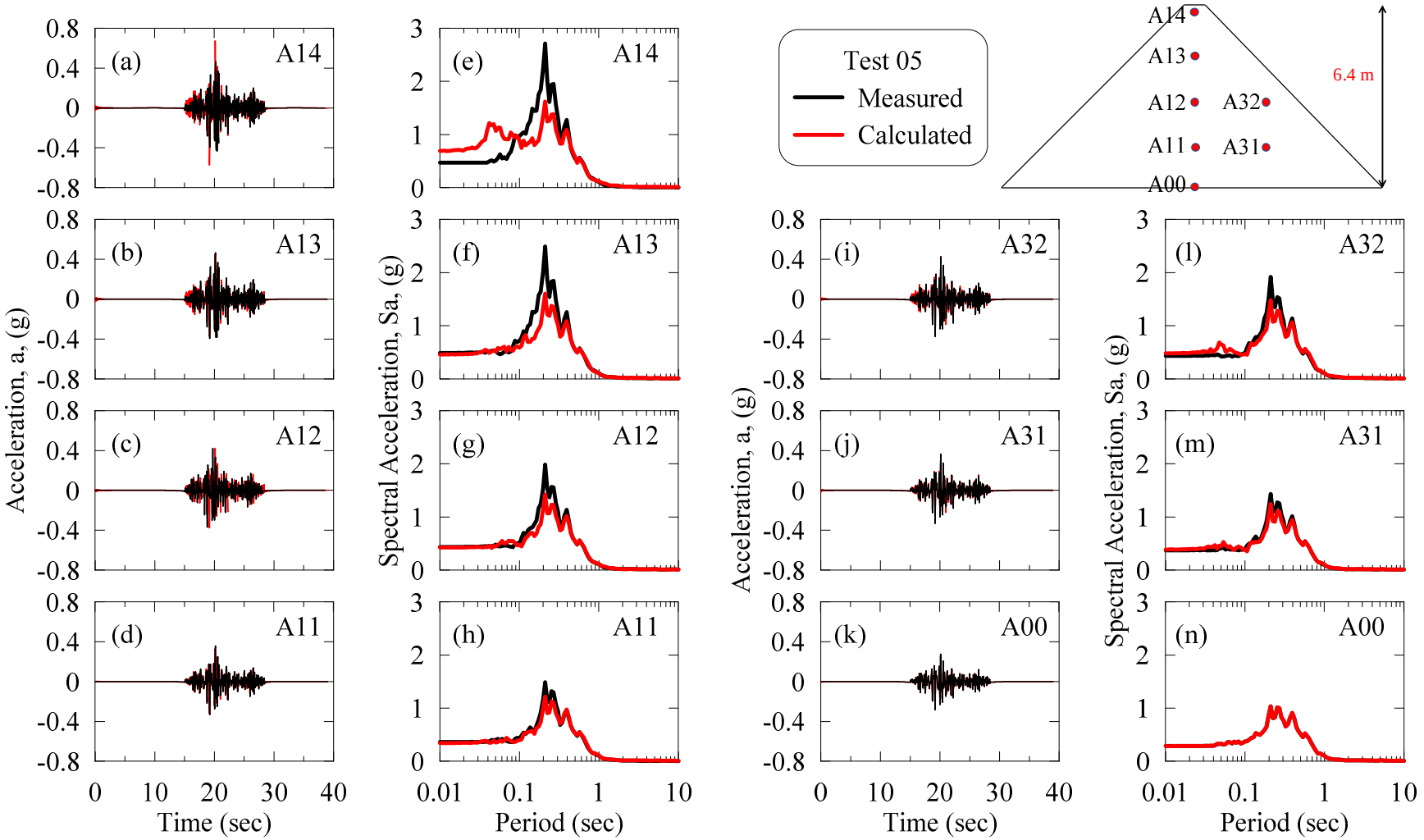

Figure A.33: Acceleration time histories and response spectra at different depths of dam during Test 05 for welded contact and the dynamic soil curves of Darendeli (2001) with non-Masing un/reloading.

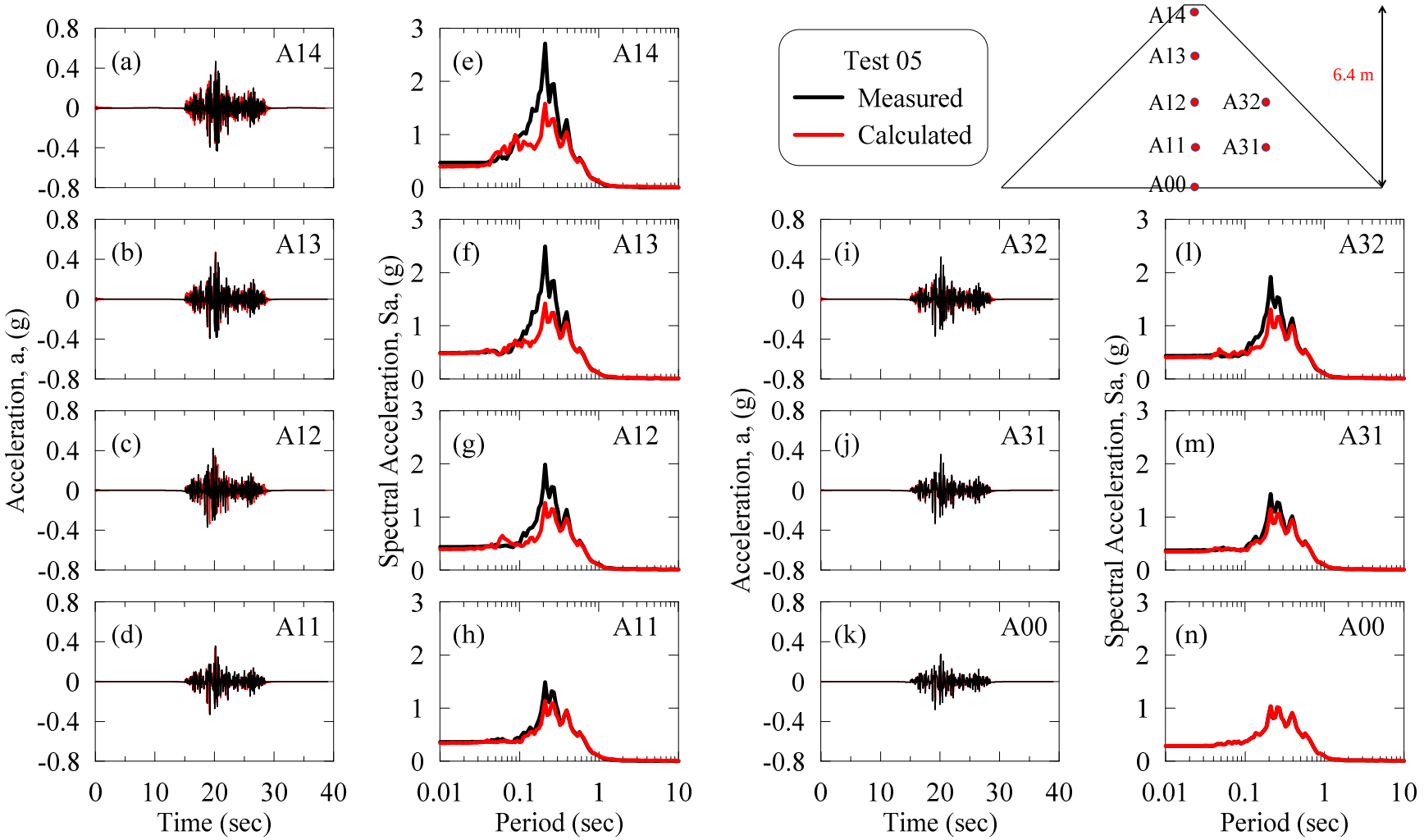

Figure A.34: Acceleration time histories and response spectra at different depths of dam during Test 05 for friction contact and the dynamic soil curves of Darendeli (2001) with Masing un/reloading.

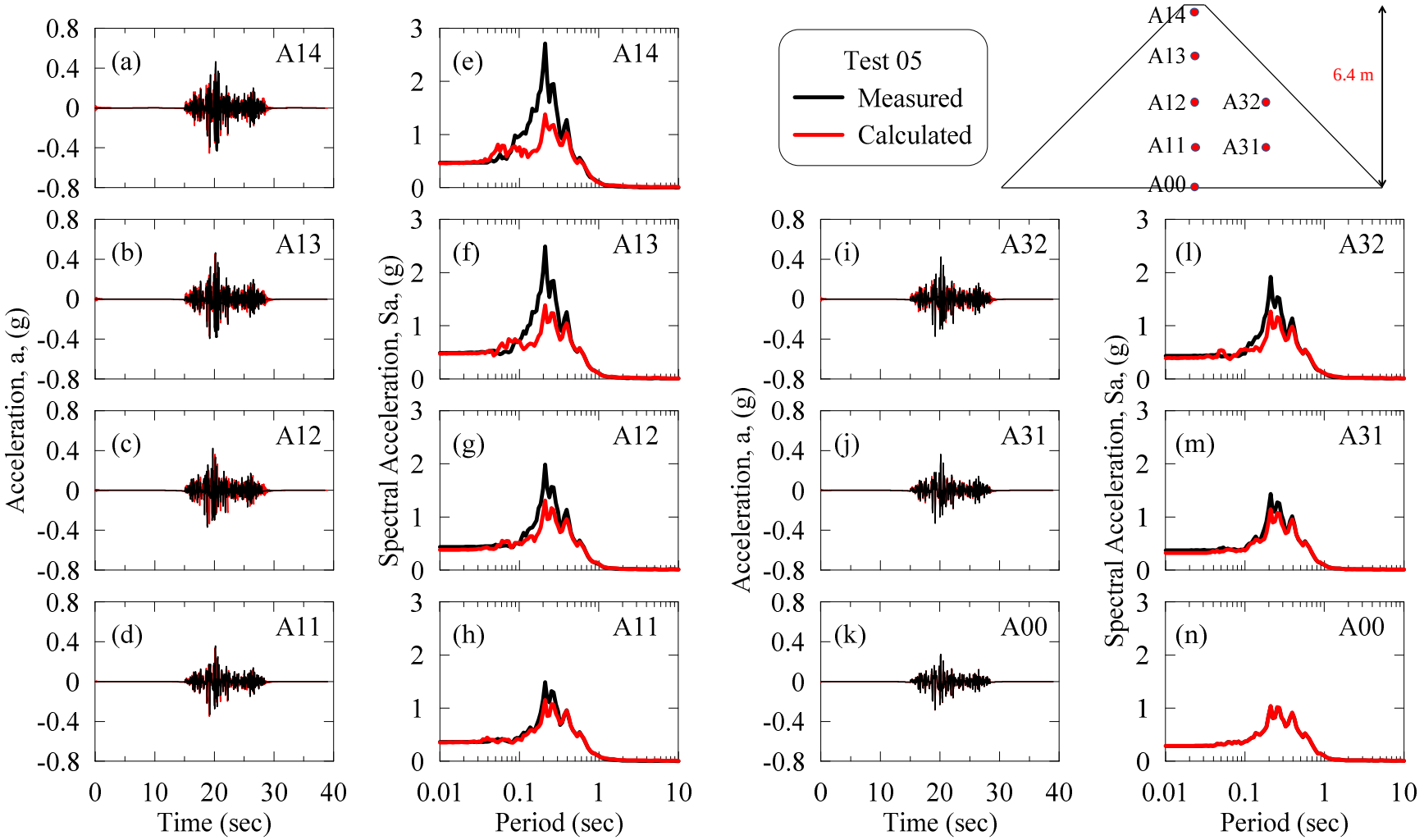

Figure A.35: Acceleration time histories and response spectra at different depths of dam during Test 05 for welded contact and the dynamic soil curves of Darendeli (2001) with Masing un/reloading.

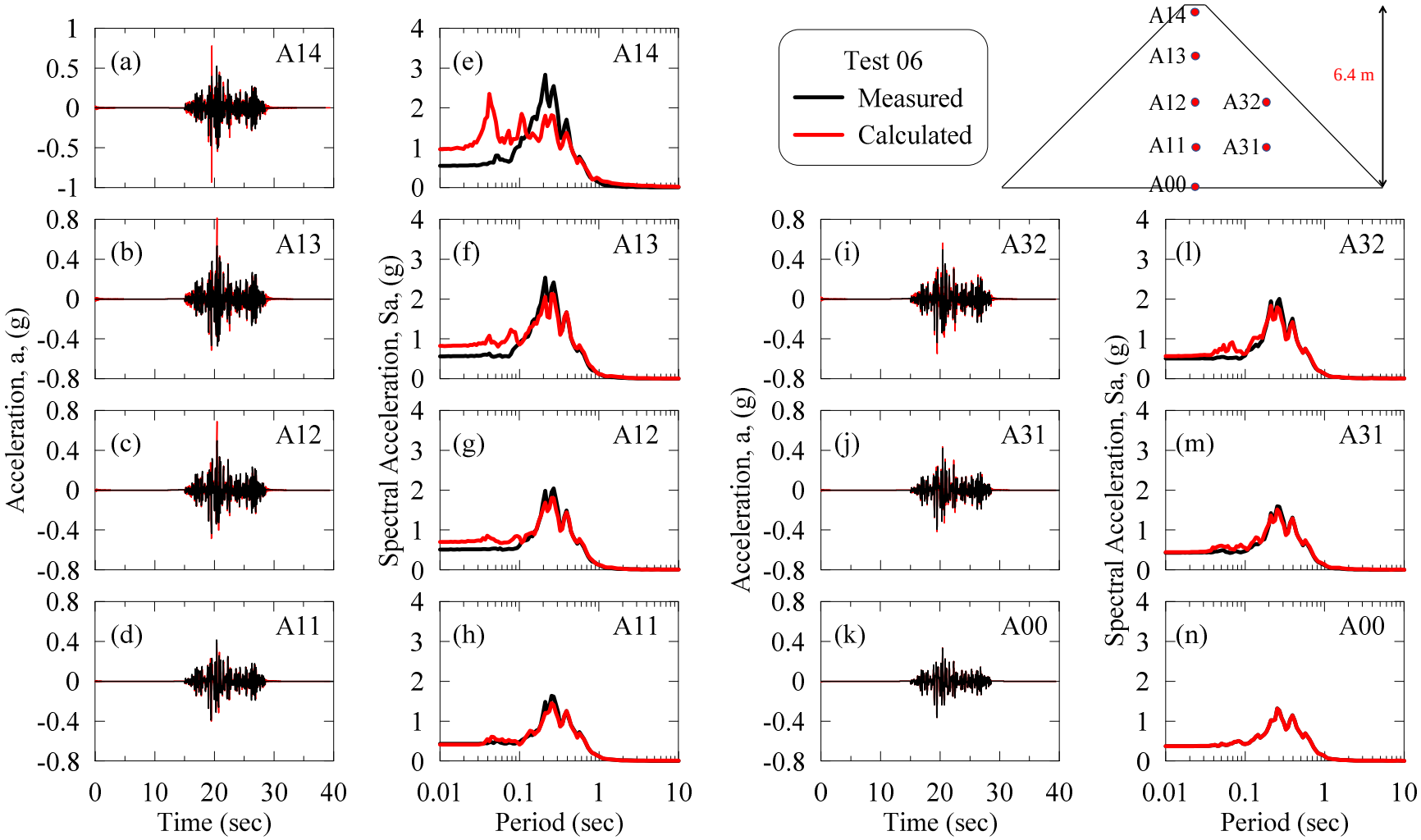

Figure A.36: Acceleration time histories and response spectra at different depths of dam during Test 06 for welded contact and the dynamic soil curves of Menq (2003) with non-Masing un/reloading.

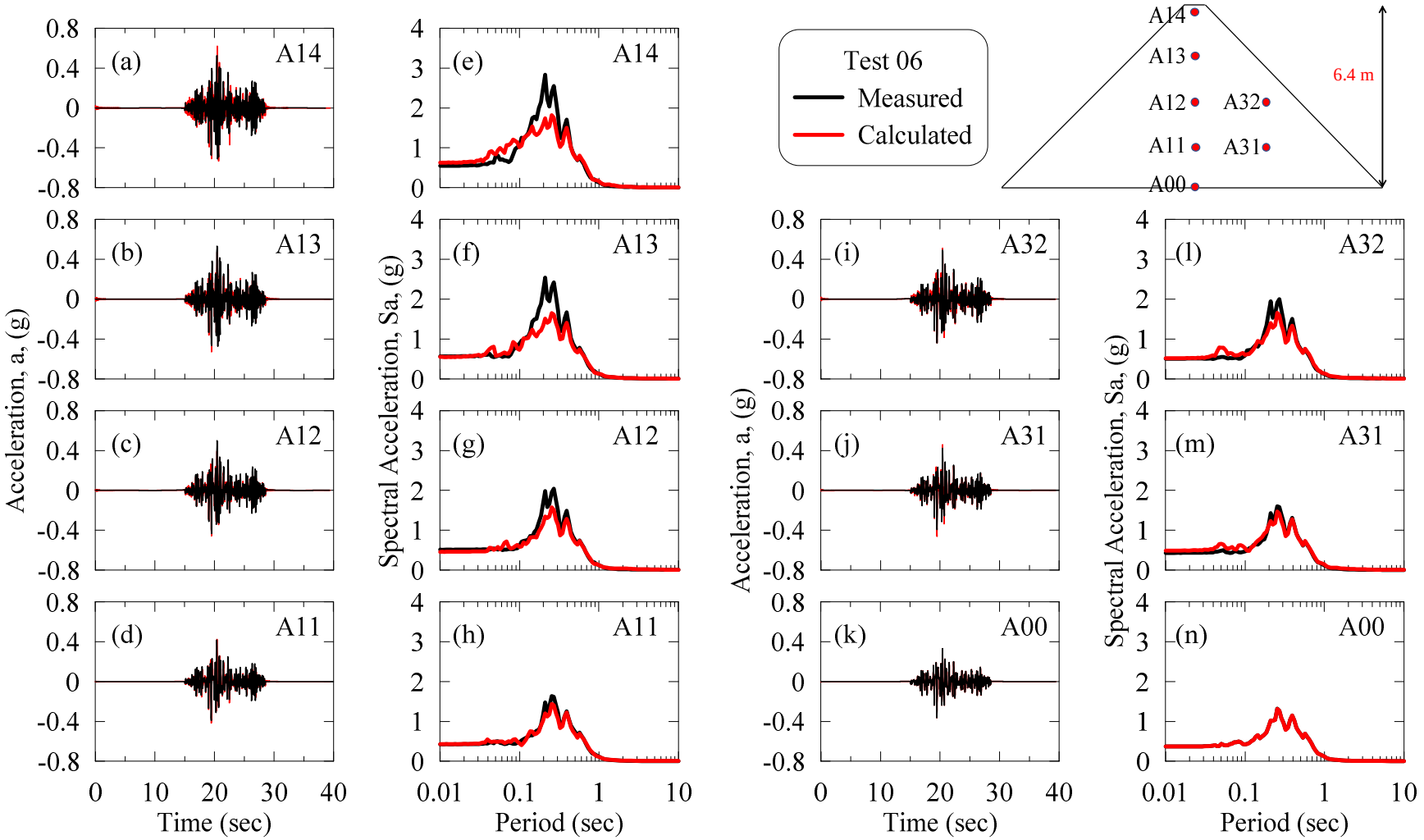

Figure A.37: Acceleration time histories and response spectra at different depths of dam during Test 06 for friction contact and the dynamic soil curves of Menq (2003) with Masing un/reloading.

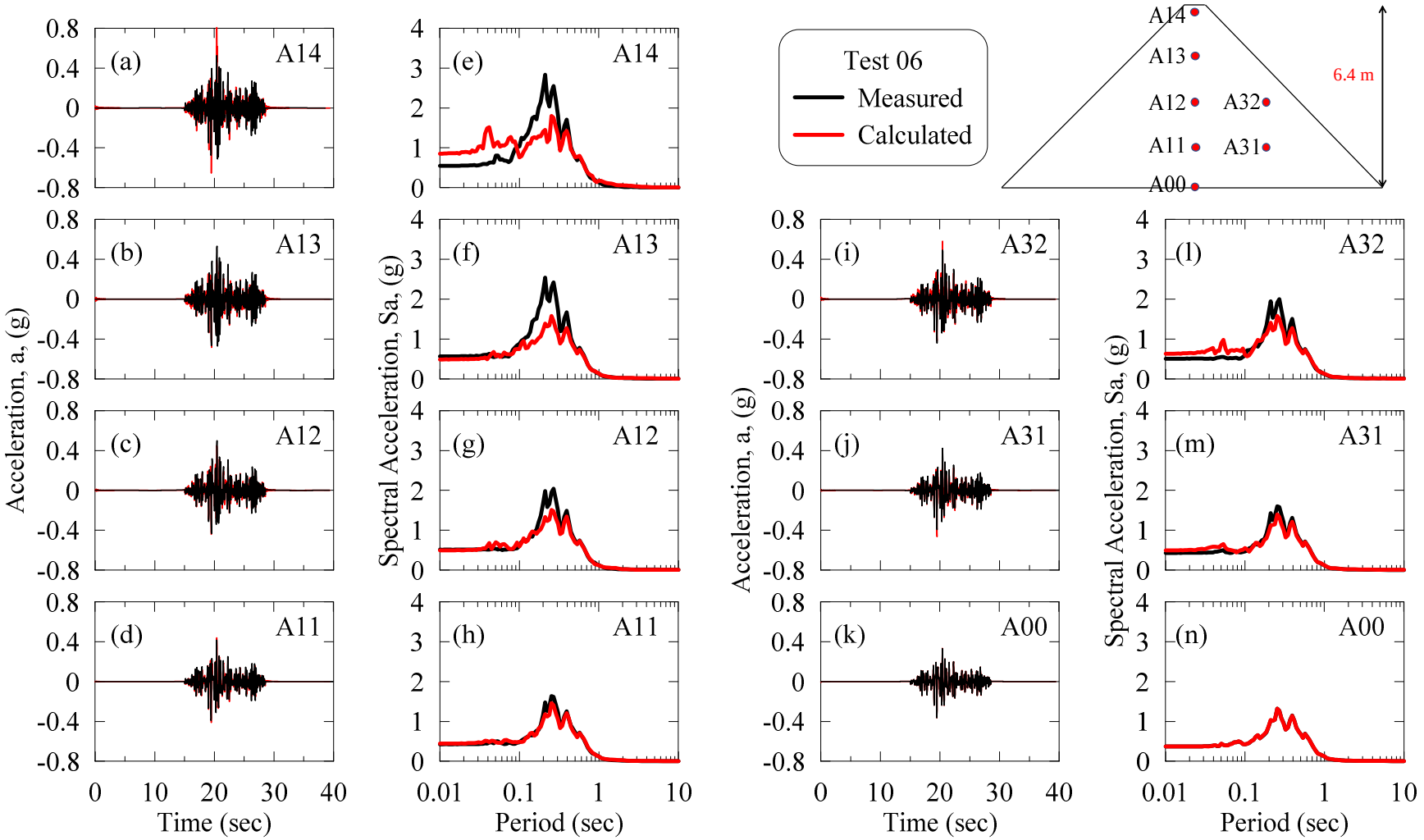

Figure A.38: Acceleration time histories and response spectra at different depths of dam during Test 06 for welded contact and the dynamic soil curves of Menq (2003) with Masing un/reloading.

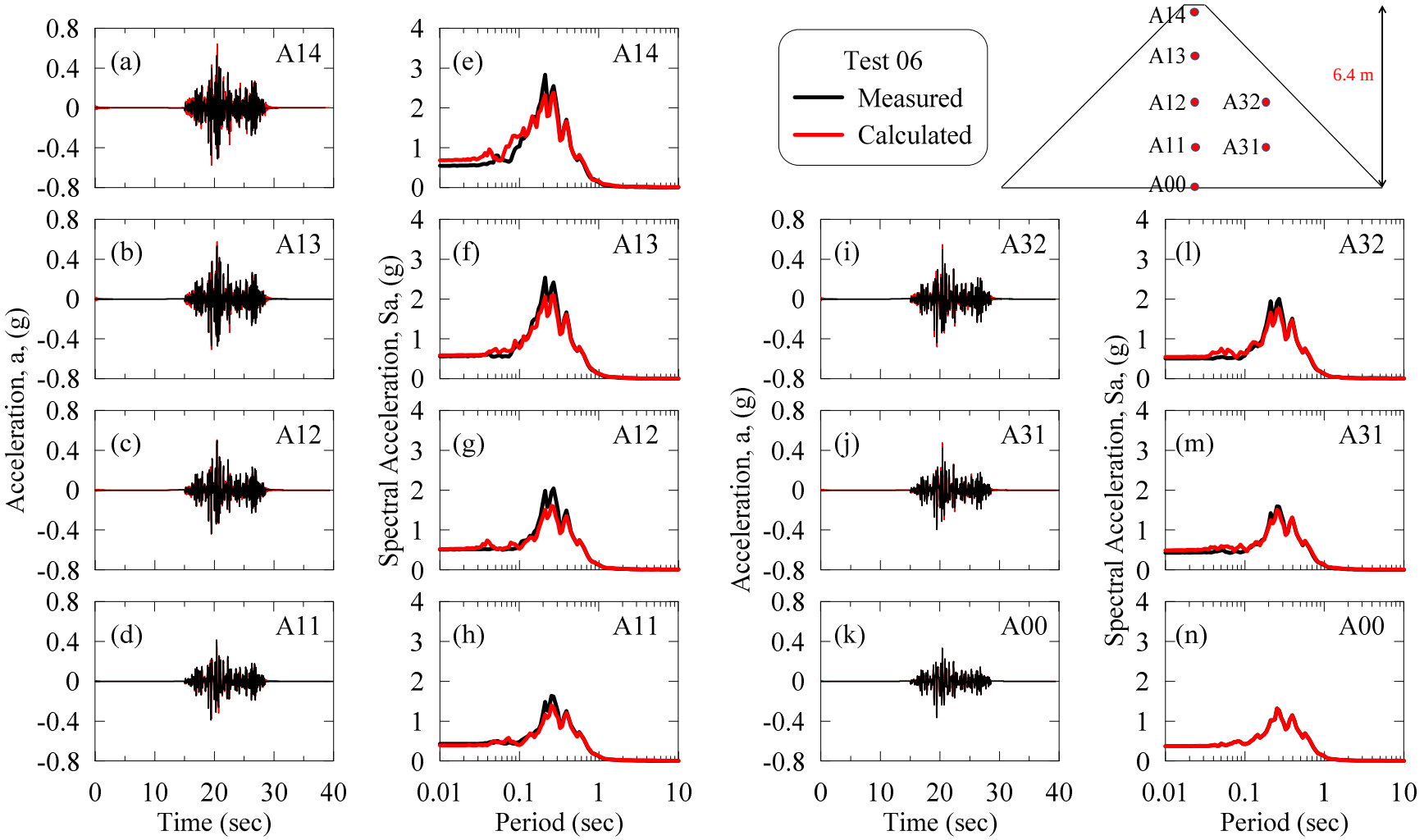

Figure A.39: Acceleration time histories and response spectra at different depths of dam during Test 06 for friction contact and the dynamic soil curves of Darendeli (2001) with non-Masing un/reloading.

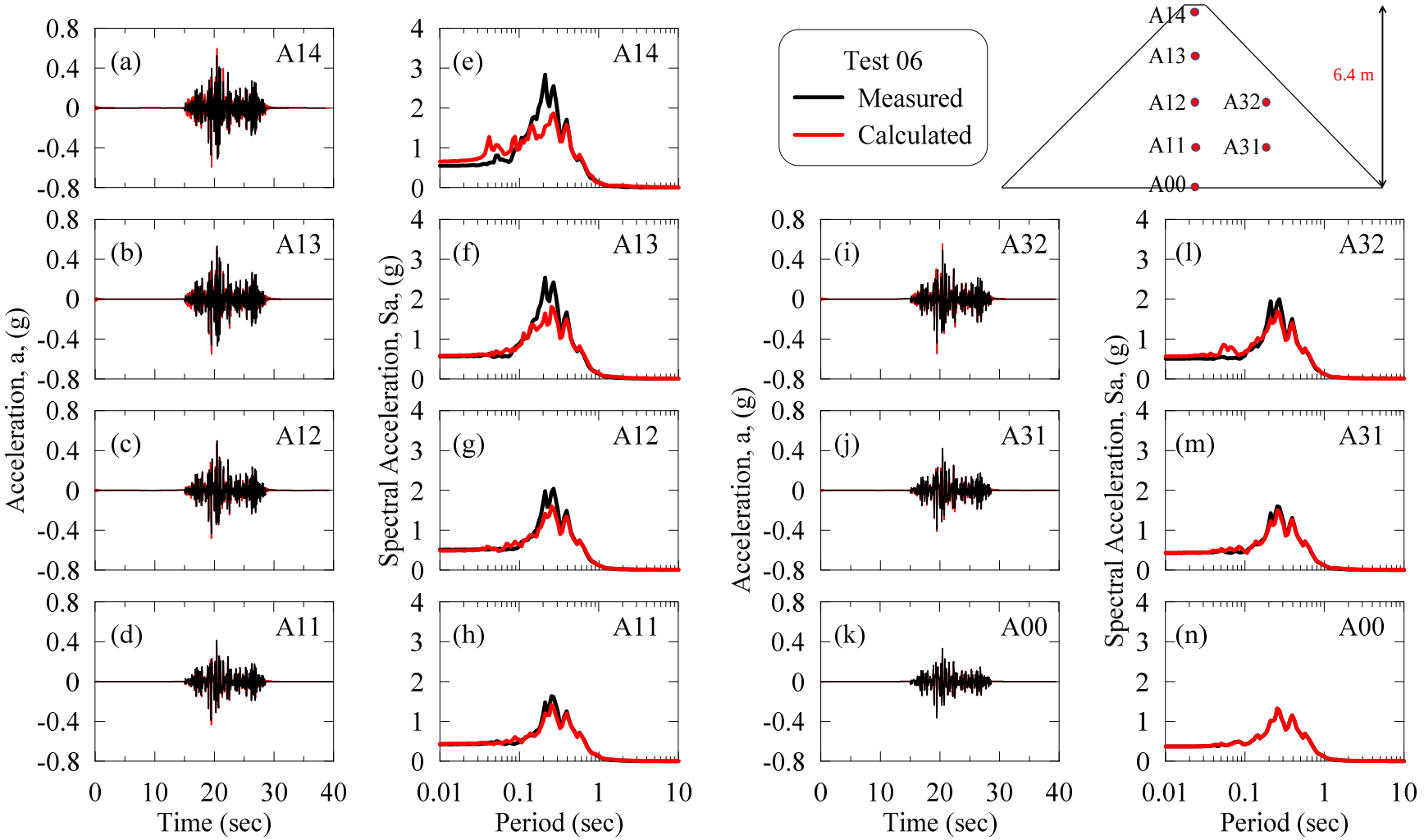

Figure A.40: Acceleration time histories and response spectra at different depths of dam during Test 06 for welded contact and the dynamic soil curves of Darendeli (2001) with non-Masing un/reloading.

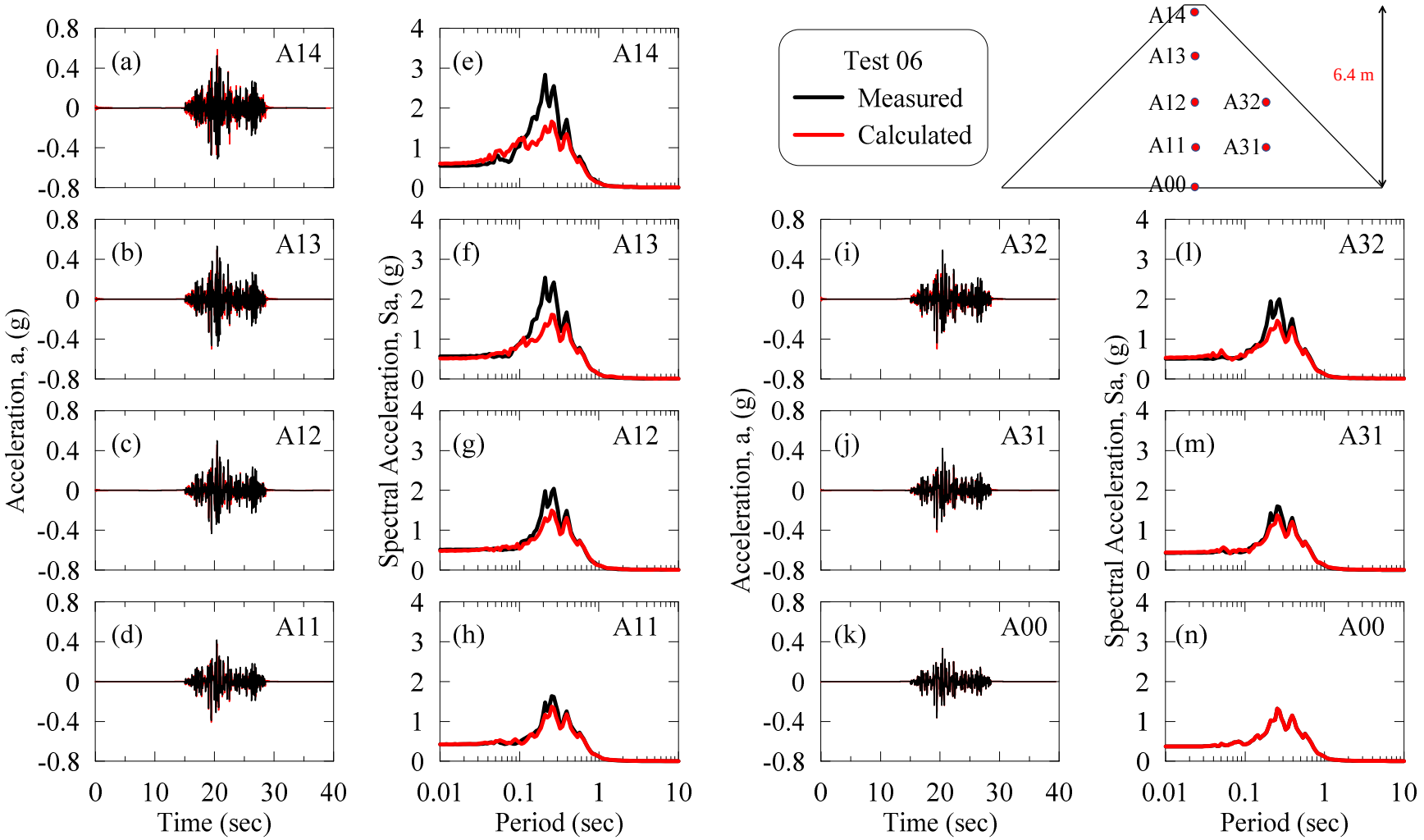

Figure A.41: Acceleration time histories and response spectra at different depths of dam during Test 06 for friction contact and the dynamic soil curves of Darendeli (2001) with Masing un/reloading.

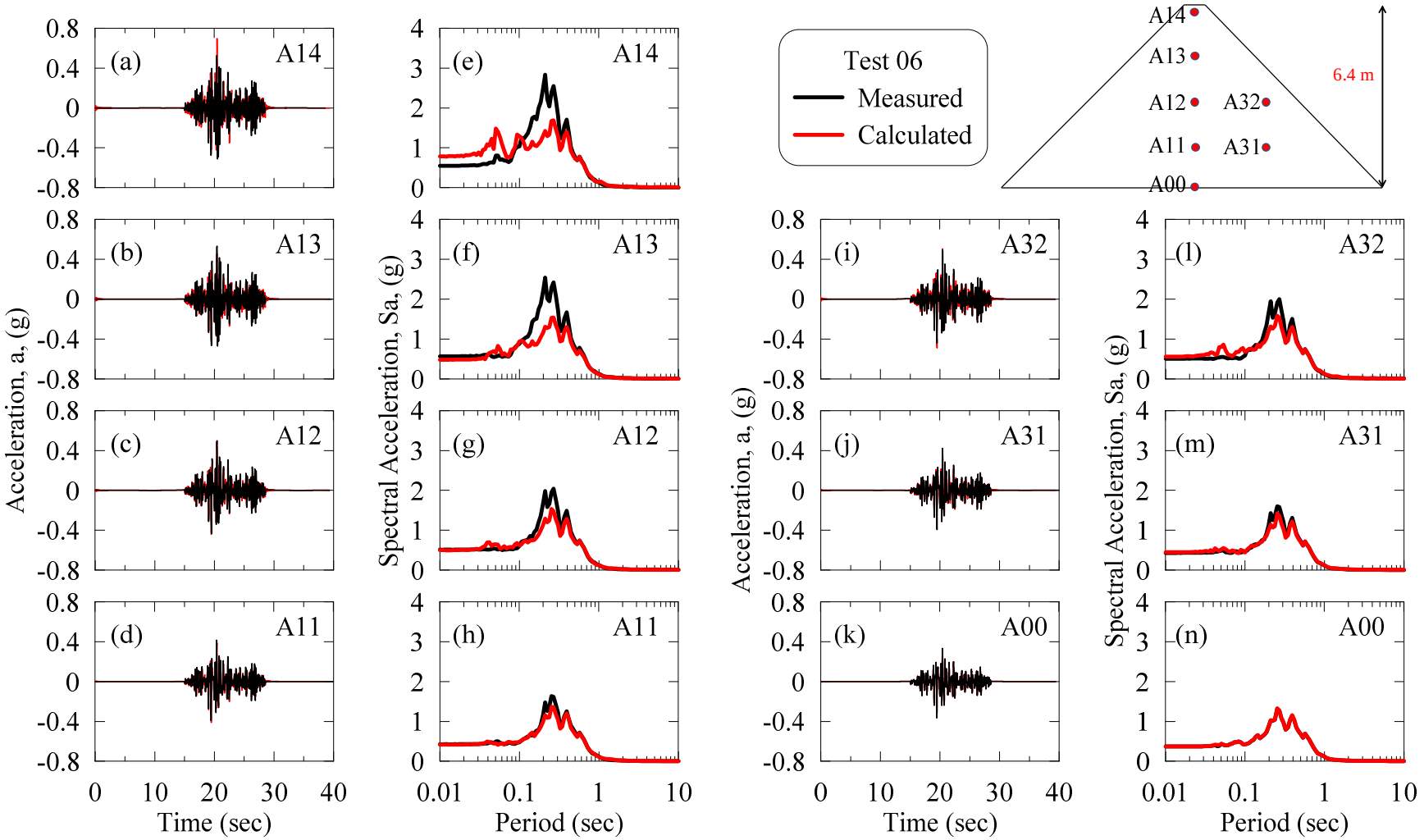

Figure A.42: Acceleration time histories and response spectra at different depths of dam during Test 06 for welded contact and the dynamic soil curves of Darendeli (2001) with Masing un/reloading.

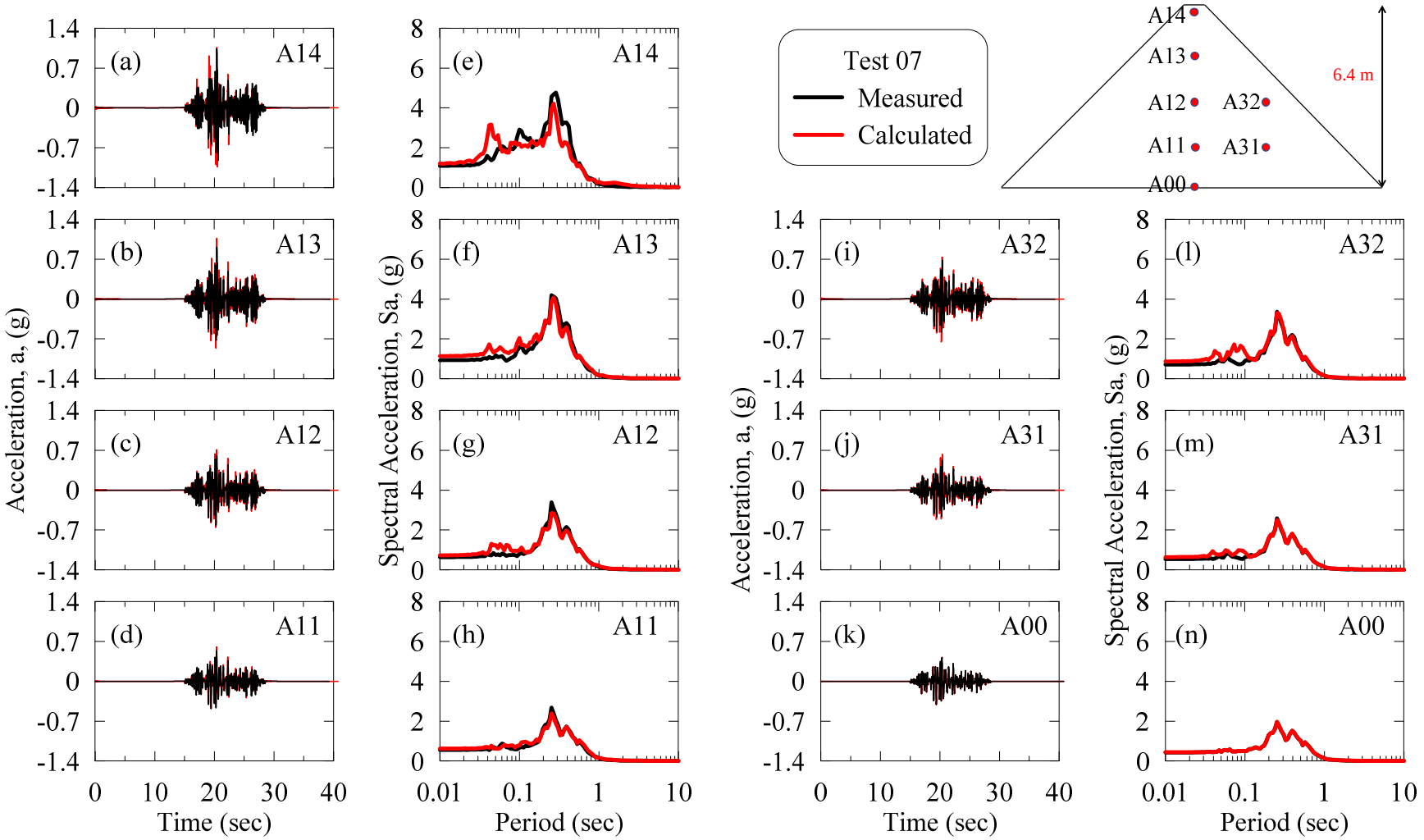

Figure A.43: Acceleration time histories and response spectra at different depths of dam during Test 07 for welded contact and the dynamic soil curves of Menq (2003) with non-Masing un/reloading.

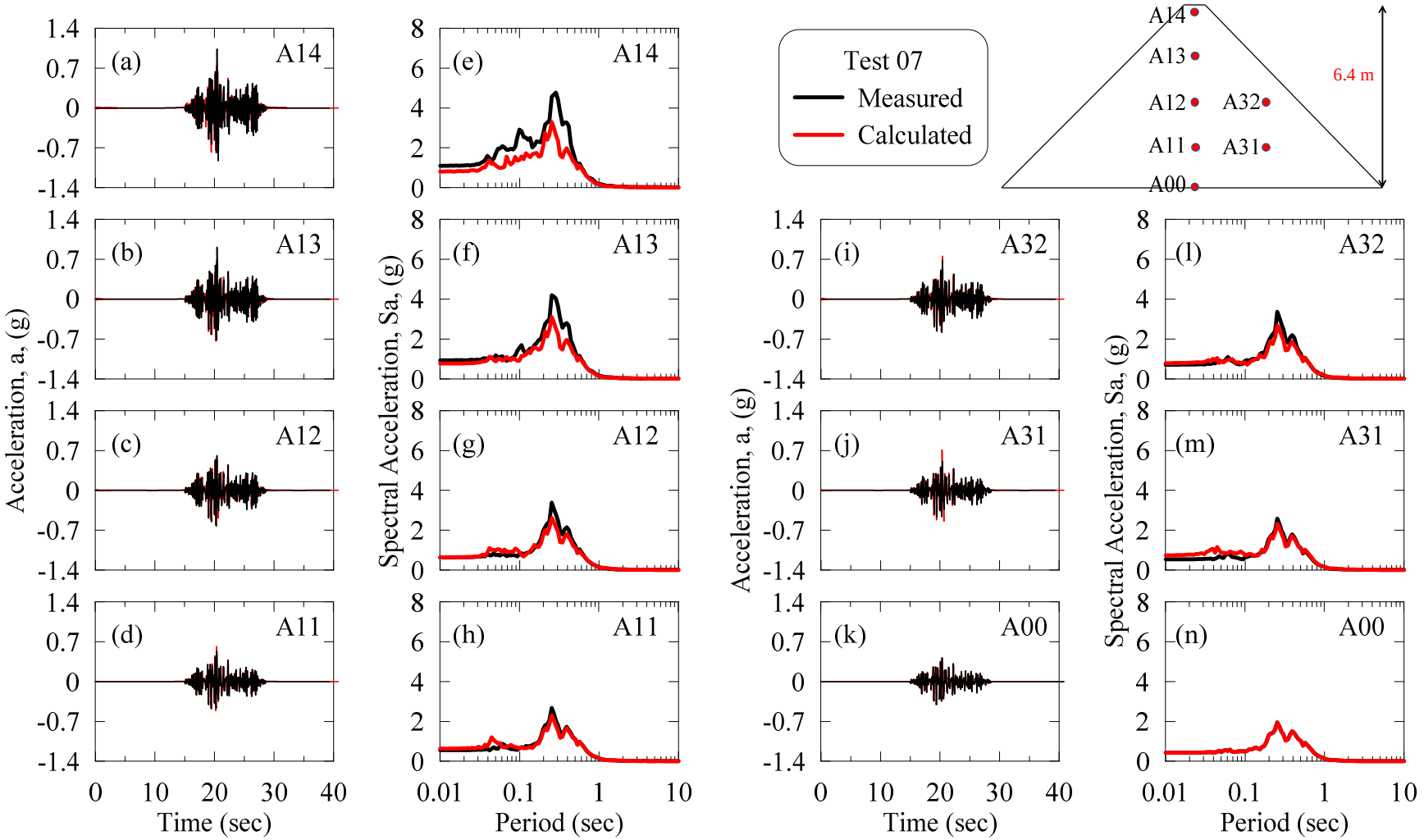

Figure A.44: Acceleration time histories and response spectra at different depths of dam during Test 07 for friction contact and the dynamic soil curves of Menq (2003) with Masing un/reloading.

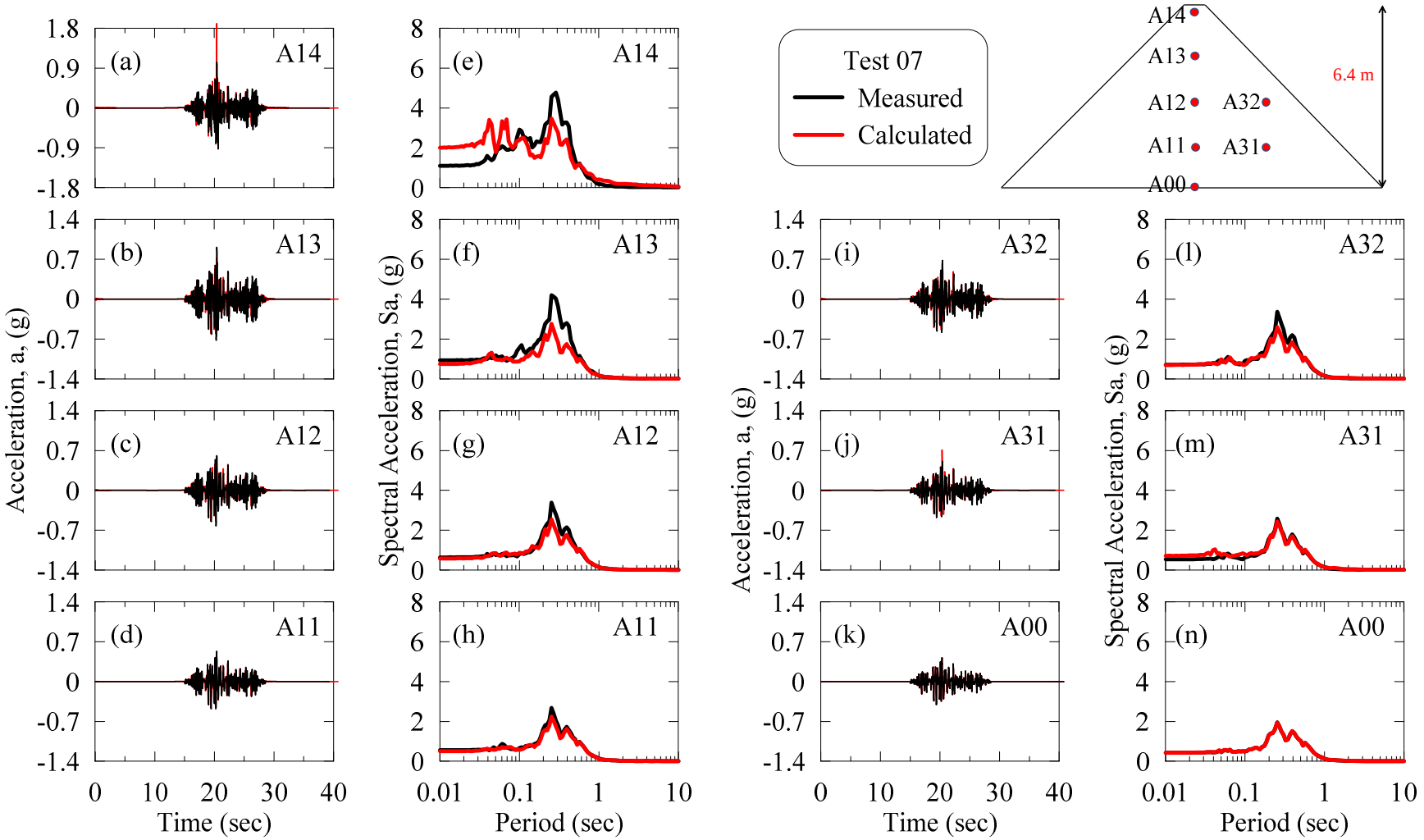

Figure A.45: Acceleration time histories and response spectra at different depths of dam during Test 07 for welded contact and the dynamic soil curves of Menq (2003) with Masing un/reloading.

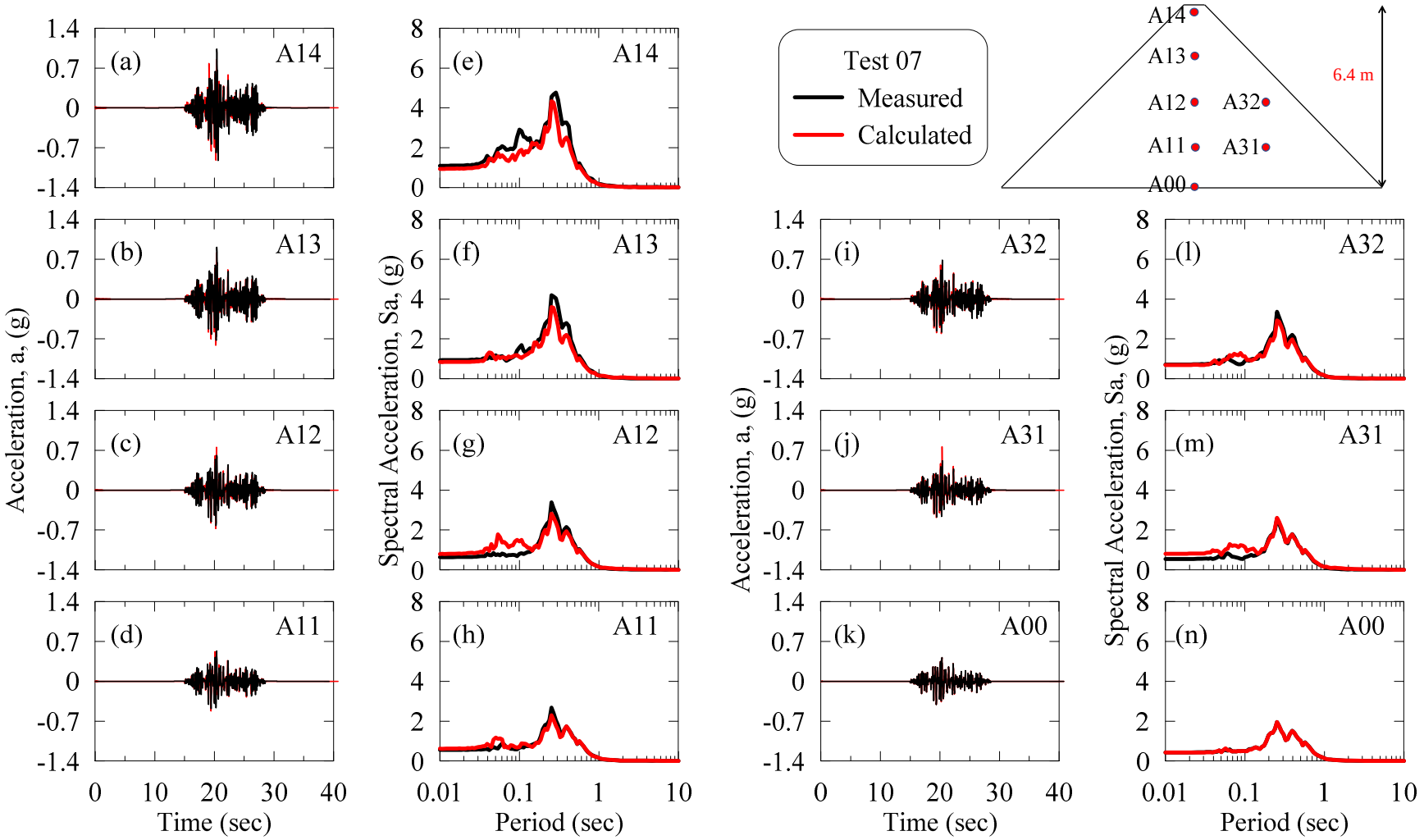

Figure A.46: Acceleration time histories and response spectra at different depths of dam during Test 07 for friction contact and the dynamic soil curves of Darendeli (2001) with non-Masing un/reloading.

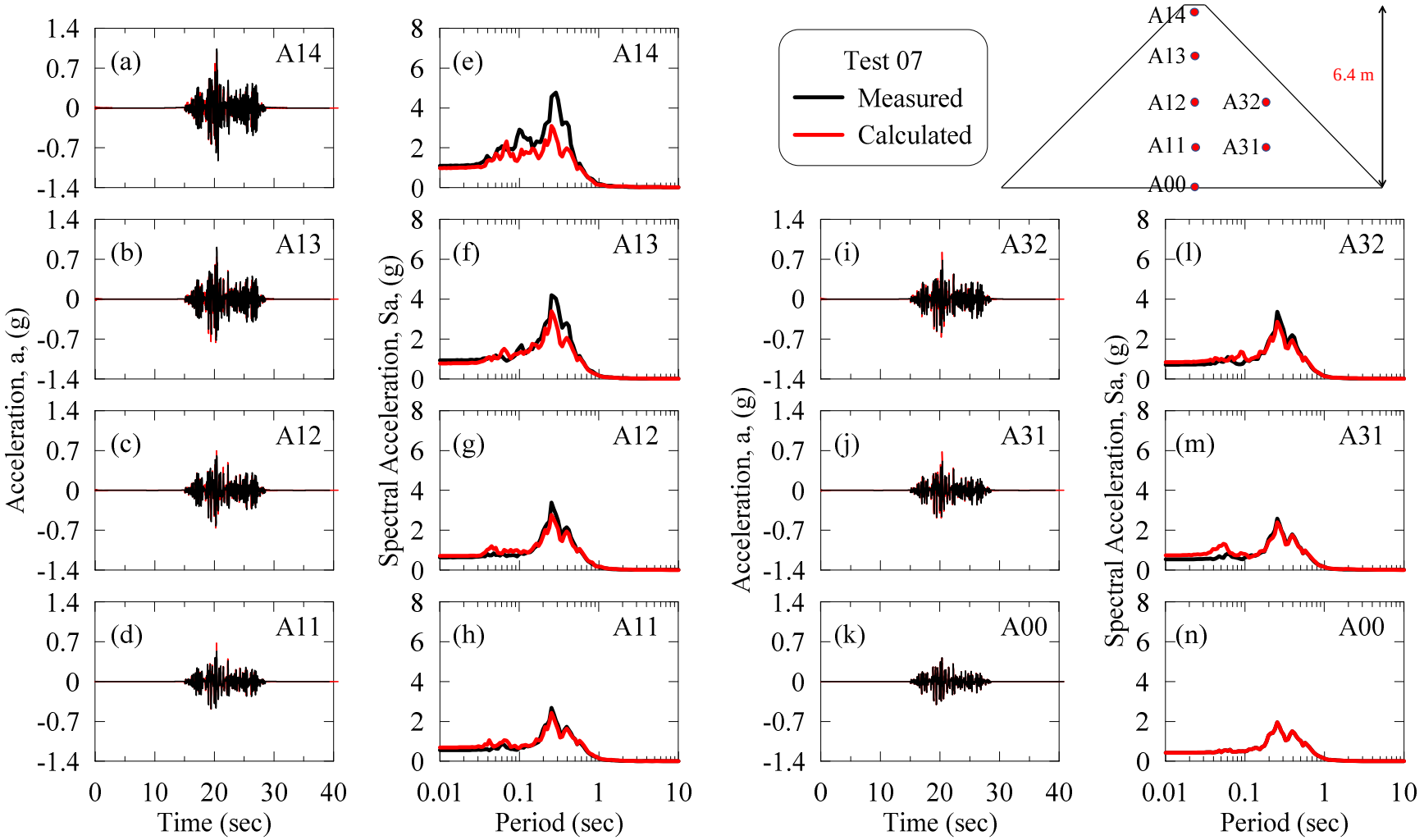

Figure A.47: Acceleration time histories and response spectra at different depths of dam during Test 07 for welded contact and the dynamic soil curves of Darendeli (2001) with non-Masing un/reloading.

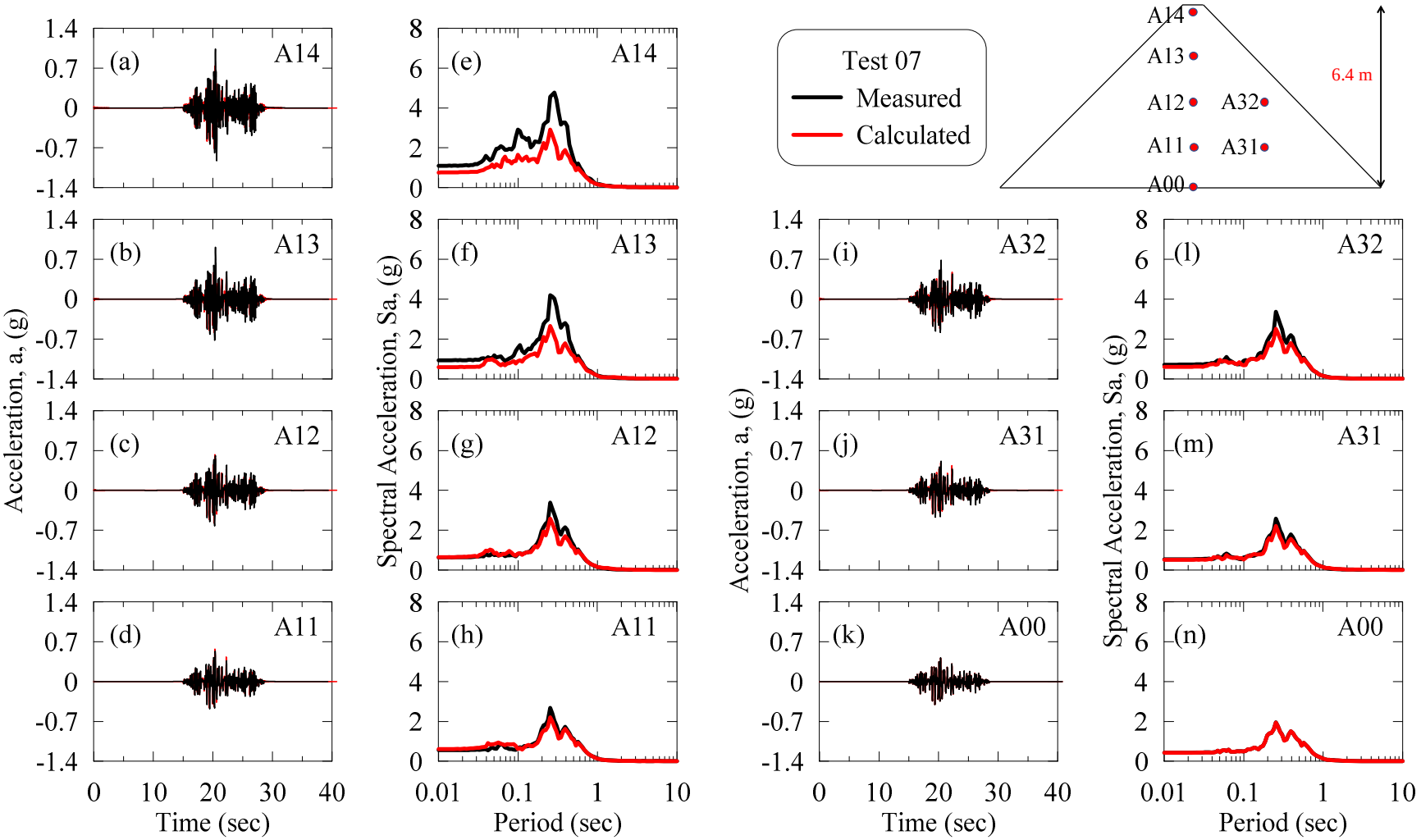

Figure A.48: Acceleration time histories and response spectra at different depths of dam during Test 07 for friction contact and the dynamic soil curves of Darendeli (2001) with Masing un/reloading.

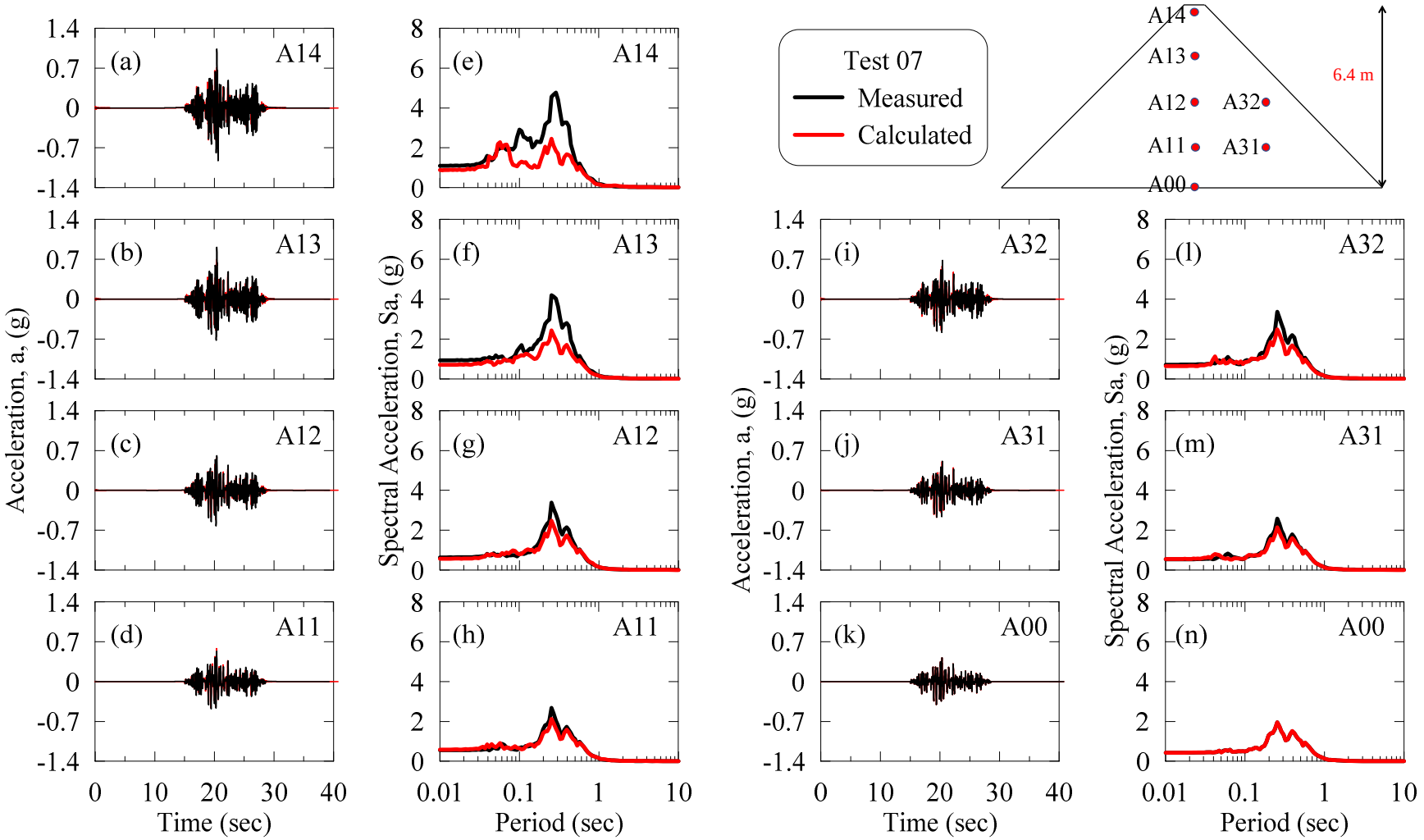

Figure A.49: Acceleration time histories and response spectra at different depths of dam during Test 07 for welded contact and the dynamic soil curves of Darendeli (2001) with Masing un/reloading.

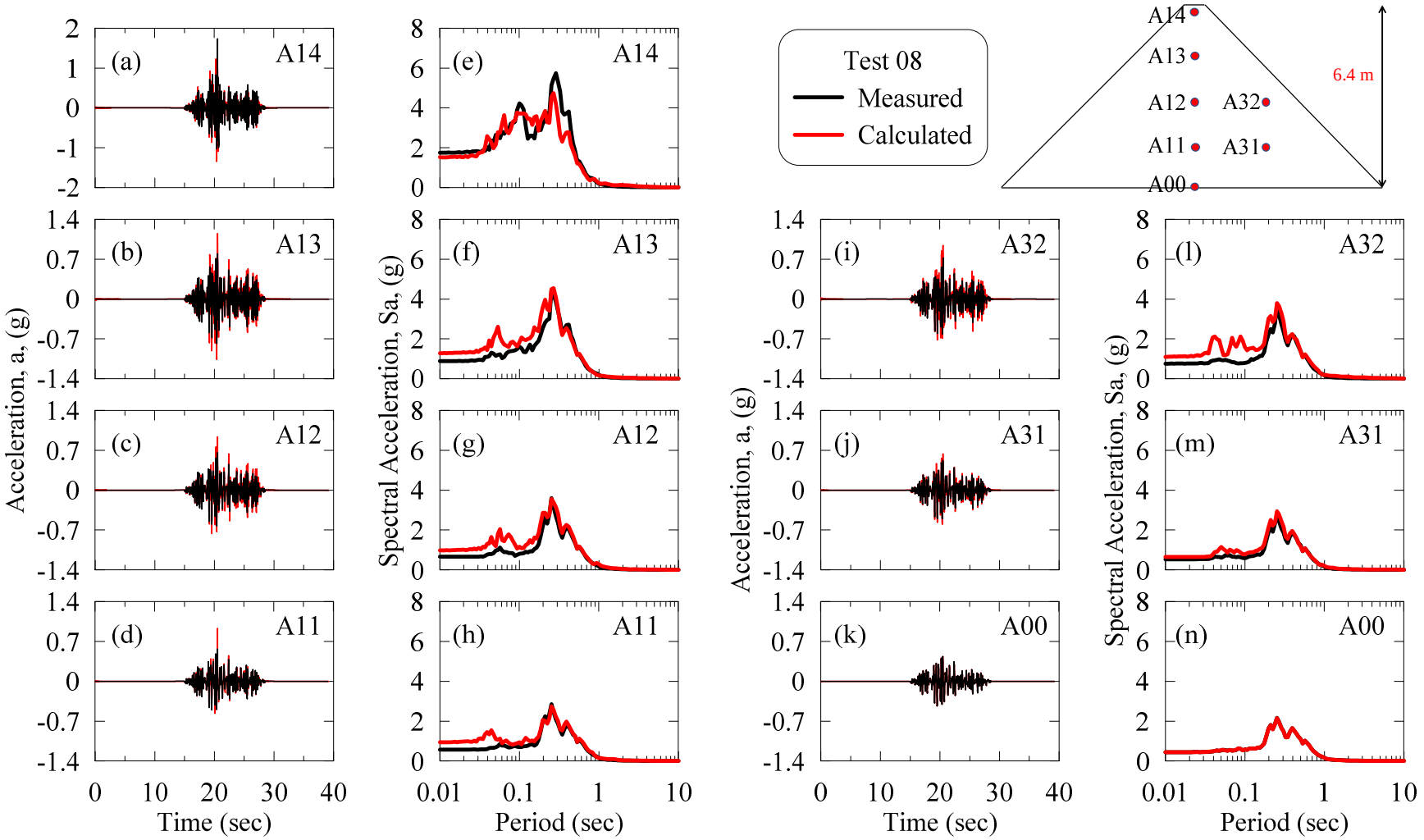

Figure A.50: Acceleration time histories and response spectra at different depths of dam during Test 08 for welded contact and the dynamic soil curves of Menq (2003) with non-Masing un/reloading.

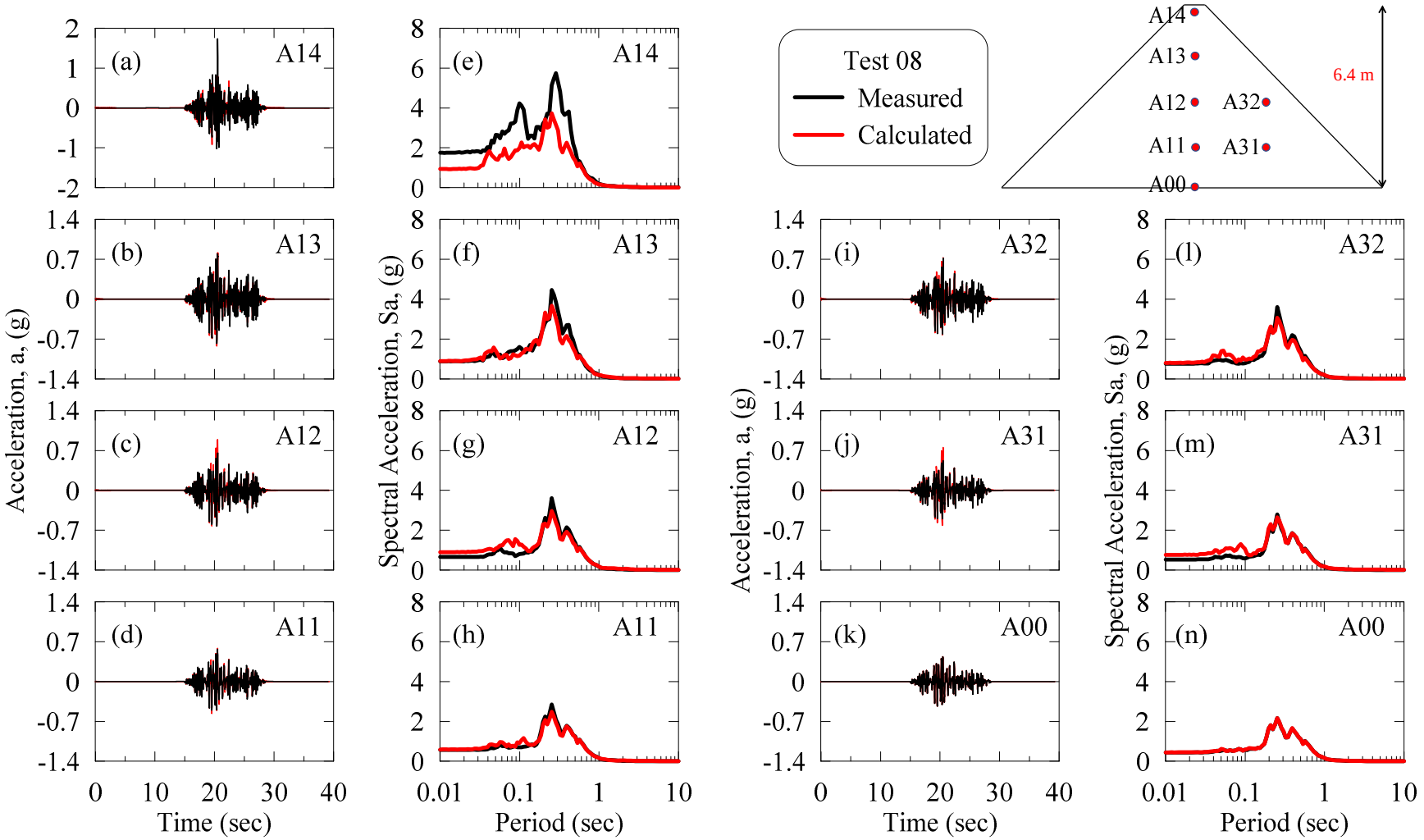

Figure A.51: Acceleration time histories and response spectra at different depths of dam during Test 08 for friction contact and the dynamic soil curves of Menq (2003) with Masing un/reloading.

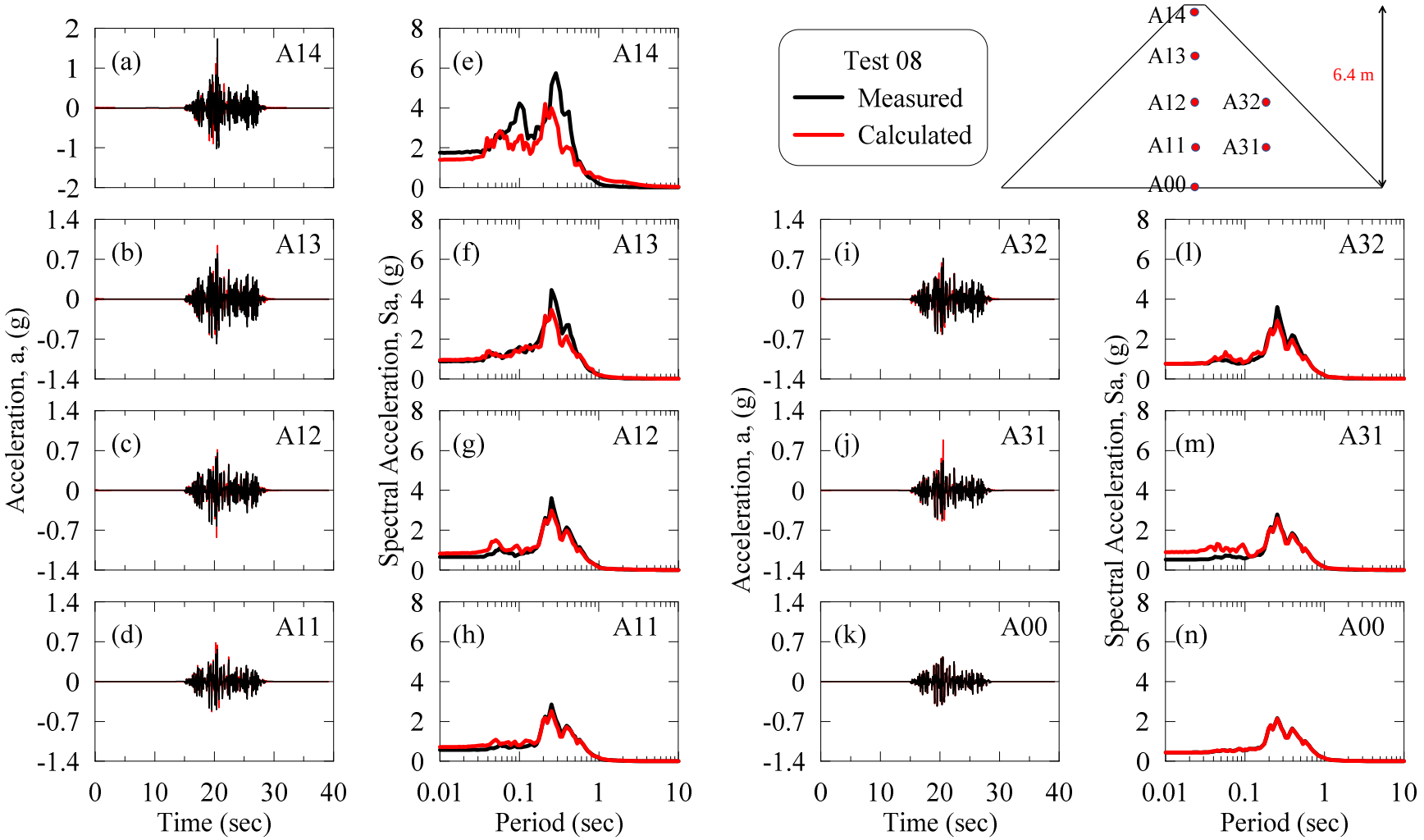

Figure A.52: Acceleration time histories and response spectra at different depths of dam during Test 08 for welded contact and the dynamic soil curves of Menq (2003) with Masing un/reloading.

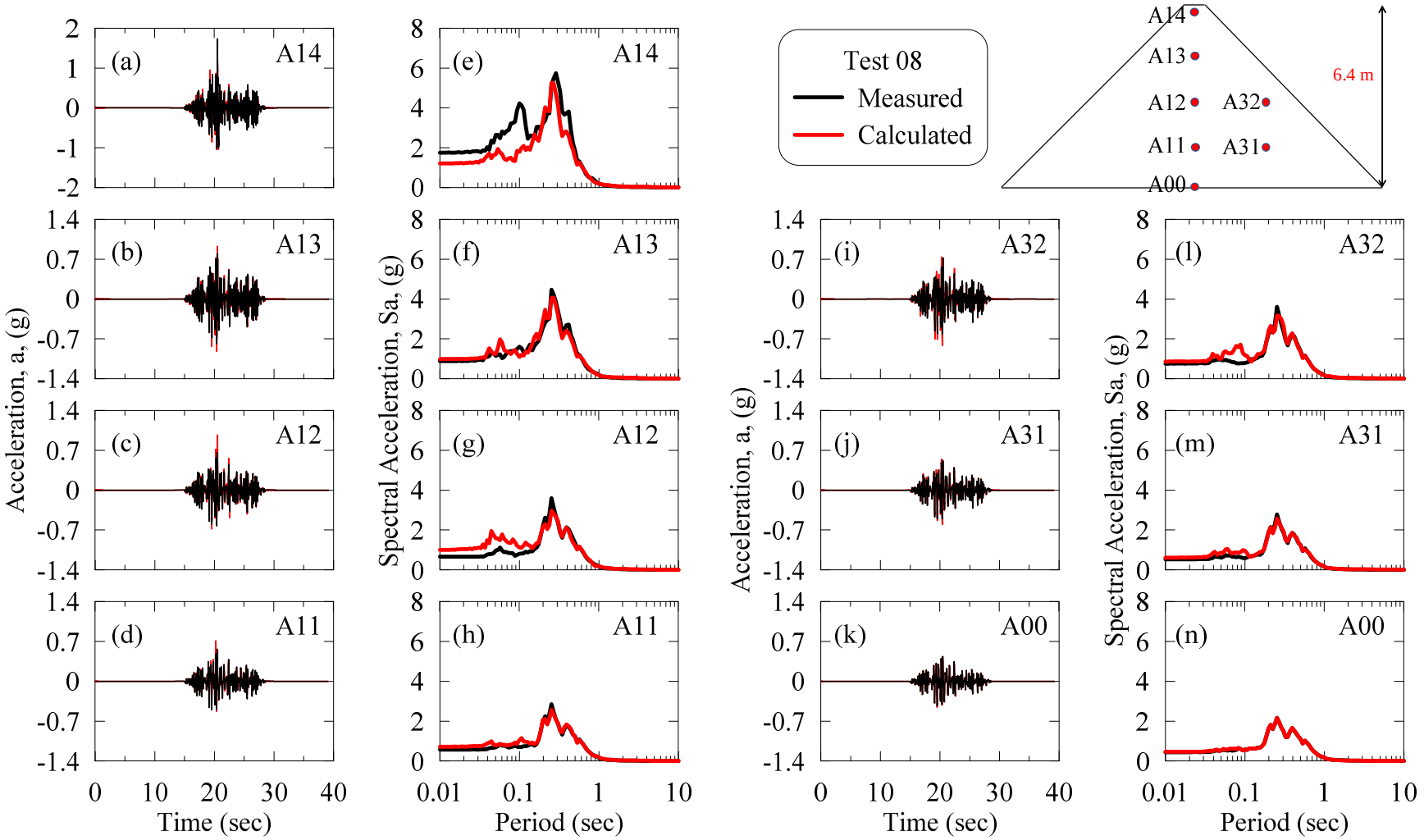

Figure A.53: Acceleration time histories and response spectra at different depths of dam during Test 08 for friction contact and the dynamic soil curves of Darendeli (2001) with non-Masing un/reloading.

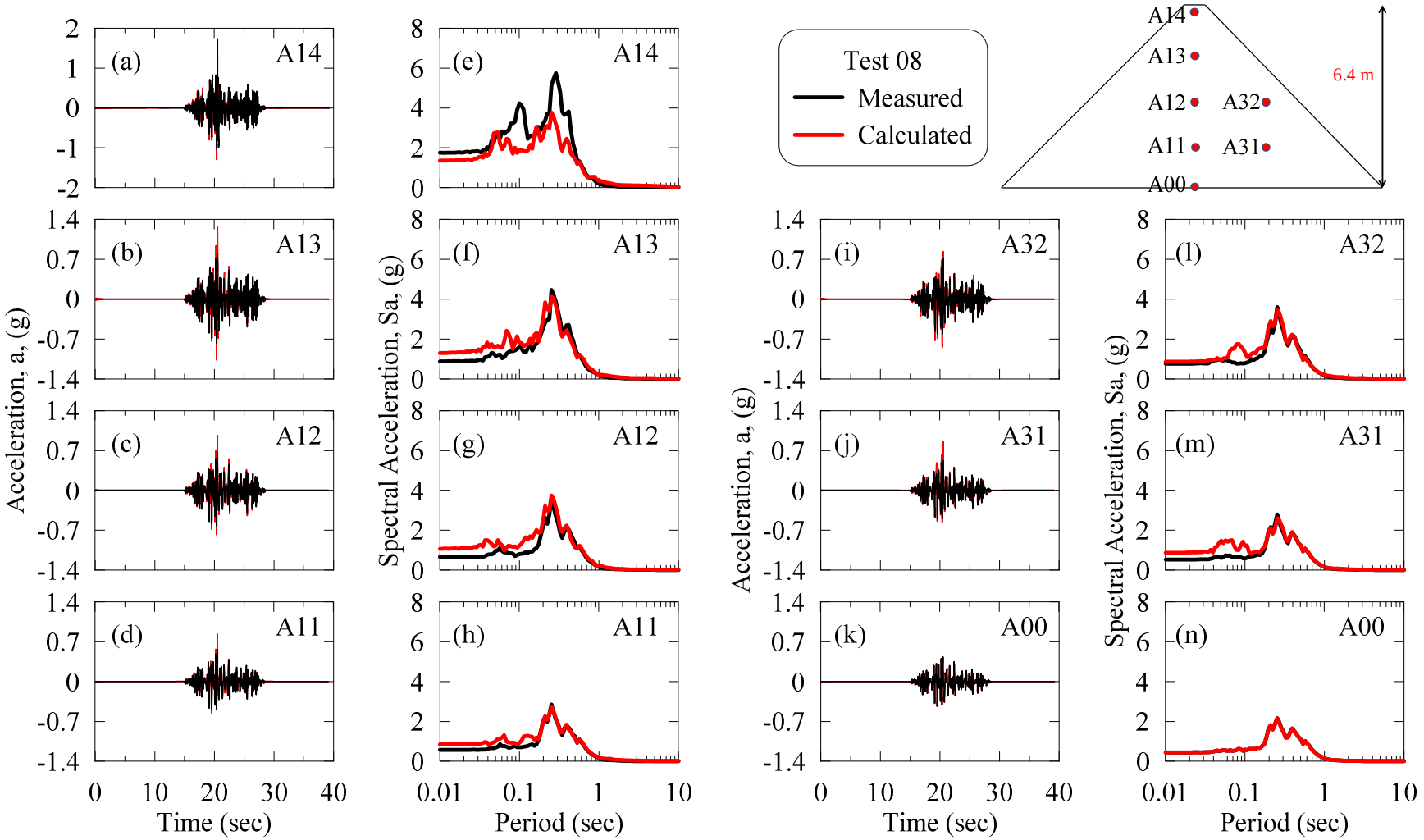

Figure A.54: Acceleration time histories and response spectra at different depths of dam during Test 08 for welded contact and the dynamic soil curves of Darendeli (2001) with non-Masing un/reloading.

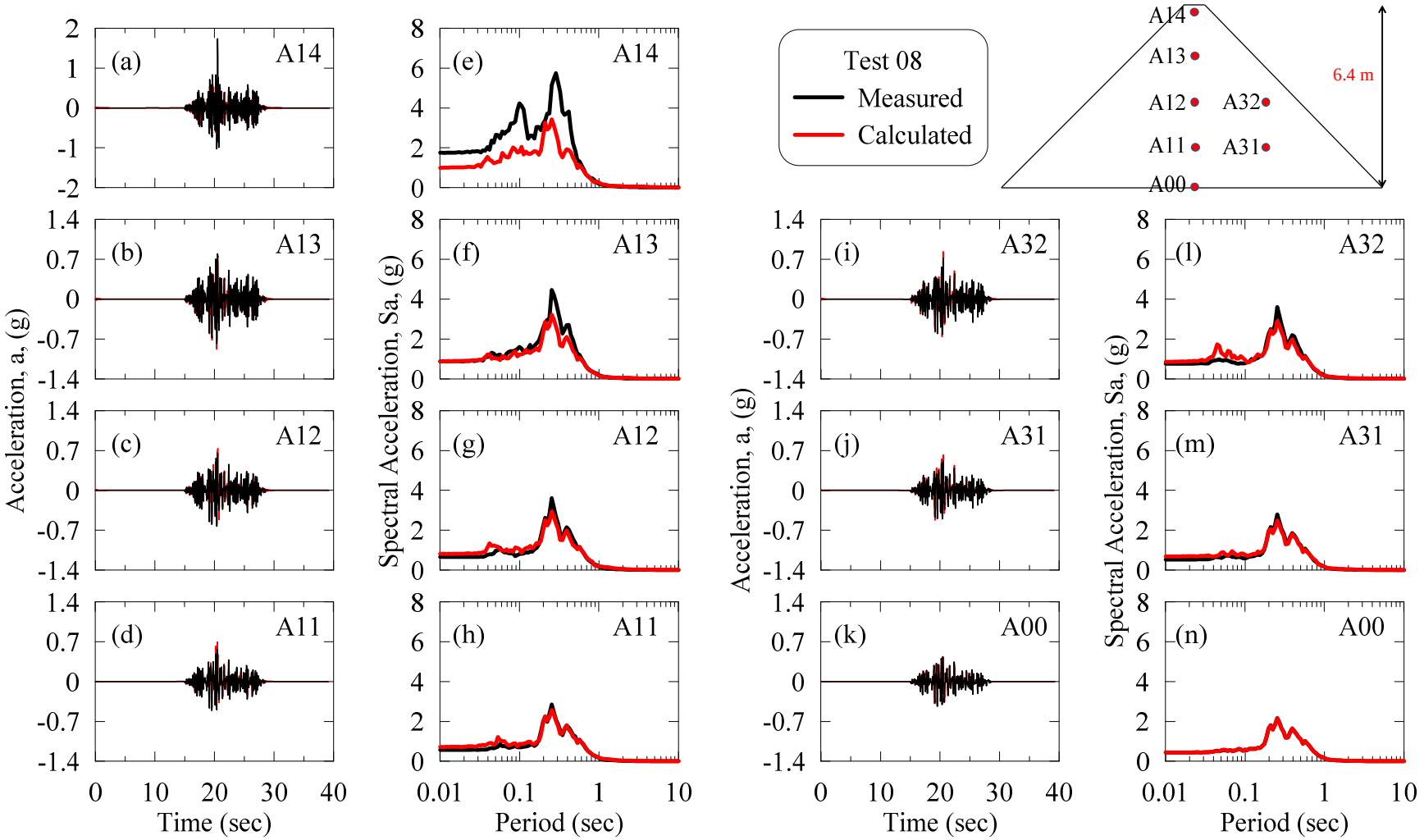

Figure A.55: Acceleration time histories and response spectra at different depths of dam during Test 08 for friction contact and the dynamic soil curves of Darendeli (2001) with Masing un/reloading.

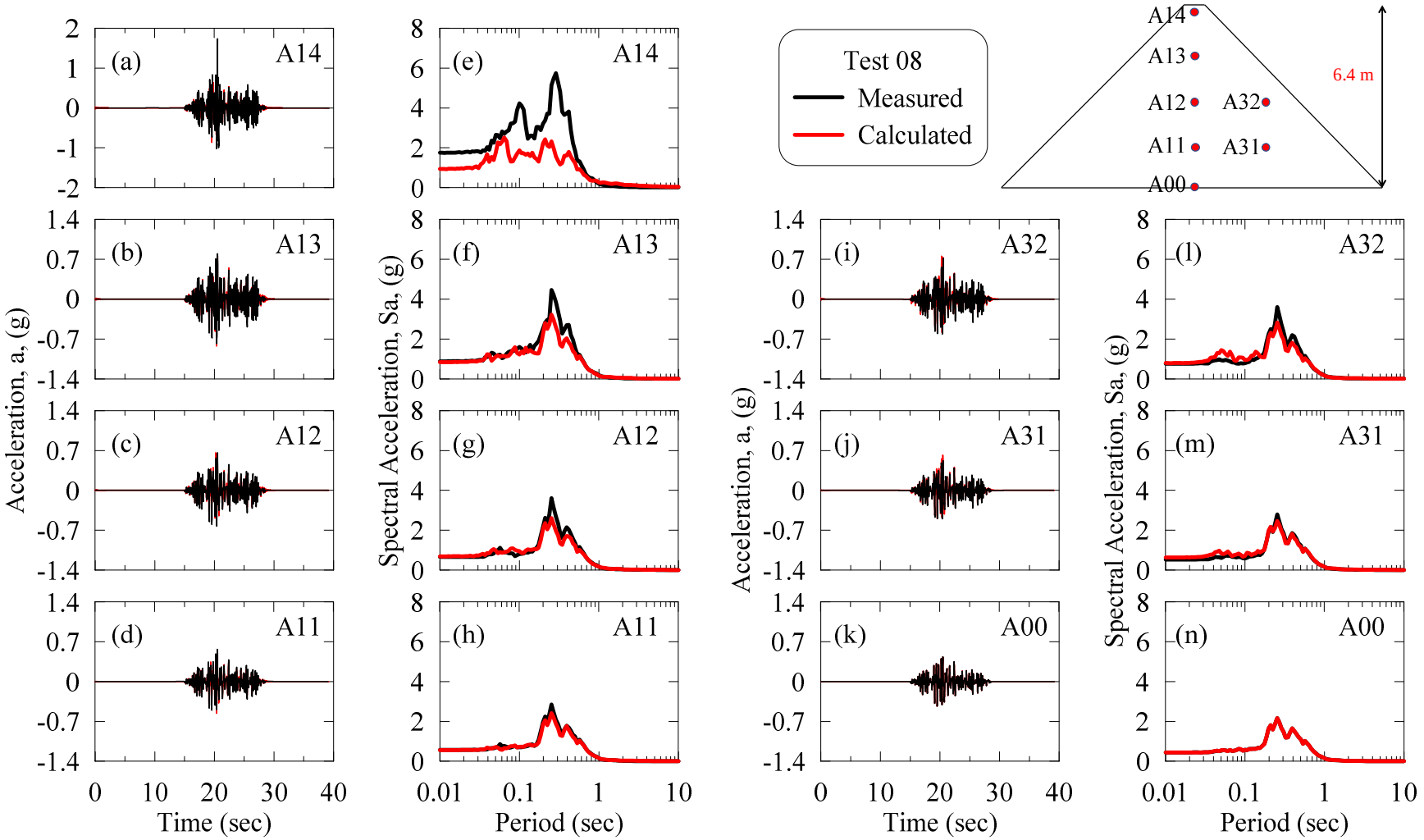

Figure A.56: Acceleration time histories and response spectra at different depths of dam during Test 08 for welded contact and the dynamic soil curves of Darendeli (2001) with Masing un/reloading.

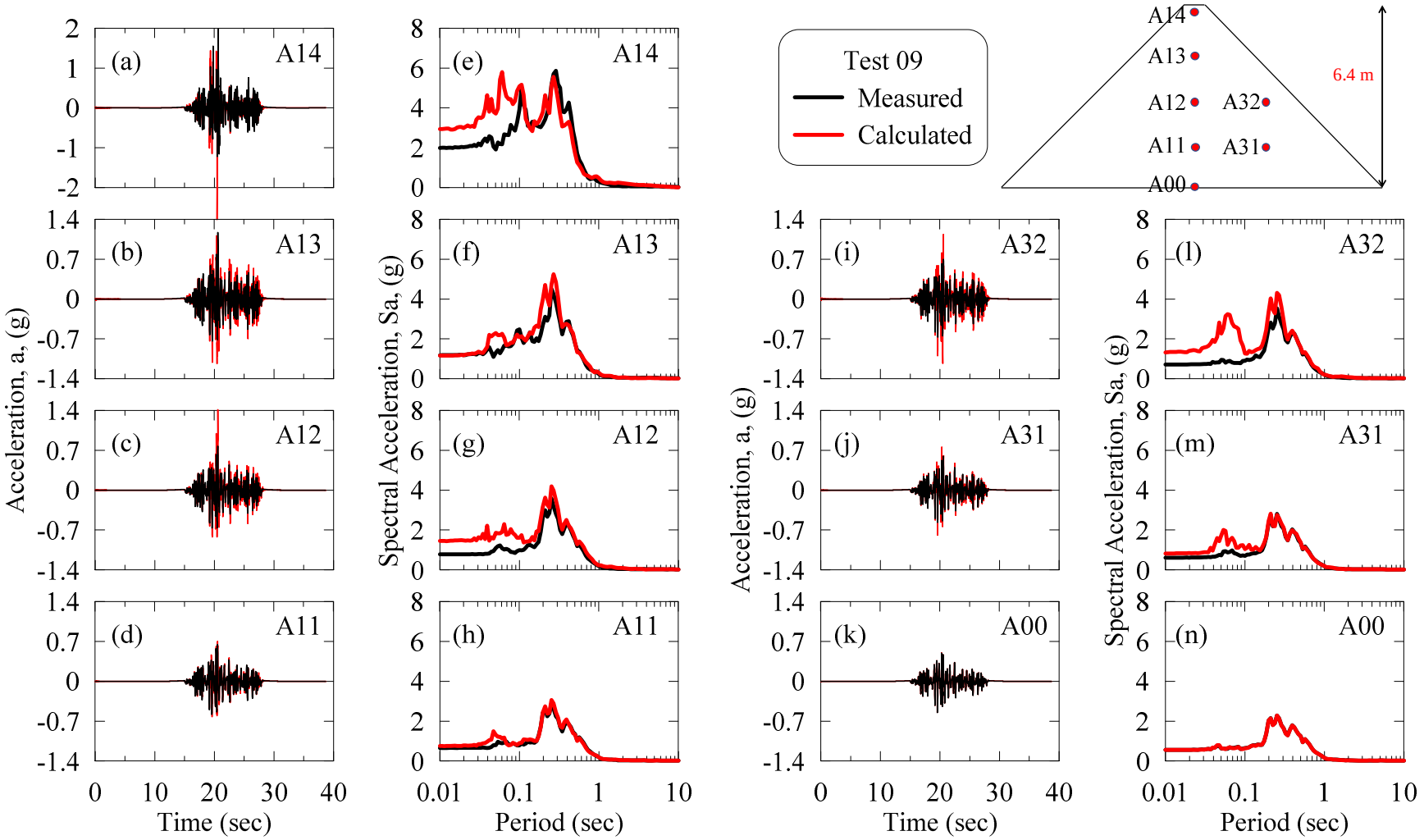

Figure A.57: Acceleration time histories and response spectra at different depths of dam during Test 09 for welded contact and the dynamic soil curves of Menq (2003) with non-Masing un/reloading.

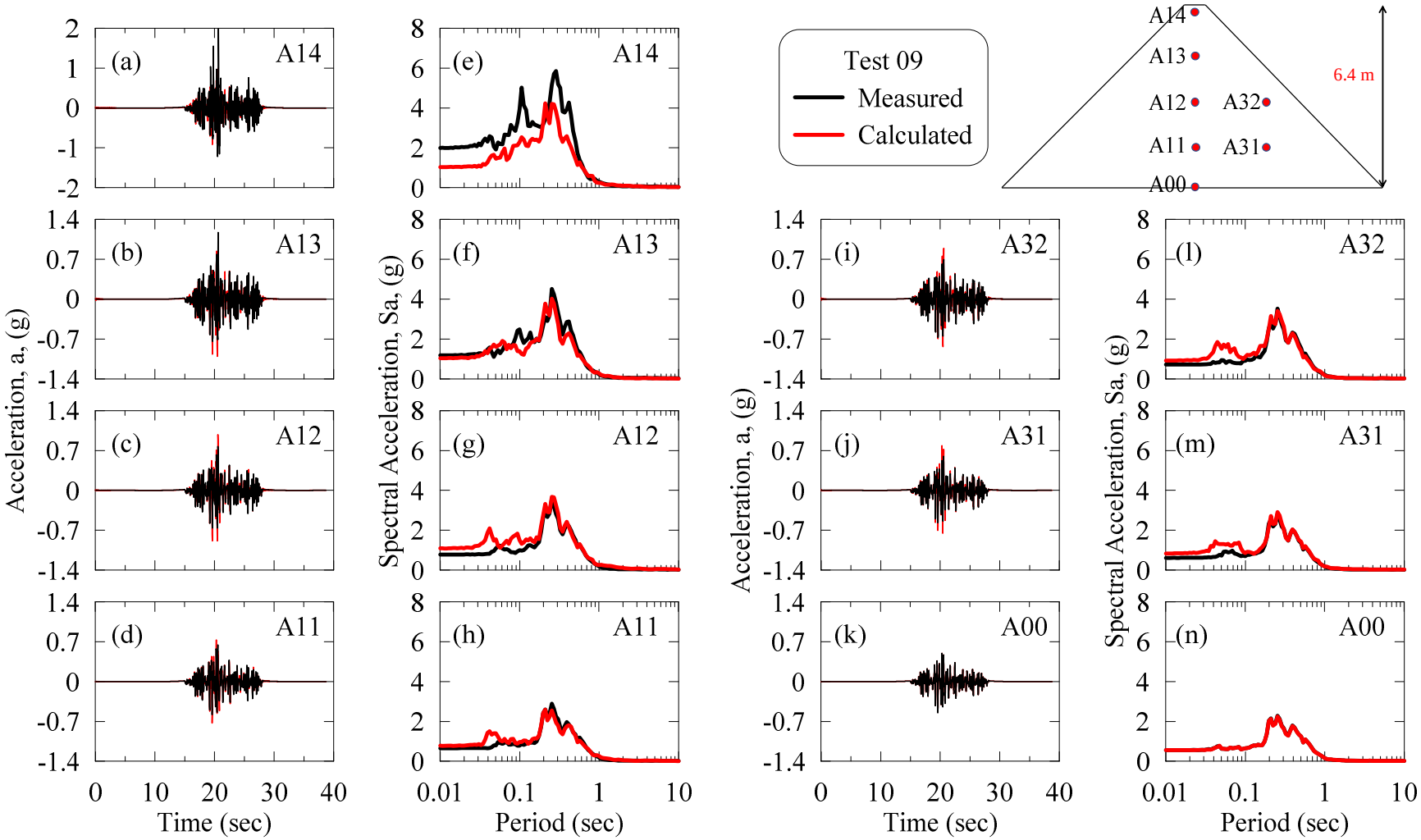

Figure A.58: Acceleration time histories and response spectra at different depths of dam during Test 09 for friction contact and the dynamic soil curves of Menq (2003) with Masing un/reloading.

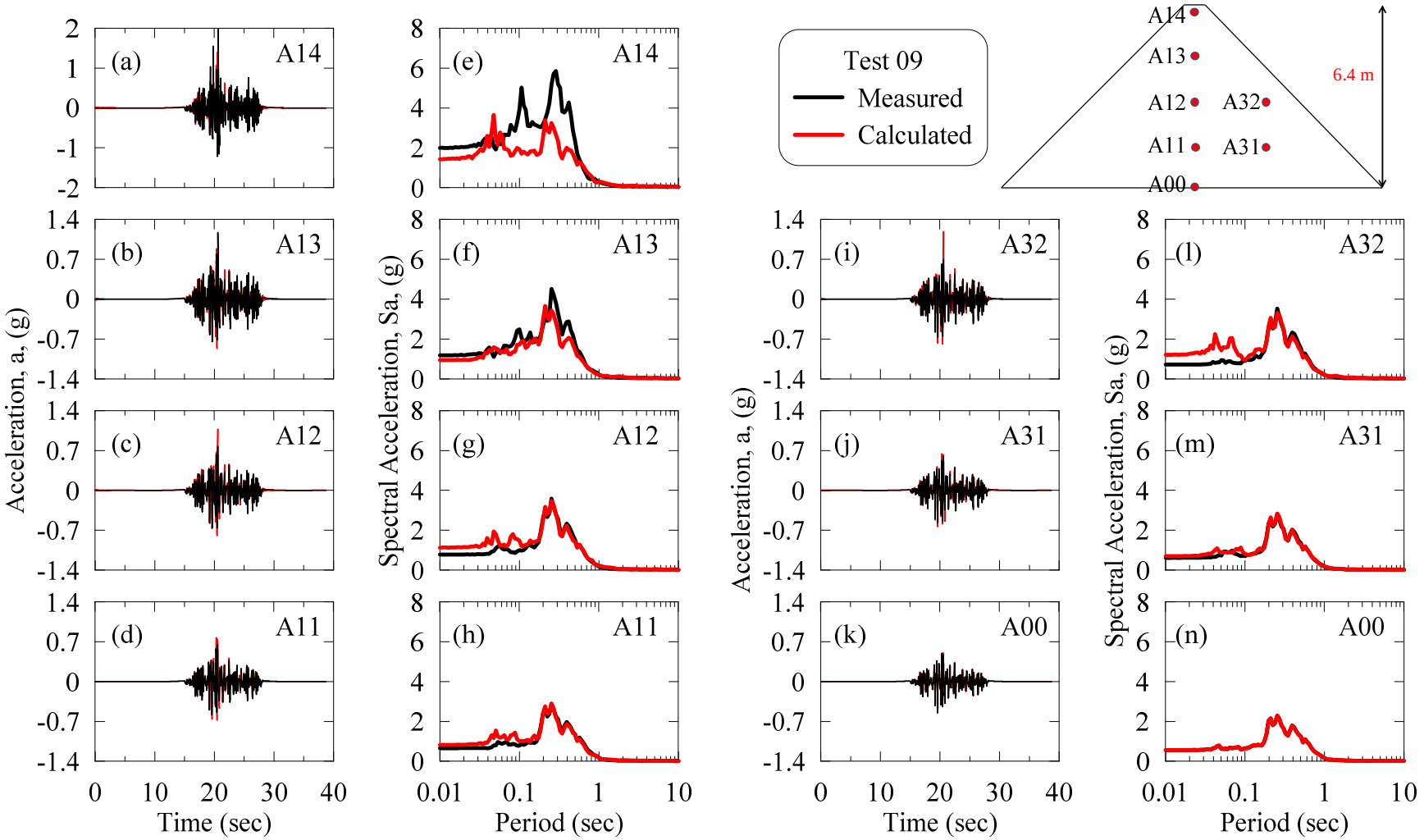

Figure A.59: Acceleration time histories and response spectra at different depths of dam during Test 09 for welded contact and the dynamic soil curves of Menq (2003) with Masing un/reloading.

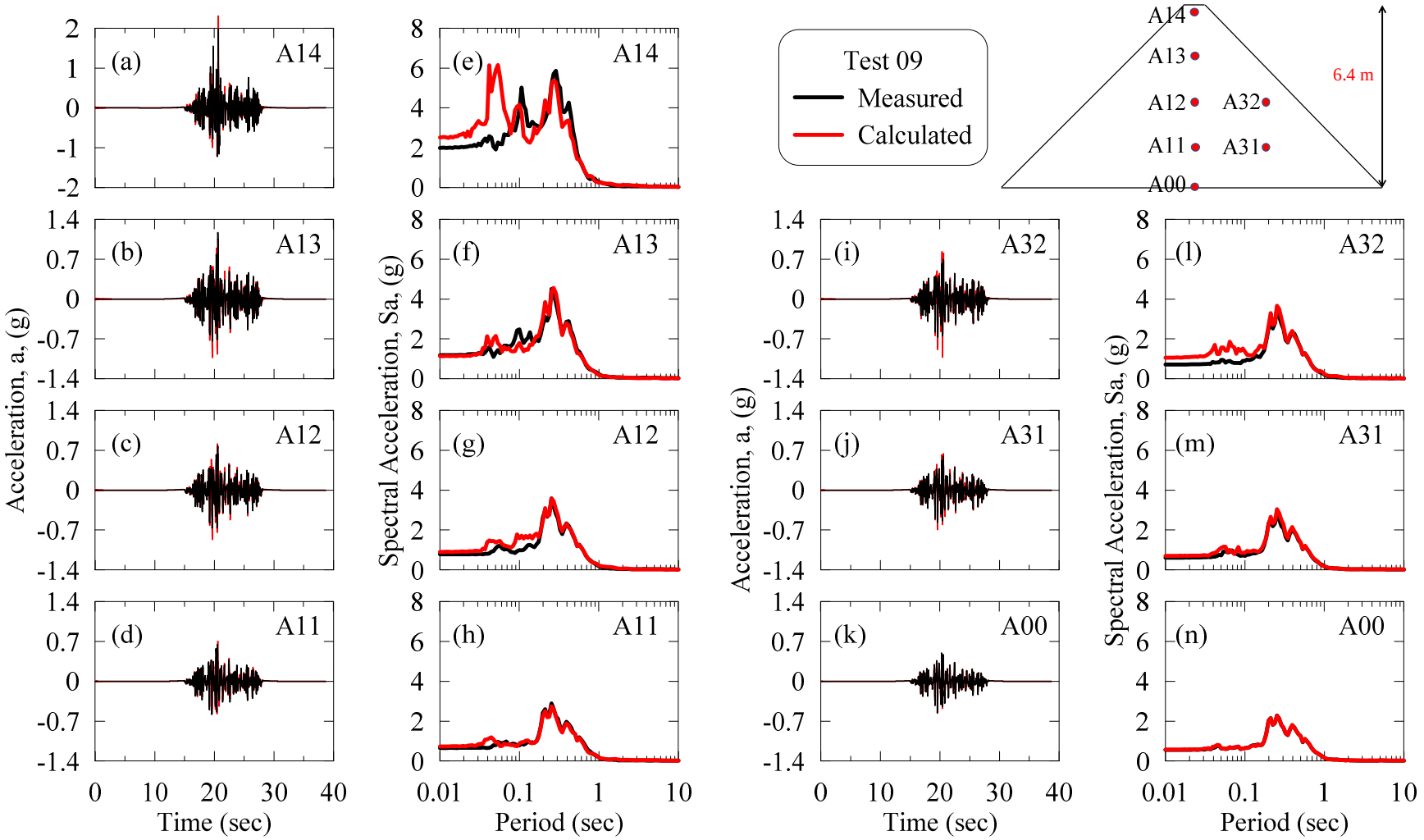

Figure A.60: Acceleration time histories and response spectra at different depths of dam during Test 09 for friction contact and the dynamic soil curves of Darendeli (2001) with non-Masing un/reloading.

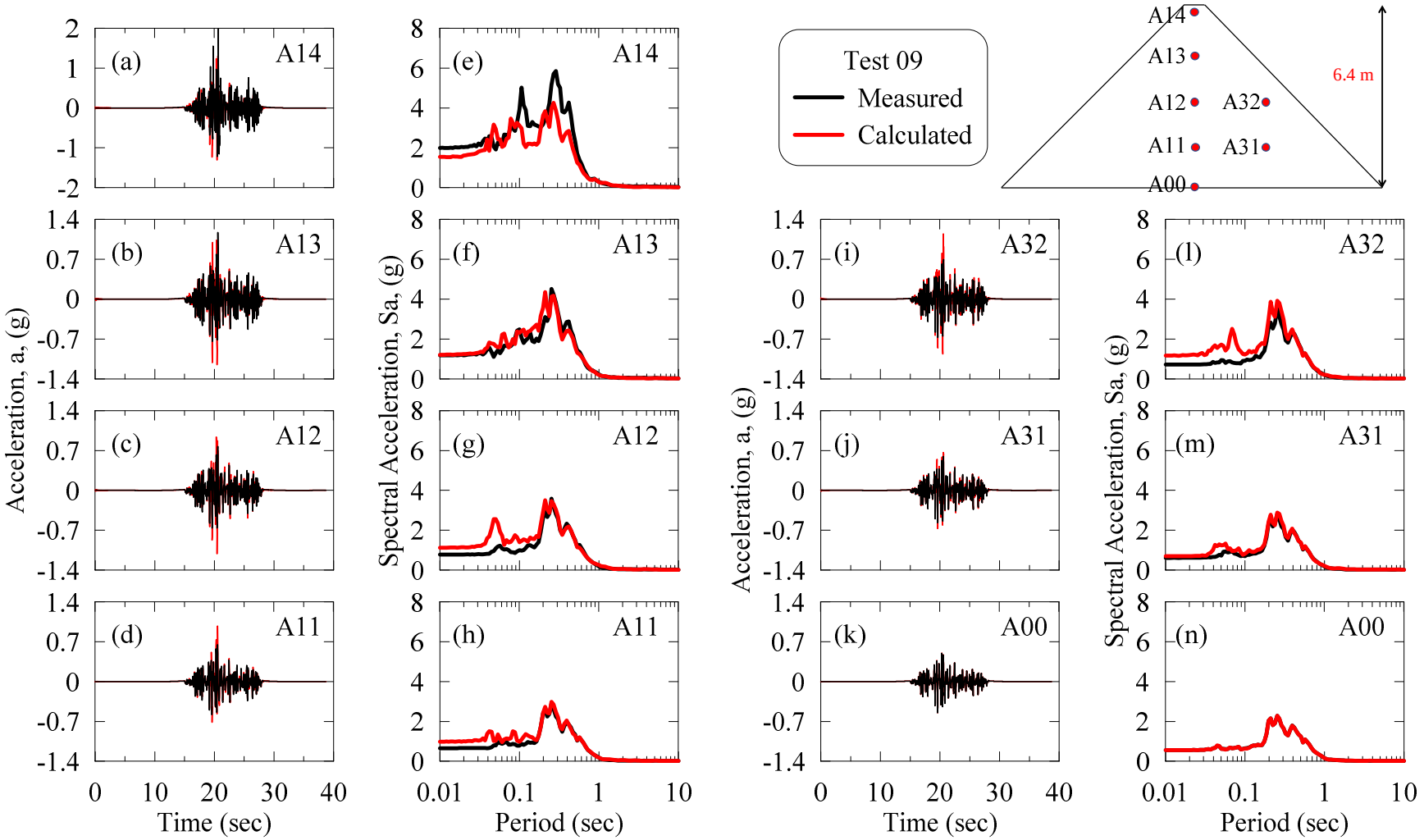

Figure A.61: Acceleration time histories and response spectra at different depths of dam during Test 09 for welded contact and the dynamic soil curves of Darendeli (2001) with non-Masing un/reloading.

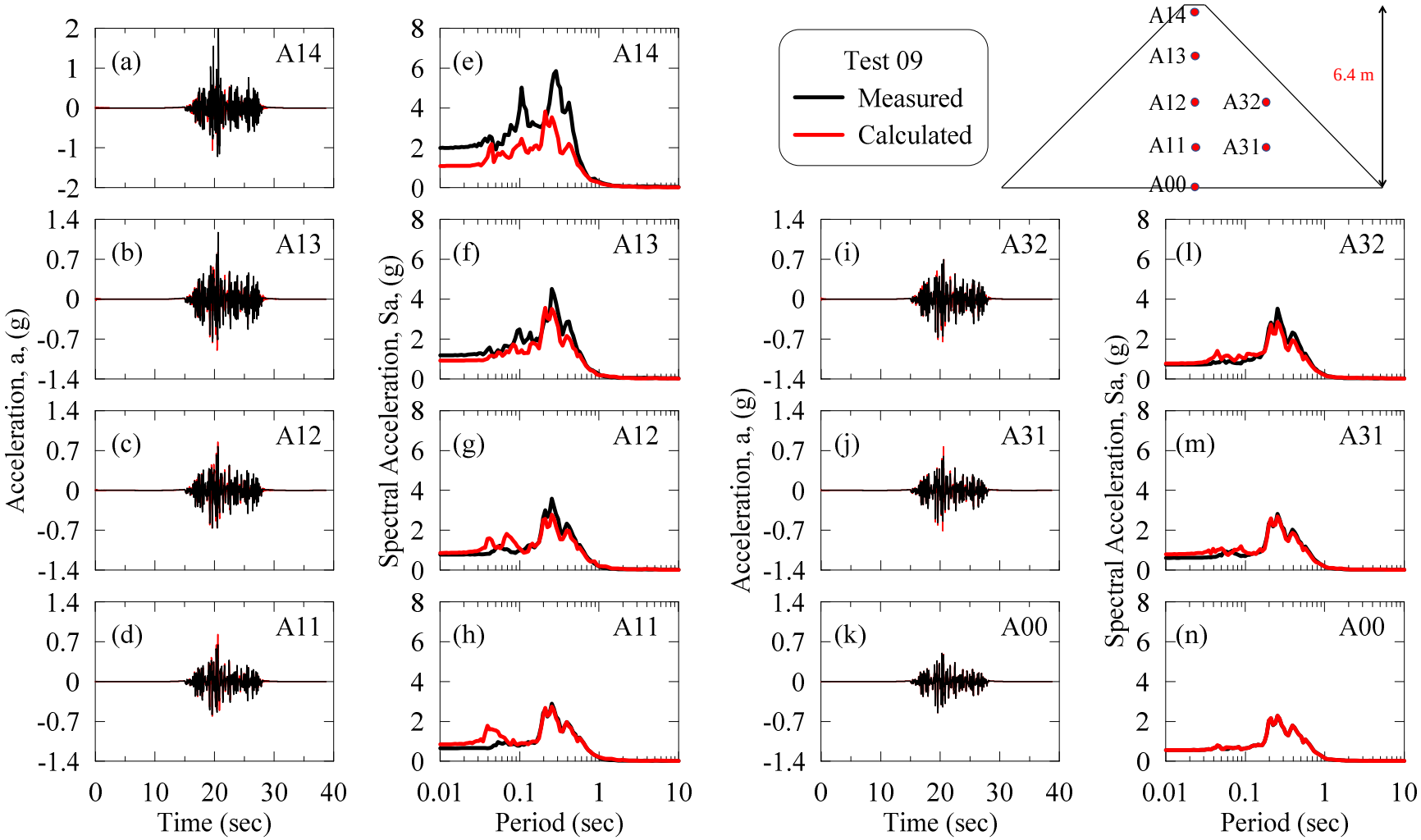

Figure A.62: Acceleration time histories and response spectra at different depths of dam during Test 09 for friction contact and the dynamic soil curves of Darendeli (2001) with Masing un/reloading.

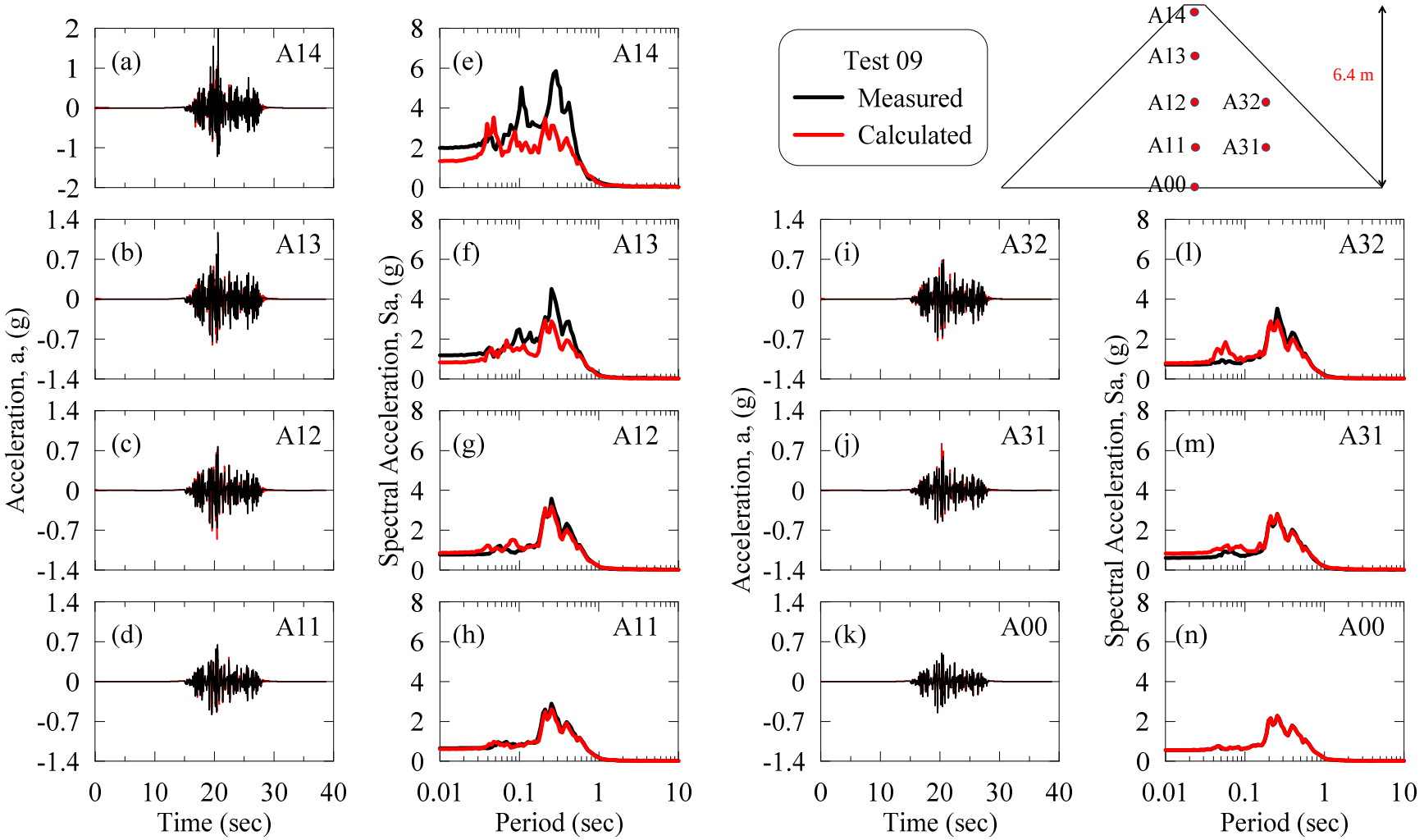

Figure A.63: Acceleration time histories and response spectra at different depths of dam during Test 09 for welded contact and the dynamic soil curves of Darendeli (2001) with Masing un/reloading.